AN EXPERIMENTAL AND NUMERICAL INVESTIGATION OF THERMOCAPILLARY DRIVEN PHENOMENA FOR EVAPORATING MENISCI IN CAPILLARY TUBES RELATED TO MICROELECTRONICS COOLING

Cosimo Buffone

Thesis submitted for the degree of
Doctor of Philosophy
THE UNIVERSITY *of* EDINBURGH
2004

DEDICATION

To my grandparents Giorgio Martino and Francesca Luzzi to whom I am deeply indebted for life.

DECLARATION

I declare that this Thesis has been composed by me, the work is my own and it has not been submitted for any other degree or professional qualification except as specified.

ACKNOWLEDGMENTS

I am proud to say that I am a highly motivated self sufficient person, well qualified in taking care of myself. I want to thank my parents for their support through all my life. I am especially indebted with my mother and grandmother because they have both taught me how to be independent at home. My grandparents have contributed enormously in teaching me during the important years of my childhood a few but essential ideas that still drive my life nowadays. The good mix of passion and physical strength of my grandfather (Giorgio) along with the calmness and perseverance of my grandmother (Francesca) are undoubtedly found in my every day life. They are both gone now but I can honestly say that their main driving forces are still alive with me. This is the most precious gift I could have ever received as it can only be passed from person to person with love.

I am also grateful to my supervisor Dr. Khellil Sefiane, for his understanding of my passionate and sometime difficult way of dealing with everyday life. He, more than anyone before, has greatly contributed in boosting my self-esteem and the knowledge of the subject we have been studying together. I am also indebted with my co-supervisor Dr. John Christy for his support, enthusiasm and guidance in many circumstances.

I would like to express my gratitude to our technicians (Bobby, Kenny, Rab and Alistair) who have helped me a lot with their invaluable suggestions in building up many test rigs.

Special thanks go to Prof. Peter Stephan of the Technical University of Darmstadt (Germany) for his help and suggestions in setting up the Thermochromic Liquid Crystals (TLC) experiment. I have visited his lab in September 2001 and learned many useful things about unsealed TLCs. I also would like to thank Dr. David Kenning of Oxford University for his passionate talks and recommendations about TLC. I am also indebted to Prof. William Easson (THE UNIVERSITY *of*

EDINBURGH) for kindly providing access to the Particle Image Velocimetry software facility. Thanks to Ms. Lynn Fitzpatrick of United Wire Ltd. for providing the stainless steel screen for the surface coating investigation.

Thanks go also to Dr. Song Lin of Thermacore Europe Ltd, Mike Bradley of Praxair Surface Technology and most of all to Mr. Luigi Buffone all involved in the heat transfer enhancement in heat pipe applications using advanced surface coating technique investigation.

Finally, I wish to thank the Engineering and Physical Science Research Council for the financial support of the project under Grant/N02122; the EPSRC Engineering Instrument Pool for providing the two IR camera systems; and THE UNIVERSITY *of* EDINBURGH Development Trust funding supports are also gratefully acknowledged.

PUBLICATIONS RESULTING FROM THE PRESENT PROJECT

Journal Papers

C. **Buffone**, K. Sefiane, J. Christy; 2004, *Experimental investigation of the hydrodynamics and stability of an evaporating wetting film placed in a temperature gradient*, Applied Thermal Engineering, Vol. 24, pp. 1157-1170. From Chapters III-V.

C. Buffone, K. Sefiane; *IR measurements of interfacial temperature during phase change in a confined environment*, Experimental Thermal and Fluid Science (Article in Press). From Chapter V.

R. Bennacer, K. Sefiane, M. El-Ganaoui, **C. Buffone**; 2004, *Numerical investigation of the role of non-uniform evaporation rate in iniziating Marangoni convection in capillary tubes*, International Journal for Numerical Methods for Heat and Fluid, Vol. 14, Issue 7, pp. 877-890. From Chapter VI.

C. Buffone, K. Sefiane; 2004, *Investigation of Thermocapillary convective patterns and their role in the enhancement of evaporation from pores*, Int. Journal of Multiphase Flow, Vol. 30, Issue 9, pp. 1071-1091. From Chapters II-III-V.

C. Buffone, K. Sefiane, L. Buffone, S. Lin; *Heat transfer enhancement in heat pipes applications using surface coating"*, Journal of Enhanced Heat Transfer (Article In Press). From Appendix B.

C. Buffone, K. Sefiane; *Temperature measurement near the triple line during phase change using Thermochromic Liquid Crystals thermography*, Experiments in Fluids (Article submitted). From Chapter IV.

C. Buffone, K. Sefiane, JRC Christy; *Micro-PIV investigation of thermocapillary Marangoni convection for an evaporating meniscus*, Physics of Fluids (Article submitted). From Chapter III.

International conferences

Apr 19-24, 2004	R. Bennacer, El Ganaoui, K. Sefiane et **C. Buffone**, *Investigation of coupled thermocapillary convection to liquid/vapour transition occurring in capillary tubes*, CHT-04, International Symposium on Advanced in Computational Heat Transfer, Norway.
July 20-23, 2003	**C. Buffone**, C. Bruno and K. Sefiane; *Liquid Metal Heat Pipes for Cooling Rocket Nozzle Walls*, 39th AIAA/ASME/SAE/ASEE Joint Propulsion Conference and Exhibit, Von Braun Center, Huntsville, Alabama, USA.
June 3-6, 2003	El Ganaoui, R. Bennacer, K. Sefiane et **C. Buffone** ; *Etude numérique de l'influence des conditions thermiques sur les transferts à l'interface liquide/vapeur dans un tube capillaire*, Congrès de la Société Française de Thermique, Grenoble, France.
April 23-25, 2003	**C. Buffone** and K. Sefiane; *Marangoni convection in capillary tubes filled with volatile liquids*, 1st International Conference in minichannel and microchannel, Rochester, NY, USA.
April 23-25, 2003	**C. Buffone**, L. Buffone, K. Sefiane, S. Lin and M. Bradley; *Heat pipe performance ehnancement for microelectronic cooling*, 1st International Conference in minichannel and microchannel, Rochester, NY, USA.

Aug 25-29, 2004	The 2004 Younger European Chemists' Conference, at Villa Gualino, Torino, Italy.
Sept 22-25, 2004	**C. Buffone** and K. Sefiane; *Experimental study of convective patterns for volatile wetting films*, 3rd International Symposium on Two-Phase Flow Modelling and Experimentation, Pisa, Italy.
Sept 22-25, 2004	**C. Buffone**, K. Sefiane, R. Bennacer and El Ganaoui; *Numerical study of heating effect on thermocapillary convection for an evaporating meniscus*, 3rd International Symposium on Two-Phase Flow Modelling and Experimentation, Pisa, Italy.

National conferences and meetings

May 12, 2004	**C. Buffone**, K. Sefiane, Temperature measurement for an evaporating meniscus in a capillary tube using TLC thermography, 22nd Hexag meeting, Warwick University, UK.
Dec 15, 2003	Set for Britain, by Britain's Younger Engineers, at the House of Common, London, UK.
Sept 9-10, 2003	**C. Buffone**, K. Sefiane, J. Christy; *Experimental investigation of the hydrodynamics and stability of an evaporating wetting film placed in a temperature gradient*, 8th UK National Heat Transfer Conference, Oxford, England, UK.

Awards

- International Travel Grant (£300) from the Royal Academy of Engineering to present two papers next September at the International Symposium Two Phase Flow Modeling and Experimentation in Pisa (Italy), March 2004.
- Set for Britain, Engineering competition – Poster Presentation, by Britain's Younger Engineers, at the House of Common, London, 15th December 2003
- 2 Small Project Grants (£470, £400) obtained at the University of Edinburgh for advanced technological techniques, 2002-03.

TABLE OF CONTENTS

CHAPTERS

I. Introduction

II. Evaporation of volatile liquids in capillary tubes

III. Thermocapillary convection study in capillary tubes using μ-PIV technique

IV. The use of Thermochromic Liquid Crystal to map temperature near the contact line region

V. Interfacial and tube wall temperature measurements during phase change in confined environment with the use of Infra Red Thermography

APPENDICES

B. Tungsten-liquid metal heat pipes for cooling heavily thermally loaded rocket nozzle walls of spacecraft engine

LIST OF TABLES

LIST OF FIGURES

NOMENCLATURE

Symbol	Definition
$A = 4\ \pi R^2$	External tube surface for heat transfer
A	Tube cross section area
B	Body
BC	Boundary conditions
$Bi = \frac{hd}{k}$	Biot number
$Bo = \frac{\rho g R^2}{\sigma}$	Bond number
$Br = \frac{\mu V_m^2}{k\Delta T}$	Brinkman number
$Ca = \frac{\mu\kappa}{\sigma R}$	Capillary number
C	Concentration
CCD	Charged Coupled Device
$CNLC$	Chiral Nematic Liquid Crystals
CPL	Capillary Pumped Loop
C_p	Specific heat
C_{sat}	Saturation concentration
d	Arc length
d_{eff}	Effective particle diameter
d_P	Particle diameter
d_s	Diffraction limited spread function
d_{sep}	IR camera spatial resolution

D	Diffusivity into air
f	Lens f-number
FPA	Focal Plane Array
g	Gravitational acceleration
h	Airside heat transfer coefficient
h_{fg}	Latent heat of evaporation
ΔH	Molar latent heat of vaporization
HSI	Hue Saturation Intensity colour system
HTL	Heat Transfer Loop
k	Thermal conductivity
$Kn = \frac{\zeta}{d}$	Knudsen number
IR	Infra Red
$\vec{1}$	Unity vector
$l_c = \sqrt{\frac{\sigma}{\rho g}}$	Capillary length
l_{evap}	Length conductive liquid layer
l_δ	Tube meniscus micro-region length
L	Meniscus distance from the capillary mouth
LN_2	Liquid nitrogen
M_g	Microscope magnification
M	Molecular weight
$Ma=\frac{\left(\frac{\partial\sigma}{\partial T}\right)\Delta TR}{\mu\kappa}$	Marangoni number
MHP	Micro Heat Pipe

$\dot{m}$	Evaporation mass flux
N	Particle image density
NA	Microscope numerical aperture
NDT	Non Destructive Testing
$Nu = \frac{2hR}{K_a}$	Airside Nusselt number
P	Total pressure in the gas phase
$\Delta P_D = -\frac{A}{\delta^3}$	Disjioining pressure
PDE	Partial Differential Equations
$Pe=Pr\ Re$	Peclet number
PIV	Particle Image Velocimetry
$\mathrm{Pr} = \frac{\upsilon}{\kappa}$	Prandtl number
P_v	Saturated vapour pressure
$P' = \frac{P_v}{\rho g R}$	Normalised vapour pressure
q	Heat flux
Q	Total Heat
$\Re$	Constant for ideal gases
ra	Average surface roughness
RGB	Red Green Blue colour system
rms	Root mean square surface roughness
R_i	Themal resistance
r, R	Capillary tube radius
$Ra = \frac{g\beta \Delta T R^3}{\upsilon \kappa}$	Rayleigh number

$\mathrm{Re} = \frac{Ma}{\mathrm{Pr}}$	Reynolds number
s	Tube wall thickness
S	Tube perimeter
S_δ	Tube meniscus micro-region area
T	Temperature
T_b	Liquid boiling temperature at pressure P
T_c	Temperature at the meniscus wedge
T_C	Critical temperature
TLC	Thermochromic Liquid Crystal
ΔT	Temperature difference along meniscus
$\vec{\nabla} T_l$	Liquid temperature gradient
$U = \frac{\frac{\partial \sigma}{\partial T} \frac{\partial T}{\partial x} R}{\mu}$	Thermocapillary velocity scale
U_r	Fluid velocity
U_r	Particle velocity
V_m	Average liquid velocity
W	Fraction of total power
X	Mole fraction
x	Axial coordinate
Δz_0	Laser sheet thickness

Greek symbols

α	Surface tension at reference temp
β	Volumetric expansion coefficient

γ	Gradient of surface tension
δ	Meniscus conductive layer mean thickness
$\kappa = \dfrac{k}{C_p \rho}$	Thermal diffusivity
λ	Laser wavelength
ν	Kinematics viscosity
μ	Dynamic viscosity
ρ	Density
ϑ	Angular coordinate
θ	Steady apparent contact angle
ϕ	Angle of incident light
σ	Surface tension
τ	Time scale
$\xi = \psi P'$	Dimensionless parameter
ψ	Dimensionless vorticity

Sub-scripts

a	Air
cond	Conduction
conv	Convection
diff	Diffusion
evap	Evaporation
l	Liquid
r	Radial direction
SL	Solid-Liquid

SV	Solid-Vapour
x	Axial direction
w	Wall

THESIS OUTLINE

The author thought that few words here can help the reader for a better understanding of the layout. This will also hopefully clarify the choices made and make the reading more interesting.

It must be pointed out that because of time and space limitation, despite all efforts made by the author the present thesis requires some basic knowledge of the field to be read. However, it must also be underlined that because each experimental technique was not previously operating at the School of Engineering and Electronics at THE UNIVERSITY *of* EDINBURGH, each Chapter gives all the relevant references along with results, discussion and analysis; therefore, in this sense each Chapter can be regarded as self-content.

Different experimental situations and different experimental techniques along with a numerical part will be presented in this work. It was a strategic choice to carry out the study in blocks and analyze the corresponding results, building up the whole picture piece by piece as a puzzle. This has helped the author in getting always more interested and deeply involved into the research being carried out. In addition, in parallel the work was being presented in international as well as national conferences and meetings, keeping high the motivation and sense of fulfilment that are absolutely necessary ingredient to succeed in a long and sometimes adverse road that a PhD can be. The author can state that strategic planning was crucial, probably more important than hard work. An enormous effort in carefully planning the work has been done all throughout the project and this in the long term has certainly paid off.

The thesis starts with an introduction in Chapter I where basic knowledge and important related works are presented. More emphasis is given to those few fundamental works that are closer to the present study. It is clearly stated how this fundamental study can be related to practical applications, although more specific information can be found in the two appendices provided where two cases of practical relevance have been studied in details. In the same chapter a section highlighting all important dimensionless parameter to be used in the study is made.

Chapter II describes the evaporation of volatile liquids in capillary tubes using a very basic experimental facility. The importance of this preliminary study is essential for what follows and thus more emphasis is given to fundamental aspects connected with the evaporation process like what happens at the meniscus contact line region.

In Chapter III the first important experimental technique is presented. Micro-Particle Image Velocimetry is the core experimental technique used in this study, as it allowed to extract important information on the liquid flow structure otherwise impossible with localised measurements. Three different experimental set-ups are described, analysed and discussed in depth. The most important information is shown here on the convective pattern inversion with extra heating applied. Important links are made with the previous chapter and a universal phenomena connected with the evaporation of liquids in small capillary tubes is deduced.

Measurements at small scale are always difficult, but it is more tricky when it comes to temperature measurements as normal techniques like thermocouples cannot be employed. Therefore, a different choice was necessary. Liquid Crystal thermography has been used to map the temperature of the tube wall close to the meniscus contact line region. This experiment described in Chapter IV was fundamental as it has proven to be a back up for the next one. In addition, it is shown that two different regions exists in the meniscus liquid phase. One close to the meniscus where heat transfer is convection dominated and the other far away in the bulk phase where the heat transfer is conductive dominated. It is also proven that as hypothesized previously, the heat necessary to sustain evaporation comes essentially from the environment surrounding the tube.

The second fundamental experimental study is presented in Chapter V. InfraRed has been really crucial in mapping the temperature of the capillary tube walls and most of all in providing, otherwise difficult to measure, important information on the interfacial temperature. It was possible to confirm the effect of the gravitational field on the liquid convection studied, outlined and discussed in Chapter III. This temperature investigation has proven extremely important to underline that there is indeed a differential evaporation along the curved liquid-vapour interface and the consequent non linear gradient of temperature generates differences of surface tension that in turn drive the observed liquid convection. Measuring the meniscus temperature profile has allowed to perform dimensionless analysis and confirm that the convection is driven by thermocapillary effects. In conclusion, both the wall and meniscus temperature measurements have permitted to set consistent and realistic boundary conditions in order to perform numerical simulations, some of which found in good quantitative agreement with the experiments.

A numerical analysis follows in Chapter VI. A numerical code based on Finite Volume Method (FVM) approximation adapted from a code developed for solid-liquid systems through a collaboration with a French team was used to simulate the liquid convection from an evaporating interface. The important contribution made here was the coordinate transformation introduced to account for a curved interface. This has proven to be a quite useful strategy as it can easily account for moving and deforming interfaces. Quantitative (when possible) and qualitative good agreement was found between numerical results and experimental data.

Chapter VIII close the study highlighting the major results obtained from the fundamental giving also some insights for further possible investigations. This is meant to stimulate the research in this fascinating, interesting and commercially attractive subject.

In the appendices two cases of practical importance have been studied. One is an experimental investigation of advanced surface coating technology for fins and the other is a conceptual (corroborated by a parametric numerical study) idea to apply heat pipe technology to cool high temperature hypersonic nozzle for future generation spacecrafts.

ABSTRACT

In the last century surface tension driven phenomena have attracted much attention due to the recognition that surface tension becomes an important parameter in small scale processes. Many industrial applications such as spreading of drops, surface acting agents, combustion, evaporation and condensation of thin liquid films rely on the effect of surface tension. The present work was inspired by the important challenges faced by the micro-electronics industry. It is well known that with miniaturization and processor speed increase, air cooling technology will no longer be able to handle the very high heat flux produced. New technological solutions are therefore needed. The general solution proposed is to pass from a single phase to a bi-phase system, because of the very high heat fluxes connected with phase change. Heat pipes are among the technological solutions proposed. In the heat pipe a fluid undergoing evaporation and condensation transfers very high heat fluxes in a self-induced convection cycle. Most of the advantages of using heat pipes makes this technological solution a quite attractive one not only for the micro-electronics industry.

Problems in these processes have only been solved for very simple cases and even then in quite a qualitative manner. Experimental difficulties in making small scale measurement of parameters such as temperature, pressure and velocity limit full understanding of the phenomena being investigated. The coupling of experimental techniques and numerical simulation can substantially help in understanding the basic mechanism taking place in surface tension driven phenomena. The present work is an experimental and numerical investigation of the hydrodynamics of a meniscus formed by a liquid in capillary tubes undergoing phase change. The non uniform evaporation process along the liquid-vapour interface leads to self-induced temperature field that in turn generates surface tension gradients along the meniscus. The interfacial stress so created drives a vigorous liquid convection that is measured by using a micro-Particle Image Velocimetry (μ-PIV) technique. Temperature measurements using advanced Infra Red (IR) and Thermochromic Liquid Crystal (TLC) techniques allowed us to measure the interfacial temperature profile (IR) and external capillary tube temperature (TLC). Measuring velocity and temperature at such scales is not

trivial because conventional techniques such as thermocouples cannot be used. Therefore, efforts have been made to compare the measurements gathered from different techniques: TLC and IR external wall measurements for the temperature field and μ-PIV measurements and numerical analysis for the velocity field. The TLC temperature measurements show the important sink effect close to the meniscus near contact line region. By measuring the evaporation mass flux and performing a heat transfer analysis based on the measured wall temperature of the system, a very good agreement was found, giving confidence to the temperature measurements performed with TLC. IR measurement of the external capillary tube wall was also taken and compares well with the TLC ones. Tube sizes ranging from 200 to 1,630 μm and four volatile liquids were investigated. Different experimental studies were conducted with both vertically and horizontally oriented capillaries, with and without external heating. It is observed that symmetrical flow patterns found in horizontal diametrical sections of the tube are dramatically distorted in vertical diametrical sections, presumably due to gravity. The IR measurements of the liquid-vapour interface temperature revealed clearly the effect of the asymmetrical flow pattern on temperature field. The direction of the induced convection rolls can be reversed by applying a temperature gradient along the capillary wall. With the tubes plunged in a pool of liquid, it is interesting to note that providing external heating to the system can substantially change the convection patterns. In particular is was revealed that the flow is enhanced when the heating element lies below the meniscus; on the contrary, when the heating element is above the meniscus and sufficient power is provided, the flow pattern is reversed with respect to the unheated situation. This important result confirms the fact that the phenomena being studied are strongly dominated by the action of surface tension. The numerical code used is a FVM with coordinate transformation in order to take into account the curved meniscus. The code was used to first reproduce some of the results obtained experimentally and successively was used to investigate those cases not easily accessible to experiment. Good quantitative (when possible) and qualitative agreement was found between experimental and numerical results.

Results gained, both of velocity and flow map, meniscus temperature and finally numerical confirmation clearly lead to the conclusion that the heat and mass transfer in such small systems is strongly affected by the mechanism taking place in the meniscus contact line region.

In this work, two cases of practical interest were also examined. The first concerns a heat pipe module for micro-electronic cooling where the effect of surface coating on the fin stack unit was experimentally investigated. The second is an extension of existing heat pipe technology to cool a heavily thermally loaded nozzle of future spacecraft vehicles of high specific impulse.

CHAPTER I

Introduction

1.1 Motivation

Fluid flow phenomena at small scale (below 1 mm) have attracted since last century lot of attention in the scientific community. Despite some of the fundamental mechanisms having been guessed over the years, much is still to be done to confirm these theories and understand deeper the phenomena. When an interface between two phases exists, surface tension driven phenomena can play an important role. Surface tension phenomena can be due either to temperature differences (termed as thermocapillary Marangoni) and/or concentration differences (termed as solutal Marangoni). In the present investigation the case of thermocapillary Marangoni will be considered. However, it is quite straightforward to extend the conclusions reached to the case of solute or thermo-solutal Marangoni. Many important applications rely on the role of surface tension. A good review on various problems involving surface tension is given by Levich and Krylov [1]. The decay of cylindrical jets (firstly systematically investigated by Lord Rayleigh), surface waves, spreading of drops, combustion, many chemical engineering processes (such adsorption, liquid extraction, surfactants), evaporation and condensation of thin liquid films (nowadays extensively used in the fast growing micro-electronics industry), hydrodynamic instability due to thermo-solutal Marangoni effect, are only some of the areas where surface tension phenomena take place. It is recognised that all these problems are solved for very simple cases and yet in a quite qualitative manner. Surface tension becomes the dominant effect in all those cases involving an interface when the characteristic dimension drops below 1 cm (typical value for the capillary length $l_c = \sqrt{\dfrac{\sigma}{\rho g}}$ of organic liquids). Experimental difficulties in small scale measurements of parameters such as temperature, pressure, velocity are still an important issue in such small configurations. This is essentially the reason of a lack of deep understanding of the mechanisms involved at small scale. Things become even more complicated when the interface undergoes heat and mass changes as in the case of evaporation or condensation. This problem has been investigated in the present study where the case of evaporation is considered. In principle there is no problem in considering condensation, because both phase changes are regulated by similar parameters and mechanisms. However, in the present study evaporation has been chosen owing to specific problems encountered in one of the possible industrial applications as will be introduced shortly.

Although, as pointed out earlier, this is a fundamental study in the general area of surface tension driven phenomena, the study has been inspired by one important industrial application. Since their appearance, computers have evolved at an exponential rate and become a normal and indispensable item at work, home, sport and leisure in general. This fast growth is also due to a substantial reduction of price, space and weight. In the 60s' Moore [2] predicted that for another decade at least the trend established for a new integrated circuit in doubling the number of components almost every two years will have been kept. Almost four decades later this statement is still valid and is predicted to be kept for the next decade at least. Reducing size and at the same time increasing substantially the speed of chips, produces a dramatic increase of heat flux generated and to be handled. It is well known that another important issue are the spots of high temperature reached in some regions of the chips that cause the entire chip to slow down. It is also recognised that the heat flux limit (~10 W cm^{-2}) that can be handled by forced convection has been well reached and overcome in many cases. New cooling solutions are thus sought in order to keep the trend imposed by the chips manufacture industry. The next generation of cooling technology will certainly rely on phase change. It is a known fact that very high heat transfer coefficients between 100 and 1000 times those reached in forced convection are achievable with phase change. The idea is thus to use liquids that in contact with the hot chip vaporize and cool the chip down; then the heat so removed is transported where it is easier to discharge in the surrounding ambient. Many technological solutions have appeared in recent years such as heat pipes (HP), capillary pumped loops (CPL), fountain atomizers and heat transfer cells [3]. All these technologies rely substantially on phase change. Particular attention is given here to problems related to the HP and CPL. Advanced designs are suited even for space applications where there is no action of gravity in helping to bring back the liquid to the hot sections. The HP born as a thermal management solution for space, has evolved since to ground applications such as electronics and biomedical cooling. The HP operational principle is given in Appendix A where some of the aspects related to an applied case will be experimentally studied. It can be anticipated, however, that the working fluid describes a cycle undergoing evaporation in the pores of the wick structure because of the heat provided by the hot source; the vapour then moves towards the condenser section transporting the heat removed that is released to the surrounding ambient by undergoing condensation. The liquid is then driven back to the evaporator section using the wick structure capillary action, closing the cycle. The most thermally loaded HP section is certainly the evaporator, essentially because of the small size of this region dictated by the chip size. Very high heat flux can be achieved in this section with peaks of 200 W cm^{-2}. Therefore, particular attention will be devoted in this study to investigate fundamental phenomena taking place when a liquid evaporates in a confined space.

The investigation of such phenomena is relevant to a wide range of applications. The heat fluxes achieved near the triple line of an evaporating meniscus are very high. Exploring the various mechanisms taking place near this region is very important in many fundamental phenomena such as thin films evaporation and condensation, boiling heat transfer, phase change in porous media, etc.

1.2 Background

The evaporation of a liquid in a confined space is the main objective of this experimental and numerical study. It is very important to make the right choice about the physical system used for this investigation. Surface tension gradients arising from temperature differences along the liquid-vapour interface lead to interfacial stress that in turn drives a convective pattern in the bulk. Different experimental studies have appeared during the past aimed in investigating these phenomena.

Early works made by Bénard [4-5] have investigated the case of a liquid layer heated from below and observed convective patterns. However, Bénard attributed it to gravity effect (buoyancy) and it was only half a century later that Pearson [6] proposed a different explanation attributing the cause of the flow to surface tension effect. Pearson was the first to introduce a new dimensionless number later on called Marangoni number, after the Italian physicist Carlo Marangoni [7]. For correctness, it must be remembered that both Marangoni and Pearson were not the first to have discovered or understood these effects [6-7]. James Thompson observed surface tension effects in drops of alcohol spreading on water surface, but his work went unmentioned till Marangoni contested the explanations brought by the Van der Mensbrugghe. Pearson [6] explanations on the causes of the observed flow were based on Cousens' investigations of drying paint films. Pearson's showed that for liquid layers thinner than 1 cm surface tension forces are responsible for the onset of motion. He also pointed out that the case of a shallow evaporating film can be treated similarly leading to similar conclusions. In addition Pearson pointed out that Cousens was carrying out experiments with volatile and non volatile liquids and says that adding a volatile liquid with higher surface tension to a non volatile liquid could inhibit the motion observed.

In subsequent studies, a different problem has been tackled. The temperature gradient along the liquid interface has been created by maintaining a temperature difference between the two end walls of a shallow liquid layer as in [8-10]. The work of Riley [10] is more concerned about the hydrothermal waves that generate at the surface of shallow liquid film with a temperature difference imposed at the sides. Hydrothermal waves propagate on the free surface in a certain direction depending on the *Pr*. For large *Pr* like Silicon oil (*Pr* = 13.9, value very close to the one of ethanol used in the present investigation) the thermal waves propagate against the surface flow driven by surface tension.

Three experimental techniques were used in the study of Riley [10]: shadowgraph, infrared and Laser Doppler Velocimetry (LDV). The author points out the extreme usefulness of the infrared camera in mapping the surface temperature distribution. However, despite accurate, LDV measurements give only one component of the velocity vector and it is a sometimes quite tedious technique due to its setup. Different flow regimes were observed; steady unicellular, steady multicellular and oscillatory flow. The boundaries of these regions were established and showed good agreement with the linear stability analysis performed. The experiments back up the findings of the linear stability theory of Smith and Davis [11-12] where, however, no effect of buoyancy was considered ($Bo = 0$). Despite no zero value of the Bond number (Bo) can be achieved on earth experiments, Riley [10] shows the existence of oblique hydrothermal waves for low Bond number (~0.222).

A different case is investigated numerically by Shieh [13], who also shows qualitative agreement with experiments. Shieh studied the case of thermocapillary-buoyancy driven convection in an insulated rectangular tank with free surface in the middle of which a heat source is placed. The situation is complicated by the fact that the liquid undergoes mass change at the free upper surface. This situation is very close to the floating-zone method widely used in crystal-growth. The floating-zone allows the formation of very pure single crystals with drastic reduction of fouling at the container walls [14]. Local horizontal temperature gradients opposed to the global imposed temperature gradient between the end walls (Villers and Plattern [8]) and vertical temperature stratification in gravitational environment (Villers and Plattern [8] and Shieh [13]) are dangerous sources of instabilities for liquids with Pr larger than one (strong coupling between thermal and momentum fields); this is very similar to the investigation being carried out in the present thesis as will be shown in later chapters. Shieh [13] shows clearly that there is significant enhancement of convection by the heat sink due to evaporation that produces a more vigorous and efficient mixing. Shieh also demonstrated that Marangoni convection drives the liquid from hot to cold regions of the flow diminishing the temperature gradients along the interface helping in stabilizing the unstable temperature stratification produced by evaporation. A comment must be made on his assumption that there is no convection in the air phase above the liquid interface. It is true that because the liquid interface is colder than the surrounding air no natural convection is expected, but there could be a substantial heat transfer due to convection because mass is transferred to the air-vapour system at high velocity (density ratio between liquid and vapour ~400 for ethanol).

Combined thermocapillary-buoyancy convection play a major role in many other significant engineering application involving free surfaces with temperature gradients. Glass manufacture [15] and welding [16] are only two among them. Many numerical studies have appeared in these areas such as Ramanan and Korpela [16] and Bergman and Ramadhyani [17]. Ramanan and Korpela [16] considered thermocapillary convection in an axi-symmetric configuration relevant to welding. As clearly pointed out by Ramanan and Korpela [16], in their study there is a substantial solute Marangoni convection due to the unavoidable surfactants adsorbed on the interface, but they do not consider this effect and concentrate instead on thermocapillary convection only. It is interesting to note the shape of the heat flux imposed at the top surface. They use a Gaussian distribution since this proved to be realistic for welding experiments as referenced. This is an important point as a similar boundary condition will be used for the present investigation in the numerical simulation chapter to model the heat flux profile along the meniscus interface. The role of *Ma* (positive and negative, depending on the direction of the imposed temperature difference along the interface) on the flow field and *Nu* is outlined in [17]. It is shown that the resulting convection helps in enhancing the heat transfer coefficient by a factor of 2-2.5. Negative *Ma* usually diminishes *Nu* whereas positive values contribute to enhance the heat transfer. However, it is shown that the role of *Ma* is drastically reduced as the *Ra* is increased and all cases tend to the curve given for $Ma = 0$ at high *Ra*.

Different works have appeared in recent years to point out that the phenomenology of small scale flow is substantially different from the common large scales extensively investigated so far. There is also an important industrial interest in small scale application for different areas. In the following a few key works will be presented to clarify some aspects of small scale flow applications.

In the work of Tso and Mahulikar [18] it is recalled that some researchers experimentally demonstrated how the continuum flow assumption does not break down when the pore size is in the range of 4.5-50.5 μm, and a good agreement has been found between value measured and predicted using the Navier-Stokes equations. Other researchers investigated the flow in microtubes with Reynolds number ranging from 250 to 20,000 and Prandtl number ranging from 0.7 to 5 noticing a reduction in the friction factor and an enhancement in the heat transfer. Although the continuum assumption is still valid for those flows with characteristic dimensions comparable with the turbulent scale, the Reynolds analogy is only valid for Pr~1. In micropores the laminar sub-layer boundary region for turbulent flow is dramatically altered by the interaction of turbulent eddies with the walls causing an enhanced mass and thermal energy transfer between the turbulent flow and the walls. For conventionally sized tubes the coefficient of heat transfer depends on the thermal fluid conductivity and on the hydraulic pore diameter. For microchannel the dependence is more complicated and involves a lot of other parameters, among which: fluid properties, velocity, wall characteristics, microchannel dimensions, fluid temperature and temperature differences between wall and fluid. Dimensional analysis taking into account all these parameters shows the existence of five dimensionless numbers: Nusselt, Reynolds, Prandtl, Brinkman numbers and the ratio of the pore dimension to the hydraulic diameter. The Brinkman number (*Br*) is the ratio of viscous heating to fluid conduction; in other words the ratio of the heat transferred form the wall by the fluid conduction to the viscous shear stresses work. *Br* could also be written as the ratio of the temperature and velocity gradients. In general *Br* does not play a role in conventional sized tubes, but becomes important in long pipelines and thus also in microchannels where the ratio of length to diameter is as large as for pipelines.

Tso and Mahulikar [18] found that the Nusselt number is a negative function of *Br*; this could explain why Nusselt number decreases as Reynolds number increases for fluid flows where *Br* plays a role. *Br* increases as the tube's dimension reduces because the temperature gradient decreases due to a lower conduction resistance of the fluid. Tso and Mahulikar [18] demonstrated that the heat transfer coefficient has a limit over which a further reduction of the channel size does not affect it anymore; the cooling effect of the fluid is balanced by the viscous dissipation. Therefore *Br* takes into account the limit in the reduction of the micro-channel dimension. The effect of *Br* is of extreme importance in the laminar regime where the gradients are strong; its effect reduces in the transition regime (lower gradients through the cross section) and becomes negligible in the turbulent regime where the eddy break-up dominates the heat transfer mechanism. The effect of *Br* on Nusselt number is opposite if the fluid is cooled or heated, due to the reduction or increase of the fluid temperature with the viscous dissipation term respectively; but in conclusion the cooling or heating capabilities are enhanced.

Palm [19] presented a literature review of the heat transfer in one and two phase flow in microchannels. The author pointed out how there is a lack of experimental results for two phase flow in narrow tubes; on the other hand there is a good amount of work in single phase flow for diameters less than 1 mm. For one phase flow in microchannel array, for a fixed amount of heat to be transferred and a given temperature difference, the product of the number of parallel channels and their length is constant. On the other hand in laminar regime the pressure drop is inversely proportional to the channel diameter at the power of four. It can be shown that at a given pressure drop and constant mass flux, the ratio of the channel length to the product of the number of channels with their diameter must be constant. To accomplish both the aforementioned conditions the product of the number of channels with the square of the diameter must be kept constant. It is evident the advantage of reducing the tube diameter to increase the heat transfer capability of the microchannel array. The same analysis could be made for the turbulent regime, but reducing the tube diameter the effect is not as strong as in the laminar regime.

Several disagreements have been found testing microchannels: lower friction factor; larger Nusselt numbers in laminar flow and decreasing Nu with increasing Reynolds number; Nusselt increases with Reynolds less than it is expected in the turbulent regime; earlier laminar-turbulent flow transition. Palm [19] pointed out how the possible explanation of the disagreement between researchers could be linked with the difficulty of measuring the necessary values. For instance, the pressure drop is inversely proportional to the tube diameter at the power of four, thus a very precise measurement of the diameter is required. Many other causes could be responsible of the results' deviation from the classical theory valid for conventional tube sizes. The flow characteristic at the tube entrance is important to determine whether or not the flow could be considered as fully developed. Also the surface roughness plays an important role and its effects at small size cannot be neglected.

The *Br* is expected to be of fundamental importance on the heat transfer mechanism, especially in the laminar regime. Another factor to take into account considering gas flow in microchannels is the Knudsen number defined as the ratio of the mean free path of the molecules to the hydraulic channel diameter. For Knudsen numbers in the range 10^{-3}-10^{-1} the no-slip condition at the wall is no longer valid as the interaction between gas molecules and wall is weak; this could explain why the friction factor at small scale is lower than for common sized channels. The viscosity and the thermal conductivity of the gas in a layer close to the wall are noticeable lower than in the bulk region.

For two-phase flow systems a remarkable emphasis has been given to boiling, but because boiling is a different mechanism from thermocapillary we will not going into details here. Palm [19] pointed out how researchers devoted more attention in the evaporation processes than in the condensation one; in fact, due to the main application of micro electronic devices, the evaporator region is directly attached to the devices to be cooled, thus the evaporator becomes the most critical part.

Li et al. [20] performed an experimental investigation on pressure drop measurements in microtubes. Experiments have been conducted on frictional resistance in microtubes (diameters ranging from ~80 μm to ~180 μm) of different materials (glass, silicon and stainless steel) with de-ionized water as the working fluid. The main reason why the Nikuradse's results are widely used is that in practice we have partially or fully developed turbulent flow in coarse tubes. The effect of roughness has therefore no great importance in laminar flow. Using the scanning electron microscope Li et al. [20] characterized the internal surface of glass and silicon tubes as smooth (relative roughness < 0.1%) and that of stainless steel as coarse (relative roughness 3-4%). Due to the very high dependence of viscosity on temperature for de-ionized water, the temperature was monitored during the experiments. A calibration set of experiments has been conducted to verify the experimental reliability.

In Li et al. [20] the measured friction factor agrees with that of laminar, incompressible, fully developed flow in conventional sized tubes; it can also be seen how the transition from laminar to turbulent regime occurs at Reynolds numbers of ~2,000 as expected. For the smooth tubes (glass and silicon), results show that the friction factor agrees with that of conventional sized tubes and the transition regime occurs at Reynolds between 2,000 and 3,000. The friction factor for rough tubes departs from that of conventional sized tube and this difference increases as the tube diameter decreases (because the relative roughness increases) as much as 35% with respect to that predicted by the conventional theory. However, the transition regime remains always around Reynolds ~2,000 also for rough tubes. The uncertainty to obtain the friction factor has been evaluated around 10%; the parameters measured important for the friction factor evaluation were: tube diameter and length, pressure drop and flow rate. The inaccuracy in measuring the tube's diameter (2%) dominates the error. Li et al. [20] showed that at small scale conventional correlation valid for larger scale are no longer applicable and more work at small scale is needed to address many issues.

Wei and Ma [21] numerically studied the case of evaporation in heated capillary tubes relevant to the present study. A mathematical model of the heat transfer in a capillary tube with constant heat flux has been presented. The authors pointed out as most investigations do not focus on the effect of the position of the meniscus with respect to that of the heat flux applied along the capillary.

The following are the assumptions made for the model of Wei and Ma [21]: heat conduction in the wall is 1-D along the axial direction; heat conduction in the thin liquid film is 1-D in the radial direction; the capillary wall is smooth and therefore the liquid completely wets it; there is no pressure gradient in the radial direction in both the liquid and the vapor phase. The heat transfer problem in the wall and in the thin liquid film has been modeled using the Fourier Law with a heat source. As pointed out also in previous works, the most important region is the evaporating film region where most of the evaporation takes place; therefore Wei and Ma [21] focused their attention on this region.

The thickness of the liquid film is very small and constant at the beginning of the evaporating region (two or three orders smaller than the capillary radius). Towards the end of the evaporating region the film thickness becomes one order smaller than the capillary radius and its gradient is important. As the heat input increases the thickness of the adsorbed film decreases, the length of the evaporating region decreases and the thickness gradient increases further. When the thickness of the adsorbed film becomes of the order of one molecular layer the heat transfer pore capability limit is reached and the evaporation region cannot exist anymore. When varying the pore radius the adsorbed film thickness and its gradient do not change appreciably, but the meniscus length decreases as the radius decreases. The disjoining pressure increases (making shorter the length of the evaporating region) as the heat flux increases; instead, the capillary pressure changes gently. The shear stresses increases dramatically as the heat flux increases and as the pore radius decreases.

As pointed out by Wei and Ma [21], the relative position of the meniscus with respect to the heat flux makes important differences. The heat flux changes the disjoining pressure drastically and as a result the adsorbed film thickness decreases till a limit over which dry-out occurs. This is an important point as we will investigate the case of extra heating element position with respect to the meniscus in the course of the present investigation.

Gillon et al. [22] experimentally investigate boundary layer instabilities in evaporating liquids under low pressure and/or microwave irradiation. The evaporating meniscus of ethyl alcohol under controlled pressure and/or microwave radiation has been experimental investigated. The meniscus is maintained at the same level by a mercury piston system and the evaporation rate is measured by the level of mercury into a tank. The surface temperature is measured by IR thermography technique and the fluid motion (especially at the interface) is recorded by a video camera. The evaporation rate as a function of the applied constrain (that for the first experiment of this study is low pressure) shows three distinct regions corresponding to three different regimes. The first region (low constrain) corresponds to the purely conductive mechanism; the second region is the convection region in the liquid bulk phase; the third region corresponds to the boundary layer's instability above the buoyancy driven convection cells.

Gillon et al. [22] used latex particles to visualise the motion in the bulk liquid phase. At low constrain the purely conductive regime leads to the evaporation rate's linear domain. Increasing the constrain a motion exhibiting axi-symmetric and stationary cells in the bulk liquid phase is set; IR thermography showed that the roll centre is cold. As the constrain is further increased, the convection cells become unsteady and increase in number becoming smaller. In the transition region between the second and the third regions of the evaporation rate versus imposed pressure (constrain) curve, the so called Smith-Topley effect takes place; the convection cells slow down. Increasing further the constraint the Smith-Topley disappear and a stronger new convection regime occurs, but now at a smaller scale in the boundary layer above the buoyancy cells; this effect is called the Marangoni instability. For large value of power there is a noticeable depression of the cell's center accompanied by the propagation of thermals in the liquid phase below the growing cell. At some point the liquid is suddenly ejected from the interface and an important increase of the particles' velocity has been noticed; this effect is called the thermal boundary layer differential vapor recoil instability.

We will report now what was observed by Gillon et al. [22] under microwave irradiation (that will be referred in the following as the new constrain). The region of purely conductive regime is very small. No stationary convective regime has been observed; this is due to the autocatalytic effect: the temperature's fluctuations induce fluctuations of the dielectric loss constant and thus increment of the local temperature fluctuation. Instead two unsteady regimes are observed. The first unsteady regime takes place in a narrow interval of applied constrains and is characterized by a small slope; the particle motion is essentially axi-symmetric. The second unsteady regime takes place for a broader interval of applied constrain, the particles motion is both clockwise and anti-clockwise and accelerated and decelerated. Very large surface temperature oscillations are observed with IR thermography.

It must be pointed out as for low values of pressure, the surface temperature decreases logarithmically as the constrain (now pressure) increases; whereas for pure microwave constrain the surface temperature simple increases with the constraint. In the latter case the evaporation process is not fast enough to carry out the heat produced, that is used to heat the system. At very large microwave constrain, a new change of the evaporation rate versus the applied constraint curve is observed; this is the vapor recoil instability regime taking place without passing through the Marangoni instability regime. The work of Gillon et al. [22] is very relevant to the present investigation although extreme conditions such as vapor recoil will not be investigated here.

Swanson and Herdt [23] developed an analytical model with a numerical solution for the evaporating meniscus in capillary tubes. The model takes into account the full three-dimensional Young-Laplace equation, Marangoni convection, London-van der Waals forces and considering non-equilibrium interfacial conditions. The meniscus was divided into three regions:

1. The film region (less than 1 μm) where the London-van der Waals forces (dispersion forces) dominate;
2. The meniscus region (larger than 1 μm) where the capillary pressure forces overcome the dispersion ones and a flow is established to supply the evaporation process that takes place in this region;
3. Hagen-Poiseuille region where a Hagen-Poiseuille flow exists.

The hypotheses under which the model have been formulated are the following: axi-symmetrical problem; steady state and two-dimensional, laminar, incompressible flow; radial pressure gradient is negligible; vapour pressure constant; bulk vapour temperature equal to the interfacial vapour temperature; smooth tube walls and no-slip condition; the hydrostatic pressure is negligible; Marangoni effects are important only in the thin film region.

The solution of the momentum equation yields to the Hagen-Poiseuille flow. The solution of the energy equation has been obtained applying the von Kármán integral method assuming a linear temperature profile. A set of dimensionless, coupled, nonlinear ordinary differential equations has been written, introducing 4 dimensionless numbers: superheat, crispation, mass flux, and dispersion for description of which the reader should refer to the work of Swanson and Herdt [23]. It should be noted that the initial condition for the liquid pressure is obtained by imposing the initial mean curvature equal to *1/R* (where *R* is the capillary's radius); usually this condition is substituted by a mean curvature of zero at the triple line. The numerical solution of the linearization equations employed first-order backward finite differences.

The results show how varying the dimensionless superheat and keeping constant the dispersion number, does not have any effect on the meniscus profile. Instead varying the dispersion number the meniscus profile changes but only near the wall. At high dispersion number the thin film extends farther along the tube, because of the strong attractive liquid-solid forces. This fact leads to a noticeable change of the capillary tube pumping capability. The dimensionless mass flux peak reduces as the dimensionless superheat increases, because the dimensionless mass flux is inversely proportional to the dimensionless superheat. The dimensionless mass flux peaks in the thin film region; therefore it is in this region that most of the evaporation takes place. Increasing the dispersion number, the mass transfer increases dramatically due to the increase of the thin film region area and the liquid-vapour pressure difference. Another very interesting result of the Swanson and Herdt [23] analysis is that the capillary pressure difference as a function of the capillary radius does not change as both the dimensionless superheat and dispersion number vary; the capillary pressure difference depends only on the capillary radius (as stated by the Young-Laplace equation). This is in contrast with previous works (especially those of Wayner cited in the next chapter) which predicts an increase of the apparent contact angle and thus a capillary pressure reduction when the heat flux increases. This difference could be due: 1) to the assumption that the meniscus radius gradient along the capillary length tends to minus infinity as the meniscus radius tend to zero (this fact could force the contact angle and thus the capillary pressure to be constant); 2) or more realistically, the low superheats are not suitable to detect contact angle variations. Swanson and Herdt [23] pointed out that further investigation (especially experiments) is necessary to verify their results. The authors suggest also to perform experiments with vapour deposited surface layers of various thicknesses and materials to show how surface coating affects the meniscus capillary pumping.

A case closer to the one investigated in the present study is certainly the one tackled by Hallinan and co-workers [24-25]. In these works it is shown that for a Heat Transfer Loop (HTL) thermocapillary instabilities arising in the near contact line region can improve by 18% the HTL heat transport capability for limited heat input. However, larger heat inputs could lead to meniscus instabilities and eventually dramatically reduce the HTL heat transfer capability. Close up pictures of the meniscus interface near the contact line are presented and the authors show that the liquid wettability is improved as heat is applied by the heating element. Thin thermocouples embedded inside the glass wall close to the tube internal surface and pressure transducer were used to measure the wall temperature and vapour pressure respectively. It is shown that the increase in vapour pressure is in phase with reduction of the wall temperature; this is due to the increases in evaporation as heat is applied that in turn cools the tube wall and increases the vapour pressure. It is also shown that when the meniscus lies below the heating element there is an increase of 20% in the heat transfer necessary to the onset of instability. A stability analysis was performed and showed that the meniscus becomes unstable when thermocapillary forces become of the same order of the disjoining pressure in the contact line region. More detailed information about the meniscus contact line regions and the forces acting there will be given in the next chapter.

Pratt [25] investigated the effects of thermocapillary stresses on wetting properties in capillary tubes. It is demonstrated that thermocapillary stresses occur when a temperature gradient appears along the contact line. The Young-Laplace equation valid for static condition is no longer applicable in dynamic conditions (when evaporation takes place). To predict correctly the meniscus's wicking height (that is the height reached by a liquid inside a vertically oriented the capillary tube plunged in a pool) the Young-Laplace equation needs to take in account also the thermocapillary stresses and the viscous dissipations. Hydrostatic pressure and surface tension tend to stabilize the meniscus while thermocapillary stresses and vapor recoil act in the opposite direction.

The experimental apparatus used by Pratt [25] is described in the following because of its relevance to the present investigation. The test chamber is stainless-steel with several ports for optical and investigation access. The two optical accesses are made by quartz windows. The test chamber is necessary to minimize convection losses, contamination of the liquid by air (the wetting characteristics are very sensitive to pollution), and to enable temperature and pressure control. The capillary is a single pore borosilicate glass pipe immersed in a pool of n-pentane. N-pentane has been chosen for its very low surface tension, high volatility, and optimum wetting characteristics on glass. Three different internal diameters were tested (0.5, 1 and 2 mm). Two thermocouples have been placed inside two holes drilled in the tube's wall near the internal tube's surface. To do this a reasonable wall thickness (from 2.25 to 3 mm) has been adopted to avoid cracks. This leads to a big optical distortion when the Pratt [25] attempted to measure the meniscus apparent contact angle. The system control consist of an isotherm refrigerated circulator and a vacuum pump to control the liquid temperature in the reservoir and the vapor pressure respectively. The heater system consists of a vapor deposited thin gold film supplied with 120 mA and 400 V. The very thin film allows the transmission of light and video recording of the meniscus is possible. However, the heater resulted to be unreliable and was replaced with a nichrome heater wire supplied with adjustable power supply capable of producing up to 90 W. The vertical translation system allows external positioning of the meniscus along the capillary by adjusting the length of the pore immersed into the pool. The data acquisition system (DAS) was used to measure the voltage drop across the shunt resistor of the heater and the wall, the vapor and the liquid reservoir temperature. A high-resolution black and white camera connected to a long distance microscope composes the DAS for optical image acquisition. The light is a white intensity light filtered to allow of green light and prevent thus the heating of the meniscus by the IR radiation. Particular attention was given to the cleaning of the equipment with special care for the capillary tubes.

Before presenting his experimental results, Pratt [25] developed a model to predict the wicking height and the heat transfer in general taking into account the thermocapillary stresses. The thermocapillary stresses are due to the surface tension gradient generated by the temperature gradient near the contact line. By measuring the temperature gradient near the contact line it is possible to give an estimation of the thermocapillary stresses. Viscous dissipation was taken into account in the model using the Fanning friction factor for laminar flow. The final wicking height is equal to the static one (predicted by the Young-Laplace equation) minus the reduction due to the thermocapillary stresses and the reduction due to the viscous forces. A stability analysis has also been performed and led to an unstable regime when the Marangoni number or the thermocapillary effects are of the same order of the disjoining pressure effects.

A few comments about the work of Pratt [25] could explain clearer the choices made later for the investigation in present thesis. For the contact angle measurement post-processing of digitized images has been done. Pratt [25] decided to make the calibration using the internal tube diameter; this allows having results with a range of error overestimated, but the uncertainty of the internal wall location is higher due to the large tube thickness. It would have been possible to obtain the real location by taking into account the refraction of a ray of light through the tube round wall. An estimation of the heat introduced by radiation from the light source demonstrated that the change in wall temperature after 1 hour of test is less than 1 K, thus neglecting this source of heat is a reasonable hypothesis.

Pratt [25] took as constraint the total input power comparing results from different tube sizes. This is a quite rough assumption because the important parameter is the heat flux going into the capillary. If one keeps constant the total input power produced by the heater the heat flux changes with a power of two as the tube diameter changes. This wrong assumption could possibly lead to several wrong results' interpretation. Pratt [25] pointed out as the largest tube (2 mm ID) is capable of transferring more energy than the others and this because of the stronger buoyancy effect at this size.

The wicking height reduction due to thermocapillary stresses is much larger than that due to flow losses and as the pore diameter increases this gap increases further. The instability manifests itself as meniscus oscillations at a critical wall temperature gradient. The relative position of the heater with respect to the meniscus strongly affects the meniscus stability. While the thermocapillary effects destabilize the meniscus, the Marangoni effect stabilizes it when the heater is below the meniscus (positive wall temperature gradient).

The heat transfer effectiveness has been evaluated plotting the Nusselt number as a function of the Marangoni number. The results for 0.5 and 1 mm pore size show that when the thermocapillary effects are small the heat transfer pore capability increase as the heat input increases; this is due to the reduction of the apparent contact angle leading to an increase of the length of the thin film region where most of the evaporation takes place. When the Marangoni number reaches a critical value, the heat transfer coefficient decreases because the thermocapillary stresses "choke the flow into the meniscus"; then at high Marangoni number the heat transfer pore capability become almost insensitive to Marangoni effects. The results are different for the pore size of 2 mm, due to the different mechanism of heat transfer implying a strong convection within the reservoir. Marangoni convection is coupled with Rayleigh convection and the evaporative pore capability increases dramatically. However, the same Marangoni insensitivity effect takes place at high Marangoni number.

Pratt [25] recommends the use of more thermocouples offset circumferentially around the capillary to have a better temperature spatial resolution.

The reduction of wicking height and thus of the capillary pumping due to the thermocapillary stresses could be counteracted using a mixture of working fluid (adding small amount of less volatile liquid); this completely change the flow characteristics: Marangoni convection is no longer only due to thermal gradients but also to concentration gradients.

Pratt [25] last suggestion is to investigate the transient behavior of the meniscus in small capillaries especially at high heat input where the meniscus tends to oscillate violently.

The very thick wall thickness had led to a very high optical distortion for contact angle measurement; also the mechanism of heat transfer has been modified, due to an important increase of wall thermal resistance with respect to the liquid bulk one. The choice to take into account the heat flux instead of the total heat power would have helped for a better understanding; in fact, in this manner results from different pore sizes can be easily compared. The heater's position along the capillary tube plays an important role. The author used in most of his experimental work the heater at the end of the capillary tube and positioning the meniscus below it. A very few experiments have been carried out with the heater below the meniscus and no consideration has been made or suggested about the heater laying at the same meniscus' height. This lack could also be due to the incapacity of measuring the wicking height with the meniscus at the heater height, due to the heater opacity. However the heat transfer pore capability could have been compared also taking into account other measurable quantities like the evaporation rate, for which no optical measurement of the wicking height is required. Using particles inside the liquid phase as tracers could have helped for a better understanding of the role of Marangoni convection and also for a better comparison of results from different pore sizes. It is also surprisingly that Pratt [25] does not mention the evaporative cooling effect. As we will see in later chapters, there is an important evaporative cooling effect even with no extra heating provided to the capillary.

In another work Pratt and Kihm [26] investigated the effect of binary mixture on wetting and heat transfer from a meniscus. To alleviate interfacial thermocapillary stresses due to the interfacial temperature gradient, the authors proposed to use a binary fluid mixture. Natural concentration gradients, due to differential evaporation, counterbalance the reduction of the capillary pumping capability, due to degradation of the liquid wettability. It was demonstrated that the addition of decane to pentane does not affect the system's heat transport capability.

The experiments of Pratt and Kihm [26] consider a heated meniscus inside a capillary pumped loop system. The evaporator is a single pore capillary and the condenser is a large vapour channel. The heater is made by a fine nichrome wire spirally wrapped around the capillary with a resistance of 1 Ω/cm. The power supply is capable of producing 90 W and the power delivered is measured with a shunt resistor. The temperatures along the pore evaporator section were measured with two rows (at 180 degrees apart) of thermocouples positioned at 0.5 mm interval in the vertical direction.

When the meniscus region is heated, the wicking height is no longer predictable with the well known Young-Laplace equation, valid in static conditions. The heat produces noticeable changes of the liquid-vapour interfacial temperature gradient at the contact line. This leads to two effects: firstly, the temperature gradient produces a thermocapillary stress that is directed towards the intrinsic meniscus region (one of the contact line sub-region, of which more details will be given in the following chapters) if the contact line is hotter than the rest of the meniscus; secondly, the evaporation induces in the meniscus a flow from the liquid reservoir and therefore there are some viscous losses along the capillary. Using a binary mixture, the difference in evaporation at the meniscus region especially near the contact line, leads to another stress that acts in the opposite direction with respect to the thermocapillary stress and the viscous forces. This fact alleviates the reduction of the wicking height and therefore the capillary pumping capability.

Pratt and Kihm [26] worked with very thick capillaries (2 mm thickness) to avoid breaks during drilling to stick the thermocouples inside the wall near the internal surface of the tube. In the present investigation capillary tubes with internal diameter ranging from 200 to 900 μm and a thickness ranging from 100 to 250 μm were used. This leads to less optical distortion for contact angle measurement and a shorter time lag response to temperature changes. In the experiment of Pratt and Kihm [26] the heater was made with a wire wrapped around the capillary. In the investigation presented in this thesis, instead, the heater will be made with a silver paint which leads to better heat uniformity and lower energy losses by radiation and convection from the heater.

The spreading of liquids on solid substrates is regulated by the same mechanisms taking place in the present case. Therefore, it is important to take advantage of the large amount of work available in the literature on spreading in order to make comparisons, drawn conclusions and most of all make predictions. As pointed out by Kavehpour et al. [27] the spreading of liquids on solid substrates is of paramount importance in many relevant industrial applications such as coating and printing of inks. A non invasive technique using a laser confocal microscope has been used to investigate the evolution of viscous micro-droplets on solid surfaces. When a liquid droplet is deposited on a solid surface, rapidly a thin film is formed with a characteristic length much larger than its thickness; therefore the lubrication theory can be used to describe these phenomena. The Ohnesorge number, defined as the ratio of the viscous forces to the surface tension forces, and the intrinsic capillary length has been introduced as a parameter to detect the spreading regime and which forces act in it. Hydrodynamic instabilities can occur when there are local variations in the surface tension, which is one of the parameters that control the spreading of drops. Marangoni instabilities are the result of thermal variation perpendicular to the fluid interface and when these instabilities arise for an applied temperature field along the interface, they are usually referred to as hydrodynamic instabilities. Thermocapillary flow arises for differential evaporation along the drop interface. The evaporation rate is stronger near the contact line and thus a gradient of temperature (due to the larger cooling effect near the triple line) and a gradient of concentration (for such a system with more than one chemical component) appear and drive the Marangoni convection. A dimensionless interfacial thermal resistance is introduced (this number is essentially the inverse of the Biot number) and by linear stability analysis it is shown that there exists a critical value of this number below which there is no instability. It is also shown that as the drops spread and their height decreases, the amplitude of the oscillations increases and the frequency decreases. It is shown that dimensionless interfacial thermal resistance is inversely proportional to the film thickness and the latent heat of vaporization. When this number becomes larger than the critical value, instabilities develop. A non-volatile liquid is compared with a volatile one, and the results show that at the beginning the spreading mechanism is similar for the two cases; when the drops spread out, the heat and mass transfer due to evaporation starts to have an effect and the spreading behaviour of the volatile liquid differs substantially from the non-volatile one with clear oscillations travelling from the edge to the centre of the drop due to Marangoni instabilities. Because these waves propagate towards the hot region of the drop (apex), it can be concluded that they are indeed hydrothermal in nature as the one described by Riley [10] and Smith and Davis [11-12].

Surface contamination is very important for the present study as will be shown in later chapters and it can be said that every surface is contaminated to some degree by chemicals that can remain adsorbed on the surface or dissolve in the bulk phase [7]. Water is very susceptible to contamination and this is one of the reasons along with its very high surface tension (that will have make difficult to control the meniscus interface along the capillary glass tube) why it was not used for the present investigation. In fact, Kirdyashkin [9] shows that conducting experiments with water and ethanol (96%), the water free top surface behaves like a rigid surface because of the surfactants adsorbed. This is why special attention has been paid to the filling procedure of the capillary tubes. As will be shown in the next chapter, the tubes were washed first, stored in clean boxes and used within days to avoid contamination by dust, for instance.

The aforementioned works deal with a great amount of phenomena taking place at small scale, the most important of which is certainly thermocapillary Marangoni convection. In the present experimental and numerical investigation the observed convection in the liquid phase of an evaporation meniscus formed in confined space such as capillary tubes is the object of study. It was thought that this convection motion could be attributed to thermocapillary effects. Through the use of three different experimental techniques (micro-Particle Image Velocimetry, Thermochromic Liquid Crystal and Infra Red thermography) important information on interfacial temperature and liquid flow patterns were gathered. These techniques along with the aid of a numerical analysis have proven to be necessary tools to confirm that the phenomena observed are indeed thermocapillary driven. It is concluded that the interfacial temperature profile is the key factor for the onset of the observed convection and that the convection can be altered by modifying this temperature distribution.

1.3 Dimensionless numbers

Various are the relevant dimensionless number for the present study and they will be used where appropriate throughout the study. The problem is complicated by the heat and mass transfer taking place at the meniscus interface because of evaporation. Each dimensionless number can be expressed as a ratio of forces or a ratio of time scales. For the system investigated here, the relevant dimensionless numbers are the following.

The Marangoni number (due to thermocapillary effect only) is the ratio of surface tension to viscous forces:

$$Ma = \frac{\left(\frac{\partial \sigma}{\partial T}\right)\frac{\partial T}{\partial x} d^2}{\mu \kappa} = \frac{surface\ tension\ force}{viscous\ force} = \frac{\tau_{diff}}{\tau_{conv}} \qquad (1.1)$$

where $\tau_{diff} = \frac{d^2}{\kappa}$ and $\tau_{conv} = \frac{\mu}{\left(\frac{\partial \sigma}{\partial T}\right)\frac{\partial T}{\partial x}}$ are the diffusive and convective time scales.

The Rayleigh number expresses the ratio of buoyancy to viscous forces:

$$Ra = \frac{g\beta \frac{\partial T}{\partial x} d^4}{\nu \kappa} = \frac{buoyancy\ force}{viscous\ force} \qquad (1.2)$$

The Prandtl number expresses the ratio between kinematics viscosity and thermal diffusivity. *Pr* is only a function of the fluid physical properties. High values of *Pr* (as in the present cases) means large coupling between thermal and flow fields:

$$Pr = \frac{\nu}{\kappa} \qquad (1.3)$$

The Reynolds number is the ratio between the inertia to viscous forces and can be expressed in the present case as the ratio of *Ma* to *Pr*:

$$Re = \frac{Ma}{Pr} = \frac{\rho\left(\frac{\partial \sigma}{\partial T}\right)\frac{\partial T}{\partial x}d^2}{\mu^2} = \frac{inertia\,force}{viscous\,force} = \frac{\tau_{diff}}{\tau_{conv}} \qquad (1.4)$$

The dynamic Bond number relates the gravitational forces to surface tension gradient ones:

$$Bo = \frac{\rho g d^2}{\left(\frac{\partial \sigma}{\partial T}\right)} = \frac{gravitational\,force}{surface\,tension} \qquad (1.5)$$

The Capillary number defines the relative importance of dissipation to surface tension. Small values of *Ca* lead to non deformable interface. For thermocapillary convection *Ca* is very small (typically 10^{-3}-10^{-7}):

$$Ca = \frac{\mu \kappa}{\sigma d} \qquad (1.6)$$

The Biot number is also important in this study because of the interface and relates the convection in the vapour phase to the conduction in the liquid. Large values of *Bi* suggest vigorous convection in the vapour and poor conduction in the liquid:

$$Bi = \frac{hd}{k} \qquad (1.7)$$

Finally, the Peclet number is similar to Reynolds number for fluid flow concerning heat transport. Because *Pe* can be obtained as the product of *Re* with *Pr*, for a fluid with *Pr*~1 (such as air), there is complete similarity between flow and temperature distribution. It is the ratio of convection to diffusion forces and for the present case can be expressed as the ratio between the fluid velocity and a reference velocity evaluated from the evaporation mass rate:

$$Pe = Pr\,Re = \frac{\dfrac{\dot{m}}{\rho A}}{\dfrac{\kappa}{d}} \tag{1.8}$$

The Brinkman number is the ratio of viscous heating to fluid conduction and is defined as:

$$Br = \frac{\left[\left(\dfrac{\partial \sigma}{\partial x}\right) d\right]^2}{\mu k \Delta T} \tag{1.9}$$

The Knudsen number is referred as the ratio between the length of mean free path and the characteristic dimension and reads:

$$Kn = \frac{\zeta}{d} \tag{1.10}$$

In all what follows the liquid-vapour interface will also be referred to as meniscus because it is formed in a small space such as a capillary tube.

1.4 Conclusions

In this chapter we have outlined most of the key works appeared in thermocapillary dominated flows yet not to be considered as an exhaustive review. The author has intentionally drawn more attention to those works directly related to the present study. More and detailed information about particular cases can be found in review work, such as the one of Levich and Kryolov [1], cited in this and following chapters. The present work can thus be characterised as a study of thermocapillary Marangoni convection. The main difference with all the cited literature is that the convection has a different origin. It is the temperature gradient self-induced because of differential evaporation along the meniscus that ultimately generates the surface tension gradient being the driving force for the observed and characterised liquid convection.

Next chapter will focus on the evaporation of volatile liquid in capillary tubes where a meniscus is present. The convection pattern in the liquid phase is unveiled with the use of particles acting as tracers. Useful experimental data such as the evaporation mass flux and the spinning frequency of the convection are presented and discussed. The very interesting conclusions reached in the next chapter will be of fundamental importance in all what follows by the use of powerful experimental techniques such as micro-Particle Image Velocimetry, Thermochromic Liquid Crystals and Infra Red.

1.5 References

[1] Levich V.G, Krylov V.S., 1969, *Surface tension driven phenomena*, Annu. Rev. Fluid Mech., Vol. 1, pp. 293-316.

[2] Moore G.E., 1965, *Cramming more components onto integrated circuits*, Electronics, Vol. 38, April 19.

[3] http://www.darpa.mil/MTO/HERETIC/

[4] Bénard, H., 1900, Rev. Gén. Sci. Pures Appl., Vol. 11, pp. 1261-1309.

[5] Bénard, H., 1901, Ann. Chem. Phys., Vol. 23, p. 62.

[6] Pearson J.R.A., 1958, *On convection cells induced by surface tension*, Journal of Fluid Mechanics, Vol. 4, pp. 489-500.

[7] Scriven L.E. and Sternling C.V., 1960, *The Marangoni effects*, Nature, Vol. 187, 16 July, pp. 186-188.

[8] Villers D. and Plattern J.K., 1992, *Coupled buoyancy and Marangoni convection in acetone: experiments and comparison with numerical simulations*, Journal of Fluid Mechanics, Vol. 234, pp. 487-510.

[9] Kirdyashkin A.G., 1984, *Thermogravitational and thermocapillary flows in a horizontal liquid layer under the conditions of a horizontal temperature gradient*, International Journal of Heat and Mass Transfer, Vol. 27, No. 8, pp. 1205,1218.

[10] Riley R.J., *An investigation of the stability and control of a combined thermocapillary-buoyancy driven flow*, PhD Dissertation Thesis, Georgia Institute of Technology, March 1996.

[11] Smith M.K. and Davis S.H., 1983, *Instabilities of dynamics thermocapillary liquid layers. Part I. Convective instabilities*, Journal of Fluid Mechanics, Vol. 132, pp. 119-144.

[12] Smith M.K. and Davis S.H., 1983, *Instabilities of dynamics thermocapillary liquid layers. Part II. Surface-wave instabilities*, Journal of Fluid Mechanics, Vol. 132, pp. 145-162.

[13] Shieh C.-Y., *Unsteady buoyancy-thermocapillary induced convection in rectangular tank with phase change*, PhD Dissertation Thesis, The University of Michigan, 1985.

[14] Pimputkar S.M. and Ostrach S., 1981, *Convective effects in crystal growth from melt*, Journal of Crystals Growth, Vol. 55, pp. 614-646.

[15] Frischat V.G.H., Herr K. and Barklage-Hilgefort H., 1980, *Probleme bei der Vorb Creitung Glastechnischer Intersuchungen in Weltraum*, Glastech. Ber., Vol. 53, pp. 1-9.

[16] Ramanan N. and Korpela S.A., 1990, *Thermocapillary convection in an axi-symmetric pool*, Computers & Fluids, Vol. 18, No. 2, pp. 205-215.

[17] Bergman T.L. and Ramadhyani S., 1986, *Combined buoyancy and thermocapillary driven convection in open square cavities*, Numerical Heat Transfer, Vol. 9, pp. 441-451.

[18] Tso C.P. and Mahulikar S.P., 1998, *The use of the Brinkman number for single phase forced convective heat transfer in microchannels*, Int. J. Heat Mass Transfer, Vol. 41, No.12, pp.1759-1769.

[19] Palm B., 2001, *Heat transfer in microchannels*, Heat transfer in micro-channels, Microscale Thermophys. Eng., Vol. 5, pp.155 –175.

[20] Li, Zhi-Xin *et all.*, 2000, *Experimental study on flow characteristics of liquid in circular microtubes*, Proc. Heat Transfer and Transport Phenomena in Microscale, Banff, Canada, Begell House Inc., ISBN 1-56700-150-5.

[21] Wei Q. and Ma T.Z., 2000, *Characteristics of two-phase flow and evaporation heat transfer in a capillary at constant heat fluxex*, Proc. Heat Transfer and Transport Phenomena in Microscale, Banff, Canada, Begell House Inc., ISBN 1-56700-150-5.

[22] Gillon P., Courville P., Steinchen-Sanfeld A., Bartrand G. and Lallemant M., 1988, *Free convection and boundary layer instabilities in evaporating liquids under low pressure and/or microwave irradiation*, PCH PhysicoChemical Hydrodynamics, Vol.10, No.2, pp.149-163

[23] Swanson L.W. and Herdt G.C., 1992, *Model of the evaporating meniscus in a capillary tube*, Journal of Heat Transfer, Vol. 114, pp. 434-441.

[24] Hallinan K.P., Pratt D.M. and Brown J.R., 1998, *Thermocapillary effects on the stability of a heated, curved meniscus*, Journal of Heat Transfer, Vol. 120, pp. 220-226.

[25] Pratt D.M., *The effect of thermocapillary stresses on the wetting characteristics, heat transfer effectiveness, and stability of an evaporating, capillary re-supplied, curved meniscus within a capillary tube*, PhD Dissertation Thesis, University of Dayton, Ohio, May 1996.

[26] Pratt D.M. and Kihm K.D., *Binary fluid mixture and thermocapillary effects on the wetting characteristics of a heated curved meniscus*, http://www.mengr.tamu.edu:70/thermal-fluidsciences/kkihm/mfhtl/lab/research/heat_transport.htm

[27] Kavehpour P., Ovryn B. and McKinley G.H., 2002, *Evaporatively-driven Marangoni instabilities of volatile liquid films spreading on thermally conductive substrates*, J. Colloids and Surfaces A: Physiochemical and Engineering Aspects, Vol. 206, pp. 409-423.

CHAPTER II

Evaporation of volatile liquids in capillary tubes

2.1 Motivation

The topic of heat and mass transfer from menisci and drops lying on a substrate has attracted much attention because many fundamental phenomena such as boiling, evaporation and condensation rely on what is happening at the near contact line region. The contact line region is the vicinity of the line where the solid-liquid-vapour phases meet. The shape of this region is dictated by the surface tension balance of these three interfaces. It is recognised that this region is of paramount importance in determining the performance (heat transfer) of many practical applications where this configuration is present. In this chapter the evaporation from menisci of various liquids formed in capillary tubes of different sizes will be investigated. The liquid convection pattern is unveiled by the use of particles acting as tracers. The evaporation and convection are characterised by measuring fundamental parameters such as the evaporation mass flux and the convection strength (by seeding the fluid with tracer particles) and a correlation between these two parameters is proposed. It will be shown that the strong evaporation takes place near the contact line region (as also pointed out in different situations by other authors) and is the key factor for explaining the findings. A theoretical model has been developed to describe the experimental findings. The analysis shows good agreement between the model and the experimental results. It will be also shown how the outcomes of this investigation could be practically exploited.

In the following we will refer to the capillary tubes also as “tube” or “pore”.

2.2 Background

Surface tension (σ) is a force per length arising from unbalanced forces at the interface as schematically shown in Figure 2.1. A liquid molecule like A experiences a nil net intermolecular force, whereas the ones close to the interface will experience a net force acting towards the liquid interior because of the weak interaction forces from the vapour molecules. Therefore, the molecules at the liquid-vapour interface tend to move inside the liquid bulk leading the interface to contract towards the liquid side. This contraction is always present but not always noticeable and it can be seen when the liquid meets a solid surface. However, if the characteristic dimension is small enough this contraction is far more evident with the formation of a meniscus. When three phases meet up a competition between the three surface tensions arises and an apparent contact angle is established. The contact angle is generally called "apparent" because it differs from the microscopic contact angle, one which does not depend on surface roughness but only on intermolecular forces as shown by de Gennes [1].

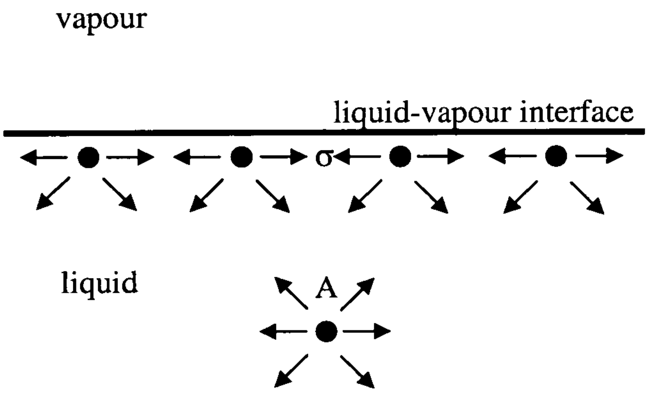

Figure 2.1 Surface tension force.

The apparent contact angle (θ) is defined as the angle formed by the liquid-vapour interface with the liquid-solid interface as shown in Figure 2.2. Note that the tangent at the liquid-vapour interface in Figure 2.2 has been drawn arbitrarily for qualitative purposes only. The force balance leads to the following Young-Dupre equation (de Gennes [1], Leger and Joanny [2]):

$$\cos\theta = \frac{\sigma_{SV} - \sigma_{SL}}{\sigma} \qquad (2.1)$$

with σ_{SV} is the solid-vapour surface tension, σ_{SL} the solid-liquid surface tension and σ the liquid-vapour surface tension. For a wide range of temperature, σ_{SV} and σ_{SL} do not vary appreciably, whereas σ is very sensitive to temperature. The usual relation between surface tension and temperature is as follows (Ganzevles and van der Geld [3]):

$$\sigma = \sigma_0\left(1 - \frac{T}{T_C}\right)^n \cong a - bT \qquad (2.2)$$

where σ_0 is the surface tension at the reference temperature, T_C is the critical temperature and n is a coefficient very close to 1 (typically between 1 and 1.3). Here, we assume $n = 1$. a and b are constants and their values depend on the particular liquid. Equ. (2.2) shows that as temperature rises the surface tension decreases and in turn (see Equ. (2.1)) the contact angle is reduced.

Figure 2.2 shows also the surface tension forces and from their balance it is clear that an unbalanced resultant force is directed to the vapour phase. Because the contact line does not detach from the solid, it means that the direction of the surface tension forces must be different from the one shown in Figure 2.2. Leger and Joanny [2] introduced the concept of solid elastic deformation that induces a reaction to balance the vertical component of the liquid-vapour surface tension, as shown in Figure 2.3. Therein, with surface tension we will refer (if not otherwise stated) to the liquid-vapour surface tension (σ). The apparent contact angle is not only a strong function of temperature, but depends on many other parameters. Surface roughness, adsorbed chemicals and contamination in general, greatly influence surface tension and in turn the apparent contact angle. The influence of surface roughness on wetting (contact angle) is so important that there are conditions under which the apparent contact angle can either increase or decrease with increasing roughness depending on the values of the contact angle with respect to the microscopic contact angle on the smooth surface (see Busscher et al. [4] and Palasantzas and de Hosson [5]). The surface tension can be altered also electrically or magnetically as shown by Perng [6]. In fact, a liquid is composed by ions although there is no net charge if no field is applied. When a field is applied the ions can be set in motion and stratification can be formed with consequent appearance of electric charges. Then by changing and/or moving the field the meniscus interface can be set in motion.

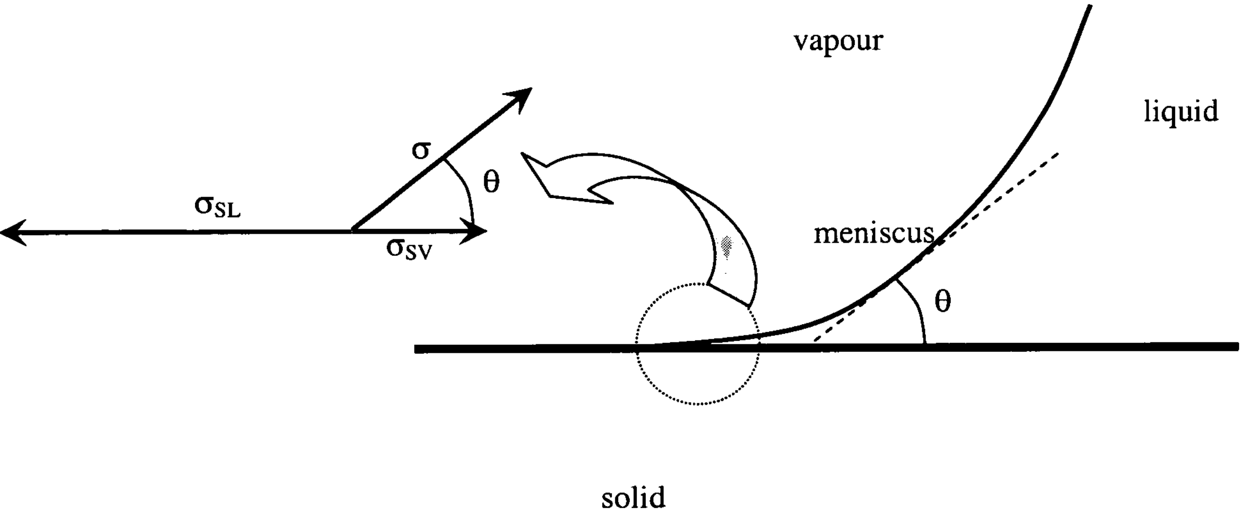

Figure 2.2 Schematic of apparent contact angle.

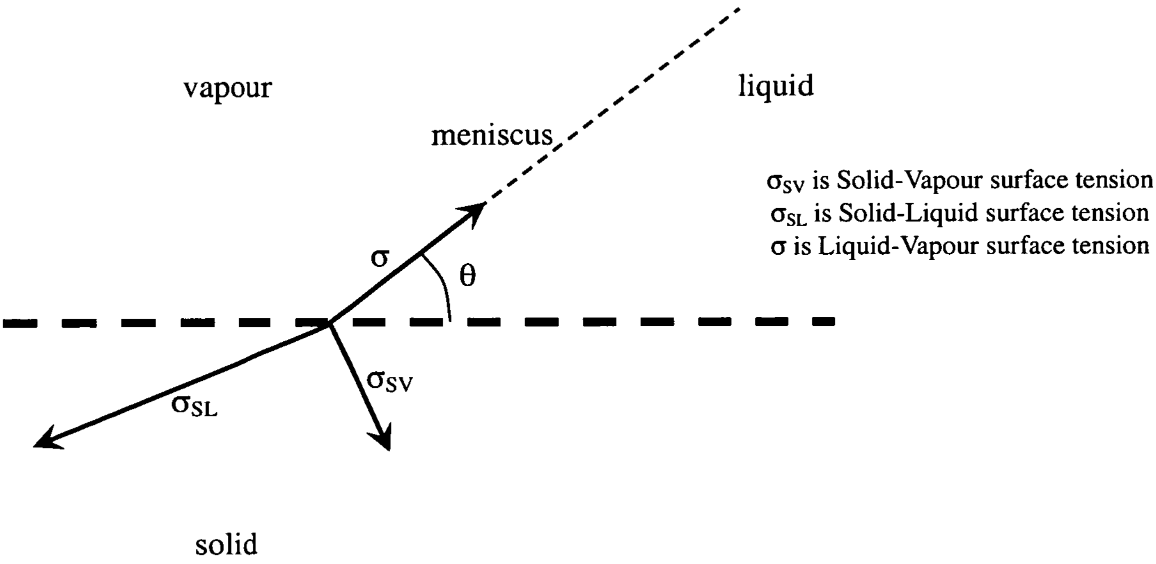

Figure 2.3 Interfacial force balance.

Surface tension related aspects have been extensively studied in conjunction with liquid spreading and most of the fundamental phenomena connected with surface tension can be found in the existing vast literature on drops. It appears soon clear that all is dictated by what happens near the contact line region. This region of the meniscus interface is usually divided in three sub-regions called: adsorbed layer, micro-region and macro-region (see sketch of Figure 2.4).

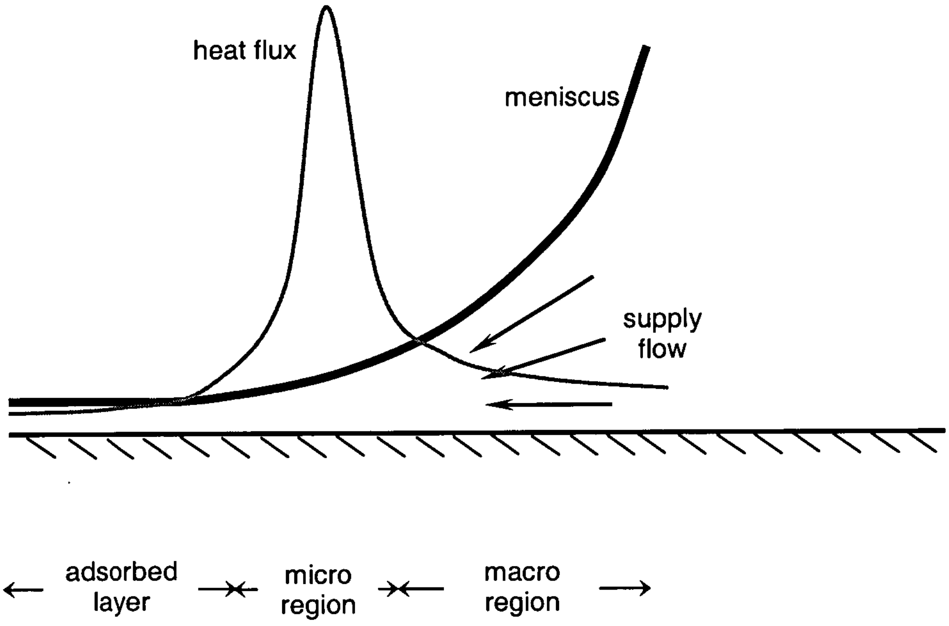

Figure 2.4 Schematic of meniscus sub-regions.

There is no universal agreement on the exact location of these sub-regions but a consideration of the governing forces can help in qualitatively locating them. In the adsorbed layer the van der Waals and London forces dominate the scenario and the liquid molecules are kept in contact with the solid; no evaporation is therefore allowed in this sub-region. This situation starts to change in the micro-region. Here, the liquid thickness starts to grow and the capillary forces therefore start to have an effect; eventually they are able to balance the adhesion forces and the molecules become free to escape from the liquid passing into the vapour phase. The molecules that escape are those with a higher kinetic energy (higher temperature) and therefore the remaining molecules (having a lower temperature) contribute in lowering the liquid temperature.

It was thought and now there are also some important experimental and numerical confirmations, as will be shown later, that the heat and mass transfer peaks in the micro-region (as schematically shown in Figure 2.4). In the following macro-region, the meniscus thickness continues to grow with a substantial increase of the thermal resistance that is reflected in the evaporation. The heat and mass flux is therefore drastically reduced in the macro-region. It was estimated by Stephan and Busse [7] that up to 50% of the evaporation takes place in the micro-region only. This region is very small measuring only 1-2% of the whole meniscus length (see Sartre et al. [8]) and the heat flux can reach values of 1.65×10^8 Wm^{-2} for the aluminium-ammonia triangular micro-heat pipe investigated by Sartre et al. [8].

The work of Sartre et al. [8] is worthy of more detailed description here. A 3-D steady-state model to predict heat transfer in micro heat pipe arrays has been presented. A Micro Heat Pipe (MHP) array for the thermal control of electronic equipment has been considered. The MHP array consists of an aluminium plate of 120 mm of length in which 19 parallel cavities with an equilateral cross section have been produced. Ammonia is the working fluid and a uniform heat flux of $7.5\ 10^4$ Wm^{-2} has been applied at the upper surface of the evaporator. The lower surface of the evaporator is cooled by natural convection and the condenser is cooled with water. The micro heat pipe does not require any wick structure for the liquid return line from the condenser to the evaporator, due to the capillary pumping force arising at the corners of the non-circular cross section. A single tube of the MHP array has been considered to obtain the thermal characteristics of the system. The analysis is focused on the evaporator due to its fundamental importance in the heat pipe thermal performance. The evaporation at the thin film region (the meniscus micro-region) induces a transverse liquid flow in the macro region and thus applying the mass and momentum conservation equations the evaporation mass flux can be obtained. The heat flux can be estimated assuming 1-D heat conduction normal to the wall in the thin film region. The capillary pressure for ammonia (polar liquid) is the summation of a term due to both surface tension and capillary radius and another term due to the disjoining pressure that is a power function of the film thickness (this latter term can be expressed as $\Delta P_D = -\frac{A}{\delta^3}$, with A Hamaker constant and δ film thickness). The three aforementioned equations define a set of non-linear differential equations for the micro-region to be solved numerically. The heat transfer in the MHP wall can be obtained by solving the heat conduction Fourier problem inside the wall. The capillary flow in the macro-region is defined by a 1-D steady state model in which the condenser has also been considered. The solution of the heat transfer problem in the micro-region, in the macro-region and inside the wall requires a different approach. The set of equations for the heat transfer problem in the micro-region is solved by the fourth-order Runge-Kutta method and give as a result the film thickness, the apparent contact angle and the heat transfer coefficient. The 2-D heat transfer problem inside the wall has been solved by an explicit finite difference method giving the internal and external wall temperatures as outputs. The solution of the flow in the macro-region (obtained by the fourth-order Runge-Kutta method) gives as output the radius of curvature, the liquid and vapour velocities and pressures. The heat transfer problem for the whole MHP array has also been solved. The heat flux initially zero in the adsorbed film, peaks in the micro-regions reaching the important peak value of 1.65 10^8 Wm^{-2} and then decreases dramatically as the film thickness increases. The capillary pressure and the heat flux decrease drastically in the micro-region as the film thickness increases. The apparent contact angle is a strong function of the difference between the wall temperature and the interfacial vapour temperature and becomes constant when the disjoining pressure is negligible. The meniscus' curvature radius ranges from its minimum value at the beginning of the evaporator to its maximum value at the end of the evaporator. Thus the meniscus cross section increases too and the wetted wall increases as well. Comparing the heat flux along the upper surface of the wall at the beginning and at the end of the evaporator shows a larger value for the beginning section; this is due to the smaller heat transfer surface area in this region. The heat flux profile of the outer and inner upper wall has been produced for the beginning and the end of the evaporator cross section. These profiles show how the maximum temperature is reached at the middle of the cross section where the heat transfer coefficient is depressed by the heat transfer between the dried wall and the vapour. From these profiles it can be seen as the upper inner temperature is minimum in the meniscus micro-region where the heat transfer mechanism is stronger than elsewhere. This study is fundamental for the present investigation, because it has numerically demonstrated that the heat transfer coefficient peaks in the micro-region being usually only 1% of the entire meniscus length. To experimentally notice this fact we will use in this study two powerful non contact methods (Thermochromic Liquid Crystals and Infra Red). In addition, it is clear that by enlarging the micro-region length, the heat transfer pore capability could be dramatically improved; this can be done in different ways by modifying the wall roughness and/or using surfactants to improve the wettability and thus the heat transfer coefficient.

When the liquid-vapour interface is formed in a large pool, it can be assumed flat under normal g-conditions. The interface is slightly curved when the solid walls are approached, but this is a local effect with no practical relevance. In low g-environments or at small scale size, things can be quite different. In the capillaries used in this study (internal diameter ranging from 0.2 to 1.63 mm) a curved meniscus is formed. The shape of the meniscus is similar to the inverse of a drop of non wetting liquid lying on a substrate and, as will clearly appear later, many comparisons could be established between the present case and the non wetting drop case. However, in the case of an evaporating drop there is an extra difficulty due to the depinning of the contact line due to mass transfer because of evaporation.

The fact that the heat flux peaks in the micro-region can be exploited for practical purposes. And in fact, this is the main reason why the contact line region has attracted so much attention in recent years, both for fundamental studies and practical application. Much work was done in the 70s by Wayner and co-workers in understanding the mechanism involved in the heat and mass transfer from evaporating thin liquid films (Potash and Wayner [9], Potash and Wayner[10], Preiss and Wayner [11], Wayner et al. [12]). The subject is however still not fully understood as it has been demonstrated by the numerous other works that have appeared in the area (see Mirzamoghadam and Catton [13], Swanson and Herdt [14], DasGupta et al. [15], Wayner [16], Reyes and Wayner [17], Khrustalev and Faghri [18], Schonberg et al. [19]). It is thus understood that if an improvement is sought, it is more appropriate to look at possible alterations at the contact line region. Different solutions have been proposed for instance in the heat pipe technology by devoting more attention to the contact line region. Khrustalev and Fahgri [18] have shown how the heat transfer can be enhanced at the contact line of a meniscus interface using grooved heat pipes, for instance. Another important improvement is given by surfactants (surface active agents). These are chemicals that usually lower surface tension and thus the contact angle. This is shown in fundamental works (most of which were carried out by Russian researchers such as Churaev [20-21] (who gives also a substantial bibliography), Rusanov and Krotov [22] and Miller and Neogi [23] along with applied ones by Fang and Shah [24].) Surfactants can enhance substantially the heat transfer at the near contact line region by lowering the surface tension and thus the apparent contact angle. However, as demonstrated by Fang and Shah [24], a change of just two carbons in the fatty acid monolayer can dramatically alter the heat transfer at the water/air or water/oil interface eventually blocking evaporation.

Some of the works on surfactants are relevant to the present study and will be presented in details in what follows.

In the work of Churaev [21] the capillaries under investigation have firstly been exposed to a steam of surfactant solution for 2-3 hours to eliminate the surfactant's adsorption at the wall. Particular care has been given to the washing process and how the capillaries were put in place. The meniscus position was allowed to move in both directions because of the difference of pressure applied between the two capillary ends. A CCD camera recorded the meniscus movements along the capillaries. The linear relationship found between the meniscus velocity and the difference of pressure applied suggests the dynamic capillary pressure is independent of the flow rate, but is different for the advancing and the receding menisci basically because in the advancing movement the meniscus meets a dry surface. Using different surfactants the results change, due to the different hydrophilicity of the capillary wall. The surfactant concentration inside the adsorbed film layer is always lower than that inside the bulk phase either for the receding or advancing meniscus. But, while for the receding meniscus the surfactant concentration beyond the meniscus is lower than in the liquid phase, for the advancing meniscus it is larger. This is due to a net surfactant flow onto or from the wetting film in contact with the capillary surface for the receding or advancing menisci respectively. Equalizing the net flow into or from the wetting film with the diffusion flow in the bulk phase, the Peclet number has been introduced; *Pe* takes into account the relative importance of convective to diffusion forces. At very low flow rate *Pe* approaches zero, diffusion dominates, the ratio of meniscus to bulk phase surfactant concentration approaches one and the dynamic interface tension has the same value of the static one (equilibrium value). Increasing the flow rate the ratio of the surfactant concentration aforementioned decreases or increases (depending on receding or advancing menisci respectively) and the dynamic surface tension becomes higher than the equilibrium value.

Fang and Shah [24] treated the case of a surfactant monolayer. Surface active agents put over the liquid surface can decrease its evaporation dramatically. Distilled water was covered by a layer of a chemical mixture composed by surfactant (cholesterol) and a solvent system (chloroform, methanol and *n*-hexane); the layer was formed as follows: surfactant was deposited as droplets with a micro-syringe till no spreading movement of the drops was observed. Before adding hexadecane on top, 15 minutes were given to leave the solvent to evaporate. The infrared radiometer has a temperature measurement range of -20÷400 °C with a temperature accuracy of ±2 °C or ±2%. The minimum detectable temperature difference was 0.1 °C at 30 °C with a noise equivalent temperature difference of maximum 0.05 °C. The system water (3 mm of height)-surfactant monolayer and hexadecane (3.9 mm of height) was heated from below using a Kapton heater. The heat transfer resistance was evaluated by measuring the time required to increase by 1 °C the surface temperature. Experiments were carried out first without hexadecane. The results show as the time required to increase the surface temperature of water by 1 °C is larger than when a surfactant monolayer is used. This fact can be explained as follows: when water evaporates the interface water/air is cooled and therefore the accumulation of heat at the interface is low and the time necessary to increase the surface temperature is long. When the surfactant is added, the cooling effect is much lower and the accumulation of heat at the interface is faster, thus the resistance is lower. When the oil (hexadecane) is added the resistance increases, because there is no cooling effect at the water/oil interface and thus the surfactant acts as an extra resistance for the heat transfer process. Therefore increasing the number of carbon atoms in the cholesterol leads to a decrease of resistance of the water and an increase of resistance in the water/oil system. Further experiments were carried out changing the mole fraction of different surfactants. The effect of mole fraction changes is higher in the water/oil system than in water. This is due, as stated by the authors, to the insufficient temperature change at the air/water interface being noticed by the IR thermocamera. This experiment demonstrated that the adding of surface active agents can noticeably change the heat transfer coefficient. In thermocapillary phenomena these effects can be amplified also by the change of wettability; the wettability dramatically influences the contact angle and thus the heat transfer at the interface. At the present very little work on the surfactant effect in a thermocapillary has appeared.

Wu et al. [25] were concerned with surfactant retardation of thermocapillary flow. The authors point out how very few and inconclusive works have been carried out on the problem of surfactants' effects on artificial provoked thermocapillary flow either experimentally or theoretically. They used a small hot rod on the top of a pool of liquid to heat the interface and so provoke a thermocapillary flow in the bulk phase, first without and afterwards with a surfactant. When a surfactant was used, the stretched interface by the induced Marangoni convection adsorbed the surfactant from the bulk phase; the concentration of the surfactant at the interface was lower than that without stretching, because the rate of convective diffusion from the bulk phase is finite. This lea-ds- to a gradient of concentration that provoked a restoring force opposed to the Marangoni convection. Three thermocouples were used to monitor the temperature at the interface near the hot rod and far away from it and in the bulk phase at a changeable depth. A non contact infrared thermometer was also used and a deviation of surface temperature of 0.1 °C between the two methods was found. The pool wa maintained at a temperature of 25 °C by a water jacket. The rod was 750 μm large and the differences of temperature imposed through it were 35, 42.5 and 50 °C. The surfactant used was sodium dodecyl sulphate and its concentration was varied discretely as following: 0.2, 0.5, 1, 1.5 and 5 mM. Surface velocity and temperature were monitored during the experiments. Surface temperature and velocity were recorded very close to the hot rod. The results agreed very well with the theoretical prediction found by solving the Navier-Stokes equations. The surface velocity was slowed down by increasing the surface concentration, as expected. The temperature decreased considerably when moving far from the heat source. An increase of surface temperature was found as the surfactant concentration was increased; this was due to the reduction of heat transfer at the interface by the blockage caused by the surfactant. This work showed that surface induced retardation of the thermocapillary flow is mainly due to the interfacial elasticity effect of the surface-liquid system. What is expected to happen in a capillary tube (like the case investigated in the present work) is far more complicated. The surfactant reduces the heat transfer at the interface and thus increases the temperature of the meniscus particularly at the contact line region; because the heat transfer at the tube centreline is weaker than at the contact line region, the surfactant presence does not influence greatly the temperature there. On the other hand, the contact angle is reduced by the surfactant and thus the heat transfer at the contact line increases; this leads to a reduction of the temperature in the contact line region. The competition between the direct blockage effect caused by surfactant on the heat transfer and those aforementioned side effects could provoke an unpredicted enhancement of the heat transfer by the enhanced surface tension gradient at the contact line leading to a more vigorous liquid convection, for instance.

The liquid polarity appears to be a quite important factor, indeed. Wei and Ma [26] have shown that the liquid polarity greatly affects the disjoining pressure. The disjoining pressure is the result of the interaction between the thin film liquid layer and the solid wall surface. This interaction takes into account the long-range interaction forces and the electrostatic interaction forces. For the apolar and weak polar liquids the long-range interaction forces predominate and the electrostatic forces are negligible; whereas, for polar liquids the electrostatic interaction cannot be ignored. The dispersion forces (disjoining pressure) play an important role in the shape of the meniscus. While for non polar fluids the disjoining pressure is a power-law of the thin film thickness, for strong polar fluids (such as water) the disjoining pressure changes logarithmically with the film thickness. The authors derived a non-linear differential equation for the liquid film thickness, starting from the augmented Young-Laplace equation; and solved the equation numerically. They chose water and carbon tetrachloride as polar and non polar fluids respectively and quartz glass as capillary material. The heat flux, the capillary radius, the wall and entrance vapour temperature were kept constant to compare the results for the two fluids. The results showed that the meniscus length for water was about one order of magnitude larger than for carbon tetrachloride (CCl_4) and the film thickness increased more gently. The disjoining pressure for water was also one order of magnitude larger than for CCl_4. The larger disjoining pressure of water led a smaller heat transfer coefficient, because the molecules cannot escape easily from the vapour-liquid surface. The authors compared also two different non polar working fluids: hexane and heptane. The results showed that when the degree of eccentricity was similar, even if the Hamaker constant was different, the meniscus length and its profile did not change appreciably.

2.3 Experimental layout and procedure

The internal diameter of the borosilicate glass capillaries used in this investigation is reported in Table 2.1 as from the manufacture specifications. This material for the tubes was chosen because it is transparent (allowing for flow visualization), cheap, strong and chemically inert to the volatile liquids to be used. It is well known that surface tension is a parameter quite sensitive to surface contamination by unwanted chemicals and dust. The tubes were therefore cleaned using an ultrasonic bath with de-ionized water for 30 minutes at 65 °C and successively dried in an oven at 60 °C for two hours. The tubes were stored in a clean vial and used within few days. To avoid contamination, the capillaries were filled from the end opposite to that where the meniscus was positioned for observation.

It is also established that surface roughness plays an important role in defining the apparent contact angle and ultimately affects the heat and mass transfer from the curved meniscus. The roughness of the internal tube surface was characterized[♦] using a profilometer. The use of the profilometer allowed us to analyze surfaces with high curvature. Large pieces have been cut and the analysis was performed far away from the edges to avoid edge effects. Two important parameters are used to characterize the surface roughness, *ra* and *rms* (see Farshad et al. [27]). *ra* is the average surface roughness. The *rms* is defined instead as the root mean square average of the measured height deviation. The surface roughness parameters are reported in Table 2.1. In order to compare the roughness for the present case, it is more appropriate to normalize both *ra* and *rms* with the tube diameter, following Li et al. [28], rather than with a surface length. From the analysis of the relative surface roughness (defined as the ratio of *ra* to internal tube radius) reproduced in Table 2.1, the tubes can be considered as smooth. However, relative roughness increases as the tube size is reduced.

All liquids used were used as received; their physical properties are given in Table 2.2 extracted from Yaws [29].

[♦] The author would like to tank Mr. Frédéric Madani (of the Centre of Material Science at THE UNIVERSITY *of* EDINBURGH) for carrying out this measurements and providing useful insights and suggestions on surface roughness characterization.

Table 2.1 Tube surface roughness analysis (samples dimensions 140x110 μm).

ID (μm)	ra (nm)	rms (nm)	relative roughness (%) $x10^{-4}$
200	1.354	1.741	6.77
600	3.479	4.588	5.79
900	4.105	5.094	4.56

Table 2.2 Liquids properties at 1atm and 25 °C (extracted from Yaws [29]).

Liquids	Boiling point (°C)	P_v ($N\ m^{-2}$) $x10^3$	ΔH ($kJ\ mol^{-1}$)	c_{pl} (J/mol K) $x10^2$	ρ_l (kg/m^3) $x10^2$	k_l (W/m K) $x10^{-1}$	μ_l ($N\ s/m^2$) $x10^{-3}$	σ (N/m) $x10^{-1}$
Ethanol	78.4	7.61	40.3	0.798	7.88	2.01	5.45	23.6
Methanol	64.7	16.2	38.0	1.073	7.88	1.69	10.7	23.5
Acetone	56.5	29.8	32.2	1.274	7.86	1.62	3.09	23.1
n-Pentane	36.3	66.8	26.7	1.635	6.22	1.48	2.46	15.5

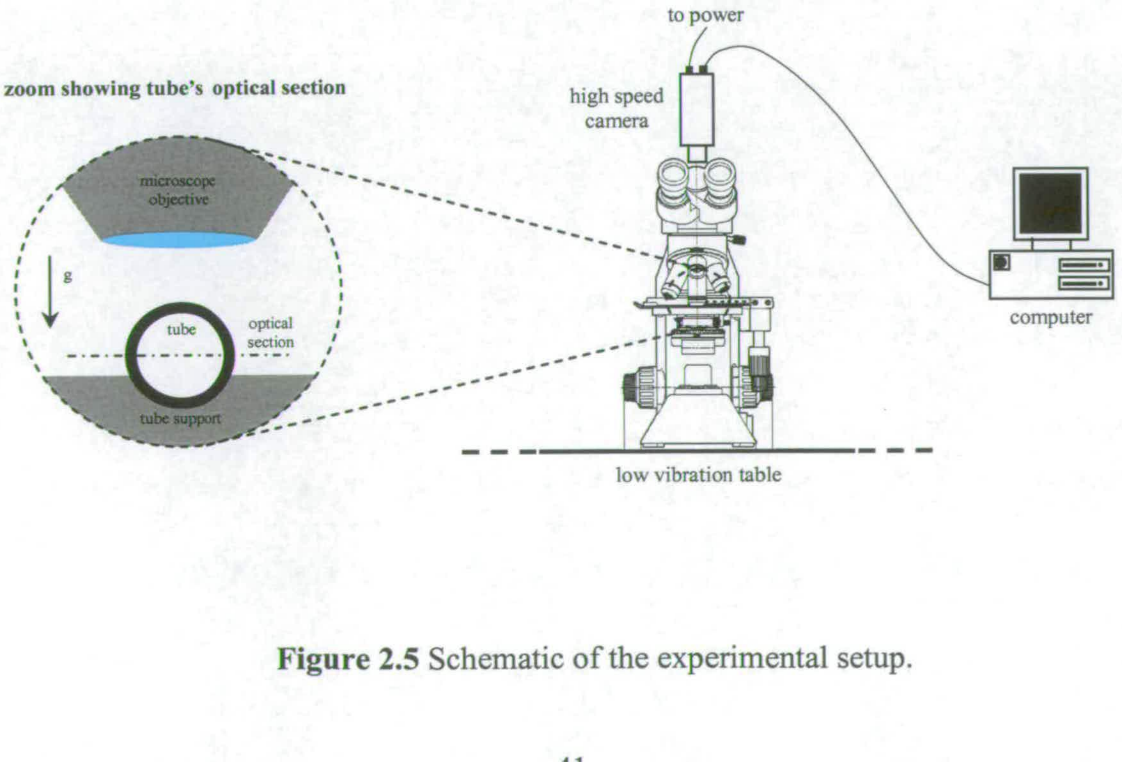

Figure 2.5 Schematic of the experimental setup.

The experimental layout sketched in Figure 2.5 comprises an Olympus Research microscope with an attached high speed camera (Phantom v4.3) capable of 1000 frames per second at 512x512 pixels. An acquisition computer is used to acquire sequences from the camera, which are analyzed using specialized software. Normal white light from the microscope is used to illuminate the sample. An IR filter has been placed between the light and the condenser of the microscope to avoid transfer of heat via light into the capillary and possible heating of the meniscus region under investigation. Preliminary tests showed how the meniscus oscillates when receding inside the pore and the evaporation rate is found to be higher without the filter. All experiments have been performed with the tubes in a horizontal position and making horizontal diametrical optical section with the microscope lying on an optical low vibration table (Newport Co.). Particles have been used as tracers in the liquid phase to visualize and characterize the convection motion (see Figure 2.6). The tracers were nylon spherical particles with mean diameter of 20 μm. This experiment has been repeated as will be shown in a successive chapter where PIV measurements were carried out, using borosilicate glass particles (spherical particles from Potters Industrial Inc.) with 3-26 μm diameter (depending on the capillary size).

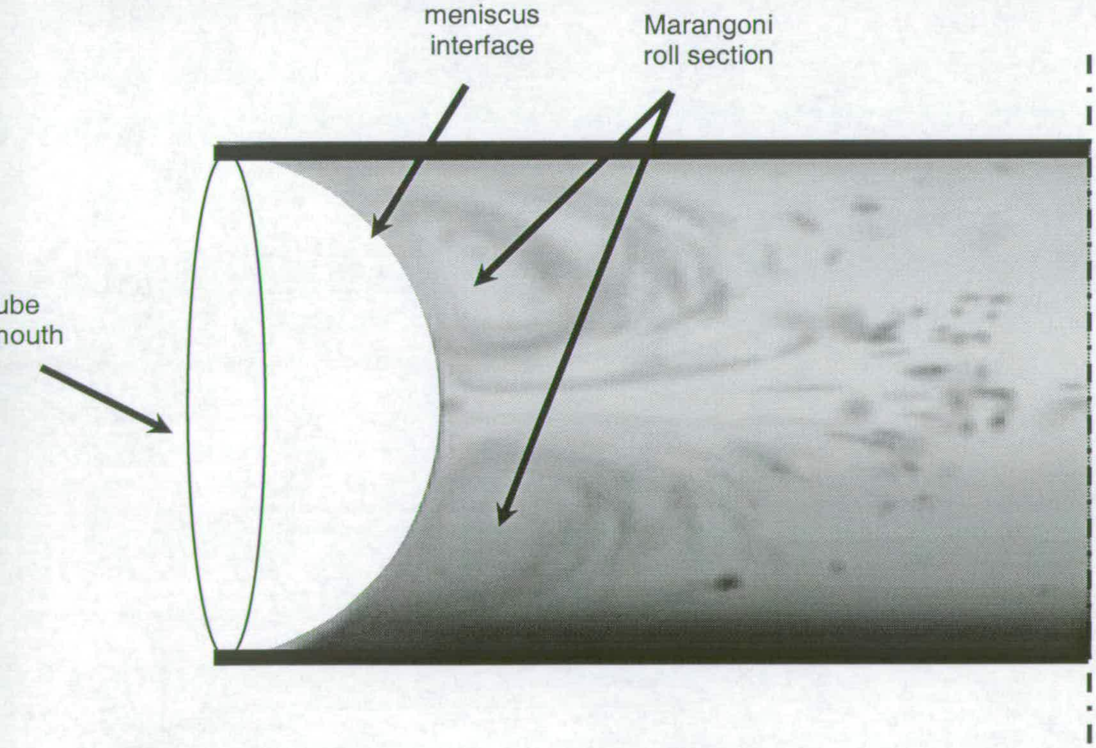

Figure 2.6 Visualization of the liquid flow pattern using seeding tracers through an optical diametrical section of the capillary tube.

Two types of experiments have been performed. In Experiment (1) (see sketch in Figure 2.7), the meniscus has been positioned at the capillary mouth using a micro-syringe, then was left free to move inside the pore.

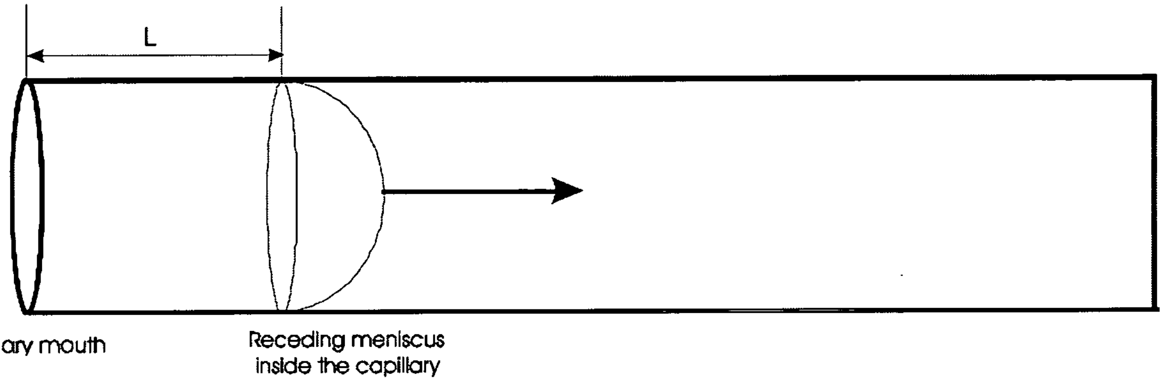

Experiment (1)

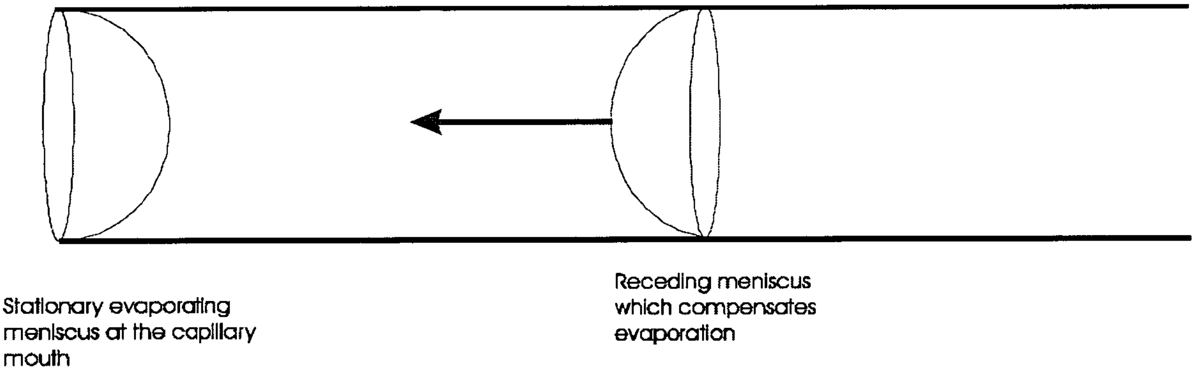

Experiment (2)

Figure 2.7 Experimental sketch: Experiment (1) with one receding meniscus; Experiment (2) with two menisci.

The capillary was connected to the syringe using polyamide tubes and the junctions between capillary/polyamide tube and polyamide tube/syringe were sealed with heat shrink. The polyamide tubes are chemically resistant to the liquids used; therefore, no contamination of the meniscus by unwanted chemicals is expected. When the capillary was filled with the volatile liquids, particular care has been taken to avoid the formation of bubbles along the system syringe/polyamide tube/capillary. In fact, it has been noticed that the presence of bubbles strongly influences the results. Each capillary was used only once. In Experiment (2) (see Figure 2.7) both ends of the capillary were open allowing the formation of two menisci: one meniscus was stuck at the capillary mouth (where convection motion was monitored) while the other receded inside the pore (at a rate used to evaluate the evaporation rate) as evaporation took place.

The necessary heating for this process comes from the capillary tube's surrounding environment and no extra heating is provided by any means. In fact, the liquid evaporating cools down the meniscus interface bringing its temperature below that of the room, inducing a heat transfer mechanism through the conductive tube's wall. These considerations will be discussed in more depth in a later section of this chapter.

During each experiment the environmental conditions (temperature, relative humidity) were monitored. The room temperature and relative humidity were 25±2 °C and 50±5% respectively. Preliminary tests made at different times showed that the environmental conditions played a marginal role on the parameters measured here (evaporation rate, tracer spinning frequency); the largest difference found in the evaporation rate was 3-4%. Motion analysis software (MAStudio) for tracking and analysis was used.

2.4 Results

In Experiment (1) (see Figure 2.7) the meniscus recedes inside the pore as evaporation takes place. Mass is lost because of evaporation at the interface and because the system is not re-supplied. This results in a meniscus moving deeper inside the tube. The meniscus moves in two distinct stages; first, it changes shape but remains stuck at the capillary mouth due to the strong adhesion forces. When the receding apparent contact angle is reached, it starts to recede inside the pore. As the meniscus recedes and evaporation continues the vapour generated has to diffuse to the mouth of the capillary. As a result, the partial vapour pressure at the liquid-vapour interface builds up as the meniscus recedes inside the pore. The difference between the vapour partial pressure and its saturation value at the interface is the driving force for evaporation.

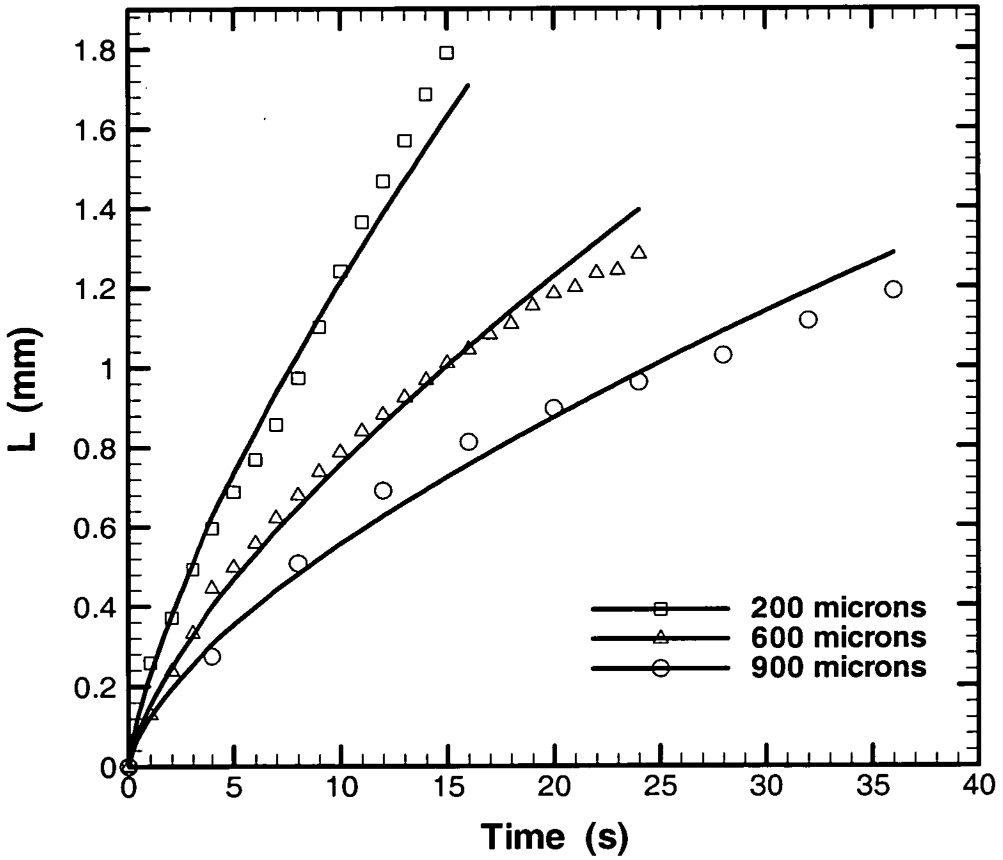

Figure 2.8 Experiment (1): meniscus position from the tube mouth (*L*) for n-pentane and various tube sizes (experimental points and power fit $y = a x^b$).

The distance of the meniscus measured from the tube mouth (*L*) is reported in Figure 2.8 as a function of time for n-pentane and various capillary sizes. This would allow us to evaluate the evaporation rate from the slope of these curves. In order to emphasize the difference between different volatile liquids, Figure 2.9 shows the meniscus position versus time for 600 μm pore size for various liquids. From Figures 2.8-2.9 it is clear that the slope of the curves (corresponding to the evaporation rate) increases noticeably with smaller tube size and with the use of more volatile liquids. The slope of each curve decreases also as the meniscus recedes inside the tube for the reason pointed out earlier about the partial vapour pressure rise and the consequent reduction of the evaporation driving force (saturation pressure minus vapour pressure).

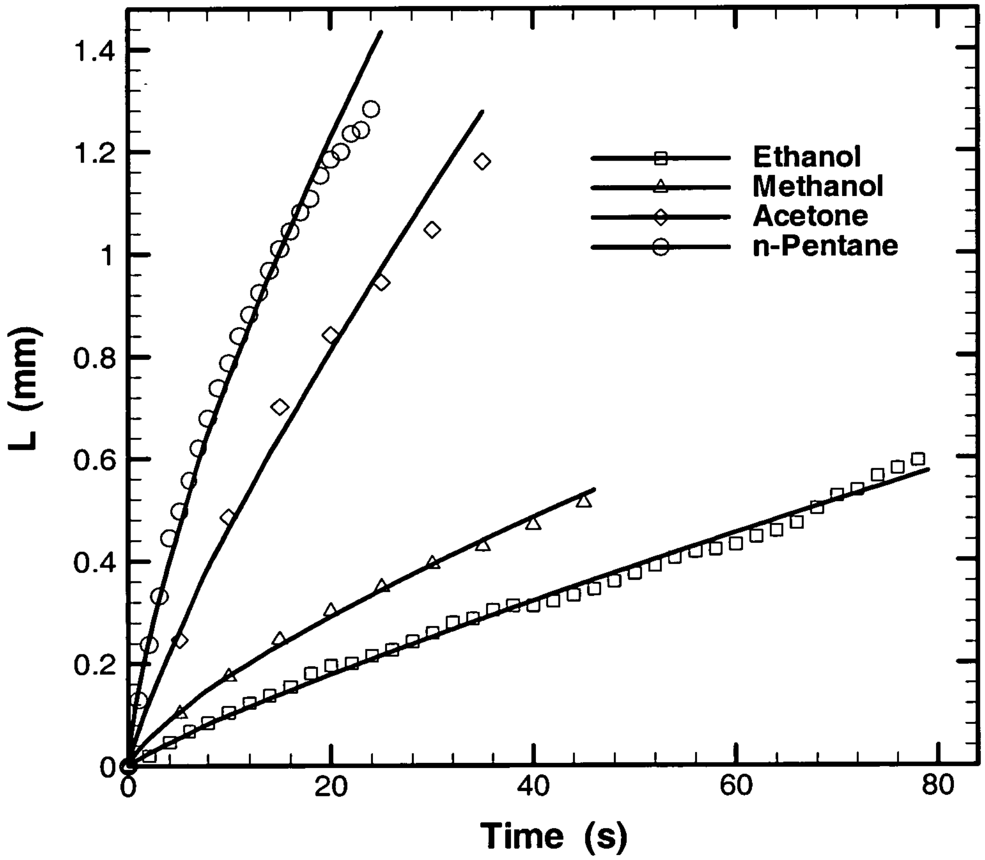

Figure 2.9 Experiment (1): meniscus position from the tube mouth (*L*) for 600 μm and four different liquids (experimental points and power fit $y = a\,x^b$).

In Experiment (1) the liquid adjacent to the interface was seeded with particles acting as tracers to reveal the flow pattern. The tracers were introduced in the liquid after the filling procedure, by approaching the interface with a small needle the tip of which was covered by particles. At a certain distance from the meniscus the particles were attracted by the interface and uniformly distributed in the liquid phase adjacent to the interface with no disruption of the important contact line region close to the capillary wall. This procedure of seeding the liquid has proved more effective than seeding the entire liquid before filling the tube. In fact, this latter approach, as well as causing blockage of the syringe, can lead to blockage of the tubing especially close to the inter-connections. In addition, it was quite difficult to control the number of particles in the region of interest (the liquid region next to the meniscus). The frequency of the liquid convection toroidal structure has been measured as the meniscus recedes inside the capillary.

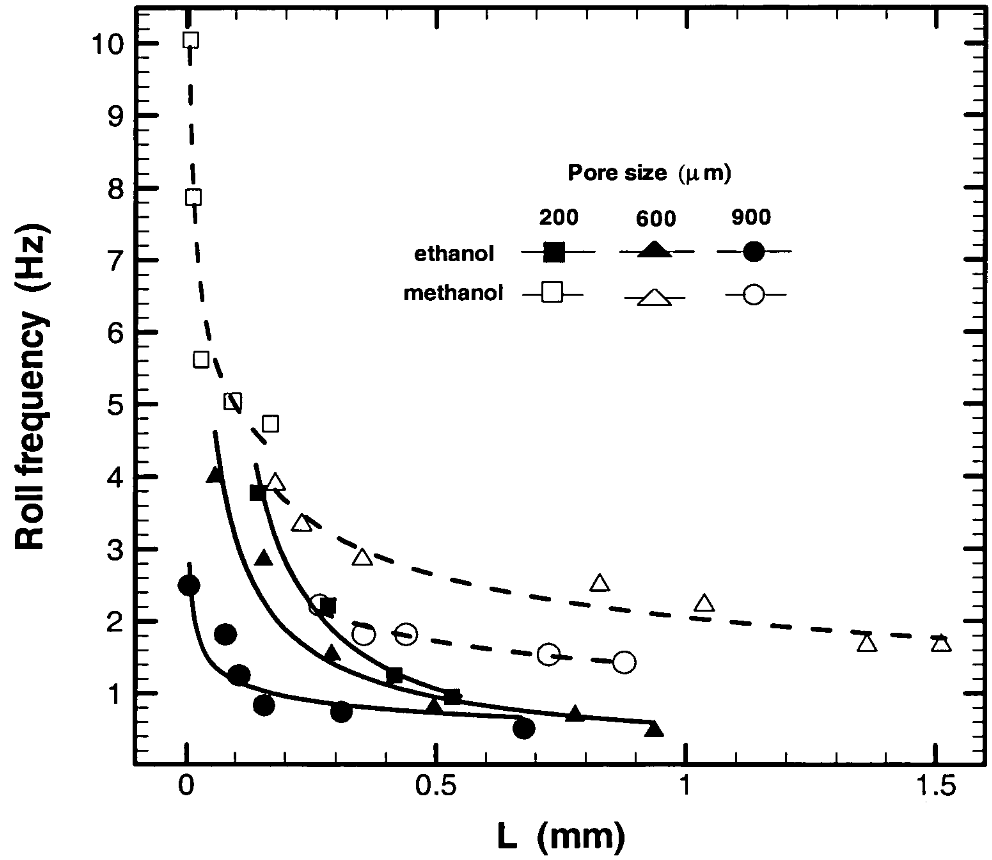

Figure 2.10 Experiment (1): tracer spinning frequency comparison for ethanol and methanol and three tube sizes (experimental points and power fit y = a x^b).

Figure 2.10 shows the tracers' spinning frequency for ethanol and methanol and various tube sizes versus the meniscus position (*L*) from the tube mouth. The tracers' spinning frequency increases as the tube size decreases for both liquids and decreases dramatically as the meniscus recedes inside the capillary; the frequency also increases with the liquid volatility.

The results for the evaporation rate and spinning frequency demonstrate the strong link existing between the evaporation process and the observed convection. The rolls shape and dimensions and their evolution have also been monitored. As the meniscus starts to move, first changing its shape, the rolls are stretched in the direction of the movement. When the meniscus detaches starting to recede, the roll shape and dimensions do not further change appreciably. Therefore it can be stated that the rolls shape and dimensions vary essentially in accordance with the change of the meniscus profile. As the meniscus detaches from the capillary mouth, its profile remains unchanged although the driving force for evaporation changes because of the partial vapor pressure rise; this has proved not to appreciably influence the rolls shape and dimensions, but only its spinning frequency.

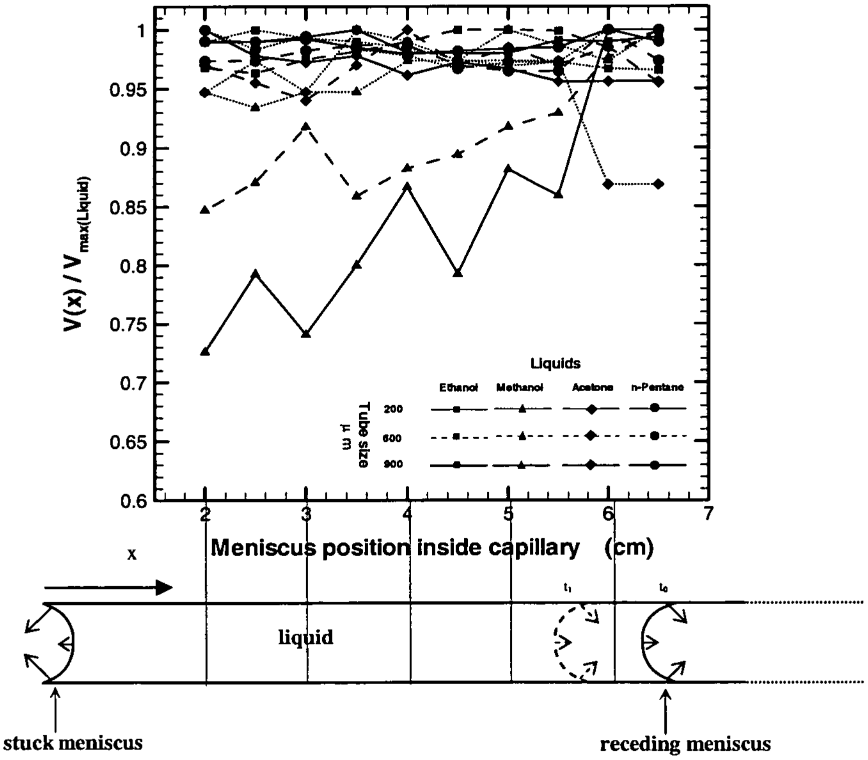

Figure 2.11 Normalized receding meniscus velocity.

The second Experiment (2) consists of partially filling a tube and leaving both ends open. In this case two menisci are formed along the pore (see Figure 2.7). The evaporation takes place at both menisci inside the capillary tube; one meniscus remains stuck at the pore mouth due to the stronger adhesion forces while the other recedes inside the capillary far away from the opposite tube end. However, the evaporation at the receding meniscus is of less importance; in fact, Experiment (1) demonstrated how the evaporation dramatically weakens as the meniscus moves far from the pore mouth. Following the receding meniscus along the pore, experiments conducted on each tube size and for each liquid confirm the assumption that the evaporation from the receding meniscus is negligible. Following the receding meniscus inside the tubes, the measured evaporation rate changes by less than 5-7% over a length of 5-25 times the internal tube diameter (depending upon the tube size) as can be seen from Figure 2.11 where the ratio between the velocity of the receding meniscus to its maximum value is reported against the meniscus position inside the tube for various tube sizes and liquids; then, the difference is reduced with smaller tube size and with the use of more volatile liquids. Therefore, the velocity of the receding meniscus is proportional to the rate of evaporation taking place at the meniscus stuck at the capillary mouth. The liquid on the meniscus stuck at the capillary mouth was seeded with particles to characterize convection. The evaporation rate and the spinning frequency of convection rolls have been correlated. In order to compare the average evaporation flux for different cases, the results for the evaporation rate have been referred to the spherical cap area rather than to the tube cross-section area. The assumption of considering the meniscus as a spherical cap is a good approximation when gravity can be neglected as shown by Kim [30]. Figure 2.12 shows both the evaporation rate and its averaged flux for different liquids and tube sizes. The overall evaporation rate increases for all liquids with increasing tube size and with the use of a more volatile liquid; this is essentially due to a larger available surface area for evaporation for bigger tube sizes. On the contrary, the average evaporation flux (over the tube cross section area) decreases with increasing the tube size. In order to point out the strong link between the evaporation process and the observed convection, the average evaporation flux and the tracers' spinning frequency have been correlated in Figure 2.13 for the case of ethanol at different tube sizes; both of these parameters are found to increase when the tube size decreases.

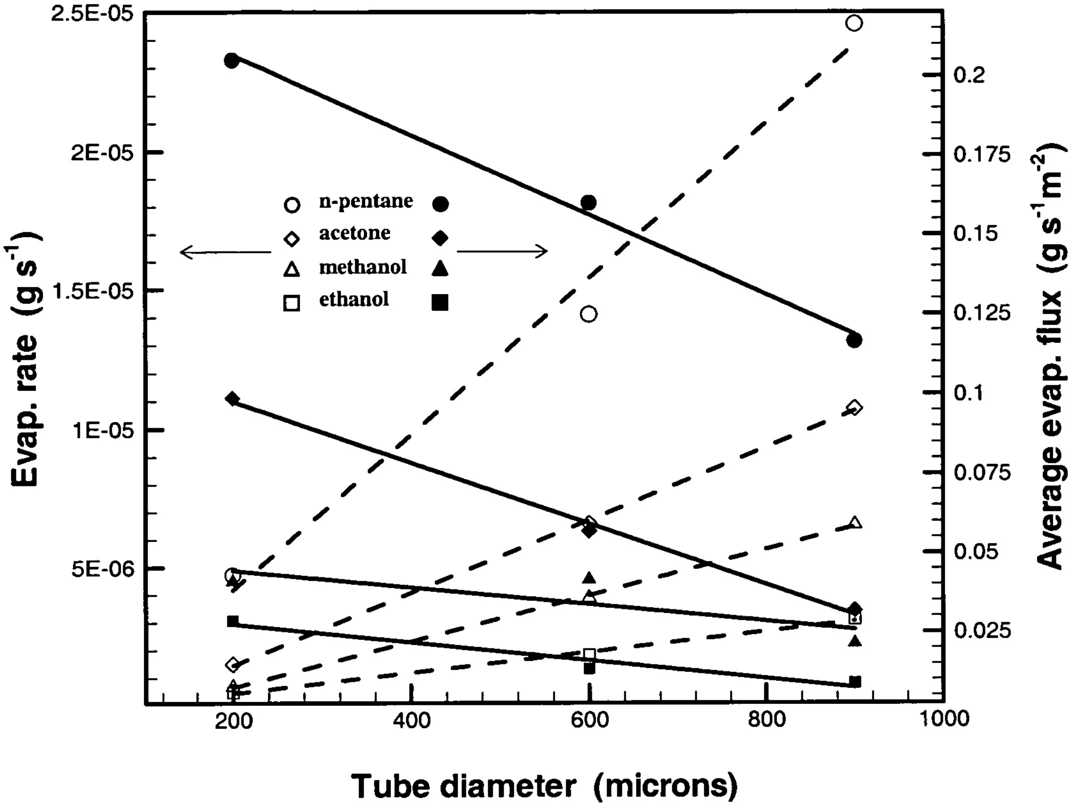

Figure 2.12 Experiment (2): evaporation rate and average evaporation flux vs. tube size.

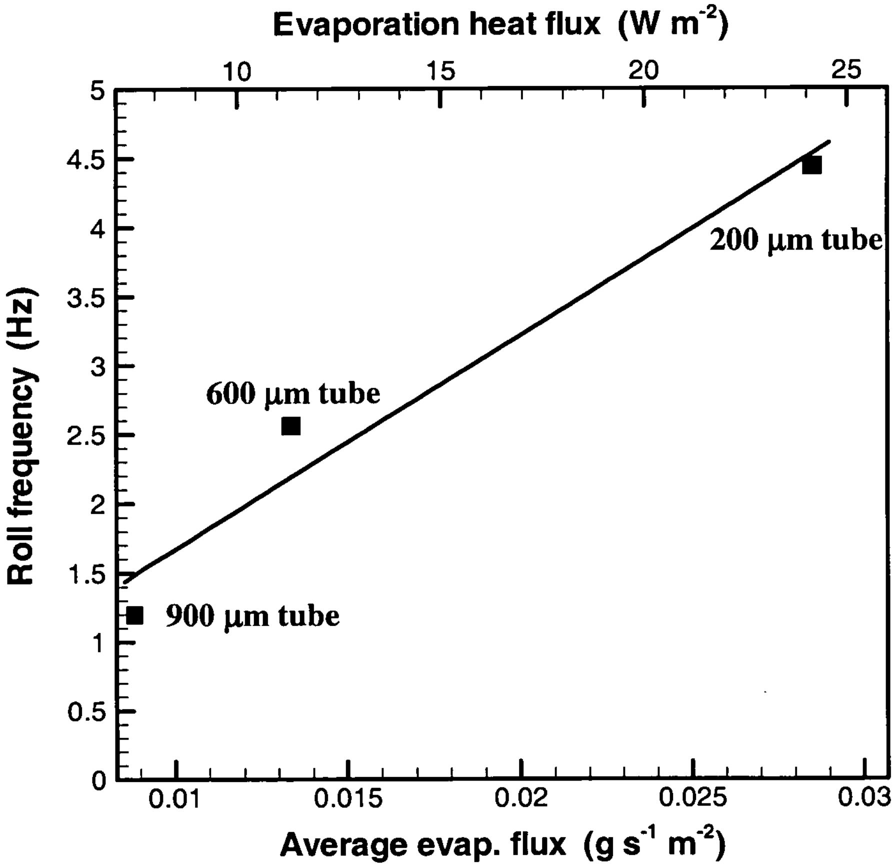

Figure 2.13 Experiment (2): tracer spinning frequency vs. evaporation flux for ethanol and various tube sizes.

2.5 Theoretical model

The aim of the following model is to describe what was observed experimentally for the two cases described earlier in a quite qualitative fashion. Therefore, a lump analysis on the complex heat and mass transfer mechanism set by the evaporating phenomena being described is appropriate here.

The thermocapillary motion observed in these experiments is due to a thermal gradient established along the meniscus interface, which takes its origin in the strong evaporation occurring at the triple line region while the centre of the spherical cap undergoes a weaker evaporation. Evaporation takes place at the interface then vapour diffuses to the mouth of the capillary. In the following an attempt will be made to calculate the temperature at the triple line region by a heat diffusion model. The temperature at the apex of the spherical cap, where evaporation is much less intense than in the wedge, is assumed equal to the temperature of the bulk liquid; this latter is taken equal to the ambient temperature (see Figure 2.14).

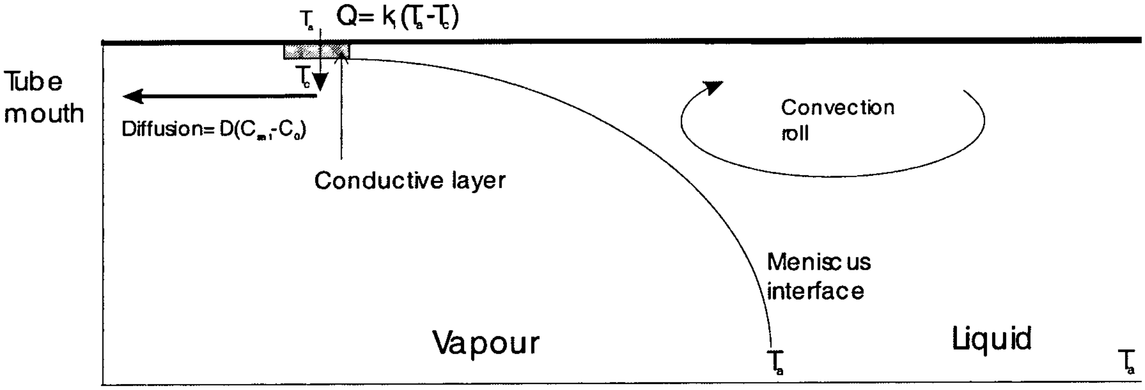

Figure 2.14 Conduction-diffusion model from a receding meniscus.

A sketch of the heat transfer paths for the present case is shown in Figure 2.15. Evaporation takes place along the meniscus interface producing a local drop in temperature. A heat transfer mechanism is induced and heat is transferred from the environment outside the tube to the meniscus interface, passing through the tube walls and the thin liquid layer. This heat is necessary to sustain the evaporation process. For an order of magnitude analysis, it is reasonable to neglect the heat conducted along the tube walls ($Q_{\text{wall cond}}$). The vapour can be assumed to be "passive" (see Meyer [31], Shien [32], Davis [33], Riley [34] and Pratt and Hallinan [35]), that is no convection is present in the vapour, because it has negligible viscosity, density and thermal conductivity compared to the liquid.

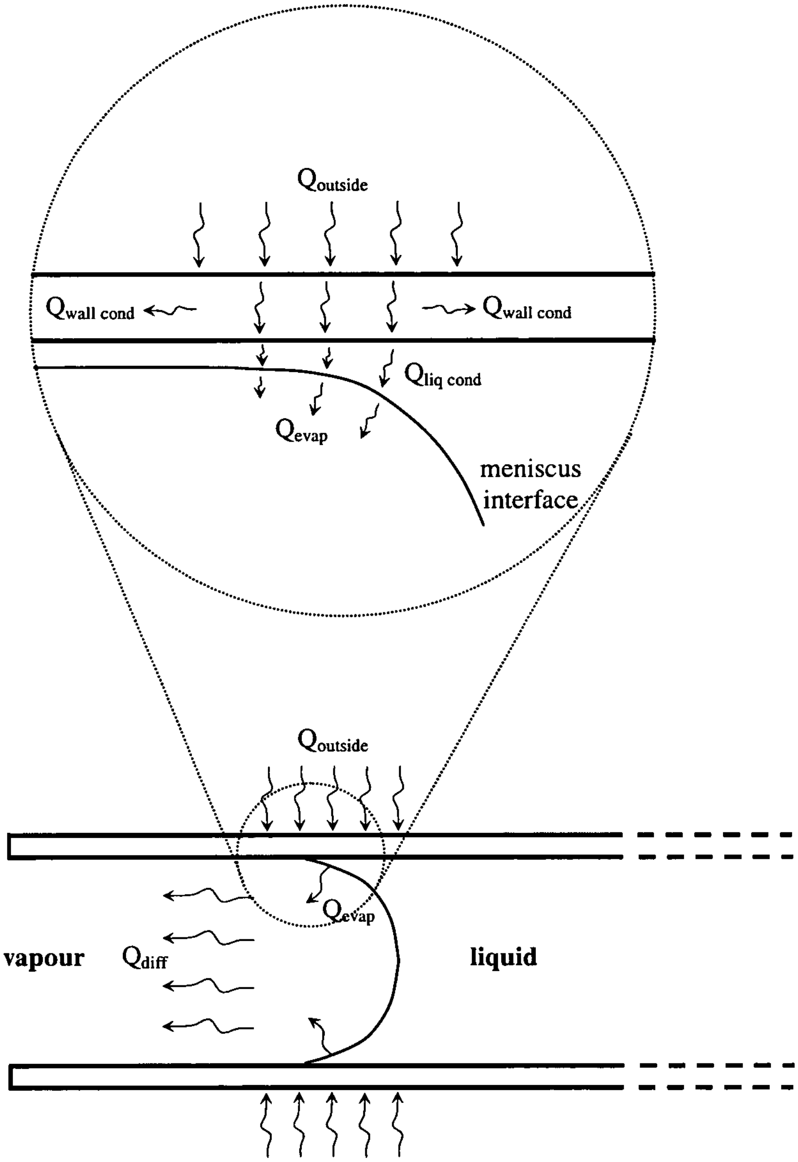

Figure 2.15 Heat paths sketch for an evaporating-receding meniscus.

The shear stresses at the interface due to surface tension gradients produce in the liquid phase the motion observed in this study by dragging the viscous liquid along the interface from hot to cold regions. Because of the very low vapour viscosity, the same stresses do not produce vapour recirculation, instead. Therefore, in accordance with other authors (Meyer [31], Shien [32], Davis [33], Riley [34] and Pratt and

Hallinan [35]) it can be assumed here that the mass transfer mechanism in the vapour phase is dominated by diffusion. It is worth mentioning that a method namely the WIKELMANN technique (as described in detail by Coulson and Richardson [36]) adopting an experimental set up similar to the one analysed here, is widely used to determine the diffusion coefficient. In the WIKELMANN method a liquid is allowed to evaporate in a vertical glass tube closed at the bottom and open at the top, and the rate of evaporation can be measured by following the falling meniscus. It is advisable to use capillary tubes smaller than 500 μm (same order or magnitude as in the present case) to ensure that the mass transfer to the tube top mouth takes place by molecular diffusion alone (Berezhnoi and Semenov [37]). Therefore we can reasonably assume that what evaporates from the meniscus interface is diffused in the gas phase ($Q_{evap} = Q_{diff}$). In other words, the mass flux at the wedge surface in the steady state is equal to the diffusion mass flux in the vapour.

For evaporation through stagnant gas (the liquid-vapour interface is impermeable to air) can be expressed as follows:

$$\dot{m} = -\frac{M\,D\,\tilde{\rho}}{L}\ln\left(1-\frac{C_{sat}}{\tilde{\rho}}\right) \qquad (2.3)$$

where M is the vapour molecular weight, D is the diffusion coefficient, $\tilde{\rho}$ is the density of air-vapour mixture, C_{sat} is the surface vapour concentration of the volatile liquid in air at the wedge corner, assumed to be the saturation one, and L is the meniscus distance from the tube mouth. Note that in Equ. (2.3):

$$\frac{C_{sat}}{\tilde{\rho}} = \frac{P_{sat}}{P} \qquad (2.4)$$

As discussed in an earlier section of this chapter, along the meniscus interface most of the evaporation takes place in the meniscus micro-layer region (see Figure 2.4). This layer is of paramount importance in the heat and mass transfer from a meniscus interface as shown by different authors (Derjaguin [38], Moosman and Homsy [39], Schonberg et al. [40] and Park and Lee [41]); this layer has a thickness of the order of δ = 5-15 μm and is extended for l_{evap} = 17.5 μm (see Park and Lee [41]). Because of its small thickness no convection can set in and the layer is commonly assumed purely conductive (see Moosman and Homsy [39]).

The local energy balance ($Q_{evap} = Q_{liq\ cond}$) at the surface of the conducting layer region of the meniscus reads:

$$\dot{m}\frac{\Delta H}{M}A_{diff} = \kappa_l \vec{\nabla} T_l . \vec{1} A_{evap} \qquad (2.5)$$

where ΔH is the latent heat of evaporation, k_l is liquid thermal conductivity, $\vec{\nabla} T_l$ is the temperature gradient, $\vec{1}$ is the unity vector, the $A_{evap} = 2\pi R_i l_{evap}$ and $A_{diff} = \pi R_i^2$. Equ. (2.5) states that all that evaporates at the meniscus wedge has to diffuse through the cross section of the tube.

Assuming 1-D conduction in the radial direction, the normal component of the heat flux can be then written as:

$$\dot{m}\frac{\Delta H}{M}A_{diff} = \kappa_l \frac{T_a - T_c}{\delta} A_{evap} \qquad (2.6)$$

where δ is the mean thickness of the conductive layer (assumed for calculation purposes in the model as δ = 10 μm), T_c is the temperature at the meniscus wedge and T_a is the wall temperature, this last being assumed to be the ambient air temperature for a conducting wall. Combining Equs. (2.4-2.6) one gets:

$$\frac{D\tilde{\rho}}{L}\ln\left(1-\frac{C_{sat}}{\tilde{\rho}}\right)\Delta H\frac{A_{diff}}{A_{evap}} = \kappa_l \frac{(T_a - T_c)}{\delta} \qquad (2.7)$$

The saturation concentration can be written as:

$$C_{sat} = \frac{P}{\Re T_c} X(T_c) \qquad (2.8)$$

where P is the pressure of the gas phase (air-vapour), $\Re$ is the molar ideal gas constant and X is the mole fraction of vapour into air.

Clausius-Clapeyron relation is used to find the mole fraction as function of temperature:

$$X(T_c) = exp\left[-\frac{\Delta H}{\Re}\left(\frac{1}{T_c}-\frac{1}{T_b}\right)\right] \qquad (2.9)$$

where T_b is the liquid boiling temperature. Equ. (2.7) can thus be re-written as follows:

$$\frac{D\tilde{\rho}\Delta H}{L}\ln\left(1-\frac{P}{\Re T_c\tilde{\rho}}\exp\left[-\frac{\Delta H}{\Re}\left(\frac{1}{T_c}-\frac{1}{T_b}\right)\right]\right)\frac{A_{diff}}{A_{evap}} = \kappa_l\frac{(T_a-T_c)}{\delta} \qquad (2.10)$$

Solving the above equation will give the temperature of the interface at the meniscus wedge. This would allow to estimate the variation of the temperature difference $(T_a - T_c)$ as a function of the distance of the meniscus from the capillary mouth L.

Defining a dimensionless length as $\tilde{L} = \frac{\delta}{L}$ and introducing $\frac{A_{diff}}{A_{evap}} = \frac{R}{2l_{evap}}$, Equ. (2.10) is written as follows:

$$\frac{D\tilde{\rho}\Delta H}{k_l}\frac{R}{2l_{evap}}\tilde{L}\ln\left(1-\frac{P}{\Re T_c\tilde{\rho}}\exp\left[-\frac{\Delta H}{\Re}\left(\frac{1}{T_c}-\frac{1}{T_b}\right)\right]\right) = T_c(T_a - T_c) \qquad (2.11)$$

Table 2.3 shows the results giving the temperature difference (T_a-T_c) between the wedge and the centre of the meniscus as the meniscus recedes inside the capillary ($\tilde{L}$

diminishes). This indicates that the temperature difference between the apex and the wedge diminishes as the meniscus recedes inside the capillary. According to Table 2.3 the temperature difference (T_a-T_c) is drastically reduced after $\tilde{L}$ = 0.01 (corresponding to L = 1 mm), therefore the driving force is weakened as the meniscus moves deeper inside the tube and the convection slows down; this is in agreement with the experimental results shown on Figure 2.10.

Table 2.3 Temperature difference and Marangoni number as a function of the dimensionless distance computed from the model.

	Ethanol		*Methanol*	
$\tilde{L} = \delta / L$	$T_a - T_c$ (K)	Ma	$T_a - T_c$ (K)	Ma
1	4.071	2194.23	5.063	4848.81
0.9	3.727	2008.81	4.644	4447.54
0.8	3.371	1816.93	4.21	4031.9
0.7	3.004	1619.12	3.759	3599.98
0.6	2.624	1414.31	3.294	3154.65
0.5	2.229	1201.41	2.803	2684.42
0.4	1.82	980.961	2.294	2196.95
0.3	1.393	750.812	1.761	1686.5
0.2	0.949	511.501	1.204	1153.07
0.1	0.485	261.41	0.618	591.856
0.01	0.05	26.9495	0.063	60.3348
0.001	0.005	2.69495	0.006	5.7461
0.0001	0	0	0.001	0.9576

The temperature that sets in at the corner T_c is lower than the temperature T_a at the centre of the cap and the Marangoni number (ratio between surface tension and viscous forces) is then defined as:

$$M_a = \frac{\partial \sigma}{\partial T} \nabla T_l \frac{\rho_l c_{pl}}{\mu_l \kappa_l} d^2 = -\frac{\partial \sigma}{\partial T}(T_a - T_c)\frac{\rho_l c_{pl}}{\mu_l \kappa_l} R \frac{\left(\frac{\pi}{2} - \theta\right)}{cos\theta} \tag{2.12}$$

where σ is the surface tension, ∇T_l the liquid temperature gradient along the meniscus interface, ρ_l, c_{pl}, μ_l and k_l are the liquid density, specific heat capacity, dynamic viscosity and thermal conductivity respectively, and θ is the steady apparent contact angle. The meniscus arc length d is taken as a characteristic dimension:

$$d = R\frac{\left(\frac{\pi}{2} - \theta\right)}{cos\theta} \tag{2.13}$$

The temperature gradient is taken as:

$$\nabla T_l = \frac{(T_a - T_c)}{R\frac{\left(\frac{\pi}{2} - \theta\right)}{cos\theta}} \tag{2.14}$$

One can describe the variation of the Marangoni number as a function of the distance of the meniscus from the mouth of the capillary tube, using the corresponding thermophysical properties of the appropriate liquid (Table 2.2). The profile of the Marangoni number versus the normalized length $\tilde{L}$ can be obtained by solving Equ. (2.11) to find the temperature difference (T_a-T_c) and then use it to calculate the Marangoni number (also reported in Table 2.3). Results for a meniscus of ethanol and methanol receding in a 600 μm capillary tube are presented in Figure 2.16 and show that the Marangoni number decreases as the meniscus recedes inside the pore ($\tilde{L}$ diminishes). Another important trend found is that methanol (more volatile) exhibits higher Marangoni numbers. Again, this qualitatively agrees with our findings reproduced in Figure 2.10 in terms of tracer spinning frequency.

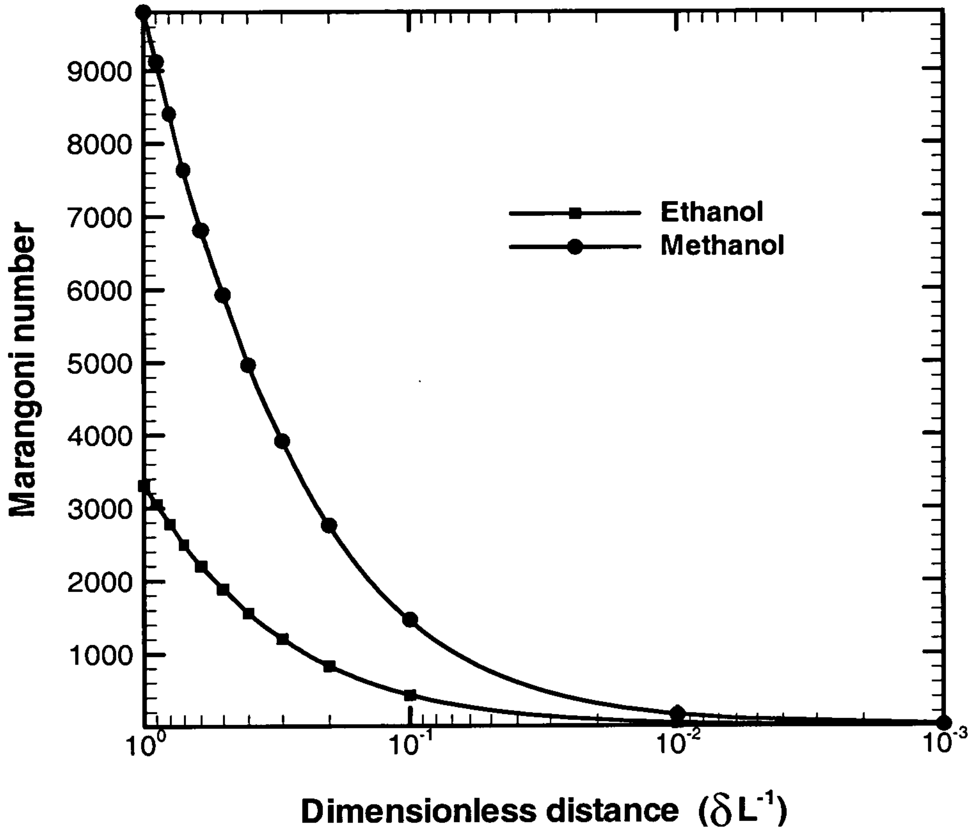

Figure 2.16 Experiment (1): Marangoni number vs. dimensionless distance for two liquids and 600 μm tube.

2.6 Discussion

The evaporation along the meniscus formed inside a confined space such as a pore is not uniform. It is larger near the wall than in the middle of the capillary (Sartre et al. [8]). The results about the evaporation rate reproduced in Figure 2.12 confirm this statement. Indeed if the evaporation was uniform along the meniscus, we should have a linear relation between the evaporation rate and the meniscus surface area, the latter being proportional to the square of the tube radius. The evaporation rate is linearly proportional to the tube radius and therefore is non-uniform along the meniscus, being stronger near the wall in the triple line region of the meniscus. The meniscus region close to the tube wall is usually (Swanson and Herdt [14], Schonberg et al. [40] and Potash and Wayner [42]) divided in three different sub-regions as schematically drawn in Figure 2.4. In the adsorbed layer of constant thickness the van der Waals forces dominate and no evaporation takes place. In a very small region (usually a few percent of the entire meniscus length) most of the evaporation takes place because film thickness is still small and the adhesion forces are balanced by the capillary ones; this sub-region is called micro-region. As the meniscus thickness increases in the adjacent macro-region, the thermal resistance of the layer increases accordingly and the heat transfer coefficient weakens as reported by Kim [30]. In the macro-region the capillary forces dominate and set about a flow to re-supply the liquid evaporated in the micro-region. Bigger tube sizes have a longer micro-region; in particular, the micro-region increases linearly with the tube radius. This is believed to be one of the possible reasons for a linear increase in the evaporation rate with the tube radius as shown in Figure 2.12.

The non-uniform evaporation cools the liquid phase differentially along the meniscus interface leading to a difference in interfacial temperature and thus in surface tension and density along the meniscus interface. For small tubes (below 1 mm) the surface tension effect is predominant as pointed out by different researchers (see Szymczyk [43] and Molenkamp [44]). Therefore, the surface tension gradient is expected to be the driving force for the thermal Marangoni convection roll visualized in the liquid phase (see Figure 2.6). It is worth mentioning that similar conclusions have been reached, investigating the evaporation of sessile drops by Deegan et al. [45]. The analogy between the present case and a sessile drop is justified. The strong evaporation that takes place near the triple line is governed by the same mechanism for both cases. Inside a pore, the convection roll has a toroidal shape and looking at it from the side with a microscope two sections can be seen (see Figure 2.6). In the spinning movement the particles are accelerated along the meniscus interface from the center to the wedge; from there they move back along the walls to the bulk phase returning to the center of the capillary and then are accelerated again along the capillary center towards the meniscus. As mentioned in the results section, the average evaporation flux is found to increase when reducing the tube size essentially because the evaporation rate increases linearly with the tube radius whereas the meniscus spherical cap area is proportional to the square of the tube radius. At the same time the intensity of the convection rolls (their spinning frequency) increases because of a higher temperature gradient along the meniscus interface. Generally speaking it is well established that convection helps the heat-mass transfer. Also for the present case, the role played by Marangoni convection is not negligible in bringing hot liquid from the bulk close to the meniscus interface where the heat-mass transfer is taking place because of evaporation.

Although convection contributes to the enhancement of the average evaporation flux, a time-scale analysis has shown that for the investigated system most of the heat transfer necessary for sustaining evaporation comes through the walls of the capillary. Another important effect must be taken into account considering Experiment (1). Diffusion in the vapour phase plays also an important role. With the meniscus stuck at the capillary mouth, the evaporation is limited by the heat transfer from the surrounding environment. When the meniscus detaches from the pore mouth and starts to move inside the tube, the limiting mechanism for evaporation is the diffusion of vapour inside the pore. Results in Figures 2.8-2.9, show that for various capillary sizes and liquids, evaporation is reduced when the meniscus recedes inside the pore. Measurements on convection (see Figures 2.10), demonstrate that the spinning intensity decreases as well. The model developed earlier attempted to demonstrate how the temperature gradient along the meniscus interface responsible for the observed convection decreases as the meniscus recedes inside the pore.

In order to evaluate the role of the strong evaporation occurring at the meniscus micro-region, a comparison has been performed with an analytical model developed by Gamayunov and Lankov [46] on a receding evaporating meniscus inside a pore.. The model of Gamayunov and Lankov [46] describes the evaporation rates in capillary tubes, without accounting for any convection and/or differential evaporation rate along the meniscus interface. The model of Gamayunov and Lankov [46] reproduces well the trend of the curve found in the present experimental investigation (see Figures 2.8-2.9) because the phenomena are diffusion controlled. However, the Gamayunov and Lankov [46] model fails in describing the effect of the tube size (see Figure 2.17). It is believed that the discrepancy is mainly due to the observed enhancement because of the strong evaporation at the meniscus micro-region and the observed convection that helps in enhancing the heat-mass transfer at the meniscus interface.

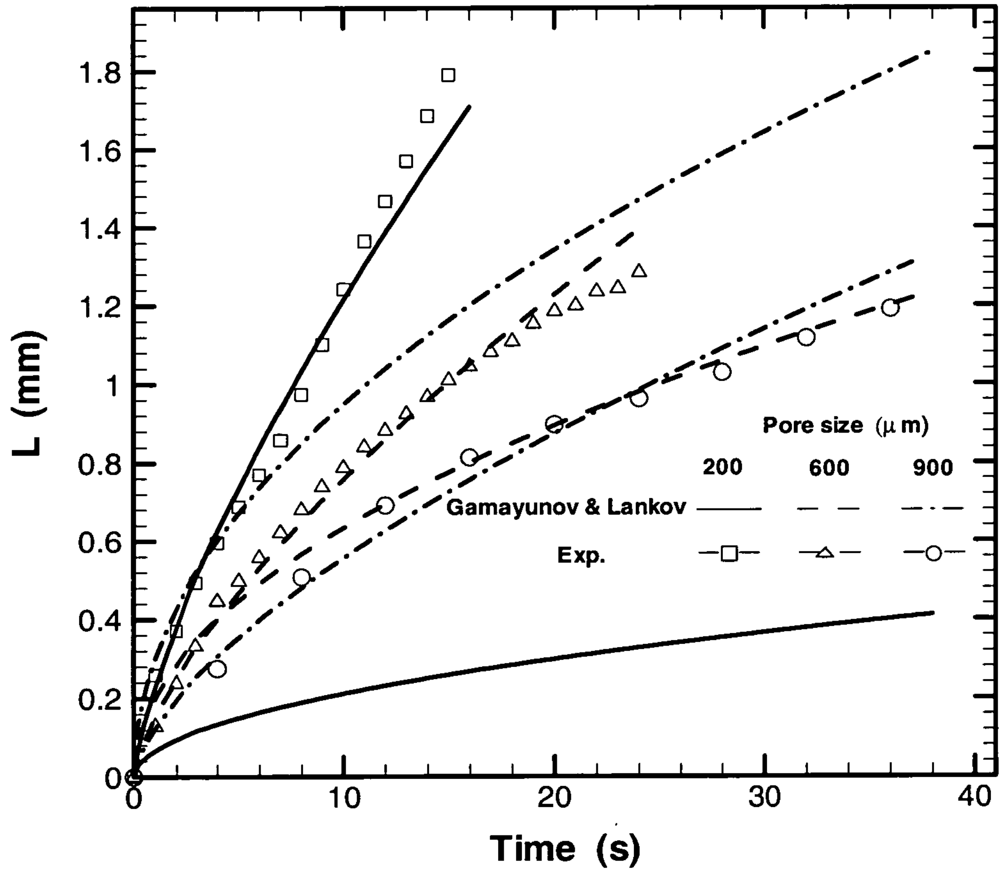

Figure 2.17 Experiment (1): Gamayunov and Lankov [46] – present experimental results comparison of the meniscus position (*L*) for n-pentane and various tube sizes.

2.7 Conclusions

Some fundamental aspects of the evaporation of volatile liquids from a meniscus formed in a confined space such as a capillary tube have been experimentally investigated. Four different liquids (ethanol, methanol, acetone and n-pentane) and three tube sizes (200, 600 and 900 μm) have been investigated in the present study. The non uniform evaporation at the meniscus interface is responsible for a strong convection in the liquid phase driven by surface tension gradient. This chapter describes the Marangoni convection in the meniscus liquid phase and how it enhances the heat and mass transfer from a pore. The Marangoni roll has been visualized using seeding particles and its characteristics (i.e., frequency, shape) have been measured and/or monitored. The evaporation rate was also measured and correlated with the spinning frequency of convective patterns. Results clearly show how both the average evaporation flux and the spinning frequency increases when reducing the tube size. Therefore, it was concluded that the heat and mass transfer from a pore is enhanced at smaller scales because of both stronger evaporation and Marangoni convection.

These findings are very important because they can be commercially exploited. In fact, in Heat Pipe or Capillary Pumped Loops a reduction in the pores size could handle larger heat flux because of a larger average evaporation mass flux in the pore.

The next chapter will introduce a powerful technique (μ-PIV) for fluid flow pattern characterization. Some of the experiments carried out in the present chapter will be recalled and further analysed with μ-PIV; many others cases involving different orientations of the tube and heated capillaries will be deeply investigated with this experimental technique.

2.8 References

[1] de Gennes P.G., 1985, *Wetting: statics and dynamics*, Reviews of Modern Physics, Vol. 57, No. 3, Part I, pp. 827-863.

[2] Leger L. and Joanny J.F., 1992, *Liquid spreading*, Rep. Prog. Phys., pp. 431-486.

[3] Ganzevles F.L.A. and van der Geld C.W.M., 1998, *Marangoni convection in binary drops in air cooled from below*, International Journal of Heat and Mass Transfer, Vol. 41, No. 10, pp. 1293-1301.

[4] Busscher H.J., van Pelt A.W.J., de Boer P., de Jong H.P. and Arends J., 1984, *The ffect of surface roughness of polymers on measured contact angle of liquids*, Colloids and Surfaces, Vol. 9, pp. 319-331.

[5] Palasantzas G. and de Hosson J.Th.M., 2001, *Wetting on rough surfaces*, Acta Mater., Vol. 49, pp. 3533-3538.

[6] Perng Y.-Y., The *unsteady moving contact line: experimental investigation*, PhD Dissertation Thesis, Evanston, Illinois, USA, 1997.

[7] Stephan P. and Busse C.A., 1992, *Analysis of the heat transfer coefficient of grooved heat pipe evaporator walls*, International Journal of Heat and Mass Transfer Vol. 35, pp. 383-391.

[8] Sartre V., Zaghdordi M.C. and Lallemand M., 2000, *Effect of interfacial phenomena on evaporative heat transfer in micro heat pipes*, International Journal Thermal Science, Vol. 39, pp. 498-504.

[9] Potash M.L. and Wayner P.C., 1970, *Fluid flow in an evaporating meniscus*, A.I.C.H.E., 63rd Annual General Meeting, Chicago, 29th Nov.-3rd Dec.

[10] Potash M.L. and Wayner P.C., 1974, *Effect of thermocapillary on the evaporating meniscus*, Report RPI TCTP-001, NTIS PB-235-737.

[11] Preiss G. and Wayner P.C., 1976, *Evaporation from a capillary tube*, Journal of Heat Transfer, Vol. 96, pp. 178-181.

[12] Wayner P.C., Kao Y.K. and LaCroix L.V., 1976, *The Interline Heat Transfer Coeficient of an Evaporating Wetting Film*, Int. J. Heat and Mass Transfer, Vol. 19, pp. 487-492.

[13] Mirzamoghadam A. and Catton I., 1988, *A physical model of the evaporating meniscus*, Journal of Heat Transfer, Vol. 110, pp. 201-207.

[14] Swanson L.W. and Herdt G.C., 1992, *Model of the evaporating meniscus in a capillary tube*, Journal of Heat Transfer, Vol. 114, pp. 434-441.

[15] DasGupta S., Schonberg J.A and Wayner P.C., 1993, *Investigation of an evaporating extended meniscus based on the augmented Young-Laplace equation*, Journal of Heat Transfer, Vol. 115, pp. 201-208.

[16] Wayner P.C., 1994, *Thermal Effects in the Spreading of a Liquid Film Due to a Change in the Apparent Finite Contact Angle*, Journal of Heat Transfer, Vol. 116, pp. 938-945.

[17] Reyes R. and Wayner P.C., 1996, *A Kelvin-Clapeyron adsorption model for spreading on a heated plate*, Journal of Heat Transfer, Vol. 118, pp. 830-882.

[18] Khrustalev D. and Faghri A., 1995, *Heat transfer during evaporation on capillary-grooved structures of heat pipes*, Journal of Heat Transfer, Vol. 117, pp. 740-747.

[19] Schonberg J.A, DasGupta S. and Wayner P.C., 1995, *An augmented Young-Laplace model of an evaporating meniscus in a microchannel with high heat flux*, Experimental Thermal and Fluid Science, Vol. 10, pp. 163-170.

[20] Churaev N.V., 1995, *Contact angles and surface forces*, Advanced in Colloid and Interfacial Science, Vol. 58, pp. 87-118.

[21] Churaev N.V., Ershov A.P. and Zorin Z.M., 1996, *Effect of surfactants on the kinetics of an immiscible displacement in very thin capillaries*, Journal of Colloid and Interfacial Science, Vol. 177, pp.589-601.

[22] Rusanov A.I. And Krotov V.V., 2000, Capillary effects of surfactants at curved interfaces, Advanced in Colloid and Interface Science Vol. 85, pp. 35-59.

[23] Miller C.A. and Neogi P., 1985, *Interfacial Phenomena*, New York, Marcel Dekker Inc.

[24] Fang H. and Shah D.O., 1998, *The effect of surfactant monolayers on the heat transfer through air/water and oil/water interface using IR image technique*, Journal of Colloid and Interface Science, Vol. 205, pp. 531-534.

[25] Wu T.C., Yang Y.M. and Maa J.R., 2000, *Surfactant-induced retardation of the thermocapillary flow at a gas/liquid interface*, Int. Comm. Heat Mass Transfer, Vol.27, No.5, pp.655-666.

[26] Wei Q. and Ma T. Z., *Effects of the Polarity of Working Fluids on Vapor-Liquid Flow and Heat Transfer Characteristics in a Capillary*, Proceeding of Heat Transfer

and Transport Phenomena in Microsystems Conference, 15-20 October 2000 Banff Centre for Conferences, Banff, Alberta, Canada.

[27] Farshad F., Rieke H. and Garber J., 2001, *New development in surface roughness measurements, characterization, and modeling fluid flow in pipe*, Journal of Petroleum Science and Engineering, Vol. 29, pp. 139-150.

[28] Li Z.X., Du D.X. and Guo Z.Y., 2002, *Experimental study on flow characteristics of liquid in circular microtubes*, Proceedings of the Int. Conference on Heat Transfer and Transport Phenomena in Microscale, Banff, Canada.

[29] Yaws C.L., 1999, *Chemical properties handbook*, McGraw-Hill, New York.

[30] Kim I.Y., *An optical study of the heat transfer characteristics of an evaporating thin liquid film*, Ph.D. Thesis, Rensselaer Polytechnic Institute, Troy, New York, 1994.

[31] Meyer R.E., 1984, *Note on evaporation in capillaries*, Journal of Applied Mathematics, Vol. 32, pp. 235-252.

[32] Shieh C.-Y., *Unsteady buoyancy thermocapillary induced convection in rectangular tank with phase change*, Ph.D. Thesis, The University of Michigan, USA, 1985.

[33] Davis S. H., 1987, *Thermocapillary instabilities*, Annual Review of Fluid Mechanics, Vol. 19, pp. 403-435.

[34] Riley R.J., *An investigation of the stability and control of a conbined thermocapillary-buoyancy driven flow*, Ph.D. Thesis, Georgia Institute of Technology, USA, 1996.

[35] Pratt D.M. and Hallinan K.P., 1997, *Thermocapillary effects on the wetting characteristics of a heated meniscus*, Journal of Thermophysic Heat Transfer, Vol. 11, No. 4, pp. 519-525.

[36] Coulson J.M. and Richardson J.J., 1999, *Chemical engineering*, 6th Edition, Volume 1, Butterworth Heinemann, Elsevier, New York.

[37] Berezhnoi A.N., and Semenov A.V., 1997, *Binary diffusion coefficients of liquid vapors in gases*, Begell House Inc., New York.

[38] Dejaguin B.V., 1965, *Definition of the concept of disjoining pressure and its role in the statics and kinetics of thin layers of liquids*, Colloid Journal USSR (Engl. Transl.) Vol. 17, pp. 191-198.

[39] Moosman S. and Homsy S.M., 1980, *Evaporating menisci of wetting fluids*, Journal of Colloid and Interface Science, Vol. 73, pp. 212-223.

[40] Schonberg J.A., Dagupta S. and Wayner P.C., 1995, *An augmented Young-Laplace model of an evaporating meniscus in a microchannel with high heat flux*, Experimental Thermal and Fluid Science, Vol. 10, pp. 163-170.

[41] Park K. and Lee K., 2003, *Flow and heat transfer characteristics of the evaporating extended meniscus in a micro-capillary channel*, International Journal of Heat and Mass Transfer, Vol. 46, pp. 4587-4594.

[42] Potash J.M. and Wayner J.P., 1972, *Evaporation from a two-dimensional extended meniscus*, International Journal of Heat and Mass Transfer, Vol. 15, No. 3, pp. 1851-1863.

[43] Szymczyk J., 1991, *Marangoni and Buoyant Convection in a Cylindrical Cell Under Normal Gravity*, The Canadian Journal of Chemical Engineering, Vol. 69, pp. 1271-1276.

[44] Molenkamp T., *Marangoni Convection, Mass Transfer and Microgravity*, Ph.D. Thesis, University of Groningen, Germany, 1998.

[45] Deegan R.D., Bakajin O., Dupont T.F., Huber G., Nagel S.R. and Witten T.A., 2000, *Contact line deposit in an evaporating drop*, Physical Review E, Vol. 62, No. 1, pp. 756-765.

[46] Gamayunov N.I. and Lankov A.A., 1985, *High-temperature evaporation of liquids from capillary tubes under the influence of a constant temperature gradient*, Teplofizika Vysokikh Temperatur, Vol. 23, No. 1, pp. 102-105.

CHAPTER III

Thermocapillary convection study in capillary tubes using μ-PIV technique

3.1 Motivation

As reported in Chapter II, a vigorous convection is present in the meniscus liquid phase. Some important parameters (evaporation mass flux and tracer spinning frequency) have been measured by observation of the receding meniscus and the use of tracer particles. There are many experimental techniques to measure fluid velocity, but they are not suitable for quantifying the local flow fields for such a small system. The most suitable solution seems to be Particle Image Velocimetry (PIV). PIV consists essentially of seeding the fluid with particles, illuminating the flow (usually using a laser source) and capturing the scattered light from the particles on a photographic or digital image. In the early stages of the technique, the scattered light from the particles was recorded on photographic film and the velocity calculated from the displacement of the particles between two successive images of the flow at known time interval. Over the last two decades, much has been done to improve the technique making it one of the most widely used techniques for flow field investigations. The advantage of PIV is that it yields an instantaneous flow field which allows determination of the vorticity. Standard PIV is quite mature and a considerable range of commercially available hardware and software packages can meet different needs [1-3]. However, when it comes to investigating fluid flow at small scales a range of different issues arises and must be addressed. Micro-Particle Image Velocimetry (μ-PIV) is a quite new area, although in rapid evolution. There is commercial interest in investigating fluid flows and building new devices at the micro-scale [4-5], for many important areas such as biomedical and electronic applications. At such small scales, the measurement techniques available for standard scales are not transportable because other phenomena which were negligible at standard scale now become important. Therefore, experimental work is needed to address these issues and to serve as a benchmark for numerical codes. On one hand, visual observation of the phenomena (such as boiling) is easily done at micro-scales with the use of high speed cameras. On the other hand, measuring important parameters such as temperature and velocity at small scales is still an issue. In the following it is explained how the fluid flow field has been observed by the use of a µ-PIV technique. µ-PIV is the core of this experimental investigation as it has enabled characterization of the observed liquid convection. Important conclusions are drawn in this chapter highlighting how the observed phenomena have a universal character and confirming that the source of the convection is the strong evaporation at the meniscus triple line region with consequent generation of temperature differences along the meniscus that in turn set in motion the liquid convection. With the use of a heating element it is shown that the convection pattern can be altered and eventually inverted because of the meniscus temperature profile alteration.

3.2 Background

PIV is a powerful and widely used technique for determination of flow fields [6]. In standard PIV, the fluid (see Figure 3.1) is seeded with particles of suitable size and density and a light sheet, created with the use of a laser and optical lenses/mirrors, is used to illuminate the flow. Light is scattered from particles with diameter larger than the laser wavelength in accordance to the MIE scattering theory: smaller particles ($\lambda \sim d_p$) lead to diffraction or Rayleigh scattering ($\lambda >> d_p$) [7].

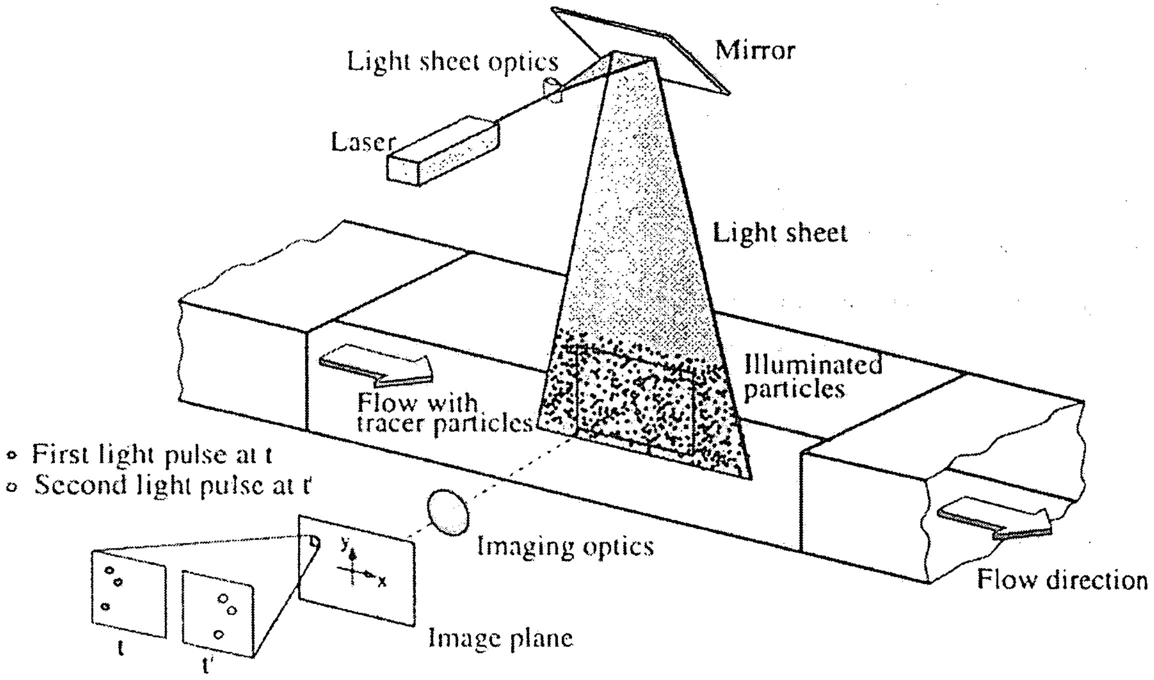

Figure 3.1 Experimental arrangement for standard PIV (from Markus et al.[4]).

The ratio between the refractive index of particles and that of the fluid is very important. All optical flow measurement techniques are based on the scattering, absorption or refraction of light in an inhomogeneous medium [8]. Usually for liquids the diffraction due to particles is one order of magnitude less than for air, therefore larger particles and/or stronger illumination is required. The scattered light from the particles is captured by a recording system. In the early stages of PIV development photographic films were used to record the images. Amazing resolutions were possible (1.1x10^9 pixels), but it was necessary to post-process the recordings manually or by digitization with consequent loss of resolution. Recent development of powerful Charged Coupled Device (CCD) cameras has replaced the more accurate but time consuming photographic films. The spatial resolution of the CCD camera (~1x10^6 pixels) is still far from the photographic one, but the post-processing has been speeded up tremendously. This has led to a rapid spread in the use of CCD cameras for PIV.

Generally speaking, there are two different approaches in PIV: single frame–multiple exposure and multiple frame–single exposure [9]. The single frame–multiple exposure technique was extensively used in connection with conventional photography. Because of rapid developments in electronic imaging devices and software, the multiple frames–single exposure has become the standard PIV approach. In the single frame-multiple exposure approach, two of the images of the seeded flow are recorded on the same frame and the particle movement is determined by auto-correlation of the images. In the double frame-single exposure approach, two images of the seeding particles are taken and cross-correlated. For both cases, PIV recordings are divided into areas called interrogation windows for correlation and in order not to lose information from those particles near the edges of the interrogation windows, an overlap between adjacent windows is usually employed. In fact for the particles near the edges of the interrogation windows, it is likely that some will move out of the window and will not produce a meaningful correlation. If the flow direction can be guessed a priori the second interrogation window could be made larger and/or moved in order to follow the same particles. Depending on the particle density (number of particles per interrogation area), there are two kinds of laser velocimetry techniques [9-10]. The "image density" N is defined as [9-10]:

$$N = C\frac{\pi d_{eff}^2 \Delta z_0}{4M_g^2} ,$$

$$d_s = 2.44(1 + M_g) f\lambda \text{, and}$$

$$d_{eff} = \left(d_s^2 + M_g{}^2 d_P^2\right)^{1/2} .$$

where C is the number of particles per unit volume, d_{eff} is the diameter of the particle image (dependent upon the particle diameter (d_P), the point spread function of the lens (d_s) and the lens magnification (M_g)), Δz_0 is the laser sheet thickness, f is the f-number of the lens and λ is the light wavelength. The aforementioned formula for the point spread function of the lens comes from the assumption of a diffraction limited lens for which the point spread function is an Airy function. The formula for d_{eff} comes from the fact that the image of a particle is the convolution of the Airy function with the particle's geometric image [6].

For low N (N<<1) one has PIV or even Particle Tracking Velocimetry (PTV) where single particles are tracked and for large N (N>>1) one has Laser Speckle Velocimetry (LSV); in this latter case one measures speckle displacements. The difference between PTV and PIV is that for the former the particle pairs can be easily detected by visual inspection of the frames, whereas statistical techniques are required in PIV to reveal the flow pattern.

Adrian [9] shows that the scattered light energy is strongly dependent on the system dimensions (field of view, distance from lens to camera and light sheet) and for small particles (with diameter of 1-10 μm) is proportional to the third power of their diameter and to the power of -3 of the light wavelength. Therefore, larger particles and smaller light wavelengths are preferable. Because photographic films are also more sensitive to short wavelengths, it turns out that green light is preferred to red. For larger particles (above 100 μm) it can be shown that the scattered energy is independent of the particles size.

Another important parameter in PIV is the illumination. In principle any light source could be used in PIV, even white light. The reason why lasers are usually preferred lies in the fact that high energy density can be achieved and it is far easier to collimate the beam and create very thin light sheets; in addition, coherent light avoids chromaticity aberration and the scattered light from the particles is of better quality. We have also seen that most recording systems (especially photographic films) are more sensitive at the short wavelengths, therefore green lasers are usually preferred.

The recording medium is also extremely important. Nowadays CCD cameras have solved many problems connected with speed and up to 100 million frames per second are achievable. The drawback is however that very few frames (usually less than 10) can be stored at this speed limiting the total recording time. Illumination properties and recording times must be tuned to suit each application. The goal is to freeze the flow; for this aim, short camera exposure times are used in conjunction with pulsed lasers. The laser can be pulsating or the light beam chopped mechanically.

Multiple frame/multiple pulse techniques [9] are also used and this approach has the important advantage of being able to choose an opportune time between the pulses in accordance with the flow velocity and the spatial resolution, whereas the time between frames can be chosen to resolve the flow time scales.

The spatial resolution of PIV is given by the laser sheet thickness, the lens' depth of view (whichever is lower) and the interrogation window size.

3.2.1 Interrogation technique by spatial correlation

There are two different kinds of spatial correlation in PIV. Single frame–multiple exposure employs auto-correlation whereas multi frame–single exposure employs cross correlation. Both auto and cross correlation give five components [11]: the self-correlation peak, the mean convolution, two displacement peaks ("reflectionally symmetric" for auto-correlation, one corresponding to the first image correlated with the second and the other for the reverse case) and the noise component. By locating the position of the displacement component, the particle displacement can be evaluated and dividing this value by the time between exposures, the flow velocity inferred. When multiple exposure is used the self-correlation peak is bigger that the other peaks (because the image of each particle is correlated with itself); the sum of the noise with mean components is higher as well. These facts make the analysis more tedious. On top of this for auto-correlation, the directional ambiguity (due to the two "reflectionally symmetric" peaks) must be solved. Adrian [12] proposed an image shifting technique to solve the directional ambiguity. The image is optically shifted in one of the velocity components by an amount that is bigger than the largest negative value given by the velocity component. With this artefact, all particle displacements are positive and the true displacements can be found by subtracting the shifting imposed. Another way of resolving the displacement ambiguity is to use two different laser wavelengths and colour film [11]. The use of colour filter can help in locating first and second particle position.

Conventional PIV is used to analyze 2-D flows because with the experimental arrangement depicted in Figure 3.1 the out of plane motion cannot be detected. When out-of-plane velocity components are present, there could be a significant loss of image pairs. One way of solving this problem could be the use of a second thicker light sheet [11]. Therefore, when using the standard PIV technique for 3-D flows unacceptable errors for the analysis are introduced. Stereo [13] and dual-plane [14] PIV have been developed in order to analyze 3-D flows.

The time between recordings and/or exposures is very important. In general short times are preferred, because with PIV we are seeking the instantaneous velocity field. However, very short times could lead to insufficient particle movement making the subsequent image analysis difficult. In the early PIV measurement it was recommended that particles be allowed to move as much as 2-3 times their diameter. Prasad et al. [15] have demonstrated that if the particles occupy almost 3-4 pixels, the image correlation peak can be located within a tenth of the particle diameter. On the other hand, large times between recordings could lead to important in-plane and out-of-plane image pair losses due to particles leaving the interrogation windows or the illuminated volume. In addition it has been proved [16] that because the particle displacement is a "low-pass filter representation" of the velocity vector, when the distance between distinct particles is much larger than the particle dimensions, the fluid flow velocity cannot be fully resolved.

The seeding particles' distribution is also crucial for PIV investigation. In PIV a homogeneous distribution of particles is advisable. Conversely, when one wants to visualize the flow field, inhomogeneous seeding is better [16].

Large velocity gradients in the interrogation windows can produce broad displacement correlation peaks, reducing their amplitude, and ultimately biasing the values towards high velocity [15-17]. This bias can be solved by adopting different sizes for the interrogation windows [18].

The micro-PIV technique is used to study micro-flows and is based on a different approach. For micro-flows a microscope is generally needed to resolve the fluid flow. The narrow microscope depth of field makes it almost impossible to align the laser sheet within it. Therefore, the laser illuminates the entire volume of fluid and the microscope is used to observe a slice of the flow because of its narrow planar depth of field. Although micro-PIV has been applied to fluid flows in very small capillaries and channels [19-23], much work is still required in order to address problems relating to the small dimensions involved. Due to the small flow dimensions and the real risk of blocking the flow, very small particles (sub-micron) are often used. However, if the particle dimensions become comparable to the wavelength of the laser, the light will be diffracted around the particles and this will affect the analysis process. On top of this, there is a serious risk of errors in the measurements due to Brownian motion (the constant and erratic movement of particles in a fluid due to its inherent temperature). Although not wanted, this effect could also be exploited. Because the correlation peaks are spread by the presence of Brownian motion, it is claimed that PIV measurements can also be used to infer temperature [24]. The scattered light from very small particles will be of low intensity and the consequent signal-to-noise ratio of the analysis too low to be accepted. Using particles that fluoresce rather than scatter the light when illuminated can solve both problems of low intensity scattered light and diffraction [25-27]. The errors due to Brownian motion can be substantially reduced by averaging the results from several runs for the same area [25-26]. However, it is advisable to choose particles large enough to minimize the effects of Brownian motion.

3.3 Experimental layouts

The aim of the μ-PIV experiments is to reveal the strong convection taking place close to the meniscus interface for an evaporating liquid in capillaries. Different situations were investigated experimentally, but the apparatus used was substantially the same. The apparatus employed for this μ-PIV investigation is schematically depicted in Figure 3.2. It consists of an Argon-Ion (green light, λ=532 nm) laser, a research microscope, a high-speed camera and a PC for image storage and post-processing. The liquid close to the meniscus interface is seeded with tracer particles in order to reveal the convection pattern.

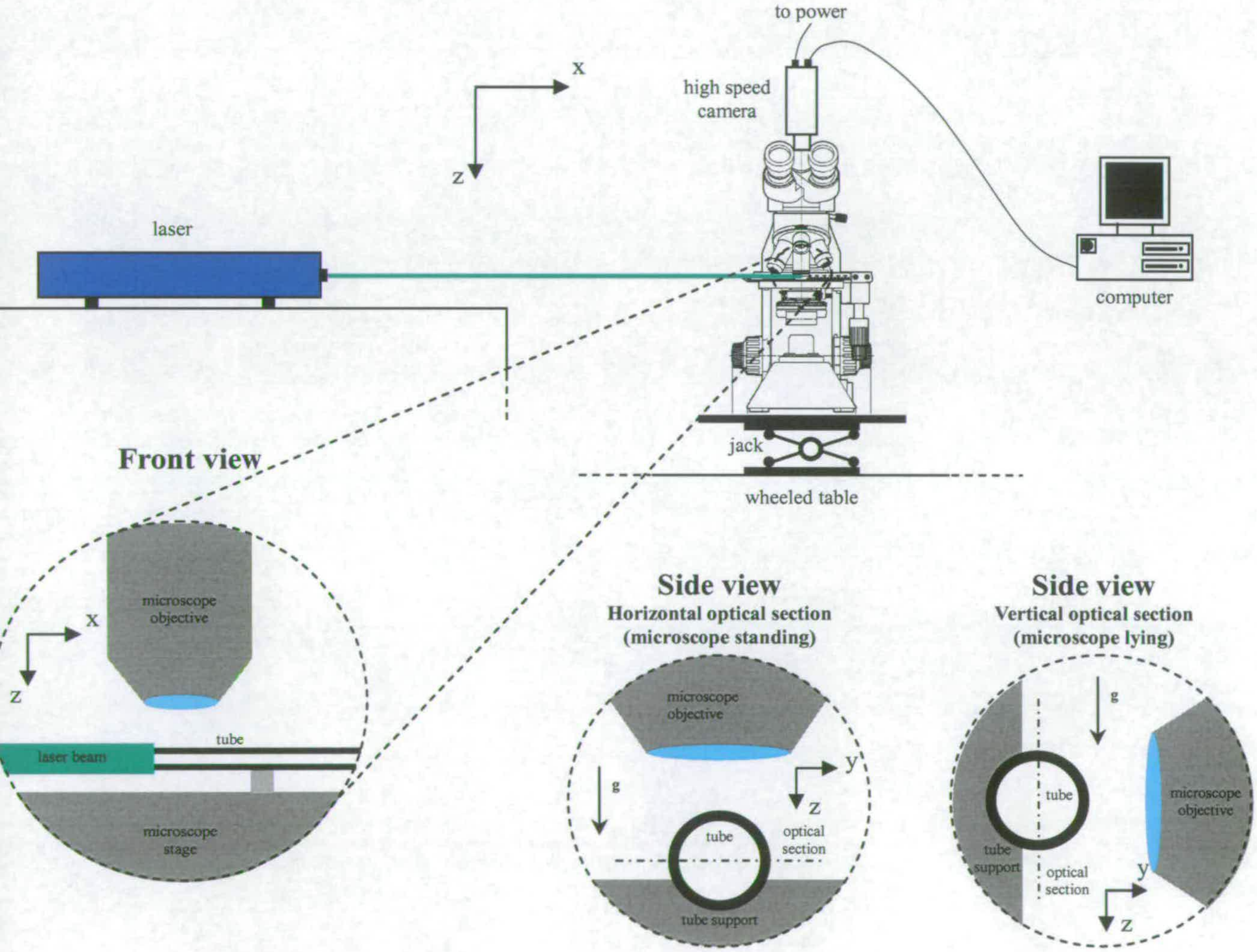

Figure 3.2 Schematic diagram of the experimental setup (unheated tubes horizontally oriented); **g** is the gravitational acceleration.

Because of the reduced sample size being investigated, the flow pattern can be clearly seen using the microscope with ordinary light (see Figure 3.3).

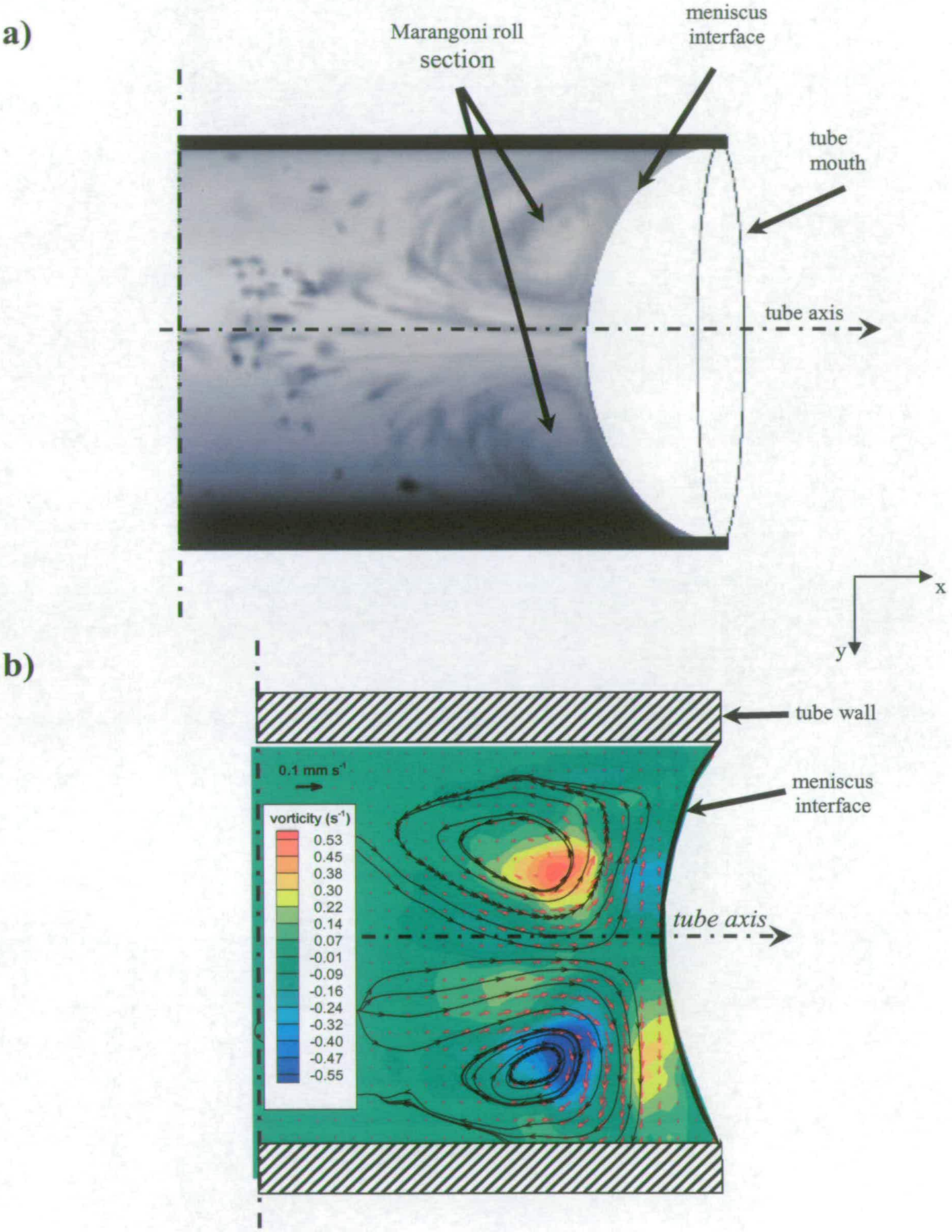

Figure 3.3 Marangoni convection pattern: (**a**) flow visualization with the use of ordinary light; (**b**) PIV analysis showing the vector map with streamlines and superimposed vorticity map.

Figure 3.3(**a**) is the seeded flow image (note that several frames have been superimposed in order to portray the particles' trajectory) and Figure 3.3(**b**) is the subsequent PIV analysis. In the PIV analysis the vector map, the vorticity and the streamlines are superimposed and the tube wall and the meniscus interface are also reproduced (a reference vector is drawn at the top left corner). In the PIV analysis, the strength of the convection is indicated by the vorticity (s^{-1}); conventionally, the value is assumed positive for an anticlockwise vortex. Although the flow pattern can be picked up with ordinary white light, coherent light from a laser has been used in order to have a much more uniform illumination around the entire field increasing the signal-to-noise ratio. The power of the Argon-Ion laser can be adjusted with a remote control unit by changing either the current or the light intensity of the beam in the range from 100 mW up to 6 W. The laser power has been kept as low as possible (100-200 mW), in order to avoid heating up the tube wall and obtaining too much reflection from the meniscus surface. The convection is caused by the temperature gradient established between the triple line and the centre of the meniscus. Heating up the wall would have affected the meniscus temperature profile and therefore the flow pattern. Attempts have been made to use a 36 mW Helium-Neon (red light, λ=612 nm) laser, but insufficient light was scattered from the particles. Greater camera sensitivity to green light rather than red may have had a considerable effect.

Because of the various tube sizes investigated, two different microscope lenses were used with depth of view of 27.45 and 6 μm and lens magnification of 4 and 10 respectively. The microscope is an Olympus Research (model BHT 112).

The tracers used were spherical glass particles (manufactured by Potters Industries Inc.) with average diameter of 11.7 μm and 3 μm (depending on the tube size under investigation) and density of 1.1 g cm^{-3}. It is desirable that the particles follow the flow. The most critical case is when the tubes are positioned with their principal axis vertical because the particles can more easily leave the region of interest due to settling. When the tubes have their axis horizontally oriented, it is less likely that the particles move far from the meniscus interface because for this configuration gravity does not act along the tube axis. In order to evaluate the influence of gravitational forces arising from the mismatch between tracers and fluid density, the following formula (coming from Stokes drag law) is used [6]:

$$U_{zP} - U_z = d_P^2 \frac{\rho_P - \rho}{18\mu} g \qquad (3.1)$$

where, U_{zP} and U_z are the particle and fluid vertical velocity components respectively, d_P is the particle diameter, ρ_P and ρ are the particles and fluid density respectively, μ is the fluid dynamic viscosity and g is the gravitational acceleration. Applying the aforementioned formula to the present case, leads:

$$U_{zP} - U_z \cong 1x10^{-5}\,\mathrm{m\,s^{-1}} \qquad (3.2)$$

whereas the particles velocity measured was $U_{zP} \cong 5x10^{-4}\,\mathrm{m\,s^{-1}}$. Therefore, we can assume the particles to behave as though they are neutrally buoyant. Attempts to use sub-micron size particles have been made, but the diffraction from the particles was too high for meaningful analysis.

The Phantom v.4.3 high-speed camera used is capable of 1000 frames per second at a resolution of 512x512 pixels (full frame) with a 16 μm square pixel; for these experiments the maximum frame rate used was 400 per second. At this frame size and for the frame rates used (100-400 per second), a total recording time of 1 minute was possible. Reduced frame size and/or frame rate could make the total recording time larger. The movie is stored locally into the camera memory and then transferred to the dedicated PC for post-processing.

The resolving power (spatial resolution) of the microscope objectives used ranged between 0.52 and 3.36 μm. The field of view ranged between 640 and 1640 μm, therefore each pixel on the CCD array of the high speed camera when projected in the flow represents between 1.25 and 3.2 μm. As described in Markus et al. [6], Adrian [10] and Meinhart et al. [26], the image of a particle on the CCD camera is the convolution of the diffraction-limited and the geometric images. Therefore the effective particle diameter projected on the camera image is:

$$d_{eff} = \left[(M_g d_P)^2 + d_s^2\right]^{1/2} \qquad (3.3)$$

with M_g being the total microscope magnification (product of microscope and lens magnifications), d_P the particle diameter and $d_s = 2.44 M_g \frac{\lambda}{2NA}$ the diffraction-limited spread function (NA is the lens numerical aperture). Applying these formulae to the present case with M_g = 40-100, NA = 0.25-0.65, λ = 532 nm, one gets d_{eff} = 3.15-4.78 μm. Projecting these values into the flow one has an effective particle diameter of 3.15-11.96 μm.

This ensures that the microscope used can distinguish between particles and that a particle image is larger than a pixel of the CCD array; the latter avoids the use of the sub-pixel approximation (Dantec Dynamics [28]) during the PIV analysis. Because the particles occupy almost 3-4 pixels, the image correlation peak can be located within a tenth of the particle diameter (Meinhart et al. [26]). Particle displacements between 315 nm and 1.20 μm on the image can thus be detected; these figures are actually better than the microscope resolving power. As highlighted by Meinhart et al. [26], one is interested in locating the particles rather than resolving their shape.

Although customised software for PIV analysis could allow more flexibility, Newport et al. [23] demonstrated, comparing three commercially available software packages, how these can be used with confidence in micro-PIV analysis. The images taken have been interrogated and validated using the Dantec FlowManager v.3.40 PIV software (Dantec Dynamics [28]). An adaptive cross correlation algorithm was used with an interrogation window of 8x8 pixels and an overlap of 50% (to fulfil the Nyquist criterion); in the measurement plane this correspond to a spatial resolution of 1.28 μm (for M=100). The interrogation window could be chosen from 8x8 up to 256x256 pixels with overlap between 25 and 75%. The PIV spatial resolution (Newport et al. [23]) is dictated by the size of the first interrogation window. With 50% overlap between adjacent interrogations windows 16,129 vectors were extracted with vector spatial resolution of 0.64 μm. In order to present clear pictures with a superimposed vector map, streamlines and vorticity, only one quarter of the vectors were plotted. Areas such as the meniscus vapour phase and the tube walls can be removed from the PIV analysis. The software package allow for different kinds of vector validation: peak validation, mean validation and manual validation. A validation method based on the ratio of the height of the correlation peak to the height of the next largest peak was used with a minimum ratio of 1.2 required for acceptance. After validation a filter has been used in order to smooth the resulting vector map. The vorticity is calculated with the following formula (Bird et al. [29]) and the streamlines located, all based on the filtered vector map:

$$(\nabla \times U)_\theta = \frac{\partial U_r}{\partial x} - \frac{\partial U_x}{\partial r} \qquad (3.4)$$

As mentioned earlier different experiments have been performed. In particular the tubes were positioned with their axis horizontal or vertical. In the former case two subsets of experiments were carried out (in a similar configuration as described in Chapter II). In one the tubes were filled from one end with the use of a syringe and the attention was focused on the receding meniscus formed (Experiment (1) in Figure 2.7). For the other set of experiments, the tubes are first partially filled with the volatile liquid so that two menisci are formed with attention being devoted this time to the meniscus stuck at the capillary mouth (Experiment (2) Figure 2.7). In order to obtain a horizontal and a vertical section of the tube, the microscope is accommodated in two positions (standing and lying) as depicted in the insets of Figure 3.2. By doing so one can observe the effect of gravity on the convection. When the effect of an extra heating element was investigated, the tubes were plunged vertically in a pool of liquid. With the tube in place, the light on the microscope was used for focusing the microscope on the area of interest. At this stage the liquid was seeded with the tracers. The microscope was put on an adjustable stage (see Figure 3.2). This allowed the final alignment of the capillary with the laser beam to be made. Each recording lasted around 1 minute, because of the limitation of the internal memory of the camera. However, the recording time was sufficient to capture the details of the flow.

Optical distortion due to the curved capillary wall has been corrected *a posteriori* in this study. Usually a square box is built around the tube and filled with a liquid (preferably the same as the one in the tube) of the same refractive index of that in the tube. In the present case, this strategy cannot be applied because of the very small sizes involved and especially of the fact that the region of interest lies very close to the tube mouth and any extra material (glue, etc.) could greatly affect the meniscus shape and ultimately the experiments. We have analysed the effect of optical distortion through the curved capillary wall and corrected for it. Figure 3.4 shows a single optical ray path. The distortion is non-linear, varying between about 19% and 25% for both fluids used (ethanol and methanol). It also leads to the outer regions of the capillary not being visible. All of the velocity and vorticity maps reported here have been corrected for this optical distortion. The position of the meniscus has also been superimposed on the flow maps.

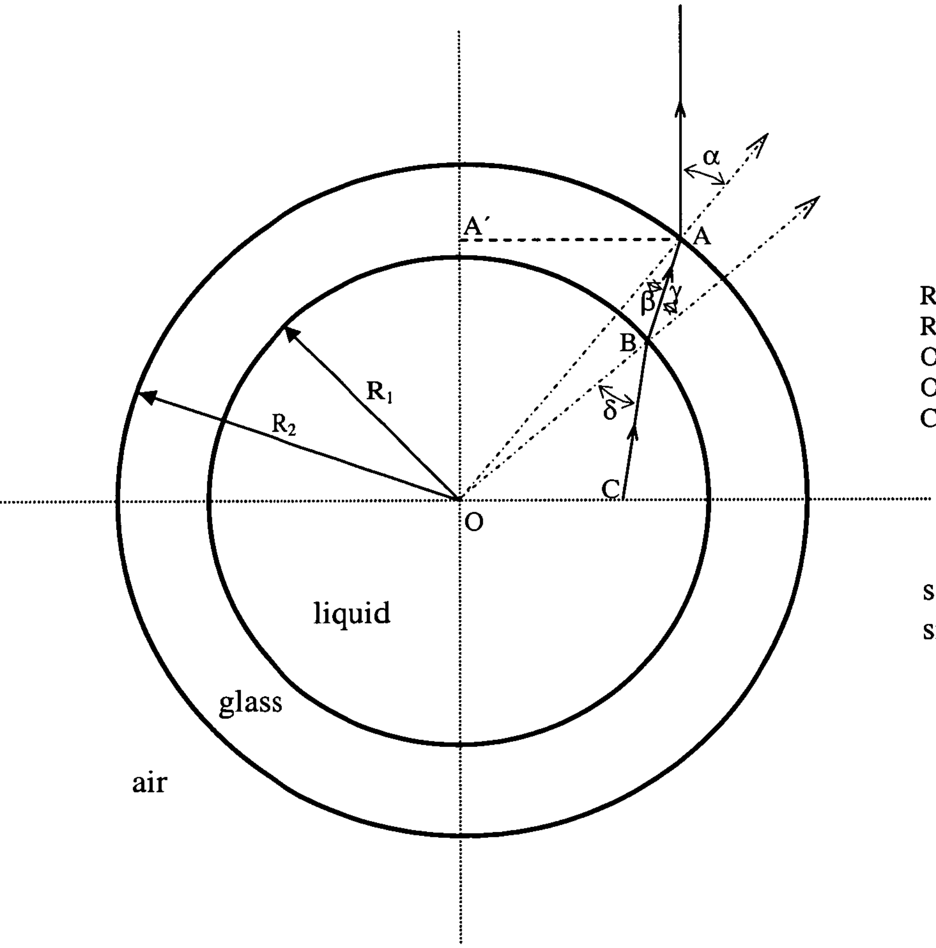

R_1	internal tube radius
R_2	external tube radius
OA	normal direction to A
OB	normal direction to B
CBA	light path

$$\sin\alpha = \sin\beta \; n_{glass}$$
$$\sin\gamma \; n_{glass} = \sin\delta \; n_{liquid}$$

Figure 3.4 Light path for optical distortion correction.

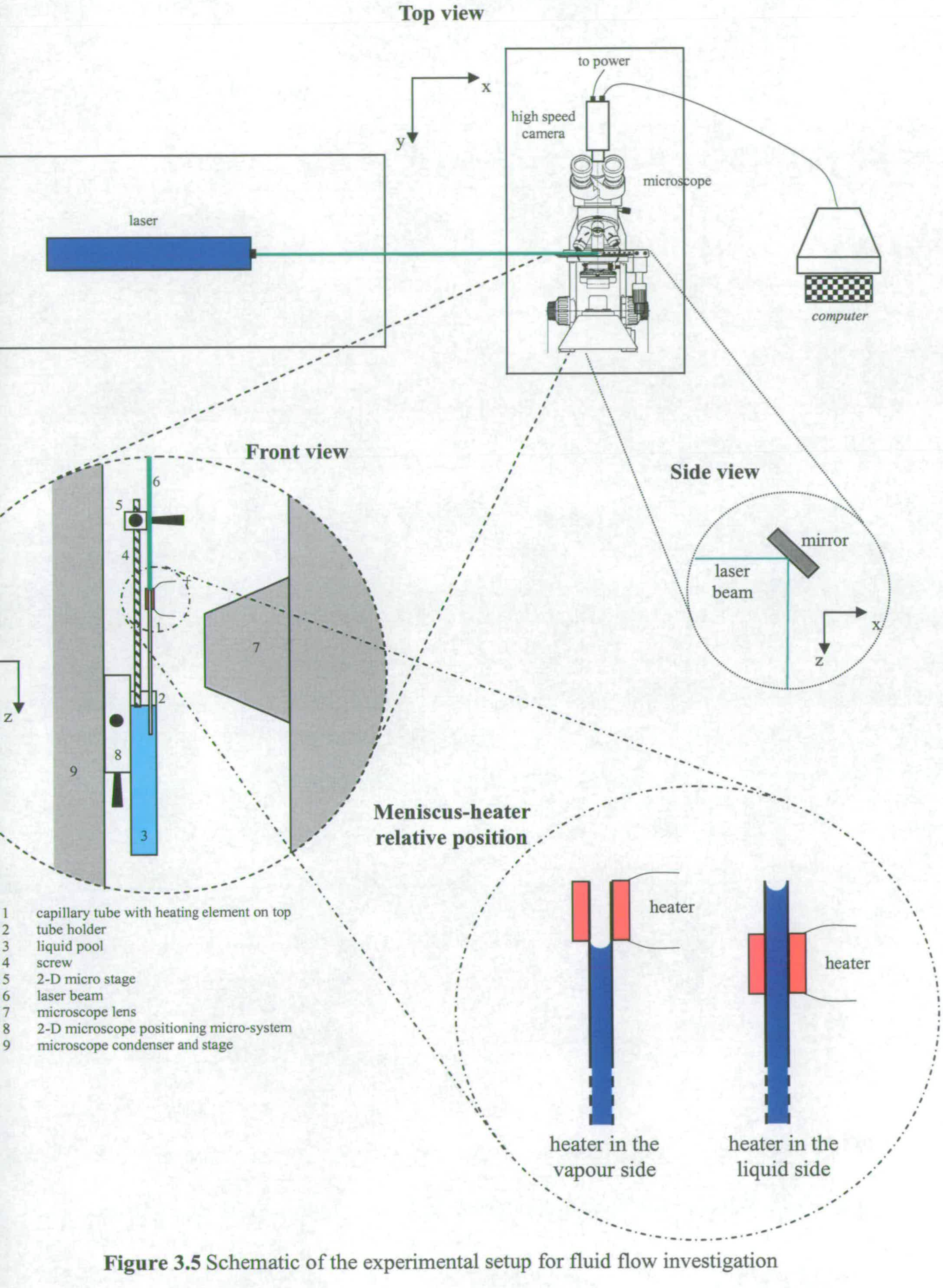

1 capillary tube with heating element on top
2 tube holder
3 liquid pool
4 screw
5 2-D micro stage
6 laser beam
7 microscope lens
8 2-D microscope positioning micro-system
9 microscope condenser and stage

Figure 3.5 Schematic of the experimental setup for fluid flow investigation

(heater tubes vertically oriented).

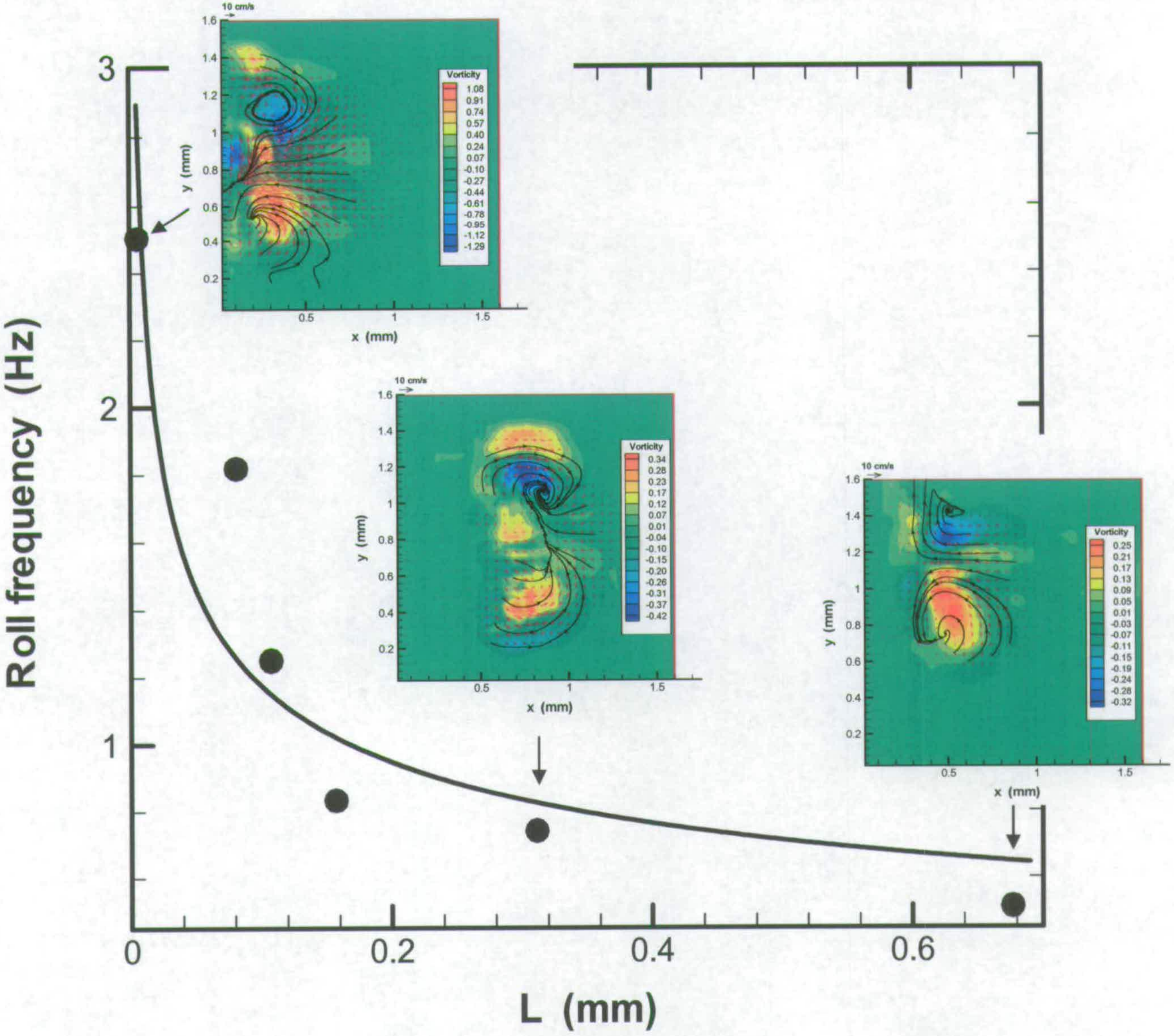

Figure 3.6 Experiment (1) of Figure 2.7: roll frequency and PIV analysis for the case of ethanol and 900 μm tube size.

3.4 Results and analysis

Three different experimental investigations were carried out. In the first, one meniscus is allowed to form in the capillary tubes that were horizontally positioned and filled from the opposite end as schematically depicted in Experiment (1) of Figure 2.7. In the next experiment, the tube was partially filled with the liquid and two menisci are formed (see Experiment (2) of Figure 2.7); again, the tube is horizontal. One meniscus is stuck at the capillary end and the other recedes inside the tube to compensate for the liquid evaporated. For this case two optical sections of the horizontally oriented tube were made in order to study the effect of gravity on thermocapillary convection. In the third experiment, the tubes were immersed vertically in a pool of liquid and the only meniscus formed is positioned at the desired height in the tube (Figure 3.5). More details about this particular experiment will be given later in this section.

Thereafter, the convection strength will be characterized by the vorticity value.

We will present the results for these three experiments in order, because important information can be gathered from one experiment and exported to the next. The results relating to the unheated tubes, horizontally oriented are presented first followed by the ones relating to the heated tubes vertically oriented.

3.4.1 Single meniscus receding for horizontally oriented capillary tubes

Three tube sizes were investigated (200, 600 and 900 μm) and filled with ethanol or methanol. For the experiment of Figure 2.7 the meniscus position was already measured in the previous chapter and by doing so the evaporation mass flux was evaluated. It was seen that as the meniscus recedes inside the tube, the evaporation rate is reduced dramatically. The meniscus is held at the tube mouth by the use of a syringe controlled by a micrometer and the liquid is seeded. Once seeded, the control on the syringe was released and measurements were taken. We present here (Figure 3.6) the PIV analysis of 900 μm tube size for ethanol plotting the results on the same graph showing the tracer spinning frequency versus evaporation mass flux (also presented in Figure 2.12). This is done in order to emphasise the fact that the thermocapillary convection studied is a direct consequence of the evaporation process as discussed in the previous chapter. As can be seen clearly from Figure 3.6, the convection strength is reduced as the meniscus moves deeper inside the pore. This is essentially linked with the vapour partial pressure rise. As the meniscus moves deeper into the tube, the vapour partial pressure in the volume vacated by the receding meniscus builds up essentially because this confined space becomes saturated with vapour as air cannot diffuse inside the tube because the meniscus is impermeable. The increased partial pressure reduces the evaporation mass flux and in turn the driving force along the meniscus interface is weakened. This is due to the fact that most of the evaporation takes place at the meniscus wedge and therefore the temperature there decreases more than at the meniscus centre. Figure 3.7 shows the effect of the tube size for ethanol. Note that the PIV frames in Figure 3.7 are not corrected for optical distortion. It is clear that reducing the tube size has beneficial consequence for the roll vorticity. The reduction of the tube diameter causes a reduction of the meniscus micro-region length. It must be remembered that the geometry studied is axi-symmetric, therefore the area of the meniscus micro-region scales as follows with the tube diameter:

$$S_\delta = l_\delta 2\pi R \qquad (3.5)$$

where l_δ is the meniscus micro-region length (that does not depend on the tube size) and R the tube radius. The meniscus cap area is proportional to the square of the tube radius. Therefore, the ratio of the meniscus micro-region area (S_δ, where most of the evaporation takes place) to the meniscus cap area is inversely proportional to the tube radius. This could explain (as also pointed out in the previous chapter) the results shown in Figures 2.12 and 3.6. Although, as shown in the previous chapter, the enhancement in the evaporation mass flux could be directly related to the change in the meniscus micro-region area, there is no contra-evidence that the enhanced convection also helps in bringing hot liquid from the bulk into regions of higher evaporation rate.

3.4.2 The role of gravity on thermocapillary convection for horizontally oriented capillary tubes

For Experiment (2) of Figure 2.7 particular attention is devoted to the role played by gravity on the thermocapillary convection. A slightly different set of capillary sizes were investigated in this case (600, 900 and 1,630 µmID tubes) and the same two liquids: methanol and ethanol. This was done because it is believed that gravity plays a role at sizes above 1 mm. Down to this scale, Marangoni convection should be dominant. In this case two sections of the capillary tube were studied. One section is horizontal and the other vertical of horizontally positioned tubes. In this experiment two menisci are present and the attention is focused on the meniscus stuck at the capillary mouth. The other recedes inside the tube to compensate for the mass lost during evaporation.

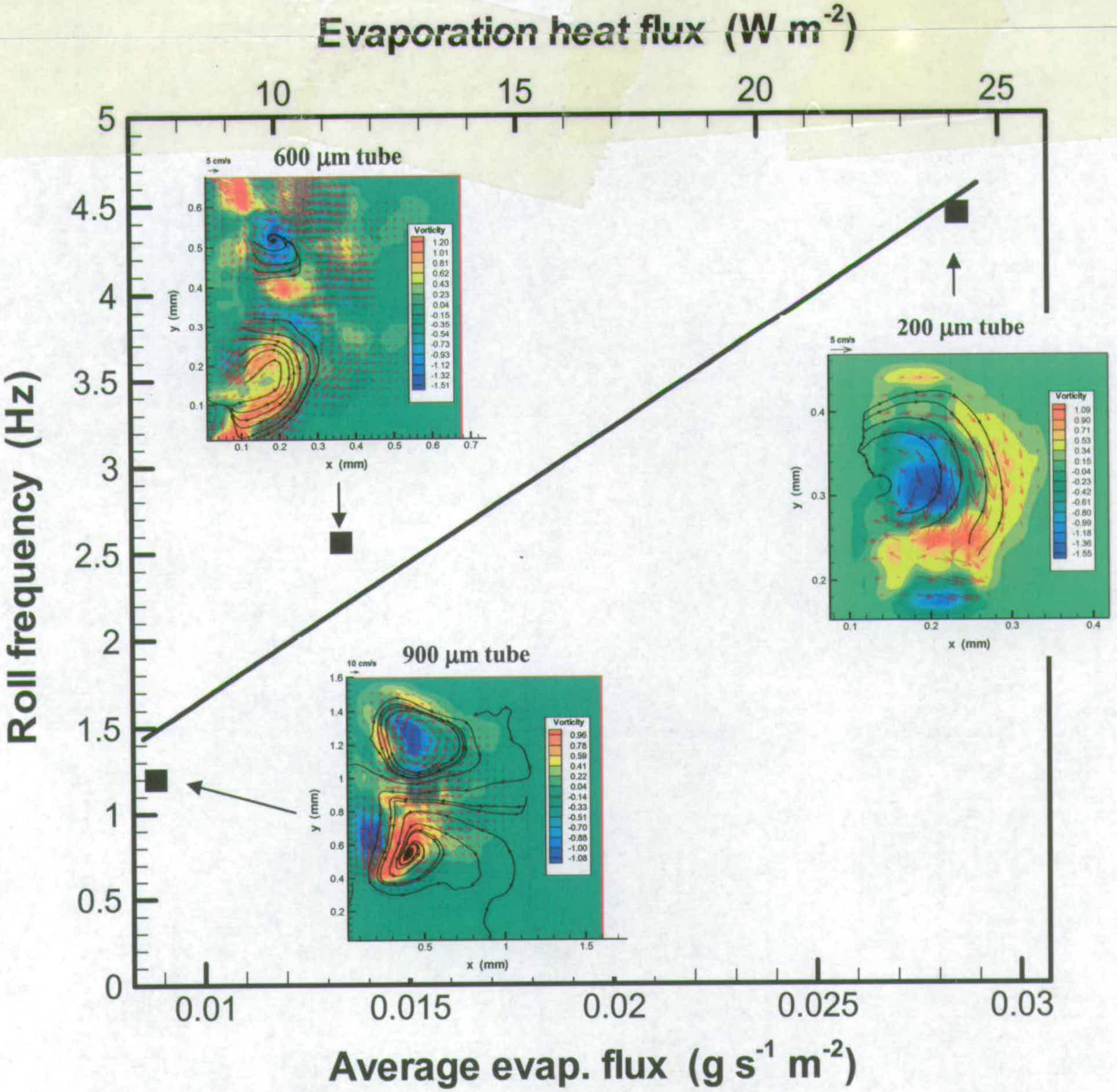

Figure 3.7 Experiment (2) of Figure 2.7: tracer spinning frequency vs. evaporation flux with PIV analysis for ethanol and various tube sizes.

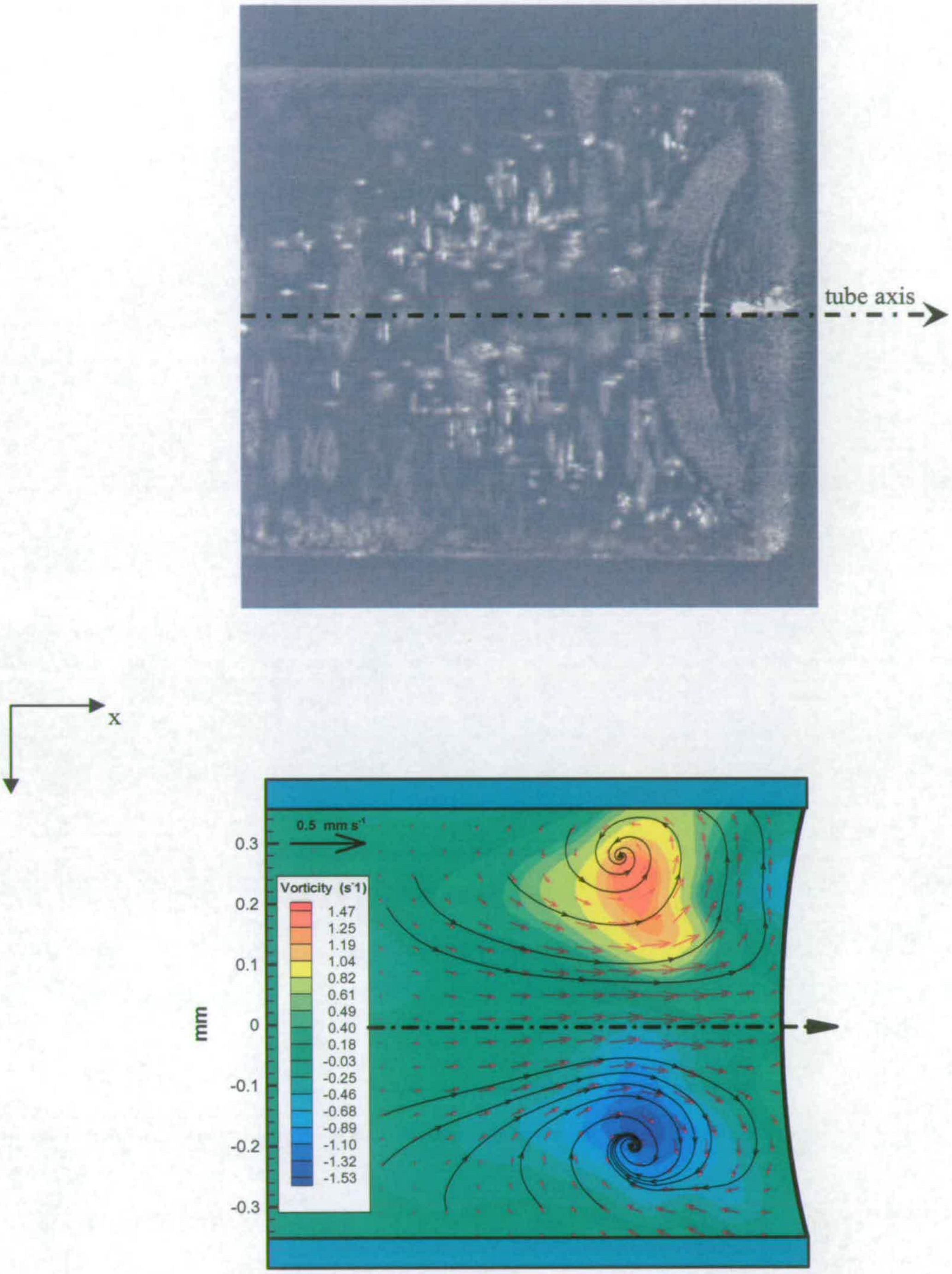

Figure 3.8 Horizontal diametrical section of the capillary tube: (above) typical PIV visualization with the use of coherent light; (below) PIV analysis.

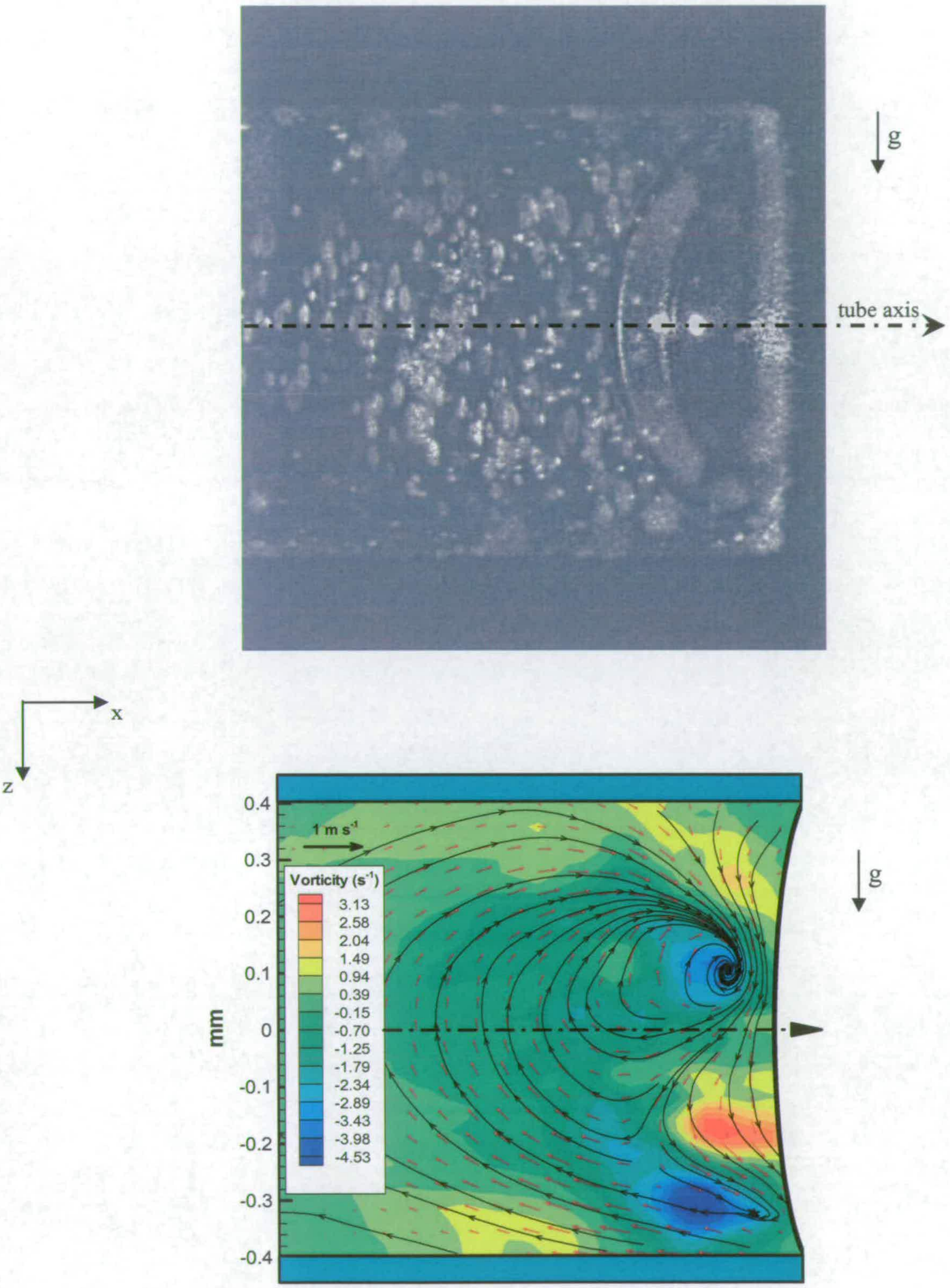

Figure 3.9 Vertical diametrical section of the capillary tube: (above) typical PIV visualization with the use of coherent light; (below) PIV analysis (**g** is the gravitational acceleration).

Two images of the seeded flow pattern and the corresponding PIV analysis are shown in Figures 3.8-3.9. The first (Figure 3.8) is taken through a horizontal diametric section of the capillary tube and the second (Figure 3.9) is a vertical diametrical section; the tube size is 900 μm and the liquid used is methanol. The horizontal section of the tube shows an axi-symmetrical flow pattern with two contra-rotating vortices of similar strength. In the vertical section a dominant single clockwise vortex is present. Figure 3.10 reports the PIV analysis of the horizontal section for ethanol (top) and methanol (bottom) at various sizes. Note that for the 1,630 μm tube the attention is focused on the downward clockwise vortex only. For clarity the vorticity value has been reproduced in Figure 3.11; clearly, the vortex strength increases with reducing tube size; in addition the vorticity is higher for methanol at all tube sizes.

The flow in the vertical sections is destabilized by gravity and an oscillatory behaviour was observed. A sequence of 12 frames showing the oscillatory behaviour is reproduced in Figure 3.12 for the 900 μm tube filled with methanol. A single clockwise vortex can be seen in frames 1 and 2; a small anticlockwise vortex appears to develop in the top right corner of frame 3 accompanied by a reduction in intensity of the main clockwise vortex. However, the strength of the main vortex then prevails with an increase of vorticity in frames 4 and 5 and the appearance of several small vortices localized at the curved meniscus interface in the lower region close to the wall where the particles dramatically change direction (see bottom right corner of frame 5 in Figure 3.12). Afterwards, the flow returns to a single roll in frames 5 and 6. In the subsequent frames the behaviour is repeated following similar patterns and strength. Two different attempts for the formation of the top right vortex can be seen in frames 7 and 9. In the sequence of Figure 3.13 (relative to 600 μm tube and methanol), the induced vortices, such as that (V) seen in the top right region of frame 2, eventually grow and strengthen in frame 3 affecting substantially the flow pattern. However, again the strength of the anticlockwise vortex dominates in the next frame. The case of methanol and 1,630 μm tube is presented in the sequence of Figure 3.14. For this size the effect of instabilities is much reduced but is still detectable (top right corner of frames 3 and 4).

Similar behaviour was found for the vertical sections of all three tube sizes filled with ethanol with a similar flow pattern to that of methanol, but a lower vorticity values at each tube size.

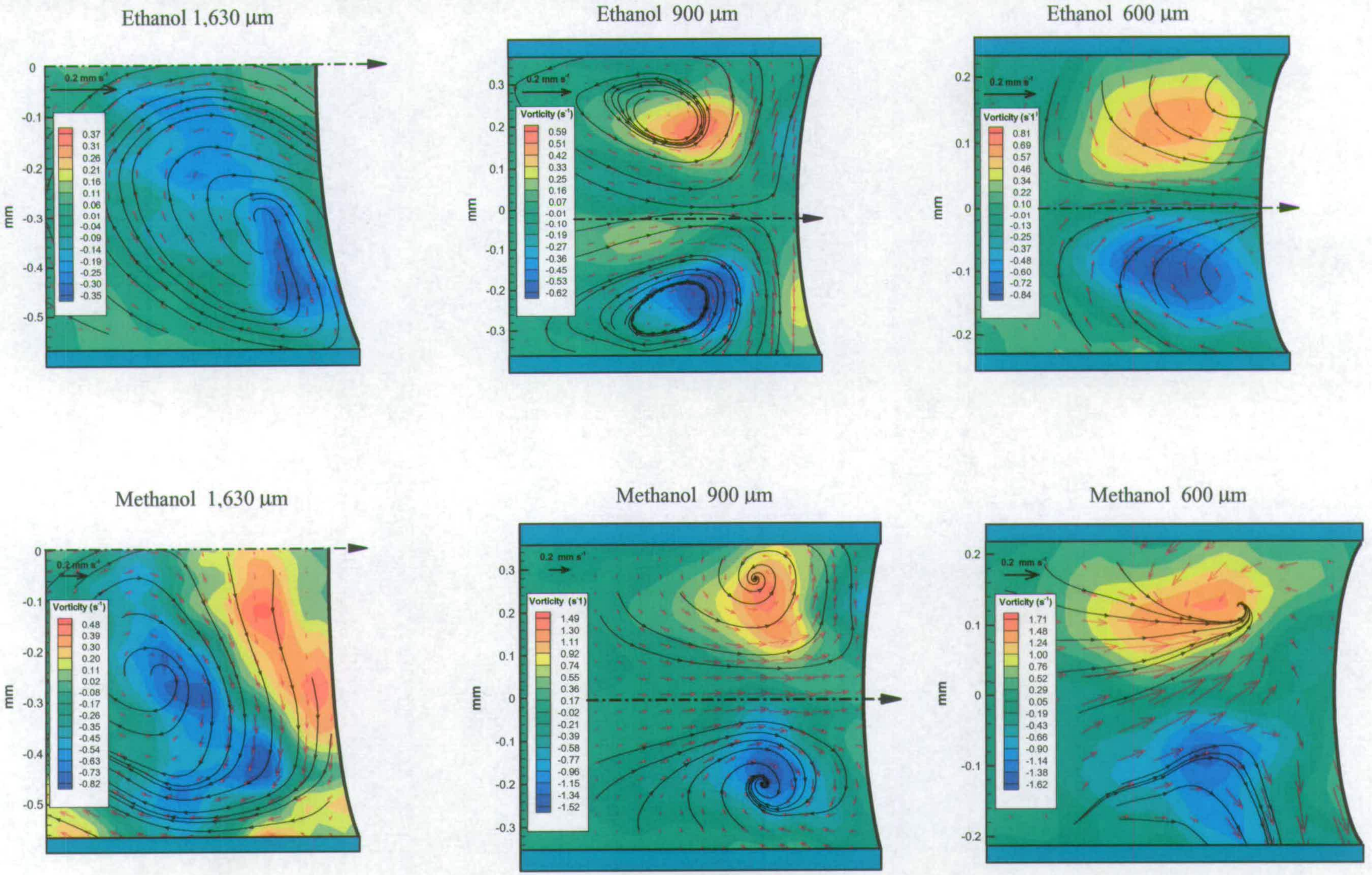

Figure 3.10 PIV analysis of the horizontal diametrical section for ethanol (above) and methanol (below) at various tube sizes.

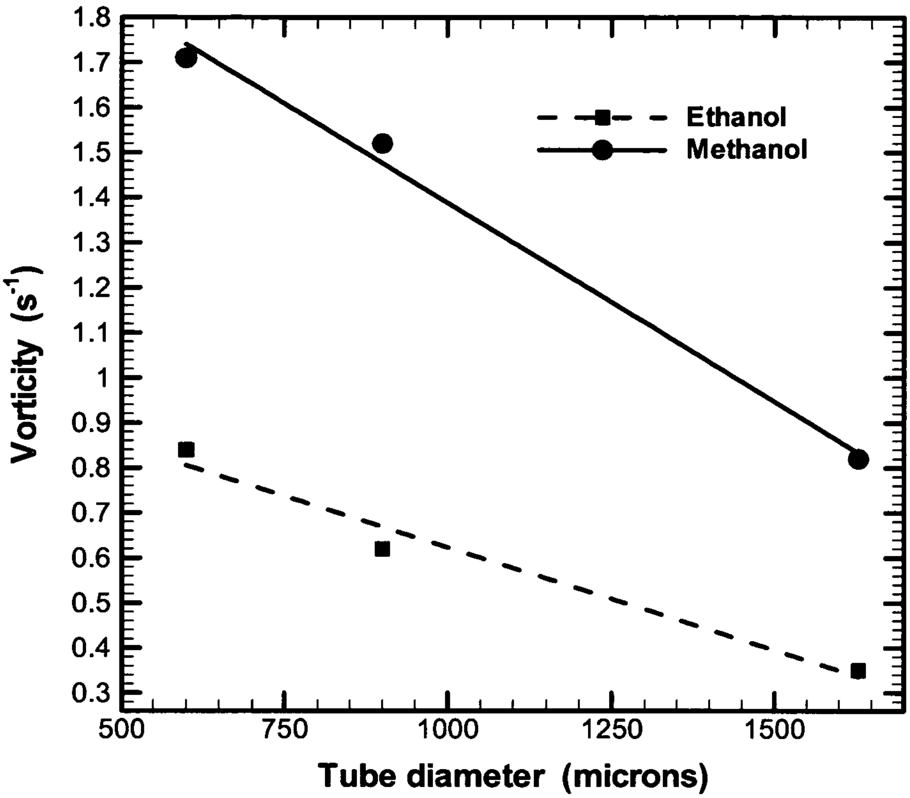

Figure 3.11 Vorticity vs. tube diameter (horizontal tube sections).

Figures 3.15-3.16 report two sequences of ethanol in a 600 μm tube to show that for this case, the instabilities taking place in the vertical section (Figure 3.15) affect appreciably also the flow pattern in the horizontal section (Figure 3.16). Once again, in the vertical section (Figure 3.15) we see the same behaviour described earlier for Figure 3.12. Interestingly and particular to ethanol at this tube size is what happens in the horizontal section (Figure 3.16). As expected, two contra-rotating vortices are present in frame 1, but the pattern is oscillatory in this case. The tracers are first attracted towards the meniscus interface producing a compression of the vortices (frame 2); then, they are pushed away from the interface (frame 4). Afterwards, a similar flow pattern to that in frame 1 is rebuilt and the mechanism is repeated from the start. It is worth noting that the vortices in Figure 3.16 have different strengths. Figure 3.17 reproduces the vorticity value versus time for the vertical section of ethanol and 900 μm tube diameter.

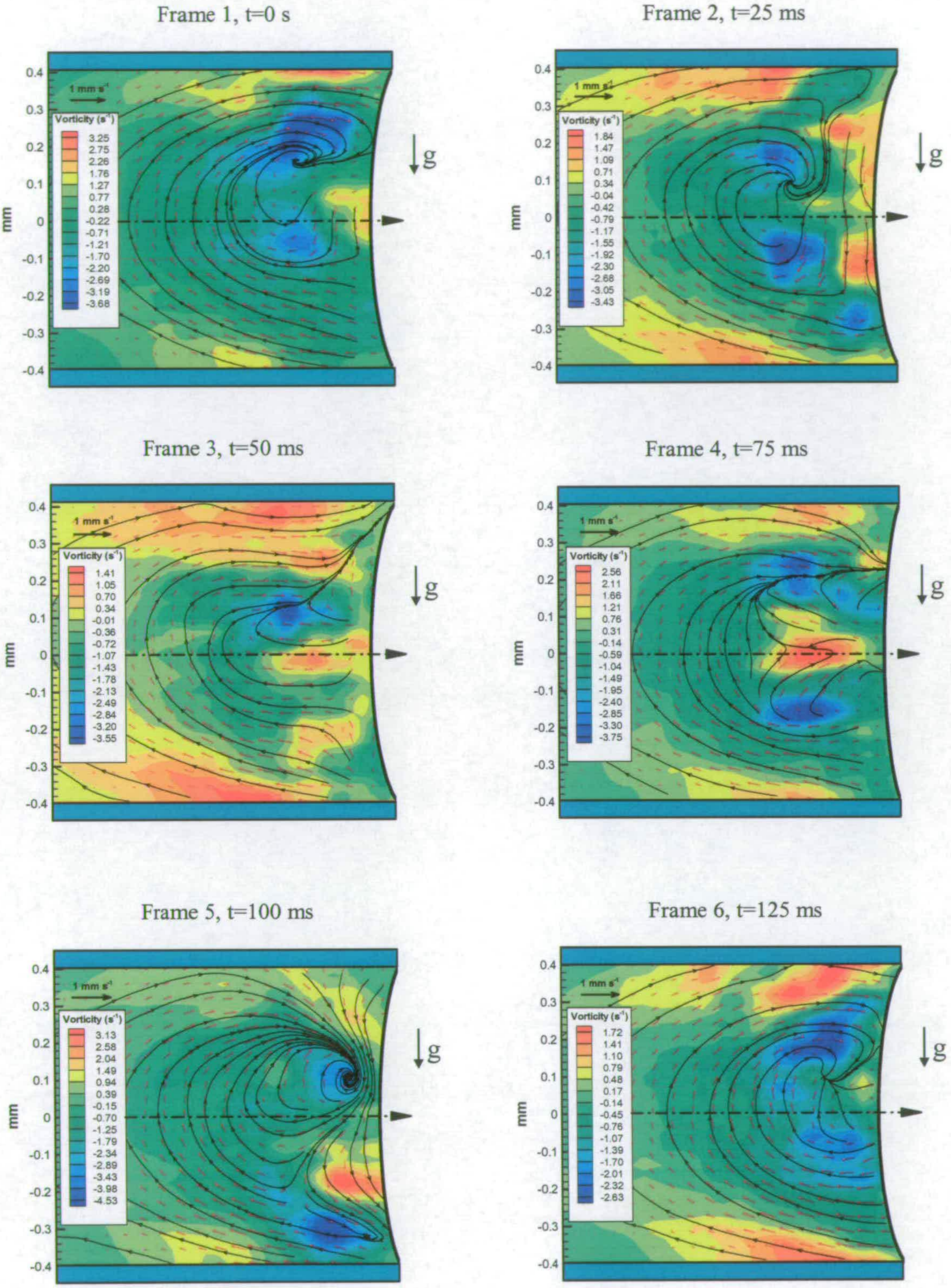
Frame 1, t=0 s

Frame 2, t=25 ms

Frame 3, t=50 ms

Frame 4, t=75 ms

Frame 5, t=100 ms

Frame 6, t=125 ms

Figure 3.12 Sequence of 12 PIV analysis frames for methanol in the 900 μm tube (vertical diametrical section). (continued)

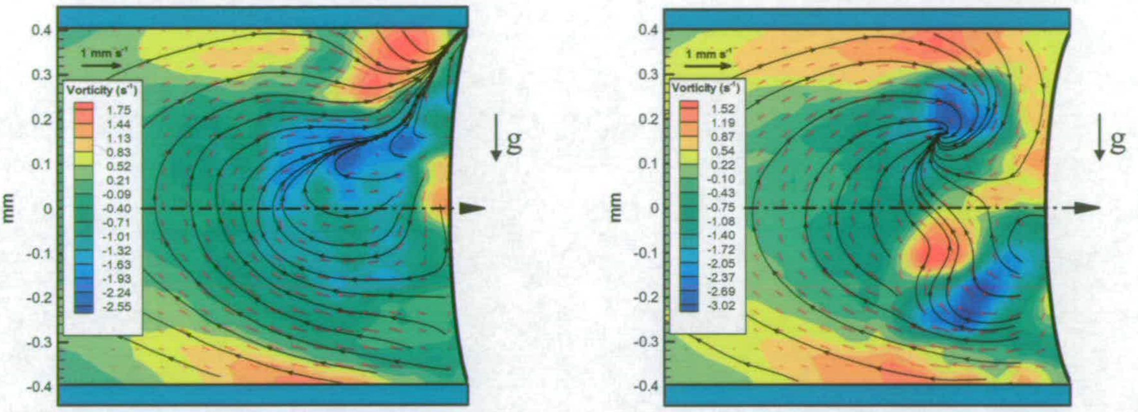
Frame 7, t=150 ms

Frame 8, t=175 ms

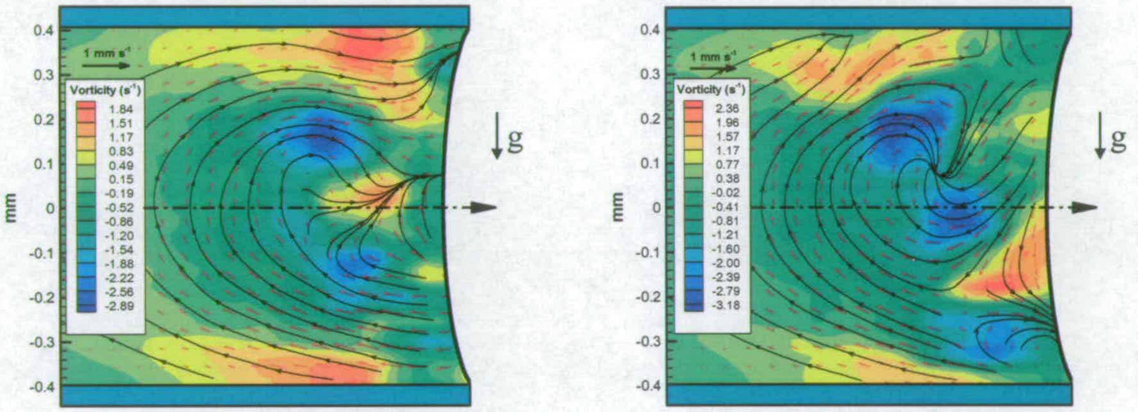
Frame 9, t=200 ms

Frame 10, t=225 ms

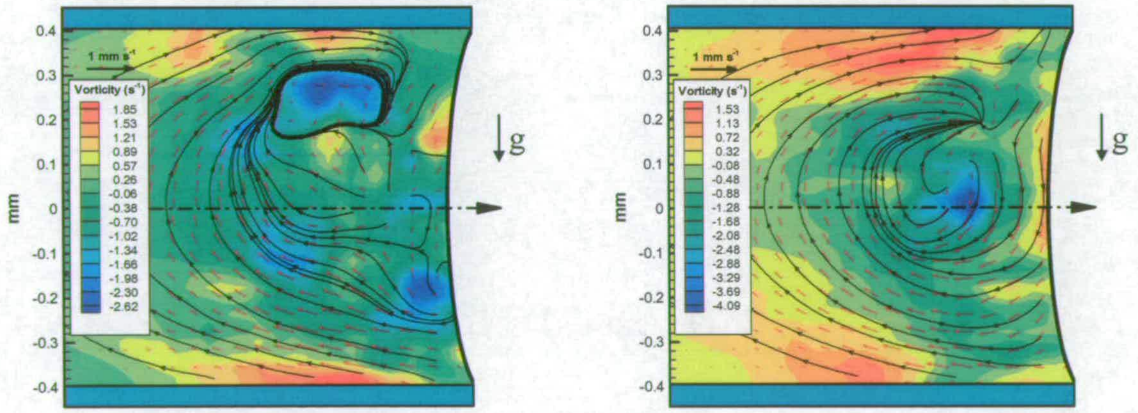
Frame 11, t=250 ms

Frame 12, t=275 ms

Figure 3.12 Sequence of 12 PIV analysis frames for methanol in the 900 μm tube (vertical diametrical section).

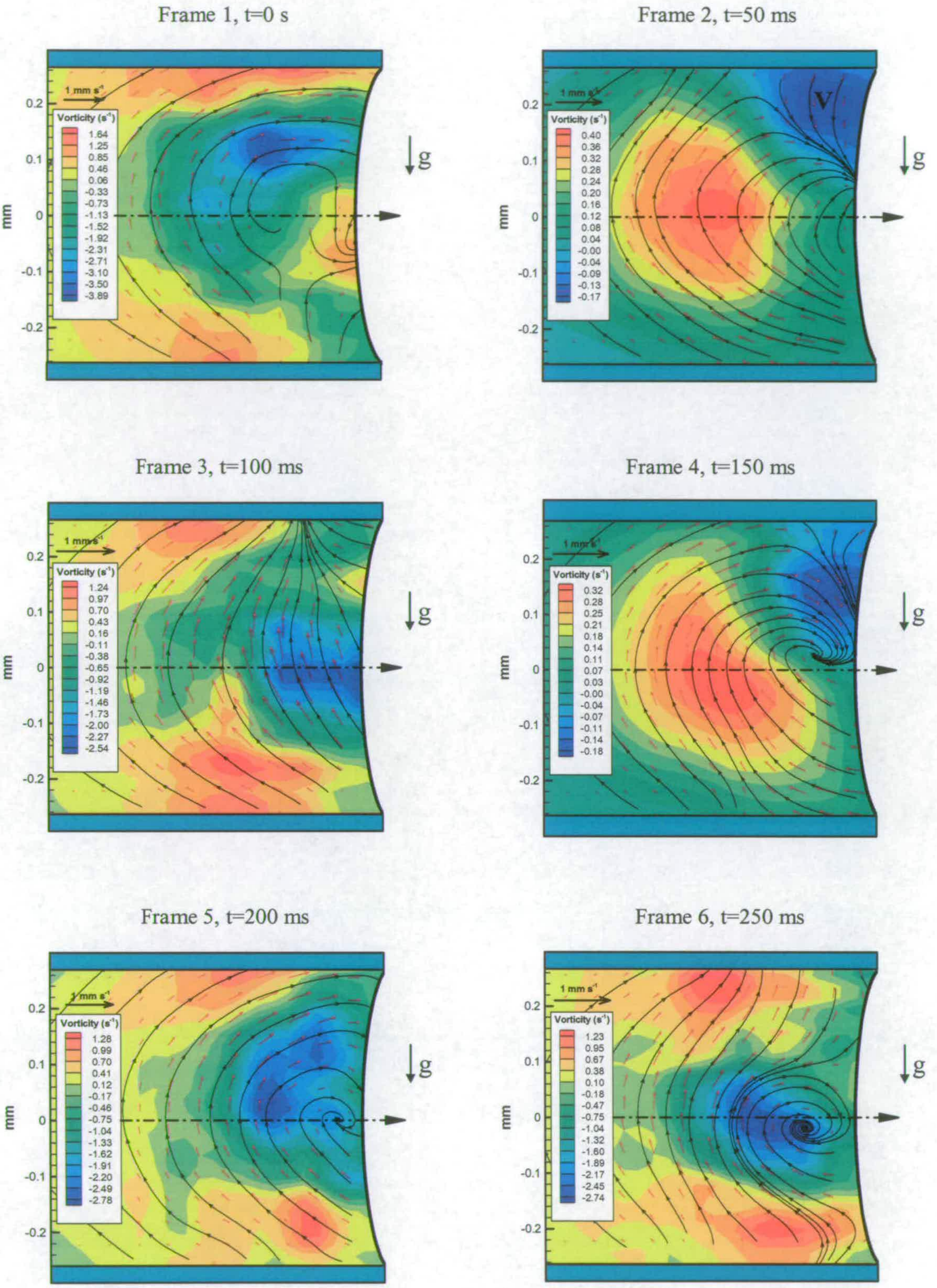

Figure 3.13 Sequence of 6 PIV analysis frames for methanol in the 600 μm tube (vertical diametrical section).

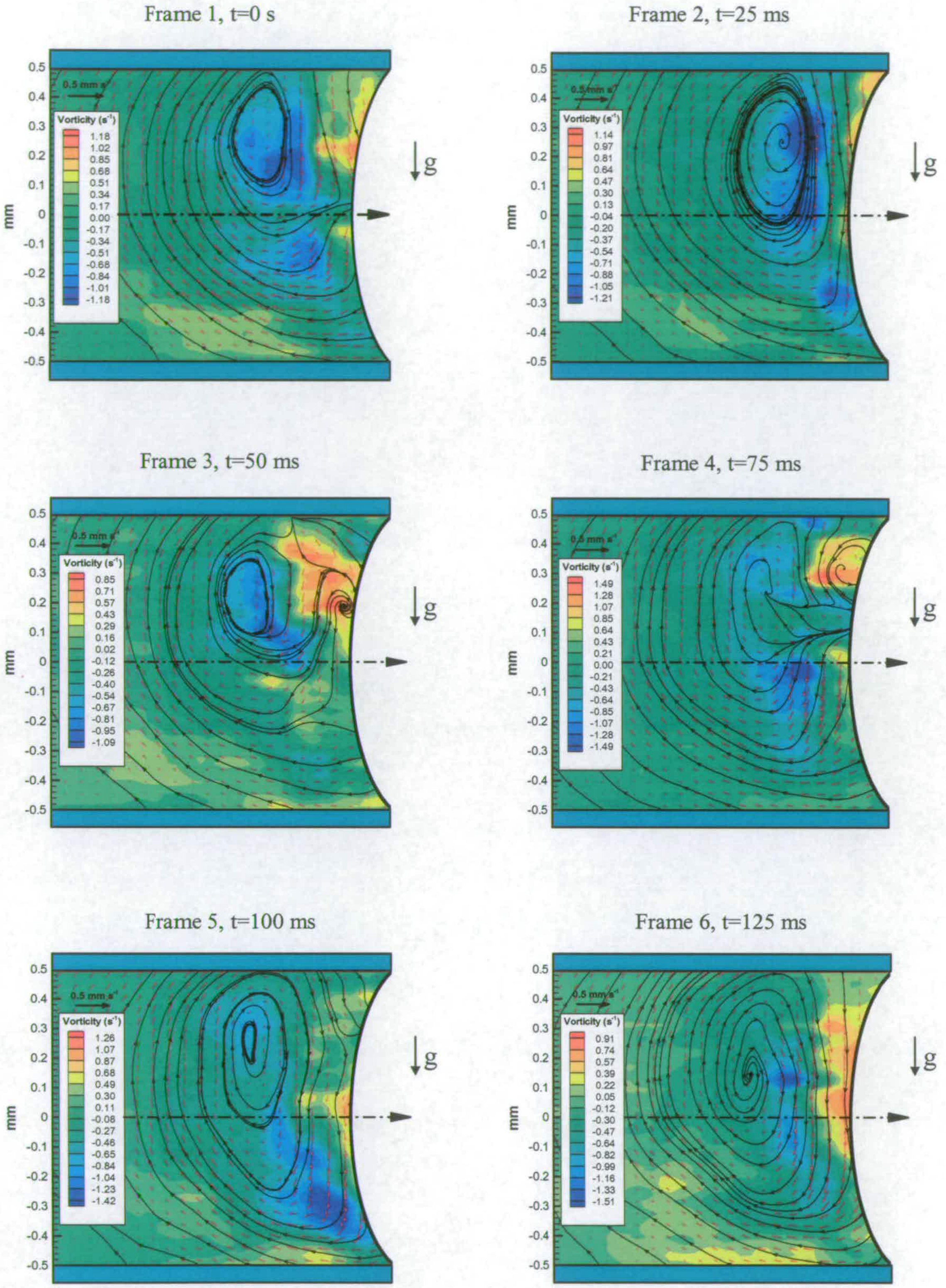
Frame 1, t=0 s

Frame 2, t=25 ms

Frame 3, t=50 ms

Frame 4, t=75 ms

Frame 5, t=100 ms

Frame 6, t=125 ms

Figure 3.14 Sequence of 6 PIV analysis frames for methanol in the 1,630 μm tube (vertical diametrical section).

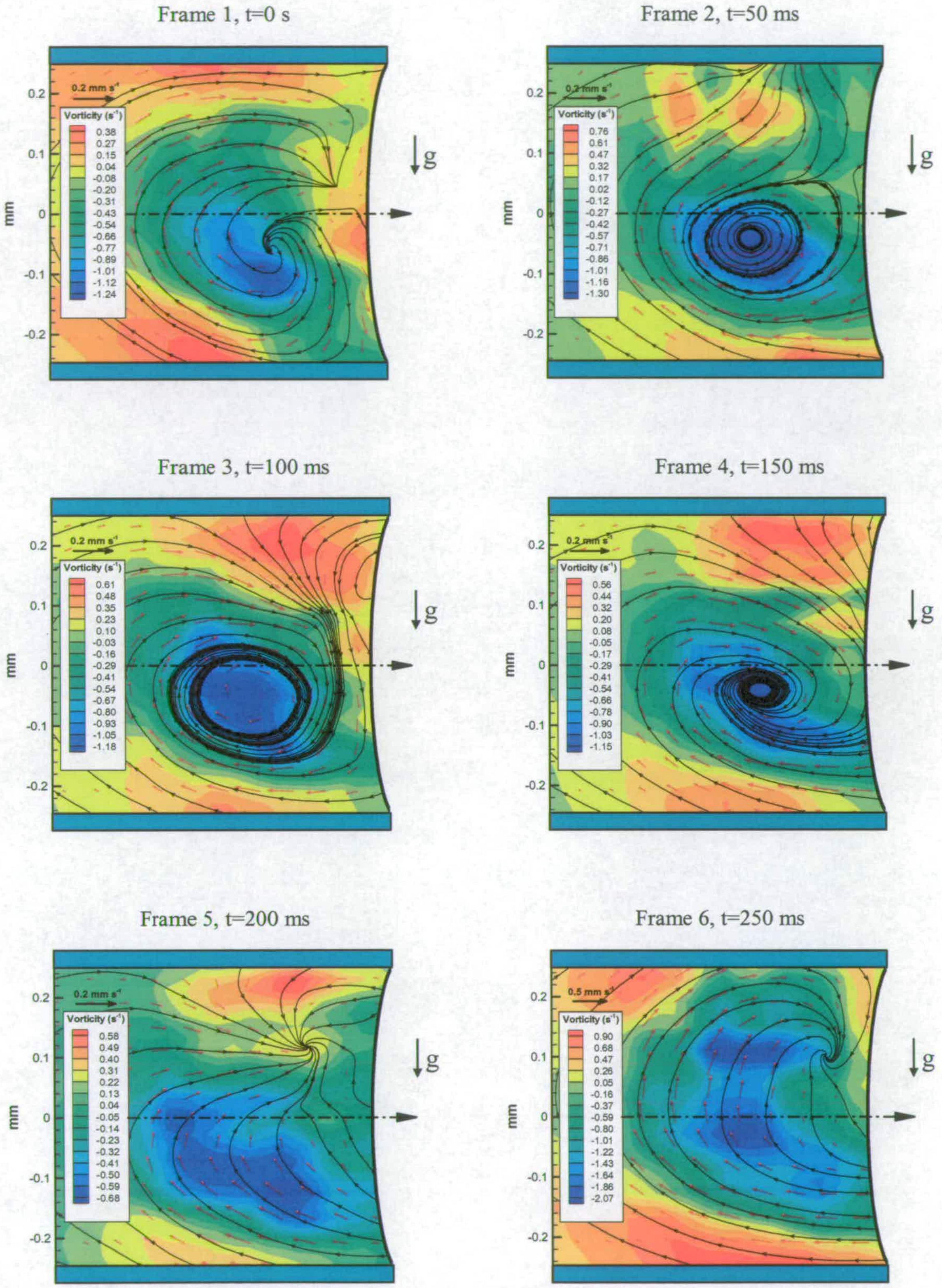

Frame 1, t=0 s

Frame 2, t=50 ms

Frame 3, t=100 ms

Frame 4, t=150 ms

Frame 5, t=200 ms

Frame 6, t=250 ms

Figure 3.15 Sequence of 6 PIV analysis frames for ethanol in the 600 μm tube (vertical diametrical section).

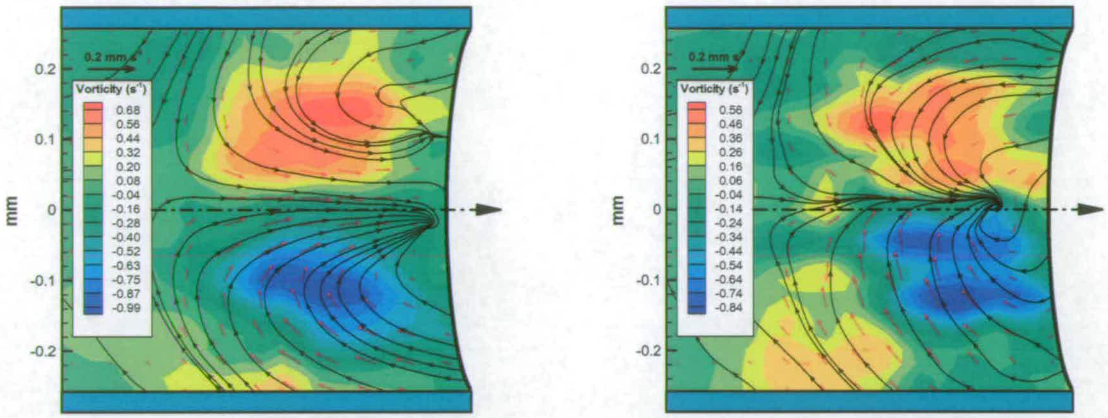

Frame 1, t=0 s

Frame 2, t=50 ms

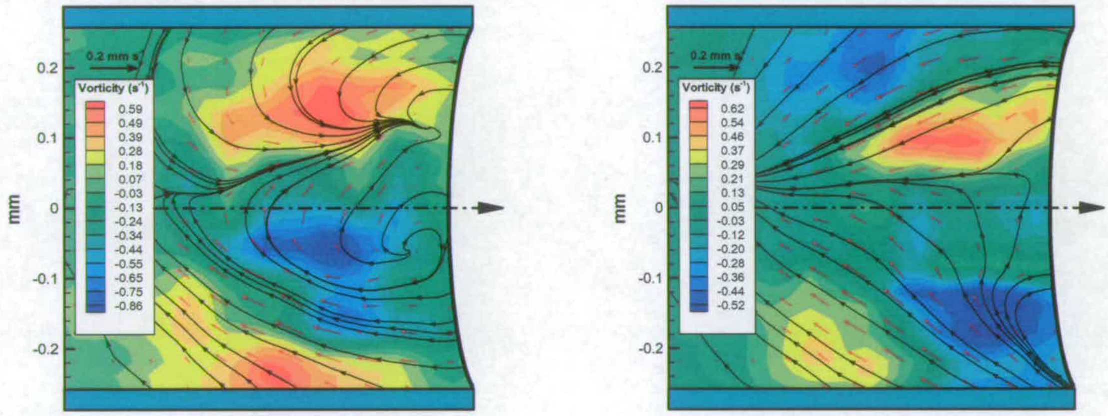

Frame 3, t=100 ms

Frame 4, t=150 ms

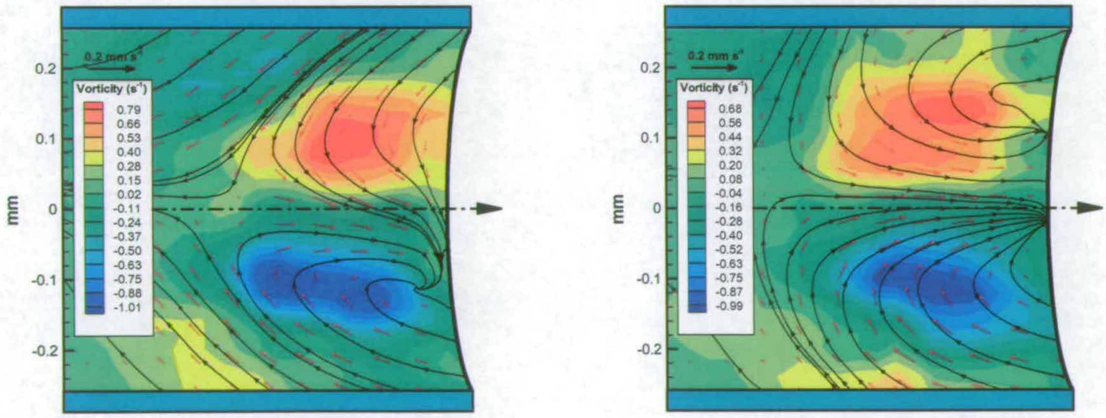

Frame 5, t=200 ms

Frame 6, t=250 ms

Figure 3.16 Sequence of 6 PIV analysis frames for ethanol in the 600 μm tube (horizontal diametrical section).

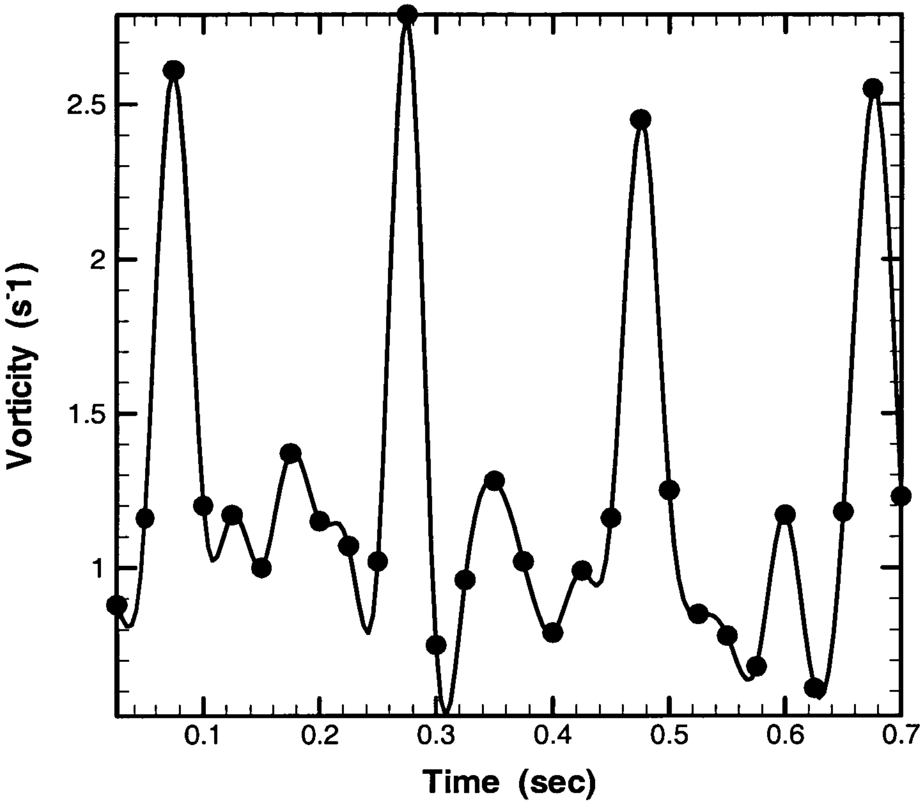

Figure 3.17 Vorticity vs. time for ethanol in the 900 μm tube (vertical diametrical section).

The pattern motion just described could be classified as either thermocapillary Marangoni or buoyancy. Thermocapillary Marangoni convection is usually confined close to the interface, whereas buoyancy is a bulk motion. Previous research has demonstrated that thermocapillary convection dominates at sizes smaller than 1 mm whereas buoyancy is usually stronger at larger sizes (Zeytounian [33]). In the present investigation, the sizes analysed ranged from 600 μm to 1,630 μm, thus a combination of the two convection mechanisms could be expected at the larger sizes. Although the temperature field self-induced by the evaporation could extend into the bulk phase ($x > 2R$), the fact that the tubes were horizontally orientated makes it plausible to state that the convection is indeed driven by surface tension only. The temperature gradient existing along the meniscus interface is self-induced by the evaporative cooling of volatile liquids in air. A detailed explanation of the mechanism involved in the evaporation of volatile liquids in confined space has been given in the previous chapter. A sketch of the temperature differences and the consequent driving forces for convection is given in Figure 3.18. For most of the known liquids, surface tension is related to temperature by a relation such Equ. 2.2. As explained in Chapter II, the evaporative cooling is larger at the meniscus wedge than at the centre; this generates a gradient of temperature and consequently of surface tension.

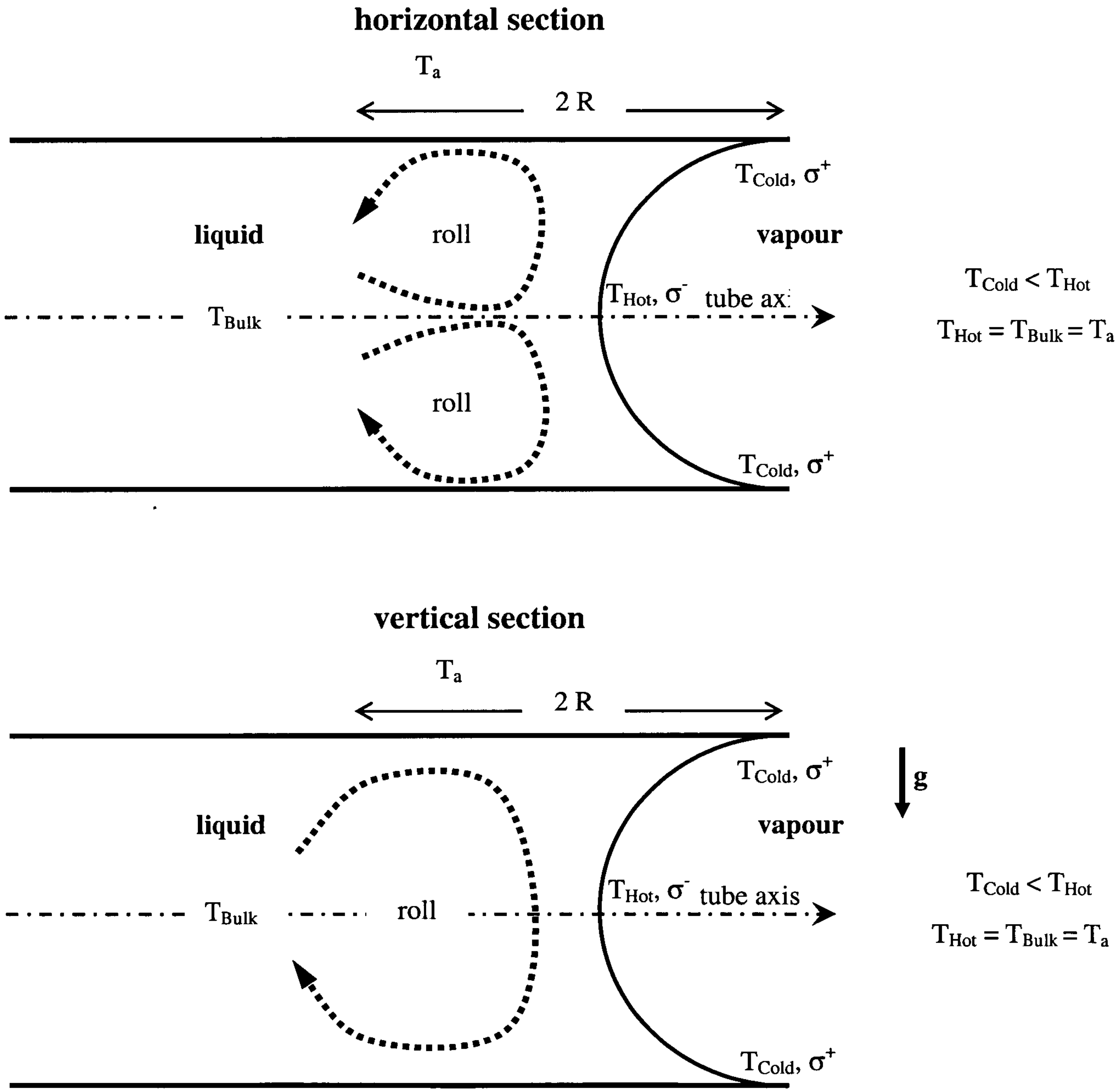

Figure 3.18 Temperature difference and driving forces for horizontal and vertical diametrical tube sections (**g** is the gravitational acceleration and σ is the surface tension).

For the horizontal sections, the driving force generated by the surface tension gradients is symmetrical with respect to the tube axis and two contra-rotating vortices are seen, such as those visualized in Figure 3.10. More complicated is the flow pattern for the vertical sections of the capillary tubes. The action of gravity distorts the symmetry created by the surface tension driving forces. The gradient of surface tension acts in the same direction as gravity in the bottom region of the tube and against it in the top region. The resulting flow pattern is characterized by flow instabilities. A strong clockwise rotating vortex as the one in Figure 3.12 is destabilized by the presence of an anticlockwise vortex that appears to develop in the top region of the tube as a direct consequence of the surface tension driving force acting in the upper part of the tube against gravity. However, the upper vortex is suddenly overcome by the strength of the clockwise one. The anticlockwise vortex and the induced clockwise vortex in the top region are responsible for the slow down of the main clockwise vortex as can be seen in frame 7 of Figure 3.12 and frame 2 of Figure 3.13. The weak surface tension gradient at 1,630 μm does not dramatically alter the flow pattern for this size and the main clockwise vortex is mostly present. The behaviour shown by ethanol in the 600 μm tube size is certainly interesting. The instabilities arising in the vertical section are so important that they also affect the flow pattern in the horizontal section. For the largest tube size in the vertical section a single vortex is observed because the gravitational effect dominates the surface tension effect. For the smaller tube sizes studied here, the oscillatory behaviour would appear to arise from the competition between gravitational and capillary forces. It can be anticipated that at even smaller tube sizes the capillary forces would prevail leading to symmetrical vortices.

It is interesting to note that the vorticity value varies linearly with the tube size (see Figure 3.11). This backs up the findings reported in the previous chapter, where it has been demonstrated that the evaporation mass flux (total evaporation / meniscus surface area) for an evaporating meniscus in capillary tubes increases linearly with reductions in the tube diameter. In fact, for an evaporating meniscus most of the evaporation takes place in the meniscus micro-region (a tiny region close to the meniscus triple line) as discussed in the previous chapter. Therefore, in the previous chapter it was concluded that an evaporation mass flux inversely dependent on the tube diameter could be due to the total evaporation rate increasing linearly with the tube diameter (because of the micro-region area increasing linearly with the tube diameter, rather than the square of the diameter) and the meniscus surface area increasing with the second power of the tube diameter.

From the analysis of the vorticity value in Figure 3.17 a clear oscillatory pattern can be seen with a frequency of 5 Hz. From these preliminary results the frequency of oscillations appears to be independent of the tube size. However, more detailed work is needed to clarify this aspect.

Measuring the evaporation mass flux allows estimation of the Marangoni and Rayleigh numbers and the drawing of conclusions on the role played by gravity in the thermocapillary driven convection described earlier. It is sensible to assume that in the steady state all the heat necessary to sustain evaporation comes from the environment surrounding the tubes. Here one can neglect the contribution due to the conduction in the liquid bulk because the liquids used have a thermal conductivity very close to the tube one and the time scale of conduction ($s^2/\kappa_w = 0.08$ s) through the tube walls is lower than the convection one ($R^2/\kappa_l = 0.33$ s). Therefore, this following balance could be written:

$$\dot{m}h_{fg} = Ah(T_a - T_w) \qquad (3.6)$$

where $\dot{m}$ is the evaporation mass flux, h_{fg} the latent heat of vaporization, A the tube external surface, h the heat transfer coefficient at the air side, T_a and T_w the air and tube temperatures respectively. For the tube external surface, it is also sensible to assume that the portion of liquid inside the tube affected by a temperature change because of evaporation is extended for a length comparable to the tube diameter as suggested by the convection roll dimensions (schematically drawn in Figure 3.18). In the case of natural convection around a horizontal tube, the following equation can be applied to determine the external Nusselt number (Incropera and DeWitt [34]):

$$Nu = \left\{ 0.6 + \frac{0.387 Ra_d^{1/6}}{\left[1 + \left(\frac{0.559}{Pr^{9/16}} \right) \right]^{8/27}} \right\}^2 \qquad (3.7)$$

where Ra_d is the Rayleigh number based on the tube diameter (d) and Pr is the Prandtl number. This allows Equ. (3.6) to be re-written as follows:

$$\dot{m} h_{fg} = \pi d\, k_a \left\{ 0.6 + \frac{0.387 \left[F\, d^3 (T_a - T_w) \right]^{1/6}}{\left[1 + \left(\frac{0.559}{Pr^{9/16}} \right) \right]^{8/27}} \right\}^2 (T_a - T_w) \qquad (3.8)$$

where k_a is the air thermal conductivity and F is a constant depending on liquid properties such as viscosity, conductivity and specific heat. By numerically solving the non linear Equ. (3.8) one can get the temperature difference (T_a-T_w). The next assumption is that because of the vigorous convection in the liquid phase of the meniscus described earlier, the temperature at the meniscus centre is the ambient one, as sketched in Figure 3.18 ($T_{Hot}=T_a$). This leads to an estimation of the temperature gradient between the wedge and the centre of the meniscus. Table 3.1 reports *Ma* and *Ra* along with their ratio (namely dynamic *Bo*). It can be seen that *Ma*, *Ra* and *Bo* decrease at smaller capillary size, but *Ra* decreases more rapidly ($\sim R^3$). This decrease of *Ma* for smaller capillaries is the opposite trend to that expected: an explanation for this will be given shortly. The low *Bo* values at small tube sizes suggest that the phenomena being described here are basically surface tension dominated. As the tube size is increased gravity plays an increasing role. This is in good agreement with the experimental observations. Note also that the difference between the *Bo* numbers for the two liquids is less than 5% for each tube size. This is due to the fact that *Bo* is a function of the liquid physical properties, which are similar for the two liquids investigated. Note also that for methanol *Ma* is higher and *Bo* is lower than for ethanol. Therefore, one expects a more vigorous convection and the expected effect of gravity to be lower for methanol. Again, this agrees with the present experimental findings. *Bo* values alone for the two liquids would not be able to justify why we observed a substantially stronger flow distortion for ethanol. The answer lies in the viscosity. Another dimensionless number should be introduced here: the capillary number (*Ca*), that is the ratio between the viscous dissipation and surface tension. Values of *Ca* are reported in Table 3.1 and they fall in the typical range of thermocapillary convection (10^{-3} – 10^{-7}).The higher *Ca* values for ethanol are probably responsible of the observed stronger flow distortion due to gravity.

Table 3.1 Dimensionless numbers (Marangoni, Rayleigh, Bond and Capillary number).

Liquid	*Tube size (μm)*	*Ma*	*Ra*	*Bo (Ra/Ma)*	*Ca ($x10^{-7}$)*
Ethanol	600	103	13	0.13	3.02
	900	151	43	0.28	2.01
	1,630	262	242	0.92	1.11
Methanol	600	457	55	0.12	2.44
	900	671	181	0.27	1.63
	1,630	1,065	940	0.88	0.90

The evaluated temperature difference ($\Delta T = T_a\text{-}T_w$) allows estimation of the convection time scale and normalization of the vorticity value of Figure 3.11. The Reynolds number is given by (see also Riley [35]):

$$Re = \frac{Ma}{Pr} = \frac{U\,R}{\upsilon} \qquad (3.9)$$

where U is the fluid velocity along the meniscus and ν the kinematic viscosity. From Equ. (3.9) the value of U is:

$$U = \frac{\frac{\partial\sigma}{\partial T}\frac{\partial T}{\partial x}R}{\mu} \qquad (3.10)$$

from which a convection time scale of $\tau = \frac{R}{U}$ can be defined:

$$\tau = \frac{\mu R}{\left(\frac{\partial \sigma}{\partial T}\right)\Delta T} \qquad (3.11)$$

In this expression, and in the evaluation of Marangoni number in Table 3.1, the product of temperature gradient and the radius has been assumed to equal ΔT.

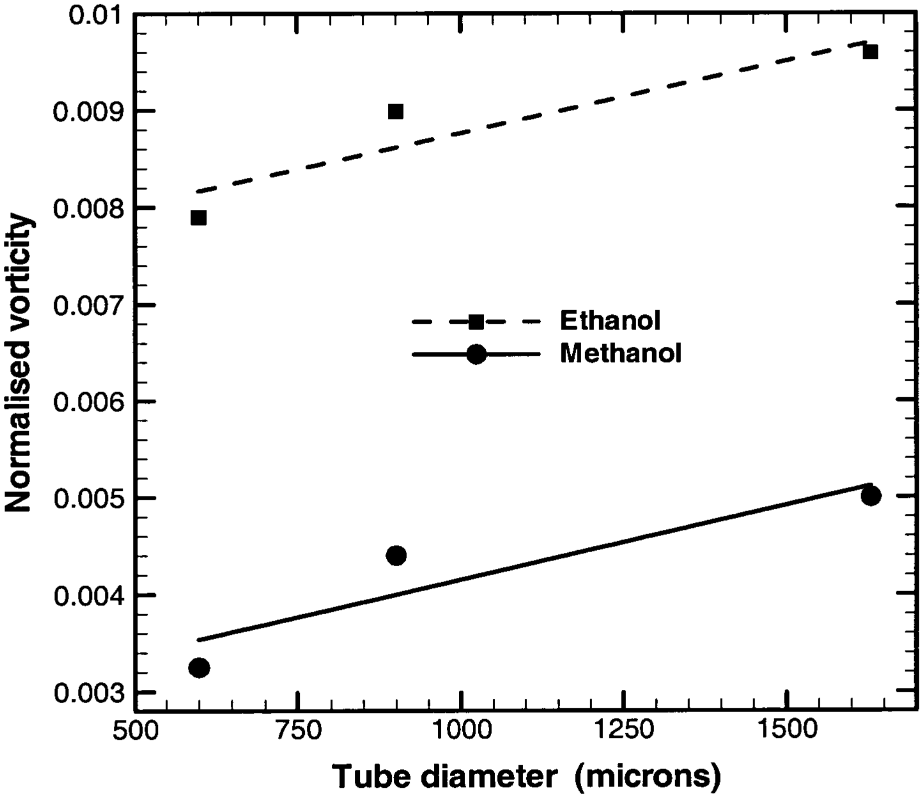

Figure 3.19 Normalized vorticity (ψ) vs. tube diameter (2R) for horizontal diametrical tube sections.

Figure 3.19 presents the normalised vorticity ψ (found by multiplying the measured vorticity by the convection time scale) versus the tube diameter for the two liquids. It is clear that ψ depends linearly on the tube diameter and is higher (almost double) for ethanol. If one introduces a dimensionless vapour pressure $P' = \frac{P_v}{\rho g R}$ (the ratio of the saturated vapour pressure to a hydrostatic pressure), it is possible to define a dimensionless vorticity, ξ, as:

$$\xi = \psi P' \qquad (3.12)$$

Figure 3.20 shows ξ versus the tube radius for the two liquids. It can be seen clearly that this parameter is independent of the tube size and liquid properties.

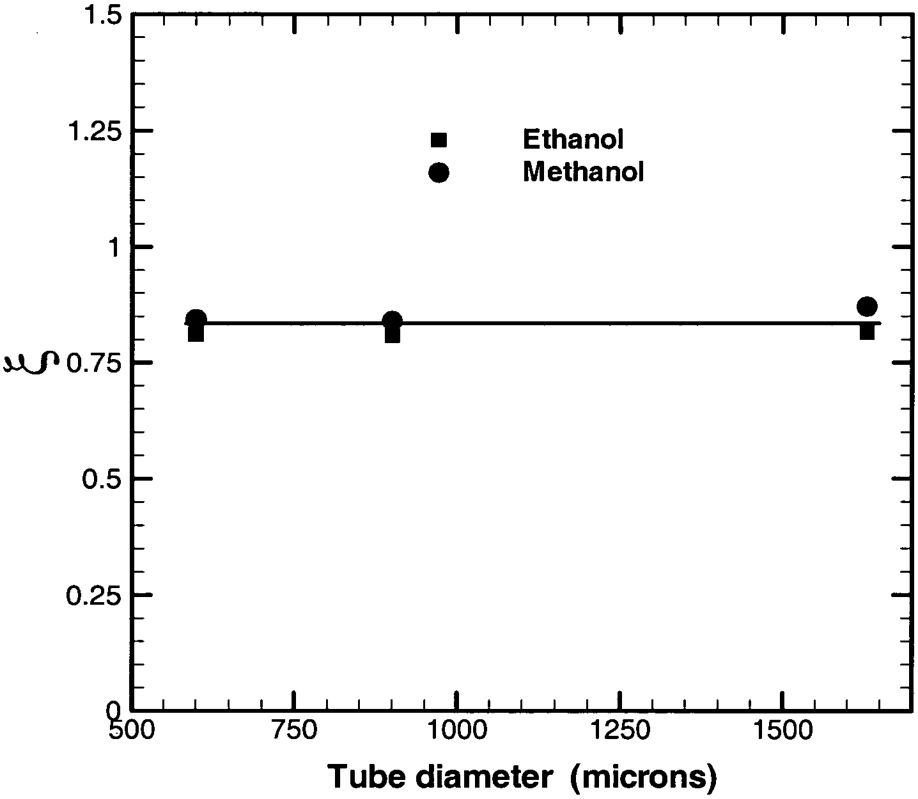

Figure 3.20 Dimensionless number ξ vs. tube diameter (2R) for horizontal diametrical tube sections.

In this relationship, the convection timescale is modified by the dimensionless vapour pressure, P'. In conventional thermocapillary studies where a temperature gradient is imposed, *Ma* is found to increase as the length scale decreased, whereas the predicted value here (Table 3.1) decreased. The reason for the decrease in *Ma* and for the need to multiply τ by P' could be attributed to the way in which $\frac{\partial T}{\partial x}$ is determined. Here $\frac{\partial T}{\partial x}$ is estimated by dividing the difference between the triple line temperature and the temperature at the centre of the meniscus, ΔT, by the tube radius, R. It is thus a mean value over the whole interface. However, we know that evaporation is strongest in a thin wedge close to the triple line and that the width of this wedge is independent of radius (hence the linear increase in evaporation rate with increasing radius). Thus $\frac{\partial T}{\partial x}$ would be expected to be independent of radius, being proportional to ΔT rather than $\frac{\Delta T}{R}$. Since $\tau = \frac{\mu R}{\frac{\partial \sigma}{\partial T}\frac{\partial T}{\partial x}R}$, this explains the effect of R in the correction, P', applied to τ.

One possible explanation for the effect of P_v is that in previous works on thermocapillary convection a linear variation in temperature has been imposed so that $\frac{\partial T}{\partial x}$ is constant, whereas in the present study the temperature gradient is a strong function of distance along the meniscus. Thus the adoption of an average gradient, without any weighting to allow for its spatial variation, will not take account of the different shape of temperature profile with distance along the meniscus caused by the different evaporative driving forces for the two fluids. If the gradient for methanol is overestimated by this approach (relative to ethanol) this may explain the correction in terms of vapour pressure.

Regardless of the physical explanation for the effect of vapour pressure, the fact that ξ is constant is an important finding as it shows that the phenomena described here are independent of the liquid properties and the tube size and depend strongly on the fact that most of the evaporation is taking place near the triple line. It can be concluded once again that the near contact line region is the key factor because it controls the heat and mass transfer at the micro-scale. It is worth noting that the parameter ξ is derived from a combination of saturated vapour pressure (related to the strength of evaporation) and vorticity, i.e. the driving force and its consequence. This is in agreement with the self-induced nature of the observed convection.

For this experiment it would be interesting to look at the flow pattern for intermediate angles ($0<\phi<90$) to have a complete 3-D map.

3.4.3 Vertically oriented heated capillary tubes

A more complicated situation, where extra heating is given to the system was then studied. A capillary tube of 600 μm has been vertically immersed in a pool of ethanol or methanol and the liquid was allowed to rise inside the tube above the pool level due to capillary forces; consequently a meniscus curved interface is formed. The liquid is allowed to evaporate in the open environment surrounding the tube at 1 atm and room temperature of 25 °C. The experimental facility used for fluid flow investigation is sketched in Figure 3.5. An electric heater was built, as shown schematically in the front view inset of Figure 3.5, on the external surface of the capillary tube by depositing a silver conductive coating with the use of an air brush. Two electrical terminals are provided and connected to a power supply where voltage and current can be read. The thickness of the paint is small enough to ensure a dissipation of up to 2 W. Moving the capillary tube with respect to the liquid pool, the meniscus inside the tube was positioned as desired relative to the electric heater. Two positions were investigated in this study (see inset of Figure 3.5). The meniscus has been positioned just below the heater (namely: heater in the vapour side) and at the capillary top (namely: heater in the liquid side). The heater power delivered was varied in steps in the range of 0.02 – 2 W; after each run the heater was shut down allowing the meniscus to rewet the pore before another power was selected. An upper limit is reached with the heater in the liquid side, because of boiling commencing in the micro-channel. With the heater in the liquid side, the meniscus remains stuck at the capillary edge no matter the power applied so long as no boiling sets in. The pool dimensions are large compared to the capillary tube, therefore the liquid level is constant regardless of evaporation. Evaporation from the liquid pool is prevented by a lid that also holds the tube. The lid has a small hole to allow for pressure balance with the surrounding environment. When the heater is in the vapour side, the meniscus is no longer anchored to the tube edge and a small heater power suffices to put it in motion.

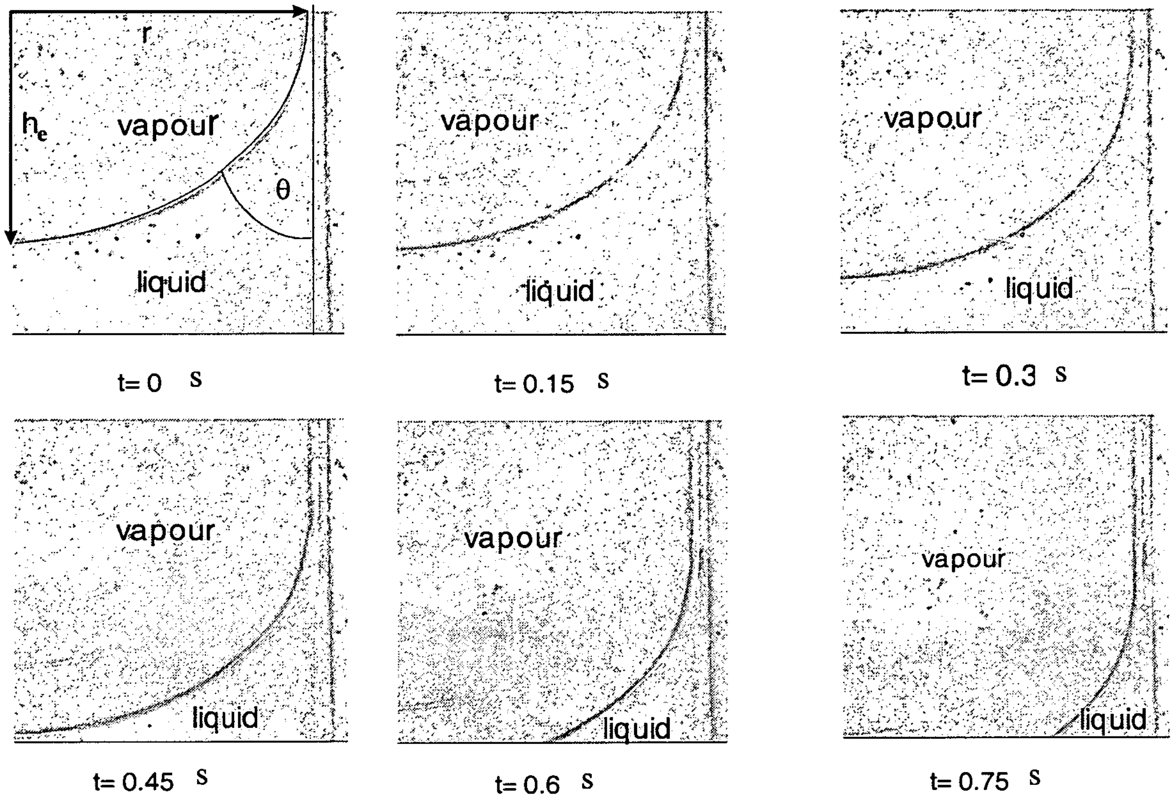

t= 0 s

t= 0.15 s

t= 0.3 s

t= 0.45 s

t= 0.6 s

t= 0.75 s

Figure 3.21 Meniscus position and contact angle change following switching on the heater.

Liquid rises inside the pore due to capillary action. The liquid wettability on a solid surface is characterized by the value of the apparent contact angle. The more the liquid wets the surface the lower the apparent contact angle. With extra heating provided, a thermocapillary stress is created at the meniscus triple line as described by Pratt et al. [36]. This stress dramatically affects the liquid wettability of the pore and the meniscus is pushed down till a new equilibrium between surface tension, thermocapillary stresses and gravity is reached. The sequence of Figure 3.21 (where the right half of the capillary tube is shown) shows how the apparent contact angle changes as the meniscus is subjected to an imposed temperature gradient. The thermocapillary stress first acts on the meniscus shape changing the apparent contact angle and then when the receding apparent contact angle is reached, the meniscus starts to slide down along the pore. The apparent contact angle was evaluated by measuring the meniscus cap height (h_e) as reported in Figure 3.21 and using the following formula, assuming the meniscus to be a spherical cap:

$$\tan\left(\frac{\pi}{4}-\frac{\theta}{2}\right)=\frac{h_e}{R} \qquad (3.13)$$

where θ is the apparent contact angle, h_e the meniscus cap height and R the capillary tube radius.

The experimental uncertainty in evaluating θ is given:

$$\frac{\delta\theta}{\theta}=\frac{1}{1+\left(\frac{h_e}{R}\right)}\left[\left(\frac{\delta h_e}{h_e}\right)^2+\left(\frac{\delta R}{R}\right)^2\right]^{1/2} \qquad (3.14)$$

Given an uncertainty in measuring h_e and R of 2%, Equ. (14) estimates an uncertainty in θ lower than 2%.

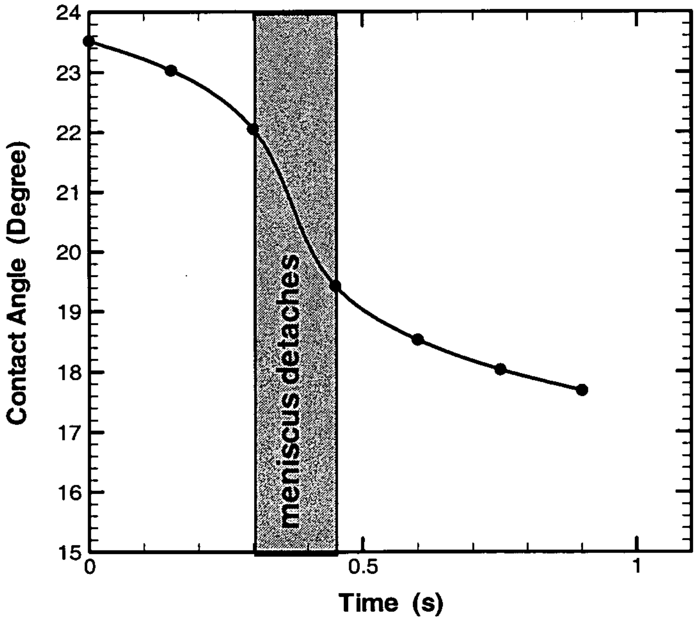

Figure 3.22 Contact angle change for 1.5 W heater power.

As can be seen from Figure 3.22, the meniscus detaches between 0.3 and 0.45 seconds after the heater has been switched on. After detachment, the contact angle approaches an asymptotic value that depends essentially on the temperature gradient at the triple line. Similar behaviour has been noticed for all sets of heater power considered, with an increasing speed of the phenomenon at larger power.

Thermocapillary stress, arising from an imposed thermal gradient, affects the liquid rise inside the pore as shown in Figure 3.23 where the steady state wicking height versus the heater power is plotted. The reduction in wicking height is greater at lower powers when the meniscus is closer to the heater essentially because of larger thermocapillary stresses.

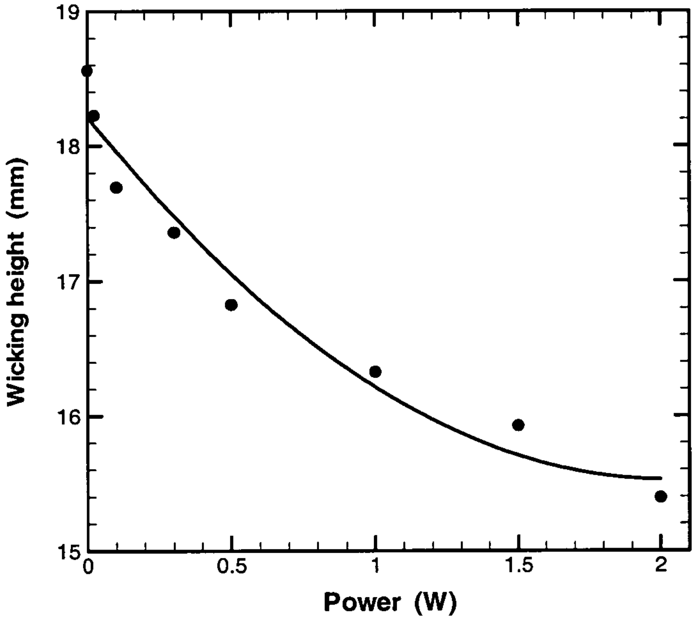

Figure 3.23 Wicking height vs. heater power.

The thermocapillary stress changes the liquid wettability (contact angle) because the apparent contact angle is reduced according to the following modified Young-Dupre equation (de Gennes [37]):

$$\cos\theta = \frac{\sigma_{SV} - \sigma_{SL}}{\sigma} \qquad (3.15)$$

where σ_{SV} is the solid-vapour surface tension, σ_{SL} the solid-liquid surface tension and σ the liquid-vapour surface tension. For a wide range of temperature, σ_{SV} and

σ_{SL} do not vary appreciably, whereas σ is very sensitive to temperature. The usual relation between surface tension and temperature is as in Equ. (2.2). As Equ. (3.15) suggests, because the surface tension decreases with increasing temperature, the contact angle is therefore reduced as temperature rises.

Pratt and Hallinan [38] reached a similar conclusion, but because they were using a normal CCD camera they were only able to point out qualitatively that there was a change in contact angle. By the use of the high speed camera employed here, it was possible to capture and quantify the change in contact angle with the meniscus triple line still anchored (see Figure 3.22).

The decrease in contact angle helps the system in dissipating the extra heat supplied because of a reduced thermal resistance along the thickness of the meniscus macro-region as schematically drawn in Figure 2.4.

The wicking height inside the pore can be evaluated using the Young-Laplace equation reported below from Pratt and Hallinan [38]:

$$\rho g H = \frac{2\sigma}{R}\cos\theta \qquad (3.16)$$

where ρ is the liquid density, g the gravity acceleration, H the wicking height, σ the surface tension, R the capillary radius and θ the contact angle. The above equation comes from the equilibrium between the capillary forces and gravity, and shows that the liquid rise is larger at smaller pore sizes and for liquids with higher surface tension. The measured wicking height deviates from the evaluated one by only 1-3%; this difference is thought to be mainly due to the error in locating the top of the spherical cap through the glass capillary.

When heat is applied, the thermocapillary stress must also be taken into account; the thermocapillary stress acts in the direction of gravity, therefore reducing the wicking height. The meniscus is pushed down until a new equilibrium is found. The effect of thermocapillary stress on the meniscus height is more pronounced when the meniscus is closer to the heater as can be seen from Figure 3.23 where the experimental plot of meniscus wicking height versus the heater power can be fitted approximately by a exponential curve.

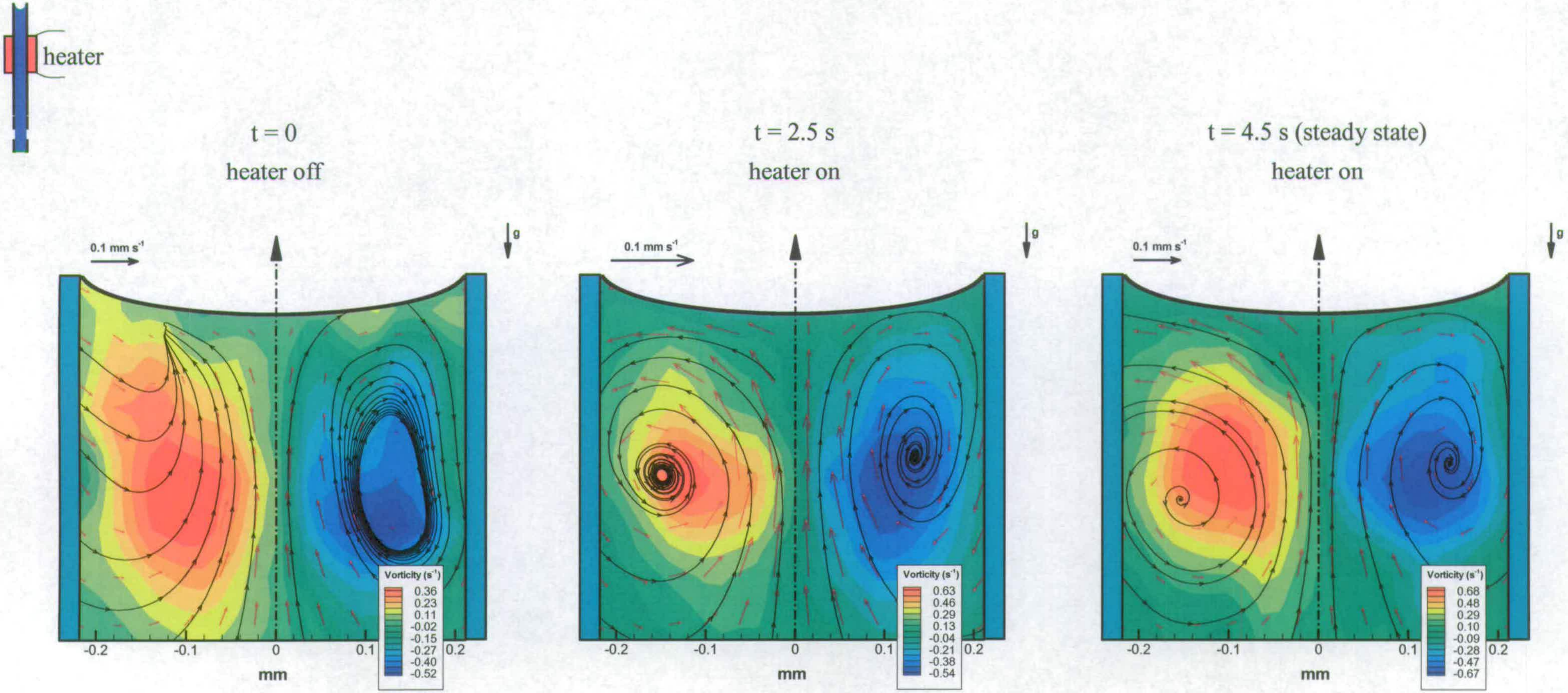

Figure 3.24 PIV sequence for ethanol as liquid and heater (0.3 W) in the meniscus liquid phase.

Without heating, a strong thermocapillary convection is observed in the liquid phase; liquid is driven by thermocapillary stresses along the meniscus interface from the centre towards the wedge where most of the evaporation takes place.

For both cases studied (heater in the vapour and in the liquid side) a μ-PIV measurement is taken with the heater off and then compared with the heater on at different powers.

Figure 3.24 is a μ-PIV measurement with the heater off (left) and on (middle and right) at total heater power of 0.3 W; the heater is in the liquid side and the liquid is ethanol. The PIV plot in the middle is produced to show that when heat is applied a transitory process takes place. It is clear that the convection is reinforced switching on the heater, but the flow pattern is kept similar. Figure 3.25 shows how the vorticity varies with the heater power. Note that the second point of Fig. 3.25 is not an outlier. Its value has been checked for repeatability. The last heater power applied is prior to the onset of boiling in the micro-channel.

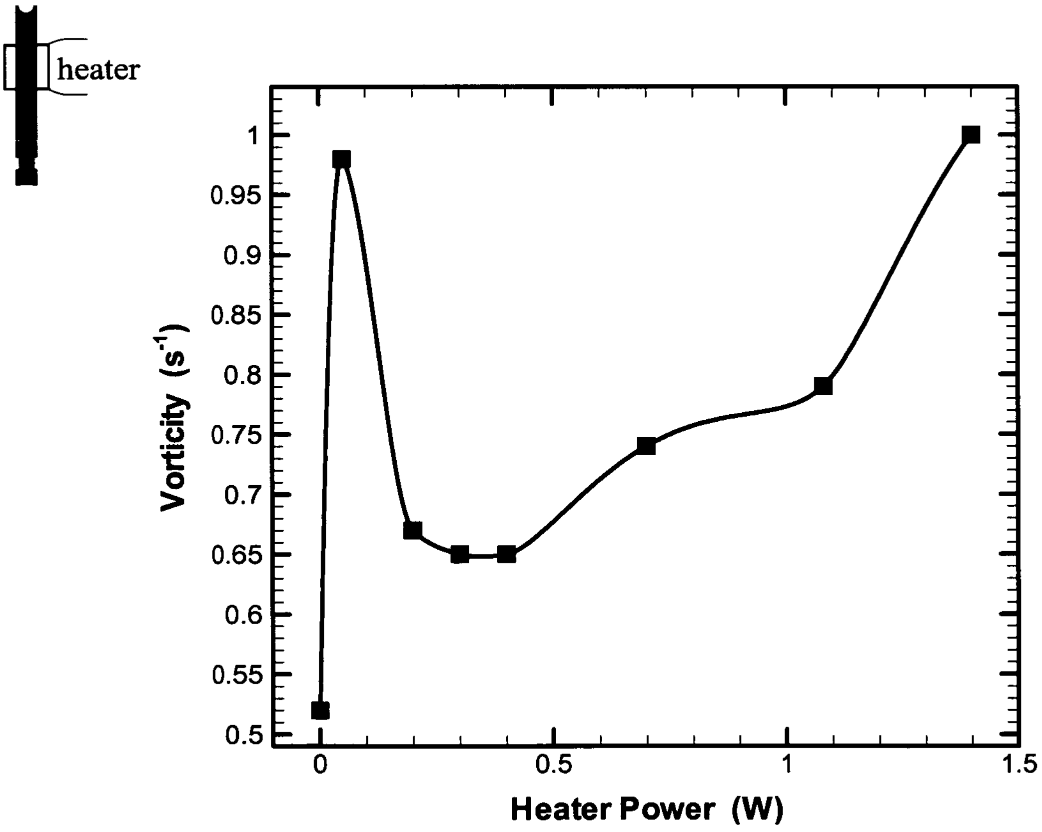

Figure 3.25 Vorticity vs. heater power for ethanol as liquid and heater in the meniscus liquid phase (points are experimental data and curve is best fit).

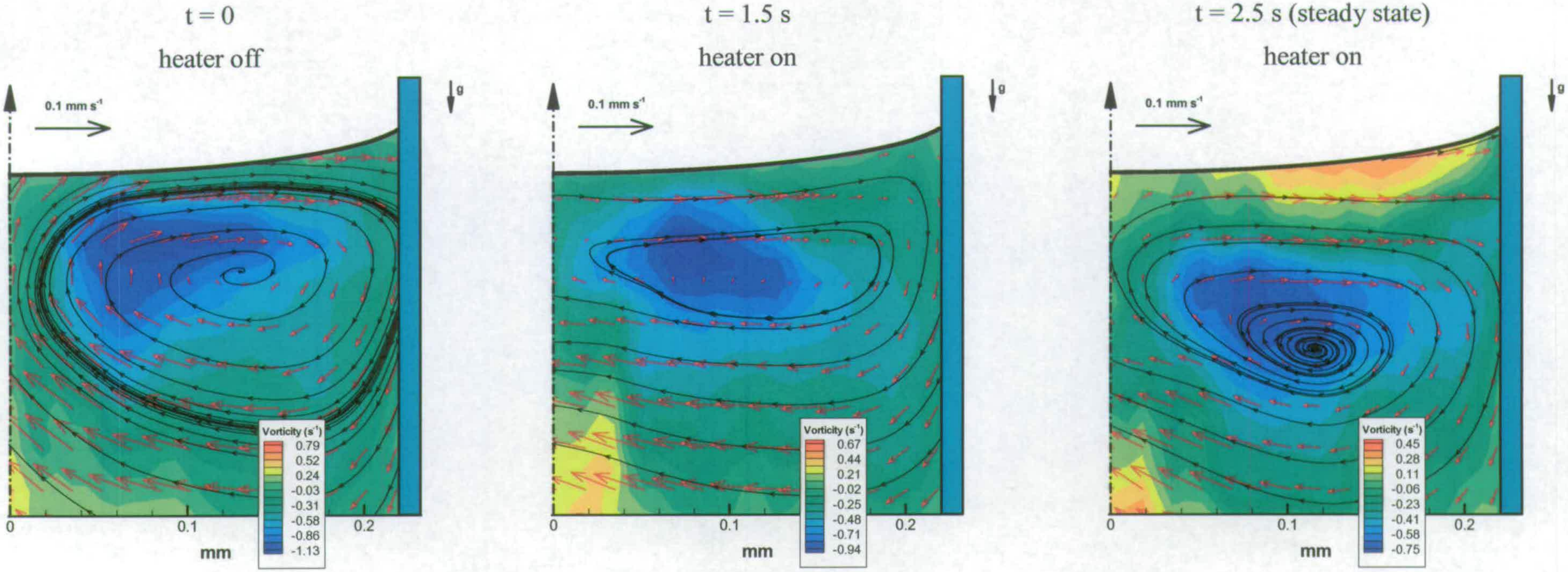
t = 0
heater off

t = 1.5 s
heater on

t = 2.5 s (steady state)
heater on

Figure 3.26 PIV sequence for methanol as liquid and heater (0.02 W) in the meniscus vapour phase.

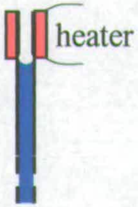

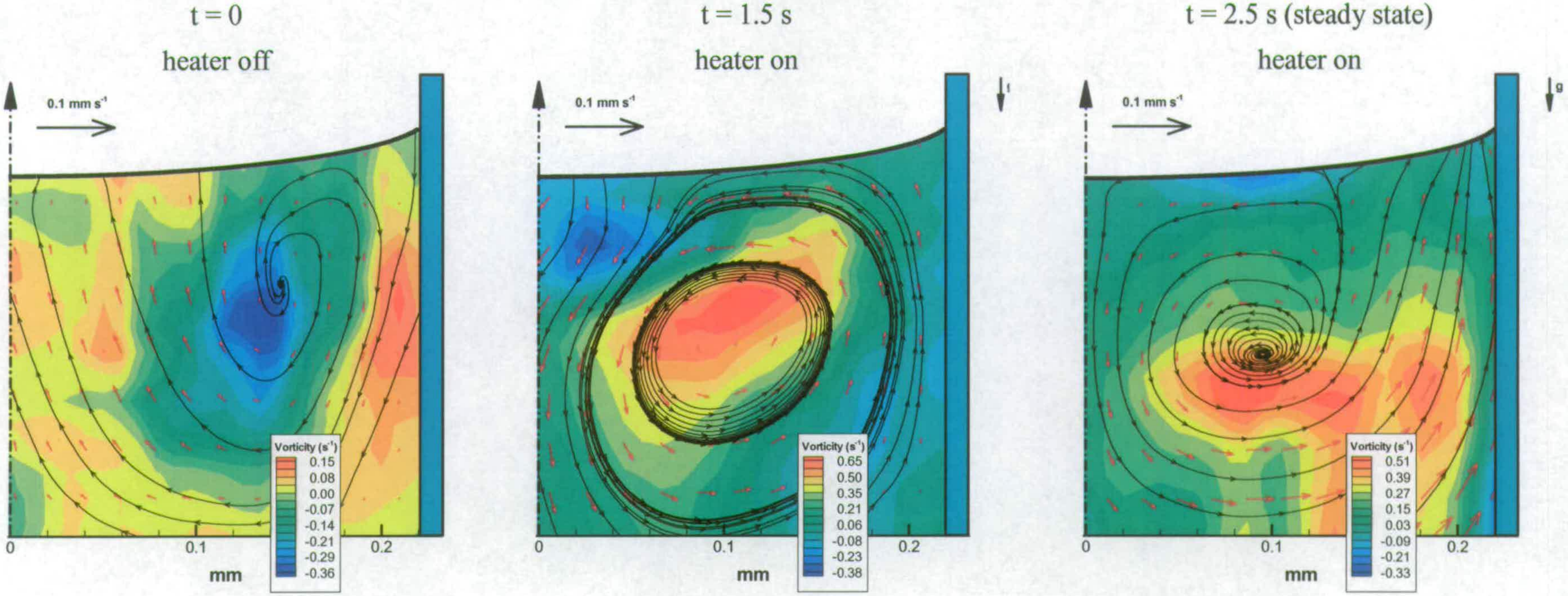
t = 0
heater off

t = 1.5 s
heater on

t = 2.5 s (steady state)
heater on

Figure 3.27 PIV sequence for methanol as liquid and heater (0.025 W) in the meniscus vapour phase.

Because of the meniscus motion, it becomes more difficult to compare the results of μ-PIV with different powers applied when the heater is on the vapour side. Fortunately the time scale of the meniscus motion (~0.3 s) is comparable (essentially because of viscous forces at the triple line) with the convection time scale (R^2/κ_l = 0.33 s) and a comparison based on the convection strength (vorticity value) is thus possible. It is therefore chosen to compare the μ-PIV results for different heater powers just before the meniscus starts to recede.

When the meniscus is positioned below the heater far away from the capillary edge, no anchorage is provided and the meniscus is freer to move on the adsorbed liquid layer at the capillary tube wall. Figure 3.26 is a sequence of the flow pattern taken at 0.02 W heater power and clearly no inversion takes place. Note that here the right half part only of the tube is presented and one vortex is thus present. However, increasing the heater power to 0.025 W the flow inversion takes place as can be seen (Figure 3.27). Figure 3.28 plots the vorticity value versus the heater power and it can clearly be seen that the convection strength increases dramatically at higher powers and changes sign according to the flow inversion.

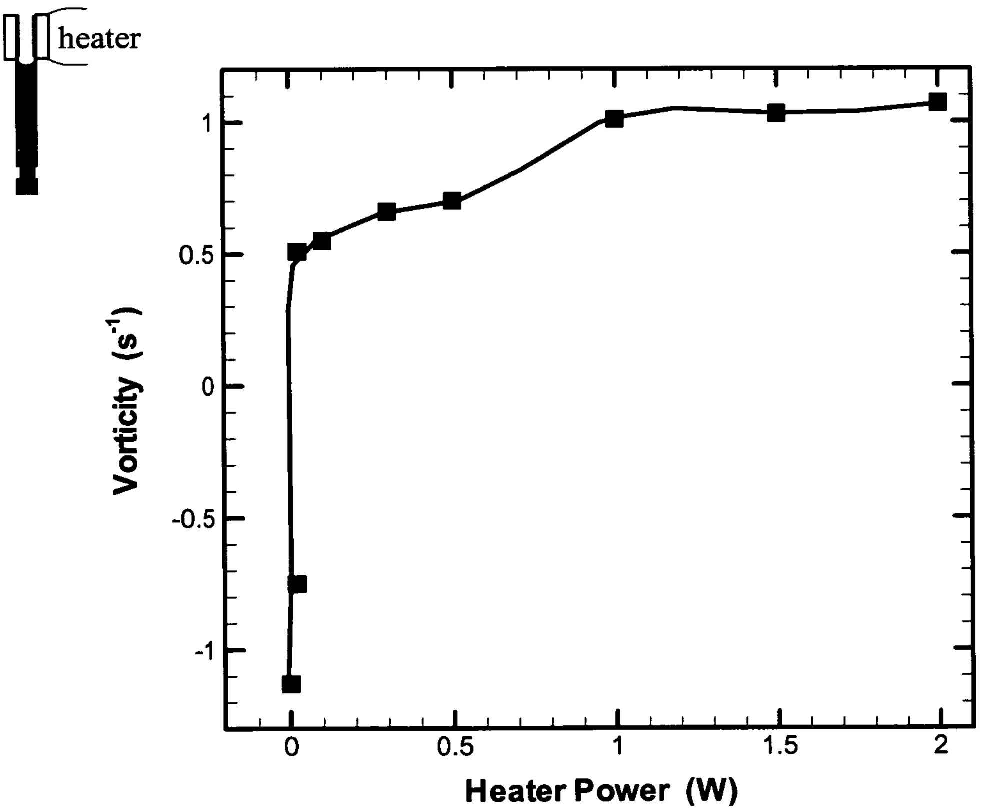

Figure 3.28 Vorticity vs. heater power for methanol as liquid and heater in the meniscus vapour phase (points are experimental data and line is best fit).

Due to the low boiling point of methanol, the liquid evaporates and the meniscus interface is consequently cooled down. Most of the evaporation takes place in the micro-region of the meniscus in contact with the wall, as already shown in the previous chapter. This causes a temperature gradient along the interface, responsible for the surface tension gradient that drives the observed clockwise convection in the liquid (see sketch in Figure 3.29, Heater "OFF" for the case of heater in the liquid side). Powering on the heater is this case will only influence the absolute temperature value along the interface but the profile is not inverted with respect to the unheated case as schematically indicated in Figure 3.29 for the Heater "ON" case. In fact, in order to get information about the temperature distribution along the meniscus, we can make the same assumption made by Pratt et al. [36]. As depicted in Figure 3.29, the temperature at the centre of the meniscus could be assumed equal to that at the correspondent point A at the wall. When the heater is in the vapour side the situation is completely different. Now the temperature gradient created by the heating element along the meniscus interface is opposite to that self-created by evaporation when the heater is off. If sufficient power is introduced by the heater, the temperature at location M (see Figure 3.30, Heater "ON" case) and therefore at the meniscus centre is lower than at the meniscus wedge. As a result, also the surface tension gradient is now opposite and the convection is ultimately inverted.

The PIV analysis performed with extra heating provided has clearly demonstrated that the convective pattern observed within the meniscus is inverted when imposing a temperature gradient along the wall and the meniscus lies below the heating element. No flow inversion takes place with the meniscus above the heating element. This suggests that the governing mechanism for the convection observed is indeed thermocapillary driven. Ultimately the inversion of the convective patterns by imposing a temperature gradient with the extra heating element, suggests the existence of a thermal gradient in the opposite direction to that prior to heating.

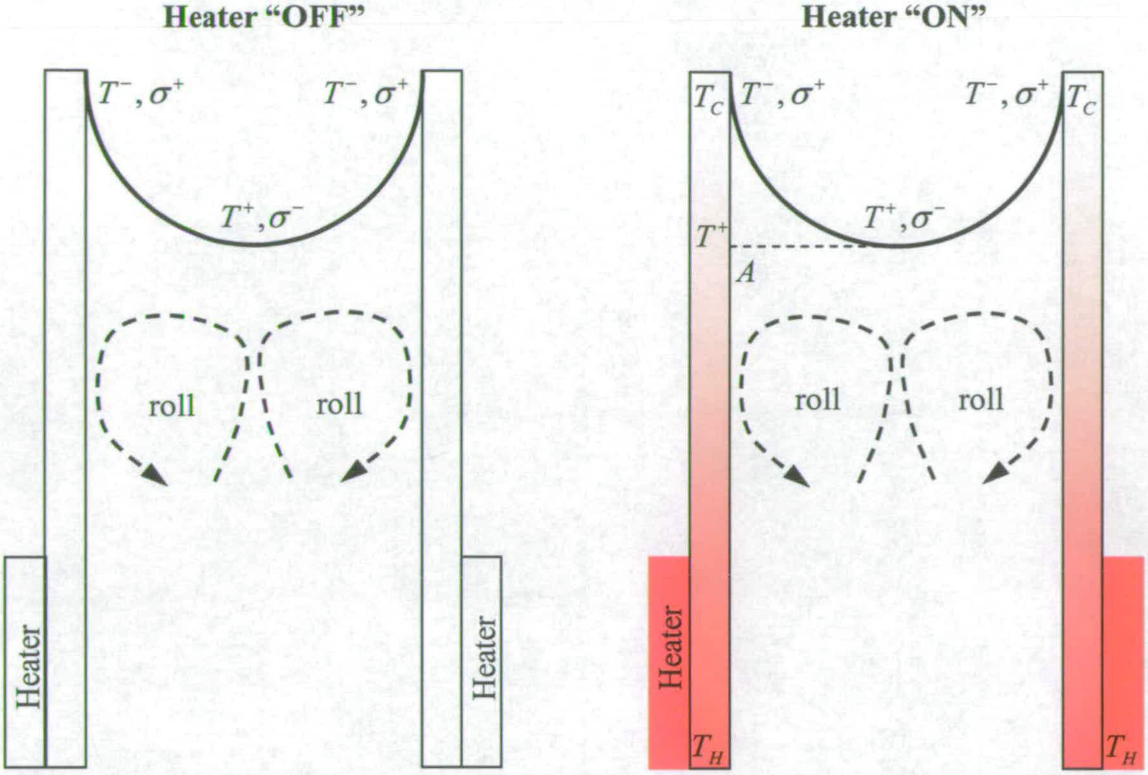

Figure 3.29 Temperature profile along the meniscus interface (heater in the meniscus liquid phase).

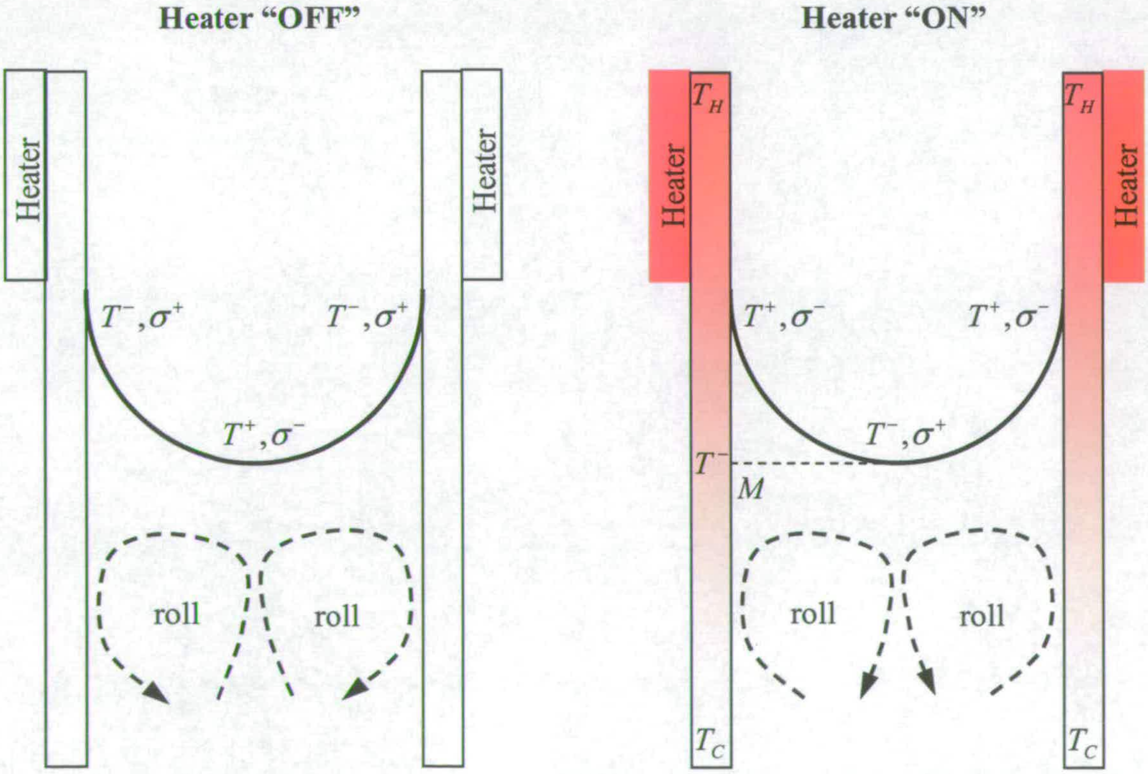

Figure 3.30 Temperature profile along the meniscus interface (heater in the meniscus vapour phase).

3.5 Conclusions and outlook

The μ-PIV technique used has indubitably given greater fundamental insight through the present investigation into thermocapillary convection. Because of the small dimensions involved in μ-PIV, problems connected essentially with the particle size are still an issue with respect to standard PIV. However, this area is growing at a very fast rate because of the commercial interest around micro-fluid devices in many areas such as micro-electronics, biomedical systems and space.

This investigation involved the study first of unheated capillary tubes in order to understand the basic mechanisms taking place. Once sufficient information was gathered with the technique, a more complicated situation was studied. The case with heated capillaries is closer to industrial applications such as heat pipes and capillary pumped loops, where a meniscus evaporates in a heated porous wick structure. The μ-PIV investigation has proven that the convective patterns in the meniscus liquid phase can be altered and eventually inverted by applying sufficient extra heating. This happens when the meniscus lies in the tube below the heating element. Experimental evidence is given to prove that no inversion can be obtained when the meniscus interface is above the heating element. This is an important experimental proof of the fact that the convection under investigation is indeed thermocapillary driven and the temperature profile along the meniscus interface is the key factor.

μ-PIV has also been used to investigate the effect of gravity on the thermocapillary convection. When the capillary tubes lay horizontally, a flow pattern distortion was observed in vertical sections through the tube. The importance of this effect changes with the tube diameter and the liquid volatility, suggesting that there is a scale at which thermocapillary stresses dominate and an axi-symmetric flow is expected. This is very important in all two-phase industrial application at the micro-scale, such as crystal growth, glass manufacture, stem cell culture growth, on earth where gravity cannot be neglected. In fact, in such applications the homogeneity of the final product is one of the more important specifications and a distorted flow pattern such as the one studied here, could have important consequences.

In the following two chapters temperature measurements will be presented by using two different experimental techniques. Measuring temperature for the self-induced thermocapillary convection investigated here is of paramount importance to fully understand the heat transfer mechanism set in by evaporation.

3.6 References

[1] Dantec Dynamics, http://www.dantecmt.com/

[2] Oxford Laser, http://www.oxfordlasers.com/

[3] TSI Incorporated, http://www.tsi.com/fluid/products/piv/softwrnt.htm

[4] Majumdar A., 2003, *Nanochannel biomolecular transport*, 1st Int. Conf. Micro-Minichannels, Rochester, NY, USA.

[5] Schmidt R., 2003, *Challenges in electronic cooling: opportunities for enhanced thermal management techniques – microprocessor liquid cooled minichannel heat sink*, 1st Int. Conf. Micro- Minichannels, Rochester, NY, USA.

[6] Markus R., Willert C. and Kompenhans J., 1998, *Particle Image Velocimetry: a practical guide*, Springer, London.

[7] van der Hulst H.C., 1957, *Light scattering by small particles*, John Wiley & Sons Inc., New York.

[8] Westerweel J., *Digital particle image velocimetry – Theory and application*, PhD Thesis, Delft University Press, Delft, 1993.

[9] Adrian R.J.,1991, Particle-*imaging techniques for experimental fluid mechanics*, Ann. Rev. Fluid Mech., Vol. 23, pp. 261-304.

[10] Adrian R.J., 1991, *Statistical properties of particle images velocimetry measurements in turbulent flow*, Laser Anem. Fluid Mech. III, Springer-Verlag, Berlin Heidelberg, pp. 115-129.

[11] Keane R.D. and Adrian R.J., 1992, *Theory of cross-correlation analysis of PIV images*, Applied Sci. Research, Vol. 49, pp. 191-215.

[12] Adrian R.J., 1986, *Image shifting technique to resolve directional ambiguity in double-pulsed velocimetry*, Appl. Opt., Vol. 25, No. 21, pp. 3855-3858.

[13] Prasad A.K. and Adrian R.J., 1993, *Stereoscopic particle image velocimetry applied to fluid flows*, Experiments in Fluids, Vol. 15, pp. 49-60.

[14] Raffel M., Westerweel J., Willert C. and Kompenhans J., 1996, *Analytical and experimental investigations of dual-plane PIV*, Opt. Eng., Vol. 35, pp. 2067-2074.

[15] Prasad A.K, Adrian R.J., Landreth C.C. and Offutt P.W., 1992, *Effect of resolution on the speed and accuracy of particle image velocimetry interrogation*, Experiments in Fluids, Vol. 13, pp. 105-116.

[16] Westerweel J., 1997, *Fundamentals of digital particle image velocimetry*, Meas. Sci. Technol., Vol. 8, pp. 1379-1392.

[17] Adrian R.J., 1988, *Statistical properties of particle image velocimetry measurements in turbulent flow*, Laser Anemometry in Fluid Mechanics III, pp. 115-129.

[18] Keane R.D. and Adrian R.J., 1993, *Theory of cross-correlation*, Appl. Sci. Res. Vol. 49, pp.191-215.

[19] Koutsiaris A.G., Mathioulakis D.S. and Tsangario S., 1999, *Microscope PIV for velocity field measurement of particle suspensions flowing inside glass capillaries*, Measurement Sci. Techn., Vol. 10, pp. 1037-1046.

[20] Heinzel V., Jianu A. and Sauter H., 2003, *Flow Pattern Measurement by PIV in the Micro-channels of a Heat Exchanger and Associated Problems Due to Fouling*, 1st Int. Conf. Micro- Minichannels, Rochester, NY, USA.

[21] Kim K.C., Yoon S. Y. and Ji H.S., 2003, *Effect of Particle Sticking on the Micro-PIV Measurement in a Micro-Bypass Channel Flow*, 1st Int. Conf. Micro-Minichannels, Rochester, NY, USA.

[22] Mielnik M.M. and Sætran L.R., 2003, *Micro-PIV investigation of a sinusoidal crossflow microfiltration module*, 1st Int. Conf. Micro- Minichannels, Rochester, NY, USA.

[23] Newport N., Curtin D. and Davies M., 2003, *A comparison of Micro-PIV experiments in a mini-channel to numerical and analytical solutions*, 1st Int. Conf. Micro- Minichannels, Rochester, NY, USA.

[24] Hohreiter V., Wereley S.T., Olsen M.G. and Chung J.N., 2002, *Cross-correlation analysis for temperature measurement*, Meas. Sci. Technol., Vol. 13, pp. 1072-1087.

[25] Santiago J.G., Wereley C.D., Meinhart C.D., Beebe J.D. and Adrian R.J., 1998, *A particle image velocimetry system for microfluids*, Experiments in Fluids, Vol. 25, pp. 316-319.

[26] Meinhart C.D., Wereley C.D. and Santiago J.G., 1999, *PIV measurements of a microchannel flow*, Experiments in Fluids, Vol. 27, pp. 414-419.

[27] Park J.S., Kihm K.D. and Pratt D.M., 2000, *Molecular Tagging Fluorescence Velocimetry (MTFV) to measure meso- to micro-scale thermal flow fields*, IMECE Conference, Orlando, Florida.

[28] Dantec Dynamics, 1998, *User Manual,* Flow Map® Particle Image Velocimetry Instrumentation.

[29] Bird R.B. Stewart W.E. and Lightfoot E.N., 1960, *Transport phenomena*, Wiley & Sons, New York.

[30] Farshad F., Rieke H. and Garber J., 2001, *New development in surface roughness measurements, characterization, and modelling fluid flow in pipe*, Journal of Petroleum Science and Engineering, Vol. 29, pp. 139-150.

[31] Li Z.X., Du D.X. and Guo Z.Y., 2002, *Experimental study on flow characteristics of liquid in circular microtubes*, Proceedings of the Int. Conference on Heat Transfer and Transport Phenomena in Microscale, Banff, Canada.

[32] Yaws C.L., 1999, *Chemical properties handbook*, McGraw-Hill, New York.

[33] Zeytounian R.K., 1997, *The Bénard-Marangoni thermocapillary instability problem: on the role of the buoyancy*, Int. J. Eng. Sci., Vol. 35, pp. 455-466.

[34] Incropera F.P. and DeWitt D.P., 1996, *Fundamentals of heat and mass transfer*, 4th Edition, John Wiley & Sons, New York.

[35] Riley R.J., *An investigation of the stability and control of a combined thermocapillary-buoyancy driven flow*, PhD Dissertation Thesis, Georgia Institute of Technology, March 1996.

[36] Pratt D.M., Brown J. and Hallinan K.P., 1998, *Thermocapillary Effects on the Stability of a Heated, Curved Meniscus*, Journal of Heat Transfer, Vol. 120, No. 1, pp. 220-226.

[37] de Gennes P.G., 1985, *Wetting; statics and dynamics*, Review of Modern Physics, Vol. 57, No. 3, part I, pp. 827-863.

[38] Pratt D.M. and Hallinan K.P., 1997, *Thermocapillary Effects on the Wetting Characteristics of a Heated Curved Meniscus*, Journal of Thermophysics and Heat Transfer, Vol. 11, No. 4, pp. 519-525.

CHAPTER IV

The use of Thermochromic Liquid Crystals to map temperature near the contact line region

4.1 Motivation

With a volatile liquid evaporating in a capillary tube, the system must be supplied with the heat necessary to sustain this process. The heat lost at the meniscus interface leads to a reduction in temperature of the liquid phase. In steady state, this process cannot be maintained if no extra heating is provided to the system. Generally speaking, this extra heating can come from the bulk fluid and/or from the ambient surroundings of the capillary tube, the latter being more probable in the steady state. In this chapter an answer to the question of where the heating comes from is given by measuring the capillary wall temperature. Measuring the capillary tube temperature is not trivial. In fact, the small scale involved (~1 mm) makes it difficult to measure temperature with standard instruments such as thermocouples. Despite the commercial availability of thin (Ø of 250 μm) and fast (0.05 s) thermocouples, readings provided by such instruments will have insufficient spatial resolution for the present case. This experiment is designed to provide a solution to this problem. We wish to map the capillary wall tube temperature and determine where the heat transfer necessary to sustain evaporation comes from. To this aim, a special experiment has been designed involving the use of Thermochromic Liquid Crystals (TLCs). Although researchers have been using TLCs for temperature measurement for a couple of decades, the technique is not yet simple to use. As will appear later, the use of TLCs, in spite of being one of the most advanced and reliable non destructive methods, it is a difficult method to implement.

The temperature differences generated at the meniscus by the evaporation of a volatile liquid in a confined space is mapped on the tube surface with the use of TLCs. The strong evaporative cooling close to the meniscus triple line generates a temperature dip in this region. Despite the thermal diffusion through the tube thickness, the TLCs' thickness and the inherent difficulties of working with unsealed TLCs, the present technique has proven to be a suitable and powerful tool for accurate temperature measurement at the micro-scale.

4.2 Background

TLCs are organic compounds that reflect light when their temperature falls within a certain range, usually termed the TLCs event temperature range. Liquid crystal thermography is a Non Destructive Testing (NTD) technique of measuring temperature of a surface experiencing temperature changes and/or differences. They can also be used to map the temperature of a fluid if the flow timescale is comparable with that of TLCs' response.

The following description of TLCs is largely a summary of references [1-4]. Liquid crystals are an intermediate state of matter between liquid and solid, exhibiting all liquid physical properties while maintaining a certain order characteristic of the solid phase. A very large combination of molecules can form liquid crystal phases. For all cases, a substantial anisotropic behaviour is exhibited. The typical liquid crystal molecule has a quite rigid portion with hydrocarbon chains (see Figure 4.1) and this feature is essential for maintaining a preferential alignment. The orientational ordering is responsible for the characteristic anisotropic behaviour of many TLC properties such as their viscosity, their elasticity and most important of all from the heat transfer point of view their refractive index. By heating up a liquid crystalline material it is possible to go from the solid behaviour to the liquid isotropic behaviour passing through different intermediated phases as schematically shown in Figure 4.2.

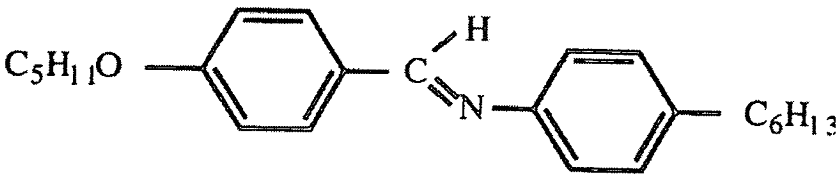

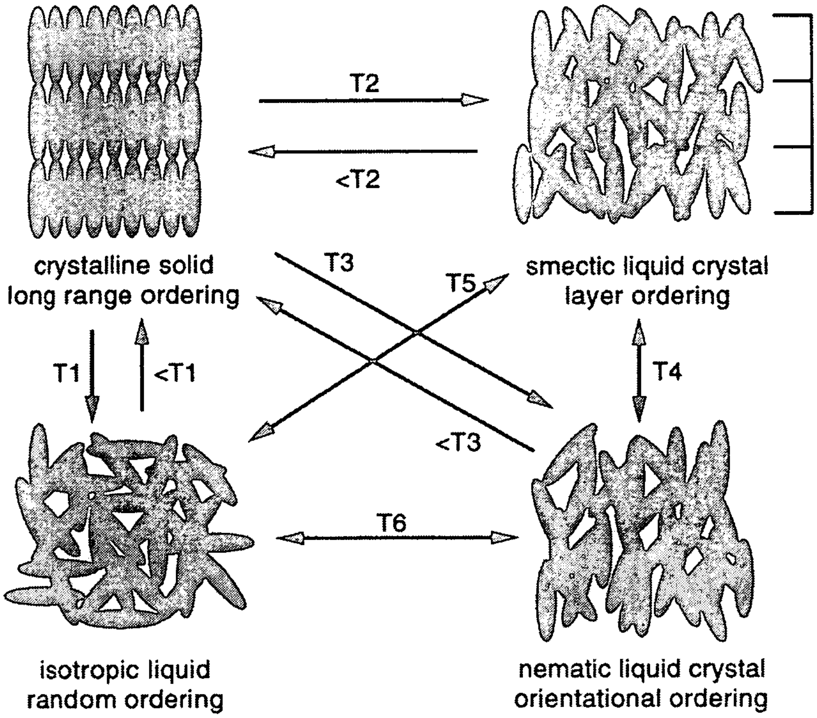

Figure 4.2 Melting stages of a liquid crystalline material (from Collings and Hird [2]).

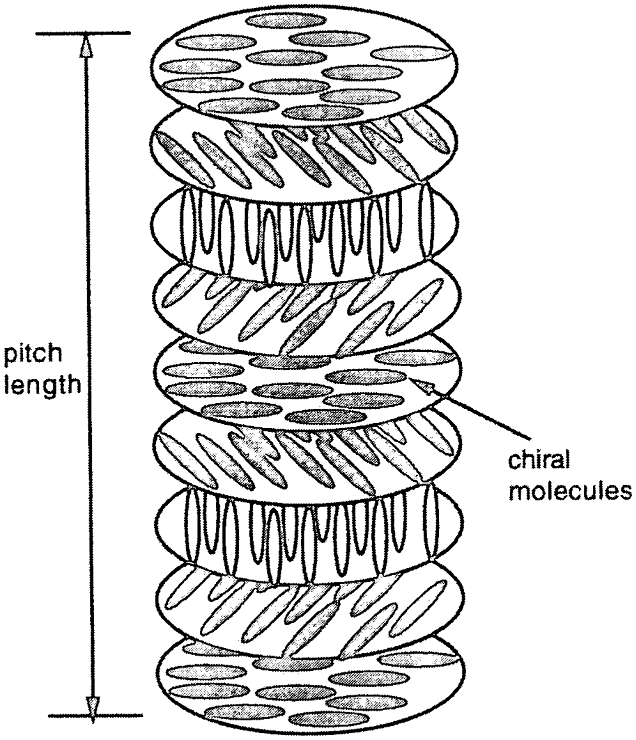

Figure 4.3 Typical CNLC helicoidal structure (from Collings and Hird [2]).

Basically, there are two types of liquid crystal phases: smectic and nematic. The former case takes place when the solid compound is heated and the lateral interaction forces between molecules are stronger than the terminal ones. In this case the material exhibits a layering order. Increasing the temperature, the lateral interaction is destroyed losing the layering order but keeping orientational order; this phase is termed nematic. A further increase of temperature gives rise to the isotropic liquid phase. However, in the heating procedure different scenarios can take place and, for instance the nematic phase can be obtained without passing thought the smectic one. Further detailed information on the basic TLC concepts can be found in specialised books [2-3] and will not be repeated in what follows. Only some basic concepts on the Chiral Nematic Liquid Crystals (CNLC) for application as temperature sensors will be given here. The average molecular orientation of a CNLC is termed the director *n*. Of all the possible NLCs the Chiral ones are the most important as temperature sensors. Basically, hereafter we refer to CNLC with the general term of TLCs. In fact, their slight molecular asymmetry leads to intermolecular forces that rotate adjacent molecules and by doing so the director *n* describes a helix (see Figure 4.3). The pitch of the helix is strongly dependent on temperature. Usually, as the temperature increases, the pitch is reduced because of a larger rotation between adjacent molecules; however, there are some cases in nature with the opposite trend. The helix is a fundamental feature for temperature measurement. In fact, the helix has the property of selectively reflecting white light with wavelength of the same order as the pitch. As schematically depicted in Figure 4.4, an incident ray is reflected from the repeating TLCs helix structure; here we assume that the angles of incident and reflected light are equal (ϕ), therefore the difference between the two paths is (from the rectangular triangle ABC of Figure 6.4):

$$\overline{AC} - \overline{AB} = \overline{AC}(1 + cos\,2\phi) = \frac{P_e}{2cos\,\phi} 2cos^2\phi = P_e cos\phi \qquad (4.1)$$

with P_e the helix's pitch. There will be constructive interference between the two rays if:

$$m\lambda = P_e cos\phi \qquad (4.2)$$

where m is a positive integer and λ is the light wavelength. Equ. (4.2) suggests that a particular wavelength of an incident white light is reflected at each angle of reflection. Thus, depending on the viewing angle, TLCs appear with a different colour. Equ. (4.2) says that the reflected wavelength depends also on the helix pitch. Earlier we have mentioned that the pitch is strongly dependent on temperature, thus the colour reflected from the TLCs is also a function of temperature. So, by capturing the colour displayed by TLCs we can infer the temperature of a surface on top of which the TLCs have been deposited. It is worth mentioning that the pitch feature is also extensively used in the liquid crystals display industry [1].

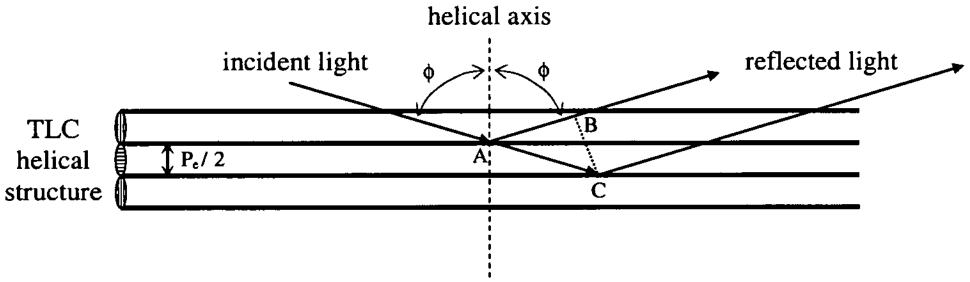

Figure 4.4 TLC-light interaction (adapted from Collings and Hird [2]).

The colour of a TLC depends strongly not only on the helix pitch and viewing angle but also on the incident light (angle and spectral composition). These factors make TLC thermography quite difficult to use for quantitative temperature measurements. In addition, there are other factors negatively affecting the use of TLCs. Chemical contamination, exposure to UV and oxygen all can rapidly degrade the TLC material [4-5]. To overcome this problem, two protective techniques have been developed over the years: microencapsulation and polymer dispersion. With microencapsulation, a polymer coating surrounds the TLC material forming capsules of 5-100 μm diameter [6]. A polymer binder is used in the polymer dispersion technique without formation of microcapsules. The latter technique does not guarantee the same level of protection as microencapsulation, but the colour appearance is substantially improved. Another factor of extreme importance from our point of view is that the spatial resolution of the polymer dispersed TLCs is not limited by the capsules' size, as it is of the microencapsulated ones.

Because of important improvement in colour capture devices and analysis tools over the last few decades, the TLC technique of inferring temperature from colour images has developed from a qualitative tool to a powerful, reliable and accurate quantitative one. Due to the fact that most of the commercial devices available try to accurately reproduce the capabilities of the human eye [1], they are usually not suitable for accurate quantitative measurements such as are needed in heat transfer studies because of the limitations of our visual system. Therefore, special hardware (such as camera, frame grabber, light, etc.) and software are required for accurate temperature measurements.

In order to infer temperature from colour images, it is necessary to calibrate the TLCs. This is the most time consuming task when using TLCs, because the calibration is not transportable. In fact, we have already pointed out that the colour appearance strongly depends on the lighting angle and its spectral composition, and most of all on the viewing angle. Some attempts have been made in the past to overcome these difficulties [5] but much is still to be done and an *in situ* calibration is strongly recommended [7].

Despite all these important difficulties, Höhmann and Stephan [8] have demonstrated that unsealed TLCs can be successfully used for microscale temperature measurement of an evaporating meniscus with an amazing sub-micron resolution. The work of Höhmann and Stephan [8] is worthy of attention, because it is very close to the present investigation. The temperature field of an evaporative meniscus has been investigated experimentally using liquid crystals. Distilled water was used to fill the slot between two plates and a meniscus allowed to form. One wall was formed by a metallic foil of 20 μm thickness (used as a heater) with black paint deposited on its surface before a small layer of TLCs was brushed over it. A Plexiglas foil covered the unencapsulated TLCs. The whole system was put in a sealed box connected to a condenser and a vacuum pump. The data acquisition system comprises two CCD cameras: one for contact angle measurement and the other with an attached long distance microscope. One CCD camera was used for contact angle measurement with illumination from the opposite side. The other camera recorded images of reflected light scattered by the TLCs. The large size of microencapsulated TLCs (5-50 μm) compared with the meniscus micro-region length, forced the authors to use unencapsulated TLCs; unfortunately their life time is of only few hours, so the authors were forced to set the experiment, make the calibration and perform the readings in a limited period of time (typically a few hours). The TLC calibration is a delicate aspect; the authors strongly recommend an in situ calibration, because the relationship between the TLC colour and the temperature is a strong function of the light setting, the viewing system and the thickness and age of the TLCs. An amazing 0.83 μm spatial resolution was achieved. Because there is a huge uncertainty of temperature measurement pixel-to-pixel, a filtering method was necessary for noise reduction and the absolute value of the temperature depended on the filter, in particular at the micro-region. The results show how the temperature drops in the micro-region where the cooling effect of the evaporation process is higher. The temperature rises in the adsorbed film due to the weakness of the heat transfer process in this region. They show that a temperature dip of around 0.2 °C is present in the meniscus micro-region.

The first works to have appeared using TLCs focused on topics about the boundary layer transition from laminar to turbulent regime [9-10], separation zones and shock wave detection, essentially because all these cases involve a local change in temperature and therefore in TLCs colour appearance. TLCs have since been used for fluid flow visualization as microencapsulated tracers [11] and later for heat transfer studies. Cooper and Groff [12] and Cooper and Petrovic [13] used TLCs for estimating the growth rate of the frozen region around a cryoprobe. Early TLC calibration was made mostly by naked eye [9,12] using only the onset of red, green and blue as the calibration points. Azar et al. [14] have used TLCs in temperature mapping of electronic devices reaching spatial resolution of 5 μm. They emphasize the fact that although Infra Red (IR) methods can provide faster temperature measurement of microelectronic chips, the two IR images taken (necessary to measure the chip emissivity map) of an isothermal base on which the chip is mounted could introduce significant errors. Kenning [15-16] and Kenning and Yan [17] have investigated boiling heat transfer using TLCs. TLCs have also been used in transient temperature measurements with a time response evaluated to be in the range between a few and hundreds of milliseconds (Parker [18] and Ireland and Jones [19]).

In the present investigation unsealed TLCs are used to map the temperature profile produced along the external tube surface by an evaporating liquid meniscus formed inside the tube. The dip in temperature found close to the meniscus triple line is also reported in a similar study by Höhmann and Stephan [8] and is confirmed in the present investigation as being due to the evaporation cooling effect. No systematic investigation was carried out using different volatile liquids and various tube sizes because of the inherent difficulties encountered with the technique. However, the experimental evidence gathered proves that the evaporative cooling at the microscale is indeed important. A heat/mass balance made with the use of the measured temperature profile using TLCs at the tube wall shows a fairly good agreement with the evaporation rate measured as shown in Chapter II and gives confidence in the TLC measurement undertaken.

4.3 Experimental layout

Recommendations for the experimental setup to be used with TLCs measurement of heat transfer studies can be found in Herold and Wiegel [20-21] and will not be repeated here. In the following we will simply emphasize the approach used in the present study.

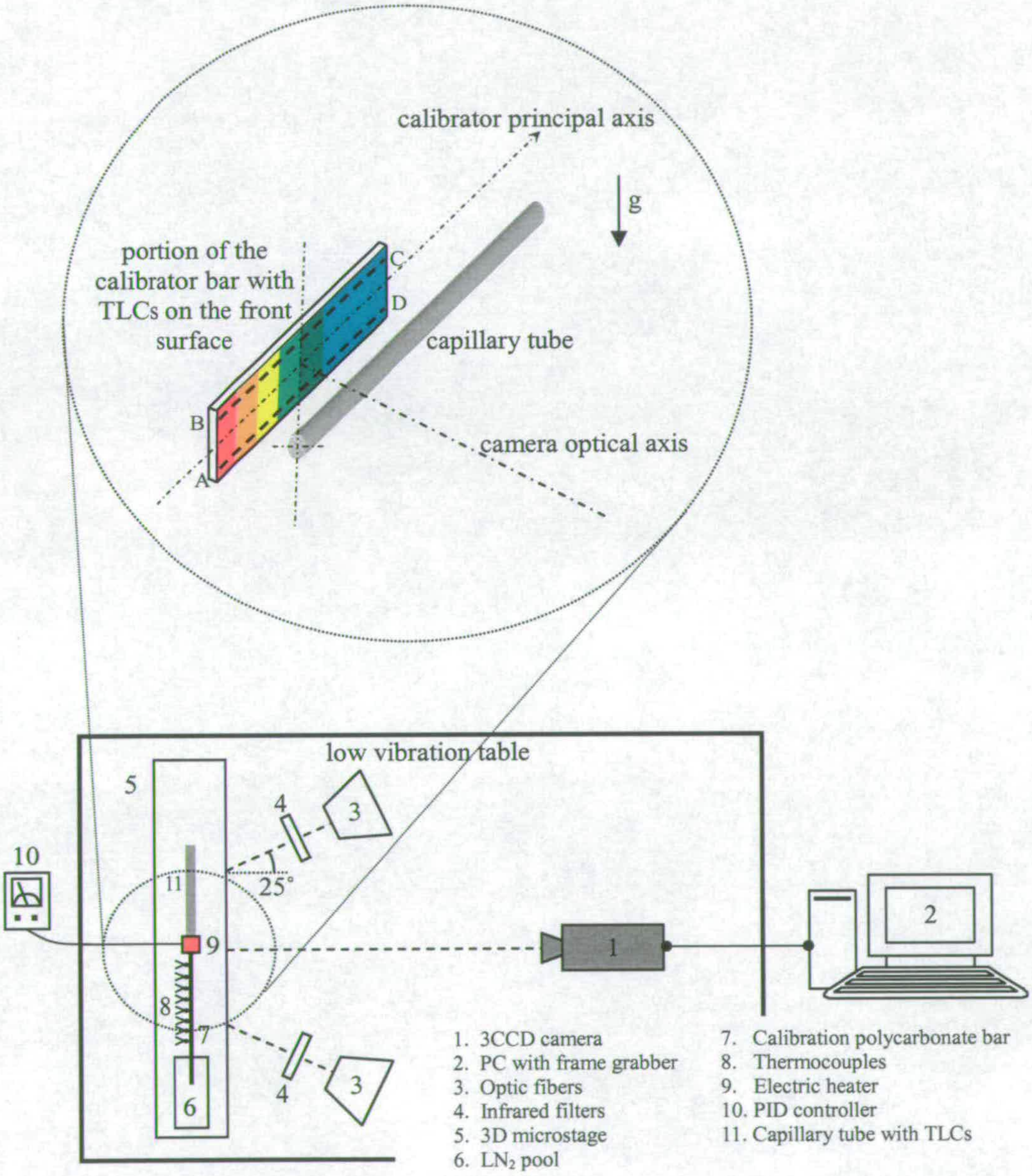

Figure 4.5 Schematic of the experimental facility.

The experiment was conducted in a totally dark environment in order to keep invariable the light spectral distribution of the primary illuminant. The experimental layout is sketched in Figure 4.5 and comprises: a 3CCD colour camera (Hitachi HV-C20); two fibre optic cables; a PC equipped with frame grabber for image acquisition and storing; the tube sample under test and a calibrator with the former positioned underneath the latter (see inset of Figure 6.5 for more details) to enable effective use of the whole CCD array. Optical fibres transmit mainly visible radiation but also near UV and near-infrared, rejecting mid- and far-infrared that carry most of the radiant heat transported by the light. Therefore, for this experiment infrared filters have been used to cut-off also the near infrared portion of the spectrum avoiding possible extra heating at these wavelengths. The fibre optic illuminator is a 3200 K white light source. All the apparatus was lying on a low vibration steel table (Newport Co.). The Hitachi HV-C20 3CCD colour camera has an array of 795x596 pixels and has both composite video Y/C and Red-Green-Blue (RGB) outputs, with 700 TV lines resolution (580 lines RGB). 3CCD means that each of the RGB primary colours is directed to a different CCD by the use of a chromatic beam splitter. The frame grabber is a Snapper PCI-24 model connected to an Intel Pentium III 800MHz double processor; the frame grabber is able to acquire separately each of the three RGB components and operates at 30 frames per second. The capillary tube containing the sample is made of borosilicate glass, has an internal diameter of 1630 μm, a wall thickness of 235 μm, is partially filled with pentane and has its axis horizontally aligned.

There are two ways of calibrating the TLCs [4]. One consists of imposing a uniform temperature on the calibrator and acquiring a colour image at each temperature in order to cover the entire TLCs active temperature range. This means that the TLCs temperature resolution depends on the temperature step chosen to calibrate the sample rather than the inherent TLCs temperature resolution. The second approach consists of imposing a known temperature difference across the calibrator that covers the entire TLCs active temperature range and taking only one colour image. The latter approach is more effective as the TLCs' temperature resolution is certainly coincident with the TLCs inherent one, but could lead to unwanted lighting and viewing skews because the active temperature range is not reproduced at the same point on the surface [4].

However, the advantage of covering the entire TLCs active temperature range in a single colour image makes this approach very attractive for the present study as it reduces dramatically the calibration time because a single colour picture is taken for the entire temperature range covered; therefore, it is adopted here. As already mentioned, the most difficult task when using TLCs is their calibration. Farina et al. [5] have carried out extensive investigation on the possibility of transporting the calibration curve, avoiding the time consuming *in situ* calibration. They have demonstrated that with the use of a system colour calibration technique the calibration of microencapsulated TLCs becomes transportable. In practice they use reference colours such as a standard colour chart (MacBeth) that has printed colours with uniform reflectance and defined tristimulus value under certain viewing parameters. Different lighting conditions such as white light, room light, sun light, primary illuminant ring light and combinations were investigated. It was demonstrated that the hue-temperature calibration chart can be transported with the use of a system colour calibration. In addition, it is proved that rotation angles up to 25° between camera-light and TLCs surface are acceptable whereas small angles (~5°) between camera and light are unacceptable. This approach could have a potential advantage when using microencapsulated TLCs. However, in the present study an *in situ* calibration approach has been adopted because of the very limited lifetime for the unsealed TLCs used (ranging from few minutes to 1-2 hours depending on the environment, as suggested by Prasley [6] and Höhmann and Stephan [8]). It is also a known fact that the TLCs aging produces a shift of the maximum scattering wavelength; that is 3-4 μm after 20 minutes up to 10-12 μm after 3 hours as reported by Herold and Wiegel [21].

The calibration is performed using a thin polycarbonate bar with one end immersed in a pool of liquid nitrogen (LN_2) and the other kept at a constant temperature by the use of an electrical heater and PID controller. Other material substrates (aluminium, Perspex, PVC, PTEF, etc.) have been tested but none gave the colour brilliance given by polycarbonate. The use of LN_2 was necessary because the expected temperature on the tube sample is below ambient; pentane (boiling point of 36.3 °C) is used here as the evaporating liquid inside the tube. The calibration bar has 8 Chromega-Constantan calibrated thermocouples (Omega Engineering Ltd.) with very thin tip (250 μm), very short response time (0.05 s) and accuracy of ±0.5 °C, attached to its back side at a distance of 0.5 mm from each other. The calibration bar was positioned with its longitudinal axis horizontal on the 3-D micro-stage; its largest faces point in the camera optical path as sketched in the inset of Figure 6.5 in order to reduce the temperature difference due to natural convection existing around the bar between the bar's front (where the TLCs sample is deposited) and the back (where the thermocouples are placed) sides. The polycarbonate front side was first covered with a matt black paint (used in order to avoid reflection from the solid material) and then a few layers with uniform thickness of TLC material were deposited with the use of an air brush. An unsealed TLC coating BN/R10C20W manufactured by Hallcreast Ltd has been used; the TLC sample has a temperature tolerance of ±0.5 °C. The abbreviation R10C20W stands for: R10C means that Red starts at 10 °C and 20W means that the bandwidth is of 20 °C and therefore Blue starts at 30 °C. The manufacturer suggests that a uniform thin TLC thickness of about 5-10 μm is required for better colour appearance. Smaller thickness will not give good colour brilliance and thicker ones will produce a broadening of the TLCs' spectral bandwidth, due to the dependence of the helix pitch on temperature resulting from high temperature gradient perpendicular to the TLCs layer [21]. The manufacturer also strongly recommends an *in situ* calibration because the calibration depends on coating thickness, surface texture and application conditions other than on the lighting parameters mentioned earlier. Table 4.1 reports the manufacturer's calibration.

Table 4.1 Manufacture Colour-Temperature calibration (Hallcrest Ltd.)

Colour	*Temperature (°C)*
Visible start	9.9
Red start	10.0
Green start	13.0
Bright green	14.9
Blue start	29.7
Colourless	38.1

The TLCs with the backing black paint were deposited on the tube sample at the same time as on the calibration bar for consistency. The calibration bar can be moved with respect to the liquid nitrogen pool and the electric heater power can be changed in order to get the temperature distribution of the TLC sample falling in its active temperature range. Once the LN_2 was introduced in the pool and the heater switched on, the colour picture of the calibrator was taken after the steady state regime was reached by reading the thermocouples output.

Once the calibration stage was performed, the electric heater was switched off and the insulation material around the LN_2 pool removed to allow the calibrator to reach room temperature before any measurements on the nearby capillary tube sample were taken. The colour images stored are post-processed with the use of Matlab Image Processing Toolbox and by transforming the RGB colour system in the HSI system, (where H stands for hue - that is the colour's dominant wavelength -, S stands for saturation and I stands for value intensity or brightness), one gets the hue. The choice of a colour primary system is not unique and here the HSI system is chosen in accordance with Farina et al. [5].

4.4 Results and analysis

Figure 4.6 shows the steady state thermocouple temperature reading on the calibrator bar with a linear fit; the inset is the colour picture indicating the thermocouples' location with respect to the liquid nitrogen (LN_2) pool and electric heater. A good uniformity of temperature is obtained across lines normal to the calibration bar principal axis, as shown in the inset colour picture of Figure 4.6 between thermocouple 1 and 2 by the TLCs' isotherm displayed at their onset event temperature.

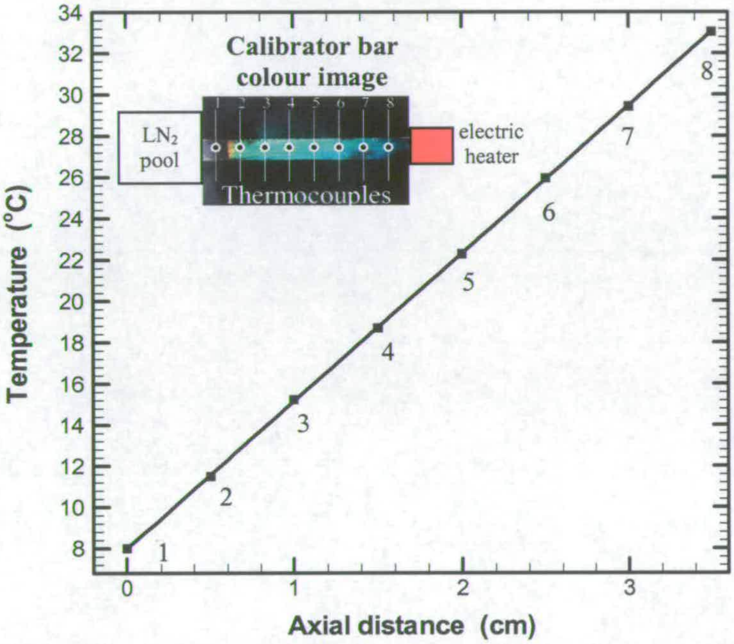

Figure 4.6 Temperature along the calibrator bar axis.

Figure 4.7 shows the calibration chart with hue versus temperature obtained as following: a rectangular region of interest (ROI) area of 500x40 pixels has been selected in the centre of the bar (region ABCD in the inset of Figure 4.5) in order to avoid edge effects; the hue value was extracted along the lines parallel to the principal calibration axis and spanwise averaged; only the monotonic portion of the hue curve along with the uncertainty envelopes is plotted in Figure 4.7. It is recognised [4-5] that the practical usable region of the calibration curve (where a one-to-one correspondence between hue and temperature can be established) is the one with monotonic increase of the hue value; despite the monotonic portion of the calibration curve ranging between 11.3 and 25.6 °C, the practical usable range in the present case is of ~4.2 °C (between 11.3 and 15.5 °C as shown in Figure 4.7). This confirms what was already pointed out by Hay and Hollingsworth [4] about the nominal and real usable range of the TLCs and justifies our choice of a TLC sample with an event temperature range much larger than the expected one on the tube capillary. The resulting calibration and the uncertainty envelope curves reported in Figure 4.7 are a 5th order polynomial fit.

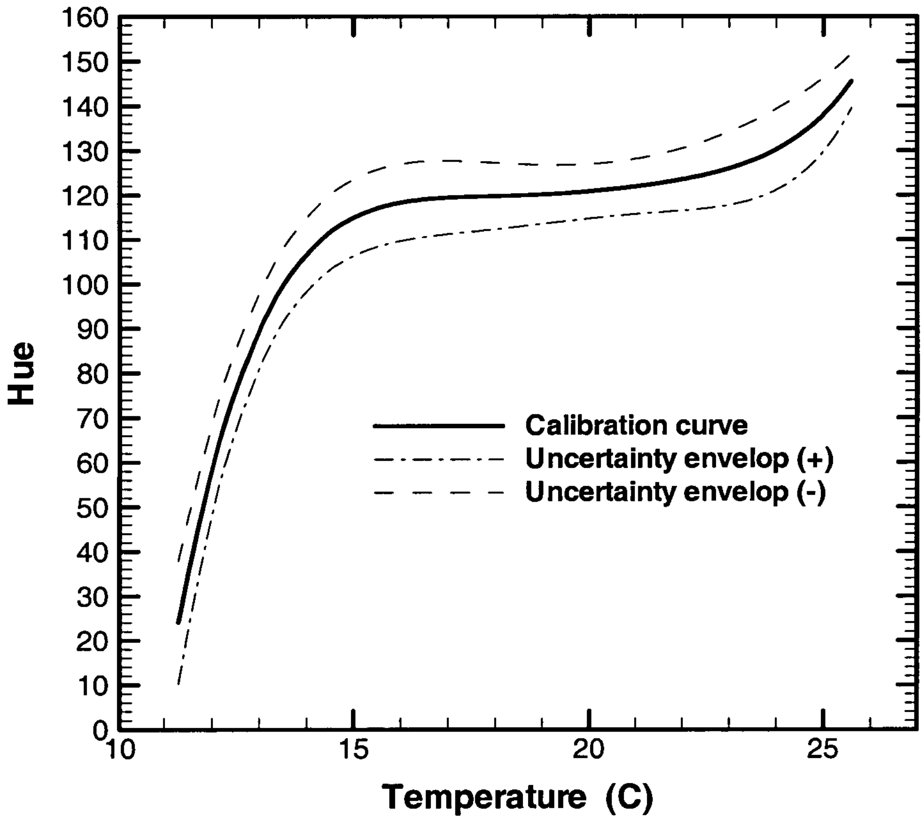

Figure 4.7 Hue-Temperature calibration chart.

Figure 4.8 reproduces the image colour of the capillary tube sample with the hue and temperature profile along the tube axis. Note that the hue profile is raw data and the tube mouth where the meniscus is evaporating is situated at the left side of the colour image (**A**). In the colour image, a few empty regions can be noted and are probably due to dust and/or air that become easily trapped into the TLC material. As can be seen from the image colour of Figure 4.8, the illumination around the sample is not uniform, essentially because of the tube's curvature. However, here we are interested in the temperature profile along the tube axis not across it and in this direction the illumination is indeed uniform. It is also worth noting from the colour image that the TLCs at the tube's left edge (**A**) appear colourless; this is probably due to the evaporating pentane inside the tube having overturned the tube edge because of its good wettability and destroyed locally the TLCs. By extracting the hue value along the axial direction (**A-B**) drawn in the colour image of Figure 4.8 and using the calibration chart of Figure 4.7, one can get the temperature along the capillary tube as indicated in Figure 4.8. Note that in Figure 4.8 only temperatures below 15.5 ˚C are accurate, as they fall in the practical usable range of the calibration chart. Despite inaccuracy, the wall temperature profile of Figure 4.8 can be divided in two regions. The first shows the important effect of convection outlined in Chapter III in the liquid close to the meniscus interface. The second linear part clearly demonstrates that there is conduction in the liquid bulk.

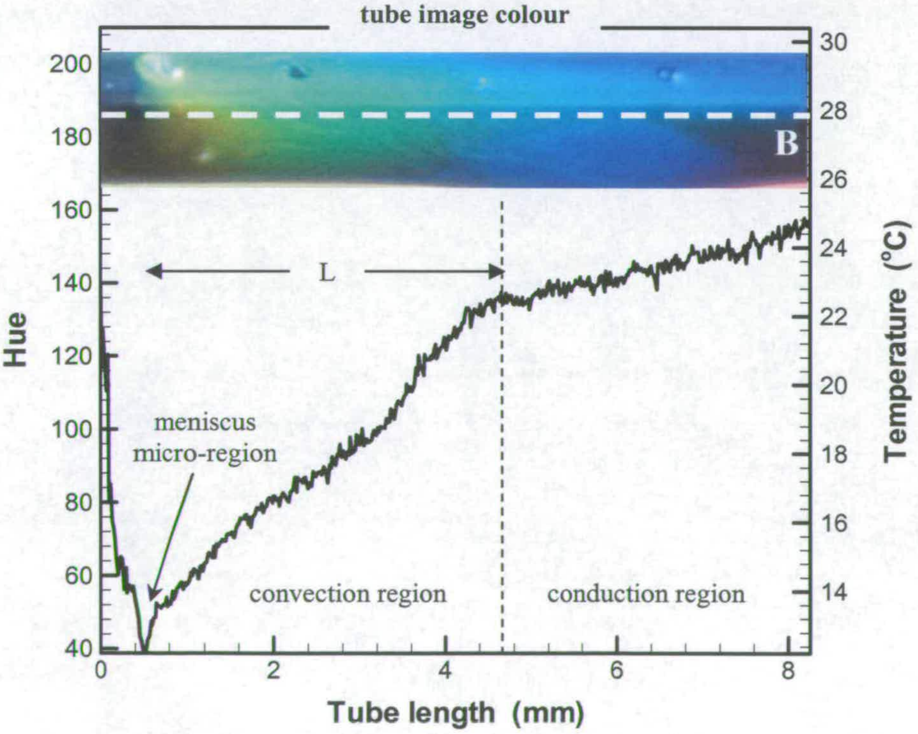

Figure 4.8 TLC colour image and inferred temperature along the capillary tube axis (**A-B**).

Figure 4.8 shows clearly the dip in temperature expected close to the tube mouth where the meniscus is evaporating. This dip in temperature is due to the evaporative cooling effect of pentane described in Chapter II being higher in the meniscus micro-region [8,22-25]. The meniscus region is usually divided into three sub-regions [22-25] as discussed in Chapter II. In Figure 4.9 the left picture is a diametrical section of the capillary tube mouth filled with pentane showing the curved meniscus interface; the inset on the right is an enlargement schematically highlighting the meniscus sub-regions. The respective lengths of the meniscus sub-regions shown are indicative only. In the adsorbed layer evaporation is prevented by strong adhesion forces. In the micro-region the adhesion forces are balanced by the capillary ones and the liquid becomes free to evaporate. Because the film thickness in this region is still small, as in the adsorbed layer, the evaporation and heat transfer coefficient in this region are at a maximum. As the film thickness continues to grow in the subsequent macro-region, the thermal resistance increases and the evaporation is therefore reduced. As numerically demonstrated by Sartre et al. [25], the heat transfer coefficient distribution forms a Dirac like peak centred in the micro-region. Through the tube's material and roundness, the black paint and TLCs thickness, the heat transfer coefficient peak is substantially diffused. The temperature profile of Figure 4.8 qualitatively proves this fact. Fortunately, the temperature dip in the present investigation is so strong (essentially because of the high liquid volatility) that is still detectable (Figure 4.8).

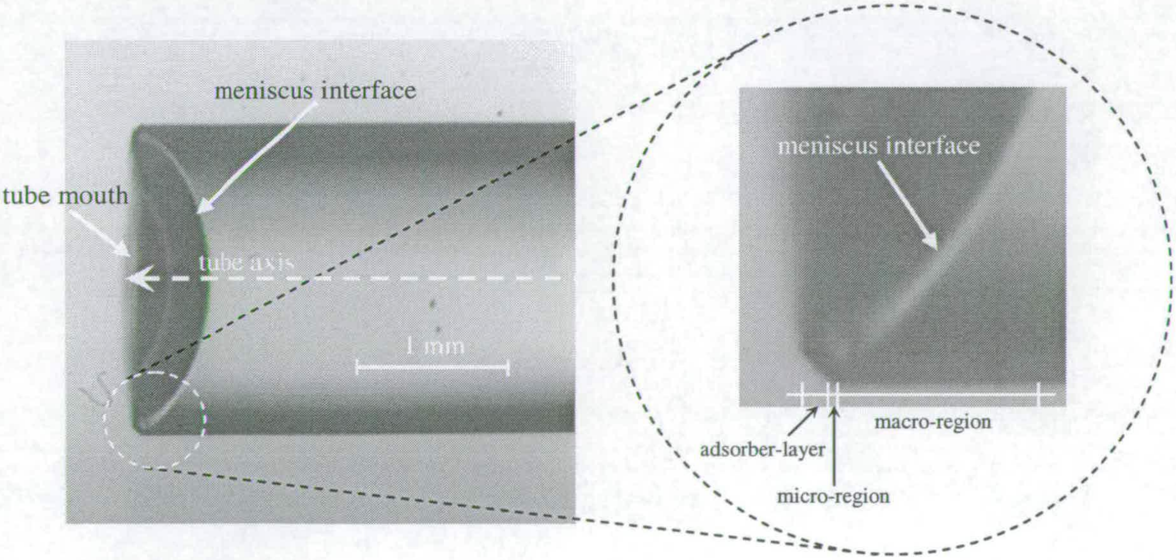

Figure 4.9 Capillary tube optical section and meniscus sub-regions (inset).

From the temperature measurement made on the tube external surface, one can infer the temperature and heat flux profile along the meniscus interface inside the tube.

A sketch showing the source of thermal resistance for the three materials encountered in the tube radial direction: liquid micro-layer, tube wall and black paint-TLCs is reproduced in Figure 4.10. The conduction heat transfer problem for the particular geometry investigated here is 2-D as will be shown later in this section, having similar values of radial and axial heat transfer rate. However, for a single order of magnitude analysis, we concentrate on the radial direction only. The thermal resistance of this material in cylindrical geometry is given by:

$$R_i = \frac{ln\left(\frac{r_{i+1}}{r_{i-1}}\right)}{2\pi k_i} \tag{4.3}$$

where k_i is the material thermal conductivity and r_{i+1} and r_{i-1} the radius of the circumferences delimiting the material i (see Figure 4.10 for sketch). The thermal conductivity of the borosilicate glass (1.12 W m^{-1} K^{-1}) is very close to that of pentane (1.48 W m^{-1} K^{-1}) and we assume that the TLCs layer and black paint thermal conductivities are also similar to these values. The thickness of the liquid micro-layer is of the order of 1 μm (Sartre et al. [25]), the tube thickness is approximately 235 μm and the TLCs with black paint thickness is of the order of 15 μm. The capillary tube diameter is 1,630 μm. Thus, clearly the largest thermal resistance is represented by the glass tube.

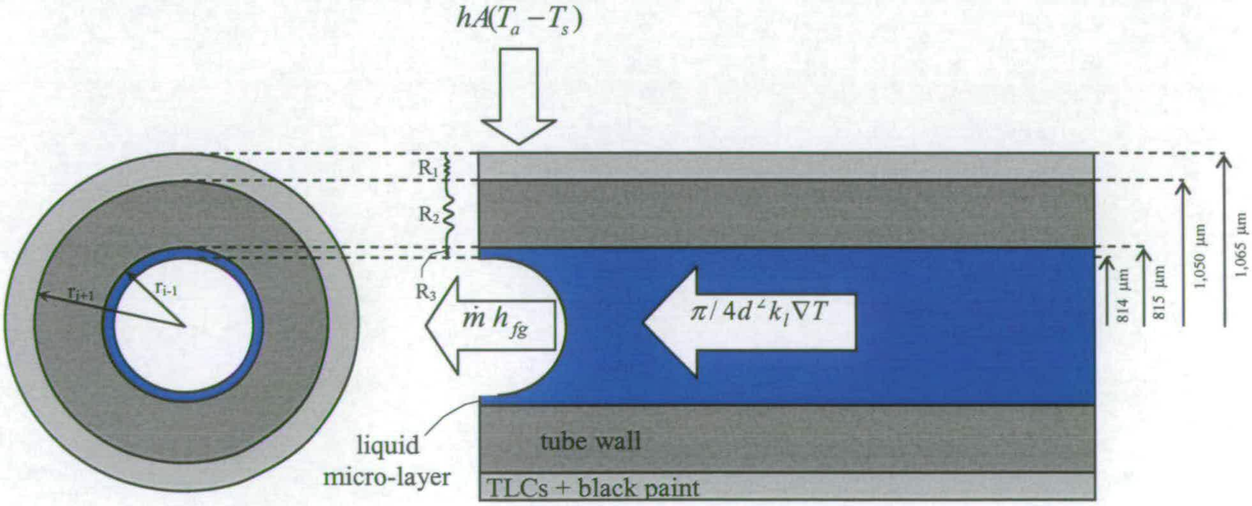

Figure 4.10 Capillary tube sections with highlighted thermal resistance and heat paths.

The heat flux at the tube-air interface along the tube axis has a profile similar to the external tube temperature one. Therefore, the profile in Figure 4.8 reflects the heat flux profile at the tube-air interface. One can approximate the temperature profile in Figure 4.8 by a Gaussian curve and express the heat flux at the tube-air interface as follows:

$$q(x)=\frac{1}{\sqrt{2\pi\alpha}}e^{-\left[\frac{(x-x_0)^2}{2\alpha}\right]} \qquad (4.4)$$

where *q(x)* is the tube-air heat flux profile, *x* is the tube axial coordinate, α is essentially the thermal resistance and x_0 is the abscise where the Gaussian is centred.

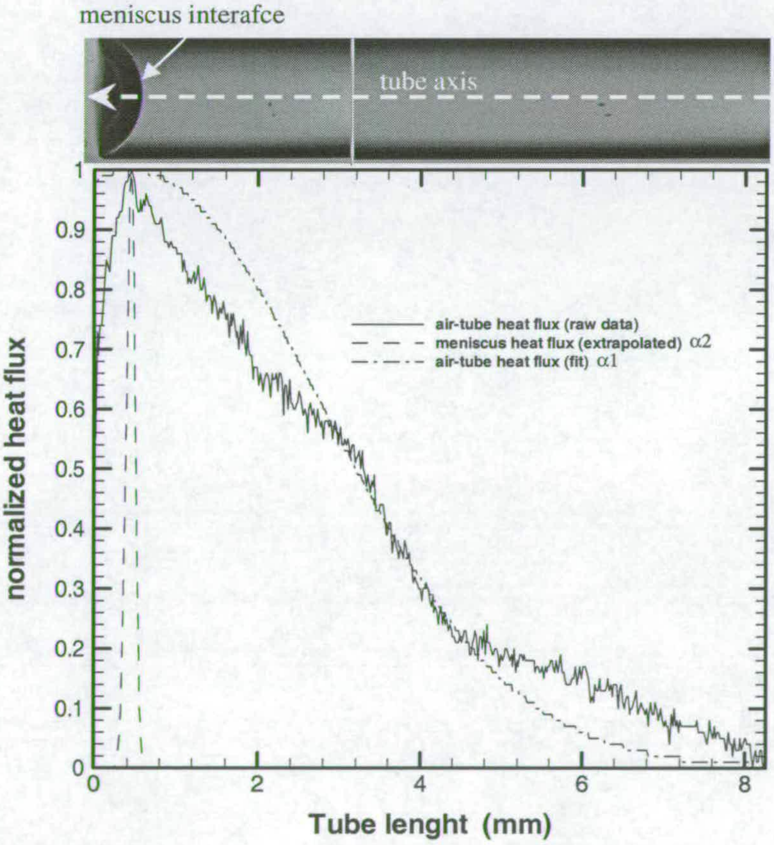

Figure 4.11 Measured axial tube heat flux and evaluated meniscus heat flux profile.

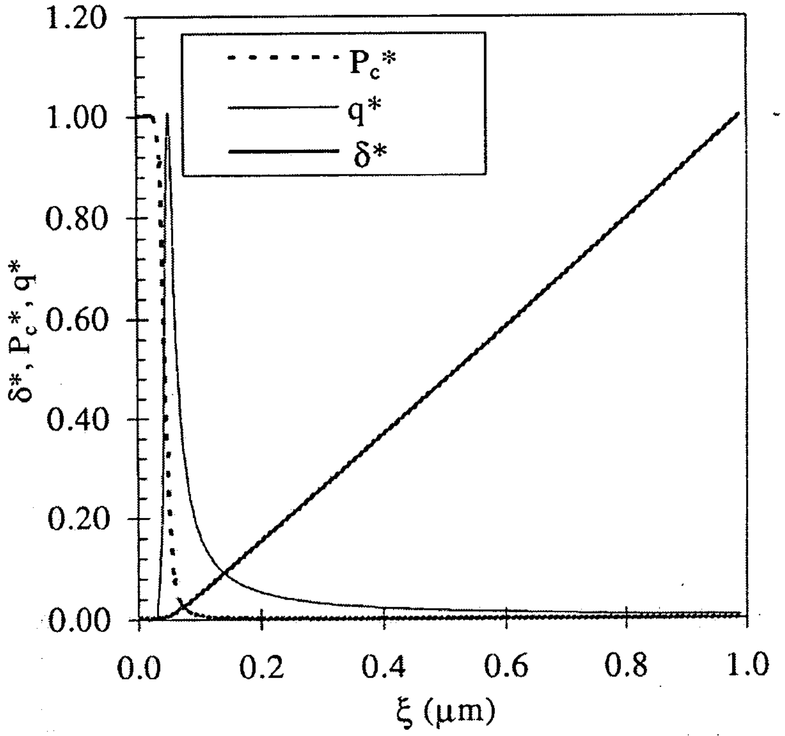

Figure 4.12 Normalized meniscus thickness (δ*), capillary pressure (Pc*) and heat flux (q*) in the meniscus micro-region. (Printed with permission from Sartre et al. [29]).

In cylindrical configurations and steady state there is uniform radial conduction: $q \cdot r = const$. The tube-air heat flux is fitted with a Gaussian of particular α_1. α_1 is then multiplied by the total thermal resistance across the three materials obtaining a new value α_2. This value is used to guess the meniscus heat flux profile as reported in Figure 4.11. Note that the curves in Figure 4.11 have been normalized. It is worth noting that the heat flux profile at the meniscus interface looks very similar to the Dirac like peak heat flux profile obtained by Sartre et al. [25] and reproduced in Figure 4.12. The heat flux profile peaks dramatically in the meniscus micro-region where most of the evaporation is taking place.

A simplified calculation follows to evaluate the micro-region temperature. As mentioned before, the heat flux multiplied by the radius is the quantity conserved as one moves along the tube in the radial direction; therefore, one can write that the heat flux at the tube-air side equals the one in the liquid layer-tube wall-TLCs systems:

$$Nu\,k_a(T_w - T_a) = \frac{(T_w - T_x)}{\sum_i \frac{ln\left(\frac{r_{i+1}}{r_{i-1}}\right)}{k_i}} \qquad (4.5)$$

with Nu the external Nusselt number, k_a the air thermal conductivity, T_w the wall temperature in correspondence of the meniscus micro-region (Figure 4.10), T_a the air temperature, K_i the material i thermal conductivity and T_x the meniscus micro-region temperature sought. For natural convection around a horizontal tube, Nu has been correlated by [26-27]:

$$Nu = \left\{ 0.6 + \frac{0.387 Ra_d^{1/6}}{\left[1 + \left(\frac{0.559}{Pr^{9/16}}\right)\right]^{8/27}} \right\}^2 \qquad (4.6)$$

where Ra_d is the Rayleigh number based on the tube diameter (d) and Pr is the Prandtl number.

Solving Eq. (4.5) gives a temperature difference T_w-T_x = 0.41 °C. So, what we measure with the TLCs is actually very close to the meniscus micro-region temperature. This estimation helps in verifying that the heat conduction is indeed 2-D for the present case. In fact, comparing the radial heat transfer rate q_r with the axial one q_x, one gets:

$$q_r = -2\pi\, r L k_w \frac{\partial T}{\partial r} \cong 1.4x10^{-3}\ W \qquad (4.7)$$

where $\frac{\partial T}{\partial r} = \frac{T_w - T_x}{r \ln\left(\frac{r_e}{r_i}\right)}$, L is the characteristic length (assumed here to be the length of the convection region in Figure 4.8), and

$$q_x = -\pi\left(r_e^2 - r_i^2\right)k_w \frac{\partial T}{\partial x} \cong 7\,\mathrm{x}10^{-3}\ \mathrm{W} \qquad (4.8)$$

where $\frac{\partial T}{\partial x}$ is evaluated from Figure 4.8 in the accurate portion of the convection region downward the meniscus micro-region (indicated by L). Comparing Equ. (4.7) and Equ. (4.8) one can conclude that the conduction in the tube wall is indeed 2-D.

The evaporation rate was also measured and therefore one can attempt here to evaluate it with the following energy balance [26,28] (see Figure 4.10 for sketch of heat flux paths):

$$q_{eva} = q_{conv} \qquad (4.9)$$

where q_{eva} is the evaporation flux (product of the evaporative mass flux $\dot{m}$ and latent heat of evaporation h_{fg}) and q_{con} is the convective heat transfer term between the tube and the surrounding environment. With respect to the model developed by Meyer [28] describing the evaporation in capillaries, here we neglect the term due to heat conduction in the liquid because it is several orders of magnitude less that the heat coming from outside the tube as will be shown shortly. Equ. (4.9) can be rewritten as:

$$\dot{m}h_{fg} = Ah\left(T_a - T_w\right) \qquad (4.10)$$

where A is the external tube surface area, T_a and T_w are the ambient and wall temperatures respectively and h is the heat transfer coefficient obtained from the Nu:

$$h = \frac{k_a}{d} Nu \qquad (4.11)$$

In Equ. (4.10) $\dot{m}$ can be expressed as:

$$\dot{m} = \int_0^{x_*} \left[2\pi\, r\, h(x)\ (T_a - T_w)/h_{fg}\right] dx \qquad (4.12)$$

where x is the distance along the tube axis. By reading the wall temperature in Figure 4.8 and numerically evaluating the integral in Equ. (4.12) one gets:

$$\dot{m} = 3.18 \times 10^{-5} \, \mathrm{g\,s^{-1}}$$

This value of evaporation mass flux is very close to the one measured ($\dot{m}_{meas} = 3.24 \times 10^{-5} \, \mathrm{g\,s^{-1}} \pm 5\%$). It is worth noting that the assumptions made with Equ. (4.9) (no radiation is considered) and the model adopted in Equ. (4.6) result in the evaluated mass flux being underestimated. However, the estimated evaporation mass flux falls in the range of the measurement uncertainties of ±5%. The contribution given by the conduction in the liquid bulk would have been about 8.3×10^{-13} g s^{-1}. Therefore, for the steady state, it can be concluded that the heat transfer necessary to sustain evaporation comes indeed from the environment external to the tube.

The present experimental investigation backs up the finding of Höhmann and Stephan [8] where unsealed TLCs have been used to map the temperature of a heated evaporating meniscus of water. Höhmann and Stephan [8] stated that in their experiment a spatial resolution of 0.83 μm has been achieved for the unfiltered spot. The unsealed TLCs spatial resolution is limited by the wavelength of visible light reflected from the TLC coating. In colder regions the wavelength of reflected light is at the upper portion of the visible spectrum (460 - 750 nm), therefore the inherent physical limitation of TLCs has been almost reached by Höhmann and Stephan [8]. With the experimental apparatus employed in the present study, the spatial resolution reached was of 16.19 μm and no attempt was made to prove the finding of Höhmann and Stephan [8] in terms of achievable spatial resolution because of the thermal diffusion experienced in the present case through the tube wall.

4.5 Conclusions and outlook

The present experimental study has proved the feasibility of using unsealed TLCs for measuring the temperature close to the contact line region of an evaporating meniscus formed in a confined environment such as a capillary tube. The evaporation of a liquid in confined space is the basic mechanism found in many heat transfer devices such as Heat Pipes and Capillary Pumped Loops, where the capillary forces become important. It is well established that the heat and mass transfer in such configurations (as boiling and drops) is strongly controlled by what happens near the meniscus contact line. Gathering experimental information on microscale applications is of paramount importance for the design and improvement of efficient and powerful micro-system cooling devices employing phase changes. Unsealed TLCs have been applied externally to a glass capillary tube inside which pentane was allowed to evaporate. The strong evaporation near the meniscus contact line region leads to a reduction of the meniscus interfacial temperature that, because of the small thickness of the meniscus micro-region and thermally conductive glass wall, is detectable on the tube external wall temperature. The important temperature dip in the meniscus micro-region is still detectable as demonstrated in this experimental study, despite the thickness of the tube (235 μm), its geometry, and the TLCs with black paint thickness (~15 μm) all contribute in broadening this information substantially.

Certainly, more work is needed to perform firstly: accurate temperature measurements using TLCs with different active colour band, and, secondly: a systematic investigation using more liquids and various tube sizes as well as different tube materials, but this is beyond the scope of the present investigation and is left open for future research in the area.

The present TLC investigation is a benchmark experiment for the following IR more systematic and accurate study. Both TLC and IR are indirect methods of measuring temperature and if a sort of agreement is found between the two there will be more confidence in the temperature measurements carried out.

4.6 References

[1] Shevell S. K., 2003, *The science of color*, 2nd Edition, Optical Society of America, New York.

[2] Collings P.J. and Hird M., 1997, *Introduction to liquid crystals*, Taylor & Francis, London.

[3] Elston S. and Sambless R., 1998, *The optics of Thermotropic Liquid Crystals*, Taylor & Francis, London.

[4] Hay J.L. and Hollingsworth D.K., 1996, *A Comparison of Trichromic Systems for Use in the Calibration of Polymer-Dispersed Thermochromic Liquid Crystals*, Experimental Thermal and Fluid Science, Vol. 12, pp. 17-12.

[5] Farina D.J., Hacher J.M., Moffat R.J. and Eaton J.K., 1994, *Illuminant Invariant Calibration of Thermochromic Liquid Crystals*, Experimental Thermal and Fluid Science, Vol. 9, pp. 1-12.

[6] Parsley M., 1991, *The Hallcrest Handbook of Thermocromic Liquid Crystal Technology*, Hallcrest, Glenvien, IL.

[7] Baughn J.W, Anderson M.R., Mayhew J.E., Wolf J.D., 1999, *Hysterisis of thermocromic liquid crystal temperature measurement based on hue*, ASME Journal of Heat Transfer, Vol. 121, pp. 1067-1072.

[8] Höhmann C., Stephan P., 2002, *Microscale temperature measurement at an evaporating liquid meniscus*, Experimental Thermal and Fluid Science, Vol. 26, pp. 157-162.

[9] Klein E.J., 1968, *Application of liquid crystals to boundary-layer flow visualization*, AIAA paper 68-376.

[10] Cooper T.E., Field R.J. and Meyer J.F., 1975, *Liquid Crystal Thermography and Its Application to the Study of Convective Heat Transfer*, Journal of Heat Transfer, Vol. 97, pp. 442-450.

[11] Rhee H.S., Koseff J.R. and Street R.L., 1984, *Flow visualization of a recirculating flow by rheoscopic and liquid crystal techniques*, Experiments in Fluids, Vol. 2, pp. 57-64.

[12] Cooper T.E. and Groff J.P., 1973, *Thermal Mapping, via Liquid Crystals, of the Temperature Field near a Heated Surgical Probe*, Journal of Heat Transfer, Vol. 95, pp. 250-256.

[13] Cooper T.E. and Petrovic W.K., 1974, *An Experimental Investigation of the Temperature Field Produced by a Cryosurgical Cannula*, Journal of Heat Transfer, Vol. 96, pp. 415-420.

[14] Azar K., Benson J.R and Manno V.P., *Liquid crystal imaging for temperature measurement of electronic devices*, Proc. of the Semiconductor Thermal Measurement and Management Symposium, 7th Annual IEEE, 12-14 Feb. 1991, Phoenix, AZ, USA.

[15] Kenning D.B.R., 1992, *Wall temperature pattern in nucleate boiling*, Int. Journal Heat and Mass Transfer, Vol. 35, No. 1, pp. 73-86.

[16] Kenning D.B.R., 1992, *Liquid crystal thermography as a tool for investigating the development of boiling*, Engineering Foundation Conference on Pool and External Flow Boiling, Dhir and Bergles Ed., Santa Barbara, pp. 79-82.

[17] Kenning D.B.R. and Yan Y., 1996, *Pool boiling heat transfer on a thin plate: features revealed by liquid crystal thermography*, Int. Journal Heat and Mass Transfer, Vol. 39, No. 15, pp. 3117-3137.

[18] Parker R., 1973, *Transient surface temperature response of liquid crystal films*, Mol. Crystals Liq. Crystals, Vol. 20, pp. 99-106.

[19] Ireland P.T. and Jones T.V., 1987, *The response time of a surface thermometer employing encapsulated thermochromic liquid crystals*, J. Phys. E: Sci. Instrum., Vol. 20, pp. 1195-1199.

[20] Herold W., Wiegel D., 1980, *The Effect of Layer Instabilities on Liquid Crystalline Thermography*, in Advances in Liquid Crystal Research and Applications, L. Bata Edition, Pergamon Press, Oxford, pp.1247-1254.

[21] Herold W., Wiegel D., 1980, *Problems of the Photographic Documentation of Liquid Crystalline Thermographs*, in Advances in Liquid Crystal Research and Applications, L. Bata Edition, Pergamon Press, Oxford, pp.1255-1259.

[22] Potash J.M. and Wayner J.P., 1972, *Evaporation from a two-dimensional extended meniscus*, International Journal of Heat and Mass Transfer, Vol. 15, No. 3, 1851-1863.

[23] Wayner J.P. and Tung C., 1985, *Experimental Study of Evaporation in the Contact Line Region of a Thin Film of Hexane*, Journal of Heat Transfer, Vol. 107, pp. 182-189.

[24] Potash J.M. and Wayner, J.P., 1972, *Evaporation from a two-dimensional extended meniscus*, International Journal of Heat and Mass Transfer, Vol. 15, No. 3, pp. 1851-1863.

[25] Sartre V., Zaghdordi M.C. and Lallemand M., 2000, *Effect of interfacial phenomena on evaporative heat transfer in micro heat pipes*, International Journal Thermal Science, Vol. 39, pp. 498-504.

[26] Incropera F. P. and DeWitt D. P., 1996, *Fundamentals of heat and mass transfer*, 4th Edition, John Wiley & Sons, New York.

[27] Churchill S. V. and Chu H. H. S., 1975, *Correlating Equations for Laminar and Turbulent Free Convection from a Horizontal Cylinder*, International Journal of Heat and Mass Transfer, Vol. 18, pp. 1049-1053.

[28] Meyer R. E., 1984, *Note on evaporation in capillaries*, IMA Journal of Applied Mathematics, Vol. 32, pp. 235-252.

CHAPTER V

Interfacial and tube wall temperature measurements during phase change in confined environment with the use of Infra Red Thermography

5.1 Motivation

As shown in Chapter IV, TLCs have allowed us to measure the temperature on the wall for an evaporating meniscus inside a capillary tube. This is of great importance because it is not trivial to measure temperature at such a small scale and because it is shown that there is indeed an important sink effect close to the meniscus triple line where most of the evaporation is taking place. Despite this important achievement, there is still one crucial piece of information needed: the temperature profile along the meniscus interface. In order to achieve that, we are faced not only with the small scale involved, but with a liquid interface. Even the smallest thermocouple available would disrupt the meniscus interface and lead to useless measurements. Therefore, mapping the temperature could be done only with a non-contact non-destructive test technique. Microencapsulated TLCs could be used in this case dispersed in the liquid, but the large size of the capsules (50-100 μm) and the low resistance to aggressive environment like the alcohols we are using here, make this possibility a very remote one. Infra Red (IR) technique could be a suitable solution to these problems. In the past this technique has been used to measure surface temperature of liquids, but in the present case the geometrical configuration makes things slightly more difficult. The meniscus interface is curved and the emissivity problem of a multi media system (tube wall and liquid) must be solved. Despite these and more difficulties faced during the experiment, IR has proven a powerful tool to measure absolute temperature of an evaporating meniscus in a capillary tube.

In this work, an IR camera has been used to map the temperature on the meniscus interface formed when capillary tubes of various size (ranging from 600 to 1,630 μm) were filled with volatile liquids (ethanol, methanol, acetone and pentane). Important information on temperature near the meniscus triple line have been gathered and some conclusions drawn on the effect of the tube size and liquid volatility. An explanation is also proposed for the asymmetry in the meniscus vertical temperature profile found. This asymmetry could have a potential impact in all those important industrial applications involving phase change such as crystal growth, glass manufacture and stem cell culture.

In addition, the IR technique has been also used to map the wall temperature of the heated capillary tubes. The fast and simple setup of the technique is generally preferred to the time consuming TLCs one. On top of this, the impressive range of temperature covered by the IR cameras used (from -20 to 2,000 °C) makes it very easy to analyze situations such as the ones with an extra heating provided when large temperature variations are expected.

5.2 Background

Interfacial temperature is a key factor in the phase change process, especially at small scales. The access to the interface temperature at the micro-scale has been a challenging task. Recently Fang and Ward [1] have investigated the cooling effect resulting from the evaporation of water in a reduced pressure environment by using micro-thermocouples near the interface. They show an increase in the cooling effect with the increase in the evaporation mass flux. They also show an important experimental result that is in contrast with classical kinetic theory and non-equilibrium thermodynamics. The temperature in the vapour phase is higher than in the liquid phase and the temperature difference is greater than expected from both the classical kinetic and non-equilibrium thermodynamic theories. It is surprising that with the thermocouple used (the smallest one of 80.3 μm diameter) they are able to read temperature within 30 μm from the interface. This study clearly shows that there is an important need for more experimental results in this area. Despite this attempt, the acquisition of information near the meniscus triple line remains quite difficult also because of the small size and curved shape of this region with high spatial temperature changes.

IR thermography has been used coupled with a high-speed camera (the latter to reveal the flow pattern), for local heat transfer measurement of mini and micro channels by Hetsroni et al. [2-3]. IR thermography is also used for local heat transfer measurement in complex geometry like plate finned tube heat exchangers as described in Herchang et al. [4], detecting transition and separation regions of the boundary layer that strongly influence the heat transfer for such applications. Because of the fast time response, one IR technique is successfully applied also to study boiling (see Sgheiza and Myers [5] and Theofanous et al. [6]).

During the last two decades different types of IR cameras have been developed in order to meet the needs of always more demanding applications and reducing the price and size of the equipment. It must be pointed out that most of the effort made in this area is for military application where detecting objects of a certain nature and/or live organisms in the dark is crucial. Here, we will summarize some of the most important features devoting particular attention to the IR cameras used for the present experimental investigation. More detailed and exhaustive information on different technologies can be found in Rogalski [7], Rainieri and Pagliarini [8], Horny [9] and Kaplan [10]. The most important part of the IR camera is indubitable the detector. There are two technological solutions: single and multi detector. The cameras used for this work were a single and a multi detector one. In single detector cameras a rotating prism, scanning the field of view line-by-line, records the flux emitted by the object on the single detector that is therefore heavily loaded; moreover, the scanning mechanism introduces some noise in the system (Kaplan [10]). Focal Plane Array (FPA) IR cameras have lowered the price, raised both the resolution and the sensitivity of IR thermography compared to the single detector technology (Rogalski [7]). The drawback is that the detectors on the matrix receive an unwanted heat flux from the surrounding objects in the ambient and from the detectors themselves (i.e., the detectors at the edge of the matrix receive more than those in the middle) as pointed out in Ranieri and Pagliarini [8] and Horny [9]. Besides, in FPA cameras there is no internal temperature reference, like in the single detector thermal scanner, to which the signal is constantly compared (Ranieri and Pagliarini [8] and Horny [9]). These two limitations could make of the FPA technology a useless tool for quantitative analysis in heat transfer studies where accuracy is among the crucial requirements. In the single detector a cold shield (at around 70 K) is placed in front of the detector in order to remove all the unwanted flux not coming from the object under investigation. This low temperature can be kept by the use of Peltier elements or liquid nitrogen. Because of its temperature, the flux produced by the cold shield can be neglected with respect to the incoming flux from the object. In the array detectors the cold shield is also used but does not remove entirely the unwanted flux; in particular, the flux produced by the ambient inside the camera between the detector array and the lenses. In IR cameras for quantitative measurement, a temperature sensor is placed on the lenses in order to correct this effect. As outlined in Ranieri and Pagliarini [8], the FPA cameras can successfully be used for quantitative measurement only if they are calibrated frequently.

Whatever the detector technology is, the spatial resolution achievable with IR cameras (~10 μm) is still far from the unsealed Thermochromic Liquid Crystals (~1 μm) (Höhmann and Stephan [11]), but roughly one order of magnitude better than microencapsulated (Farina et al. [12]) and polymer dispersed (Hay and Hollingsworth [13]) TLCs (~50-100 μm) as discussed in Chapter IV. On the other hand, we have also seen in Chapter IV that working with TLC is still quite time consuming especially because of the necessity of an *in situ* calibration. Besides, the time response of IR cameras with photon detectors is of the order of micro-seconds as shown by Conn and Avery [14] (because radiation travels at the speed of light),whereas the time response of TLCs has been evaluated to be in the range between a few and hundreds of milliseconds (Parker [15] and Ireland and Jones [16]).

5.3 Experimental technique and setup

The IR technique is the most advanced non-contact and Non Destructive Test (NDT) method. The IR method of measuring temperature is based on the fact that all objects, above absolute zero, emit infrared, radiant heat, at a rate that is directly related to the temperature of the object. The IR sensor detects the wavelength of the energy emitted by an object and by the use of integral equations, the temperature can be obtained once the body material and surface quality are known. One important thing to point out is that in the present investigation a microscope lens is needed. It is recognised that there are a few affordable materials (still quite expensive) transparent to IR radiation like germanium and zinc selenide, and all lenses must be made of these materials to work with IR cameras. Therefore, as will be shown in the present study, it is acceptable to use only a portion of the detector array, because of a non appropriate lens dimension.

The radiant energy incident on a surface is partially reflected, partially absorbed and partially transmitted through the material. If we call r, a and t the ratio of the energy reflected, absorbed and transmitted to the total incident energy, one gets:

$$r(\lambda) + a(\lambda) + t(\lambda) = 1 \qquad (5.1)$$

Reflection, absorption and transmission for a material depend on the radiation wavelength (λ). The surface of an object is really important in determining the reflection from it. A special body that has $a = 1$ and $r = t = 0$ at all wavelengths is called black body. A body does not only absorb radiation, but also emits it. Usually good absorbers are also good emitters. Emissivity is defined as the ratio of the body radiant energy to the black body one. Usually absorption (a) and emission (ε) are a function of temperature and the body's nature as well as wavelength. The Kirchhoff principle states that the ratio between emission and absorption for a body is only a function of temperature and wavelength:

$$\varepsilon = F(\lambda,T,B), \quad a = G(\lambda,T,B), \quad \varepsilon/a = \Phi(\lambda,T) \qquad (5.2)$$

The emission coefficient for a black body is called ε_0. Grey bodies are those which emit radiation with the same spectral distribution as a black body but of reduced intensity; i.e. grey bodies have a lower emission coefficient. Therefore, knowing ε_0,the Kirchhoff principle allows us to get the emission or absorption of a grey body once the other of these two is known. Selective emitters are those with an emissivity that is a function of the wavelength. For selective emitters spectral emission ($\varepsilon(\lambda)$) is not equal to total emission (emissivity). Gray bodies are those with equal spectral and total emission.

The Stefan law of radiation for a black body is:

$$q_0 = \int_0^\infty \varepsilon_0 d\lambda = \sigma_0 T^4 \qquad (5.3)$$

where q_0 is the total radiant heat flux from the black body. The black body spectral emission ε_0 is given by the Plank law:

$$\varepsilon_0(\lambda,T) = \frac{C_1}{\lambda^5\left(e^{\frac{C_2}{\lambda T}} - 1\right)} \qquad (5.4)$$

where C_1 and C_2 are the Coblentz constants. The Wien law states that the Plank emission coefficient has a maximum given by:

$$\lambda_{Max} = \frac{A}{T} \qquad (5.5)$$

where A = 2,880 µm K. The Wien law says that this maximum shifts to the lower wavelengths when increasing the temperature. Figure 5.1 gives the emission curves for a black body at different temperatures. Clearly, the Wien law is noticeable.

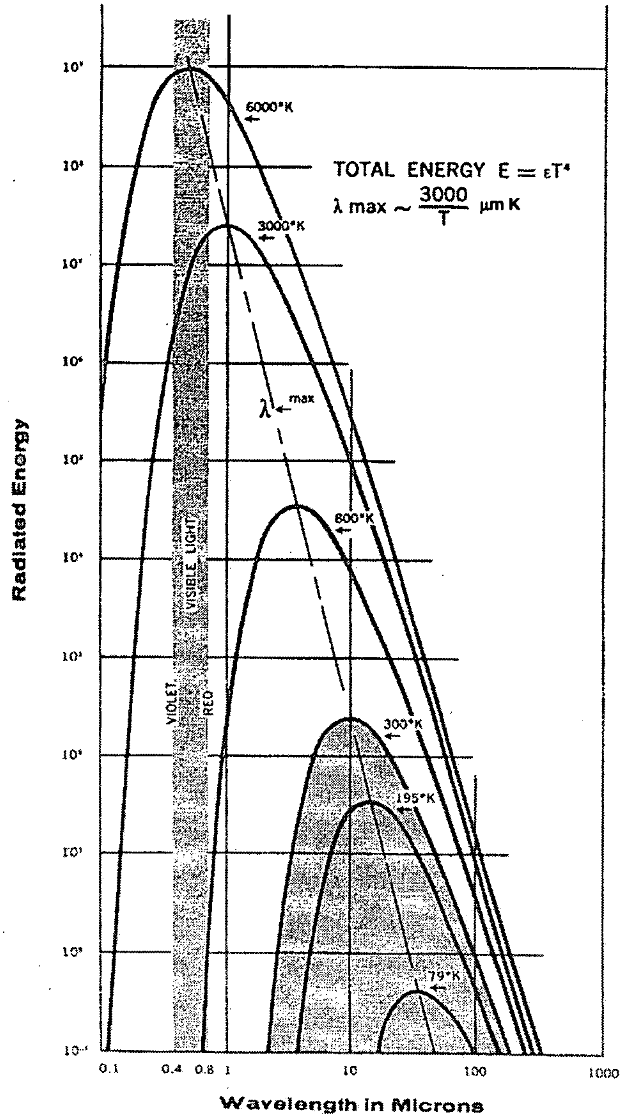

Figure 5.1 Radiated energy from blackbody source (from Kaplan [10]).

What the IR camera measures is the heat flux emitted by a body. By this measurement and knowing the body emissivity and surface characteristics, one can infer the body temperature.

When the emissivity of a body is low ($\varepsilon = 0.1$), as for metals, and its temperature is close to ambient, it is very likely that the IR camera will detect the transmitted and reflected components characteristic of the ambient surrounding the object. In order to avoid this, it must be remembered that the radiant heat flux is proportional to the fourth power of temperature; therefore, the ambient could be masked if the body temperature is sufficiently above ambient. This is the reason why it is common practice to mount the object whose temperature must be measured, on a thermoelectric stage set at a temperature above 50-60 °C [17] sufficiently higher than ambient temperature (~25 °C). A pixel-by-pixel emissivity calculation necessary for those applications involving micro-chips for instance (made with different materials with large variation of emissivity between these materials) can be performed by powering the thermoelectric stage at two temperatures well above the ambient and measuring the radiant heat flux [17].

The advantages and disadvantages of the IR technique can be found in specialised books such as Kaplan [10] and will not be repeated here. However, it must be said that the strong advantages for the present application are due to the quite small target size to be analysed and the great spatial resolution achievable with IR cameras.

Two different IR cameras are used for two different studies. In the first investigation the principal objective was to measure the interfacial temperature of an evaporating meniscus formed in horizontally oriented capillary tubes; and, for this case the FLIR ThermaCAM SC3000 system was used. The second study's principal objective is to measure the tube wall temperature for vertically oriented capillary tubes controlling the relative meniscus position with respect to the heating element as also done with the μ-PIV investigation of Chapter III; for this study, the Agema 880 system was employed.

5.3.1 Horizontally oriented capillary tubes

The IR camera used within one of the IR studies is the FLIR ThermaCAM SC3000 that has a thermal sensitivity of 20 mK at 30 °C, an accuracy of 1% or 1 K of full scale for temperatures up to 150 °C and 2% or 2 K of full scale for temperatures above 150 °C. The GaAs, Quantum Well Infrared Photon FPA detector has a spectral range of 8 to 9 μm centred in one of the two atmospheric "windows" with a resolution of 320x240 pixels and is Stirling cooled to 70 K. The system provides for automatic atmospheric transmission correction of temperature based on the input distance from the object, atmospheric temperature and relative humidity. The field of view at minimum focus distance (26 mm) is 10x7.5 mm and the Instantaneous Field Of View (IFOV) is 1.1 mrad. A continuous electronic zoom (1-4 times) is also provided. The system can acquire images in real time or at high speed (up to 750 Hz) with a reduction of the picture size so that each frame contains more than one image. The images acquired are transferred to a dedicated PC with a special built in ThermaCAM research software (by FLIR System). The spatial resolution of the system depends essentially on the IR camera spectral range (8 to 9 μm for the camera used), the IFOV of the camera and the microscope lens. However, the limit of the camera spectral range and the IFOV cannot be lowered whatever the lens magnification is. In fact, the Sparrow Criterion (that is more demanding than the well known Rayleigh Criterion) states (see Payne [18]):

$$d_{sep} = \frac{0.5\lambda}{NA} \tag{5.6}$$

where d_{sep} is the minimum separation distance (resolving power or spatial resolution), λ is the wavelength of light and NA is the numerical aperture of the microscope objective. The microscope objective NA is limited to 0.95, without oil immersion. A long-distance objective (like the one used in the present case) further limits the NA. It is reasonable to assume a NA of 0.5 that makes the spatial resolution the same as the wavelength λ. The Sparrow Criterion is a physical limit and therefore does not depend on magnification. Increasing the magnification will make the blurred image appear larger but not less blurred. The IFOV, defined as the "angular projection of the detector element at the target plane" (from Kaplan [10]), of the camera is 1.1 mrad, which leads to an image spatial resolution of 31.25 μm for the focus distance of 26 mm. Although the camera can resolve ~10 μm, the microscope lens ultimately further limits the spatial resolution.

Figure 5.2 shows a sketch of the experimental setup for the first sets of experiments. The apparatus consists of the IR camera and a microscope lens (1) with a dedicated PC (2) for acquisition, equipped with specialized software for image analysis. The capillary tube (3) is positioned on a two-dimensional micro-stage positional system (4). The IR camera is mounted on a tripod with refined adjustable height. The capillary tubes were positioned horizontally on the stage. Once the capillary tube has been focused by the use of the micro-stage, a further adjustment is made with the electronic focus of the camera. An IR image of the empty tube has been taken and the tube was subsequently filled with the liquid from the opposite end. Particular care has been taken during the filling procedure in order to avoid the tube moving before a second IR image with the filled tube being taken, making useless the subsequent IR image subtraction operation. After initial filling, the tube is no longer recharged to account for the mass lost during evaporation as done in Experiment (2) described in Chapter III.

Case (1)

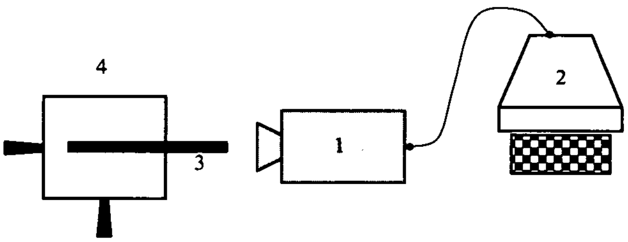

Case (2)

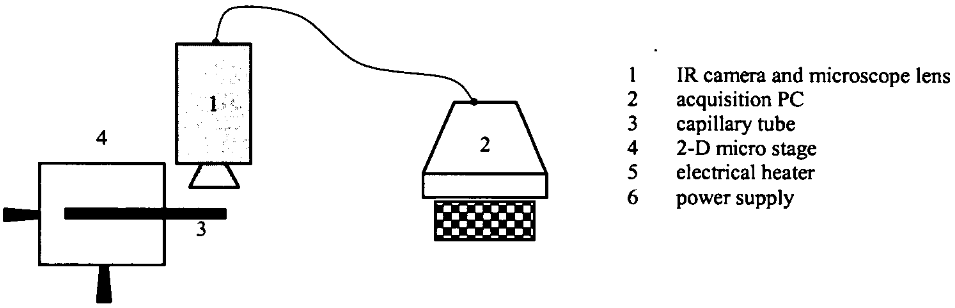

Case (3)

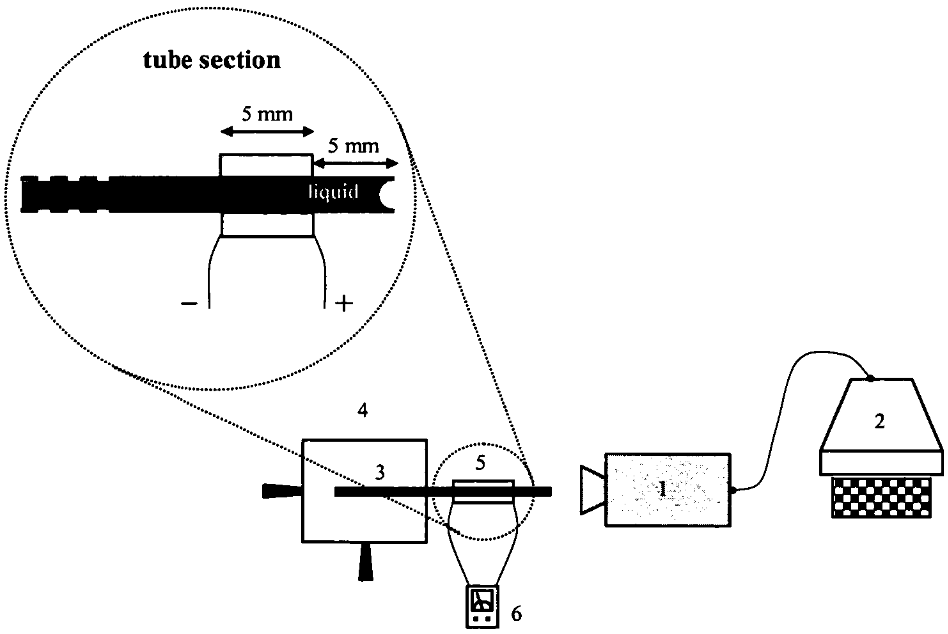

Figure 5.2 Sketch of the experimental setup (top view) for IR investigation with the use of FLIR ThermaCAM SC3000 camera.

Three different tube sizes (600, 900 and 1,630 μm diameter) and four liquids (ethanol, methanol, acetone and pentane) were investigated. Three sets of experiments have been performed for each liquid and size (see Figure 5.2). In Case (1), the IR camera was pointed at the capillary tip along the capillary axis. In Case (2), the IR camera was pointed to the capillary side. This experiment is carried out with the aim to back up the findings of Case (1). In fact, in Case (1) the target is formed by three different media: air outside the tube (that should be transparent to IR); the capillary tube; and the liquid. The tube and liquid have different emissivity and in addition reflection can take place on the solid surface. Different emissivity values can be set with the IR system used for different regions of the IR map. An accurate emissivity for the used liquids is difficult to obtain from the literature. The assumption adopted in this work is to consider the same emissivity for all the liquids used. The author is aware of the potential inaccuracy in the measured temperature; however, this will have no effect on the temperature profile. This latter and its trend are the most important parameters being investigated in this study. In addition, it is well know that IR systems are built and work extremely well to detect temperature differences. When it comes to temperature, instead, the readings become less precise as the emissivity of a target is a very sensitive parameter depending on many factors. It would have made more sense to measure the emissivity spectral composition $\varepsilon(\lambda)$ of all liquids and tubes used, but this was not done in this study as the principal objective here is to measure temperature differences instead of absolute temperature. An IR image subtraction technique is proposed here as will be described in more detail in the next section to overcome the reflection problem. In Case (2), the target is composed only by the solid tube and the transparent surrounding air. For each IR image taken, two sections have been made: horizontal and vertical. The capillaries were also heated using a heater (as sketched in Case (3) on Figure 5.2) built by depositing a thin layer of silver coating on the external tube surface. The purpose of this experiment is to demonstrate that in spite of the extra heating provided compared to the previous configurations, the temperature profile along the meniscus interface is altered but not inverted as the heater lies in the liquid side of the meniscus (this is also shown in Chapter III). The temperature at the meniscus triple line, where most of the evaporation takes place, remains always less than the one at the meniscus center. This case is also important for application purposes (heat pipes, for instance) where a liquid evaporates inside a heated wick porous structure. The heater was powered with a DC power supply and the power was raised step-by-step till the onset of boiling was observed. The meniscus was positioned at the capillary mouth above the heater position. The aim of Case (3) is to see how the temperature profile induced by evaporation along the meniscus interface changes with the external heat power applied.

The meniscus interface is not flat, therefore a view factor is usually employed to account for the radiant heat change with the angle of view between the IR sensor and the target. Because the difficulties in measuring the angle of view are increased by the important optical distortion through a small, thick and round tube, no attempt is made here to account for the view factor. However, it is believed that the conclusions reached are not dramatically affected by the view factor as the meniscus contact angle has similar values for all investigated cases.

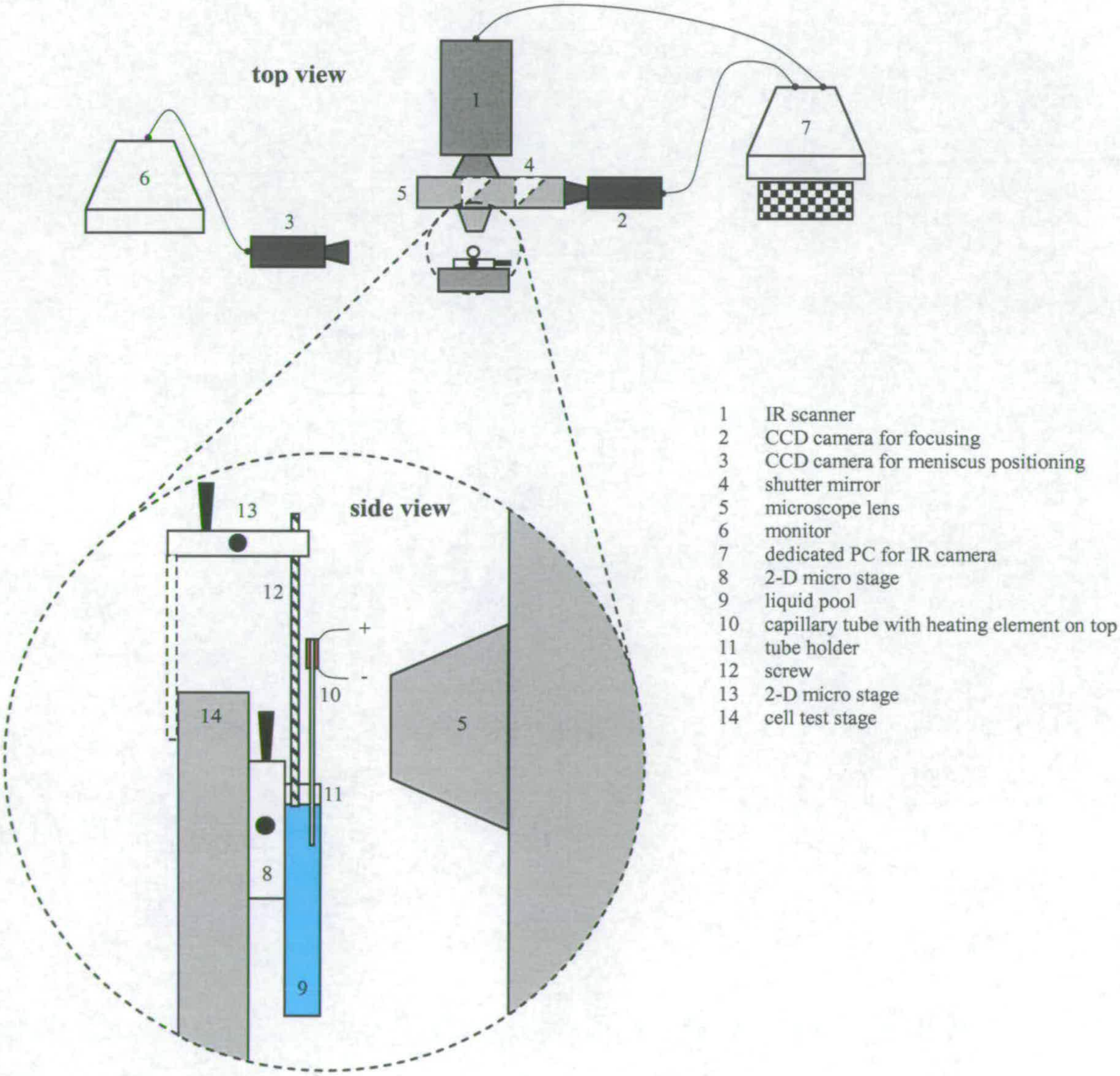

Figure 5.3 Experimental layout for IR measurements with the use of Agema 880 system.

5.3.2 Vertically oriented capillary tubes

The layout for the second experiment is sketched in Figure 5.3. The IR camera is an Agema 880 model mechanically scanned line by line and cooled to 70 K by liquid nitrogen. The IR detector is a MCT (Mercury, Cadmium, Telluride) based on the SPRITE (Signal Processing In The Element) technology widely used in the top grade military applications. The scanner has two internal blackbody reference sources scanned 2,500 times per second. This leads to an accuracy of ±2% of the full scale for temperature below 2000 °C and a superb sensitivity of 0.07 K at 30 °C. The microscope attached to the camera allows for a target size of 1.4x1.4 mm. The camera array is of 140x140 pixels leading to an optical spatial resolution of 10 μm. However, the IR camera works in the long wavelength band of the spectrum (8-12 μm), therefore the spatial resolution expected coincides with this latter physical limit of the camera. A CCD camera is used to first optically focus the specimen with the help of tiny fibre optic. The shutter mirror then shuts off the camera, the fibre optic are turned off and the IR scanner is allowed to see the target. A final adjustment is made before any measurement is taken essentially because the optical focus does not exactly coincide with the IR one. A third CCD camera connected to a monitor is used to adjust the meniscus at the wanted position in the tube acting with the two micro-stages (8 and 13 in Figure 5.3) either on the liquid pool or the screw (see Figure 5.3). The tube is vertically immersed in a pool of liquid as also described in Chapter III and the liquid is allowed to rise inside the tube above the liquid level into the pool under capillarity action. A matt black paint is deposited longitudinally on the quarter of the capillary tube pointing to the IR scanner, the other part of the tube being transparent to visualise the meniscus position with the third positioning CCD camera. This black paint is used because from the smooth external tube surface there could be a non negligible reflection and there is a real possibility that the IR scanner detector sees itself. In addition the emissivity of the target can be set with confidence to 0.99 with the paint. Because of the thin black coating (~5-10 μm) with respect to the tube diameter, we can neglect its thermal resistance and assume that the temperature read is the tube one. IR images and movies (at 750 Hz) can be viewed on a monitor where a quick post-processing is possible; storing is also allowed. The images are then transferred to a dedicated PC for full post-processing made with a special built in software (by FLIR Systems).

5.4 Results and analysis

Firstly the results of the horizontally positioned tubes investigated with the use of the FLIR ThermaCAM SC3000 camera will be described and analyzed and then we will describe the experiments performed on the vertically oriented capillaries using the Agema 880 camera.

5.4.1 Horizontally oriented capillary tubes

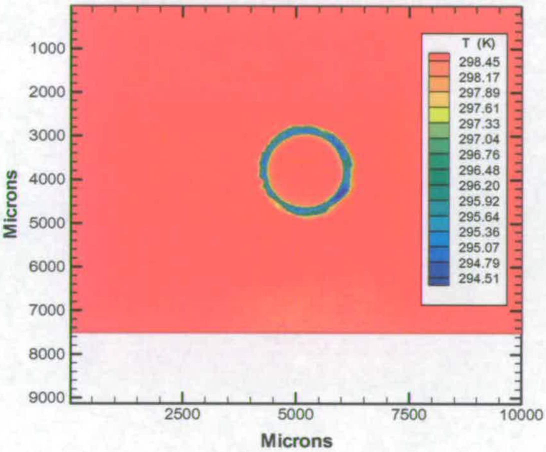

Figure 5.4 IR image of an empty capillary tube cross section ($\phi = 1{,}630\ \mu m$).

In both experimental investigations, capillary tubes made of borosilicate glass were used that is an opaque material to IR radiation. The IR image for Case (1) taken with an empty capillary shows (Figure 5.4) on the glass a temperature lower than that of the surrounding ambient, both inside and outside the tube. The tube is at ambient temperature, therefore an isothermal picture is expected. The result of Figure 5.4 is thus related to unwanted flux detected by the camera. This is the so called Narcissus effect described extensively by Horny [9] and is due to the reflected energy on the sample from the surrounding objects and especially from the IR detector itself. While for a single detector IR camera the Narcissus effect is localized at the field of view centre, for the FPA camera it affects the whole field. We expect no such reflection from the liquid because of the meniscus interface's high curvature and locally corrugated shape. The apparent temperature due to reflection could have been mitigated as proposed in Horny [9] by inclining slightly the tube. However, by doing so the points of the tube cross section would have been at different distance from the camera detector and therefore leading to a different temperature reading. This is particularly important in the present investigation where we are looking for the temperature gradient close to the meniscus triple line region. In order to remove the apparent temperature of Figure 5.4, two IR images of the capillary tube have been taken: one empty (Figure 5.4) and the other filled with methanol (Figure 5.5), and then subtract the first from the second one (Figure 5.6).

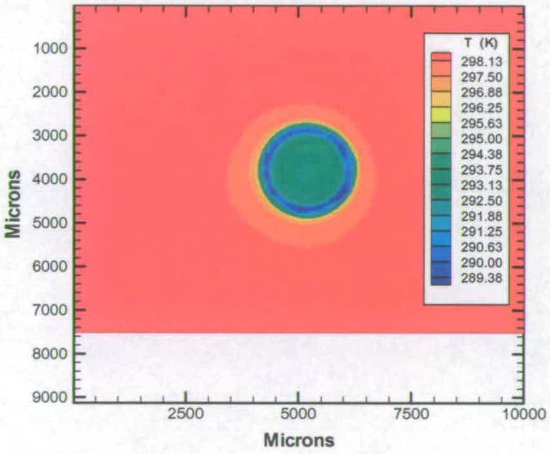

Figure 5.5 IR image of a capillary tube cross section filled with methanol (ϕ = 1,630 μm).

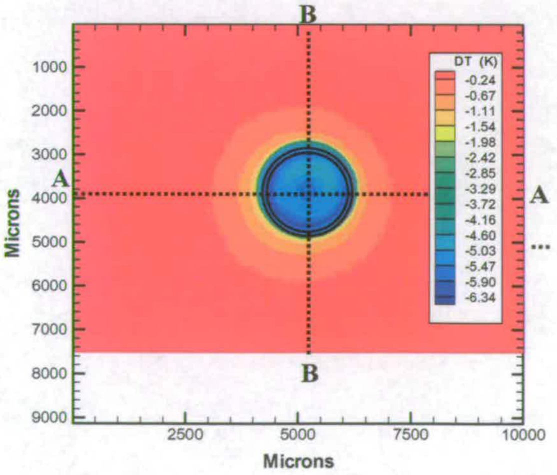

Figure 5.6 IR image subtraction (IR image of Figure 5.5 minus IR image of Figure 5.4).

By doing so it is assumed that the reflection from the tube does not change substantially for a tube's temperature change of 15 °C maximum, because of the evaporation when the tube is filled with respect to the empty tube. The subtraction allows measurement of only the evaporation cooling effect of the liquid. The temperature displayed on the IR image of Figure 5.6 is the difference between the actual temperature and the ambient one. Two black circles show the position of the tube. Because air is a transparent medium to IR, the temperature information in air has no meaning and the meaningful value on the temperature profiles in subsequent graphs stops right at the outside walls.

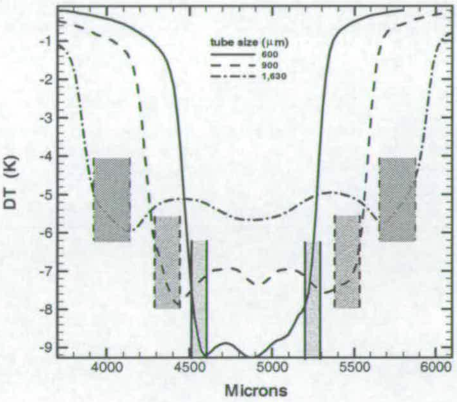

Figure 5.7 Temperature profile along the horizontal sections of various tube size (methanol).

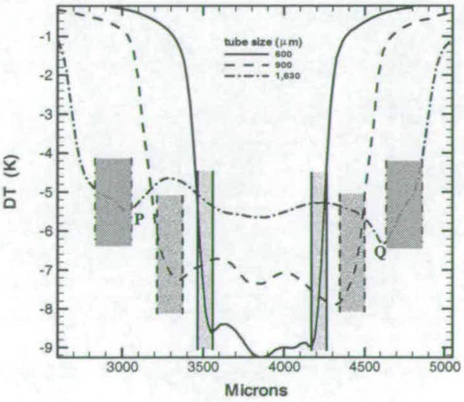

Figure 5.8 Temperature profile along the vertical sections of various tube size (methanol).

Two sections (**A-A** horizontal and **B-B** vertical) like the ones of Figure 5.6 are presented in Figures 5.7-5.8 for methanol and different tube sizes. The position of the capillary tube walls is shown by vertical boxes of different grey level and delimited by the same line pattern of the temperature profile for the corresponding tube size. From now on, only the subtracted IR image will be given. Similar trend was found for all the other three liquids investigated although the results are not reproduced for brevity. However, Figures 5.9-5.10 show the effect of the liquid on the temperature profile along the horizontal and vertical sections of the respective IR image for 1,630 μm tube size.

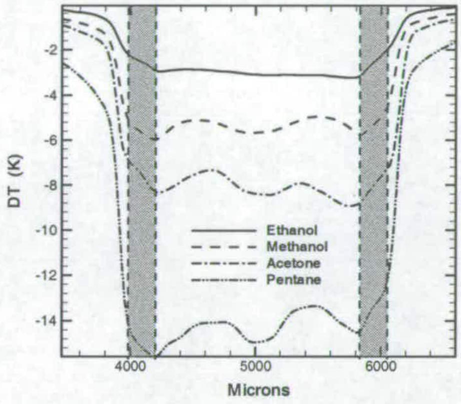

Figure 5.9 Temperature profile along the horizontal sections of 1,630 μm ID tube and various liquids.

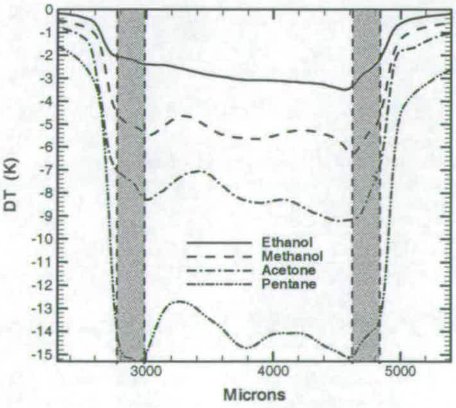

Figure 5.10 Temperature profile along the vertical sections of 1,630 μm tube and various liquids.

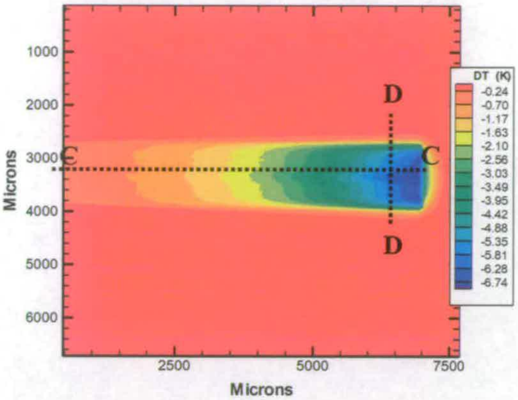

Figure 5.11 IR image of 900 μm tube from the side and methanol as liquid.

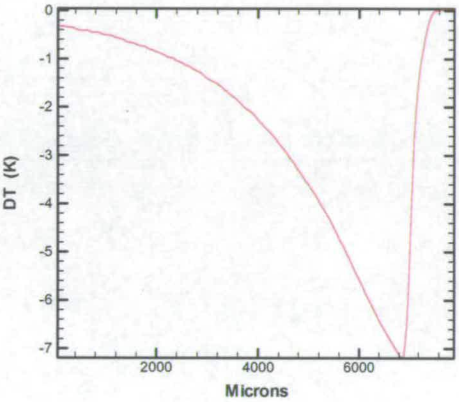

Figure 5.12 Axial section (**C-C**) of the IR image in Figure 5.11.

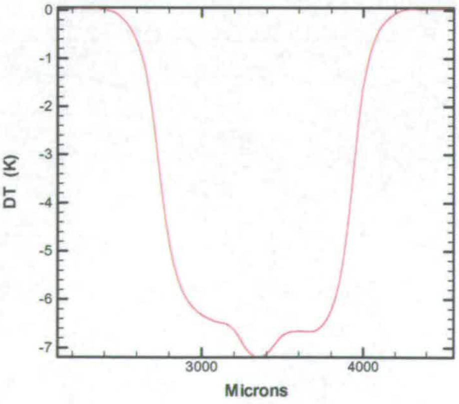

Figure 5.13 Radial section (**D-D**) of the IR image in Figure 5.11.

For Case (2) the IR measurements on the side of the tube are reported in the following. Also for this case, a reference IR image with the empty capillary was taken for image subtraction. The IR image of methanol and 900 μm along with an axial and radial section (**C-C** and **D-D**) are presented in Figures 5.11-5.13. A similar trend is found for all the other three liquids and various sizes, although not reproduced for brevity. It is worth noting that the temperature profile of Figure 5.12 is similar to the one obtained with the use of TLC (Figure 4.8). In addition the temperature at the meniscus micro-region in Figure 4.8 is very close to the one shown at the external tube in Figure 5.9 for pentane. It can be concluded that the temperature measurements with both methods are indeed reliable.

In the following the results of Case (3) for the heated capillaries will be presented. Figure 5.14 illustrates an IR image for the case of pentane and 900 μm tube diameter with the heater powered at 1 W; the temperature profile along horizontal and vertical sections is shown in Figures 5.15-5.16 respectively (note that for comparison the profiles with the heater off are also reproduced). As mentioned earlier, the interest here is in the Marangoni number evaluation and therefore the temperature gradients at the meniscus triple line versus the applied heat power are reproduced in Figure 5.17 for the three indicated positions around the tube cross section.

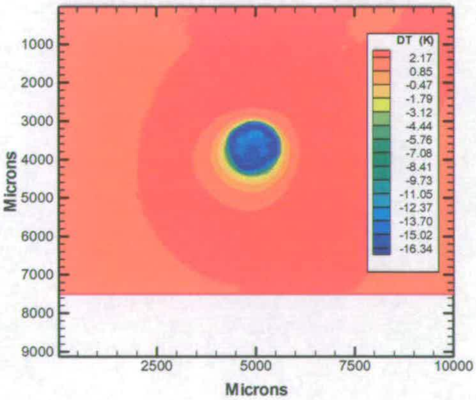

Figure 5.14 IR image of 900 μm heated (1 W) tube and pentane as liquid.

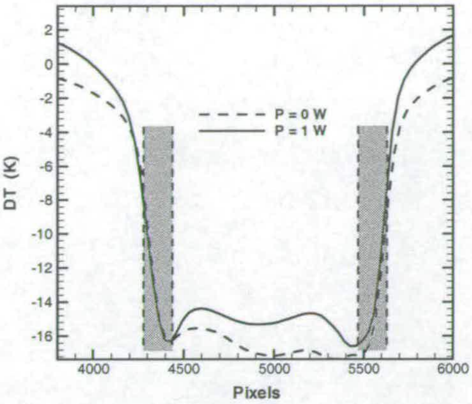

Figure 5.15 Horizontal section of the IR image in Figure 5.14.

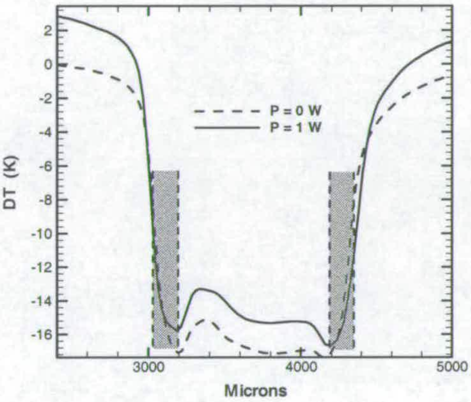

Figure 5.16 Vertical section of the IR image in Figure 5.14.

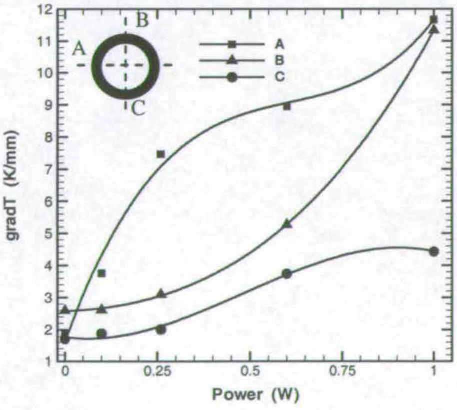

Figure 5.17 Temperature gradient vs. the heater power at the meniscus triple line at three positions around the tube cross section.

In this first set of experiments the spontaneous evaporation of volatile liquids in confined spaces such as capillary tubes was investigated. The temperature profile along the liquid-vapor meniscus interface is self-induced because of the differential evaporative cooling. Most of the evaporation takes place at the meniscus interface in the proximity of the wall (as described in Chapter II), therefore this region of the meniscus is colder than the centre. This generates the differential evaporation cooling along the meniscus interface. Experimental evidence of this fact is the temperature profiles shown in Figure 5.7. Following the line **A-A** of Figure 5.6, the temperature goes from the ambient value outside the tube to a negative dip at the liquid-solid interface (namely meniscus triple line) and then rises again in the liquid. The apparent local minimum at the capillary centre in Figure 5.7 is an artifact: the curved meniscus at the tube centre is out of the IR camera field of focus (see Figure 5.18) and therefore appears at a lower temperature; in reality, the temperature along the meniscus interface rises continuously from the wedge (where it is minimum) to the meniscus centre but this cannot be detected by the IR camera used because of its limited field of focus (100 μm) compared to the meniscus cap height (~500 μm).

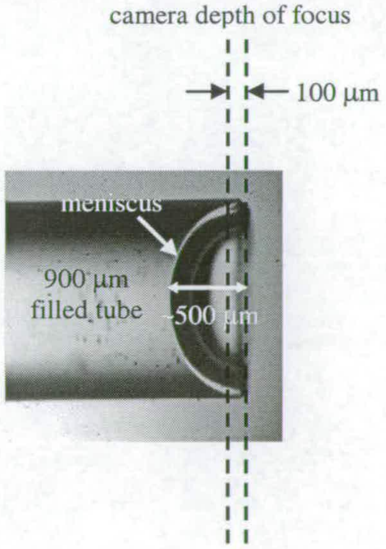

Figure 5.18 Depth of focus limitation of the IR system used for a curved meniscus.

By moving the micro-stage positioning system, it is possible to get the temperature along the entire curved meniscus interface. This can certainly be done but is not trivial, because in order to cover the entire meniscus interface at least 5 different IR images at different depth must be taken and successively integrated. Because the gradient of temperature at the meniscus triple line is responsible for the strong Marangoni convection observed and described in Chapter III, the attention was concentrated here in measuring the temperature near the triple line region only.

It is interesting to note that the temperature profiles along horizontal and vertical section are different as seen in Figures 5.7-5.8. The horizontal sections of Figure 5.7 are symmetrical with respect to the tube axis, whereas the vertical ones of Figure 5.8 are not. The temperature of the liquid in the top part of the meniscus (location P in Figure 5.8) is higher than in the bottom part (location Q). This is presumably due to the role played by gravity on the convection in the liquid inside the tube. It is well recognized that despite the fact that convection helps the heat and mass transfer by bringing hot liquid into colder regions, it also reduces its own driving force because of a reduction in temperature differences. In this particular case, the convection arising from the differential evaporative cooling along the meniscus reduces the temperature gradient between the centre and the wedge of the meniscus helping also to stabilize the self-induced destabilizing temperature field created here in a g-environment. Hot liquid is brought from the centre to the wall of the capillary where most of the evaporation is taking place. The experimental evidence of the role played by convection on the temperature profile can clearly be seen by analyzing these temperature profiles along horizontal and vertical sections of the capillary tubes in conjunction with the flow pattern in the meniscus liquid phase as shown by the μ-PIV results of Figures 3.8-3.9. Figure 3.8 represents a horizontal section of the capillary tube and shows a symmetrical flow pattern. The pattern of Figure 3.9, instead, being a vertical section of the capillary, is strongly asymmetrical. The top part of the vertical section (location P in Figure 5.8) results to be hotter than the bottom (Q) because hotter liquid is brought from the bulk phase as schematically described in the vertical section of the capillary shown in Figure 5.19 by the convection unveiled in Figure 3.9. This flow dissymmetry could have important consequences in many industrial applications such as crystal growth of semiconductor materials [19-20], glass manufacture [21] and artificial stem cell where the quality and homogeneity of the final product is a fundamental requirement.

By decreasing the capillary size, the evaporation per unit area increases as discussed in Chapter II and the temperature at the meniscus triple line decreases as seen in Figures 5.7-5.8. On top of this, the temperature gradient near the meniscus triple line increases with the reduction of the tube size as shown in Figures 5.7-5.8.

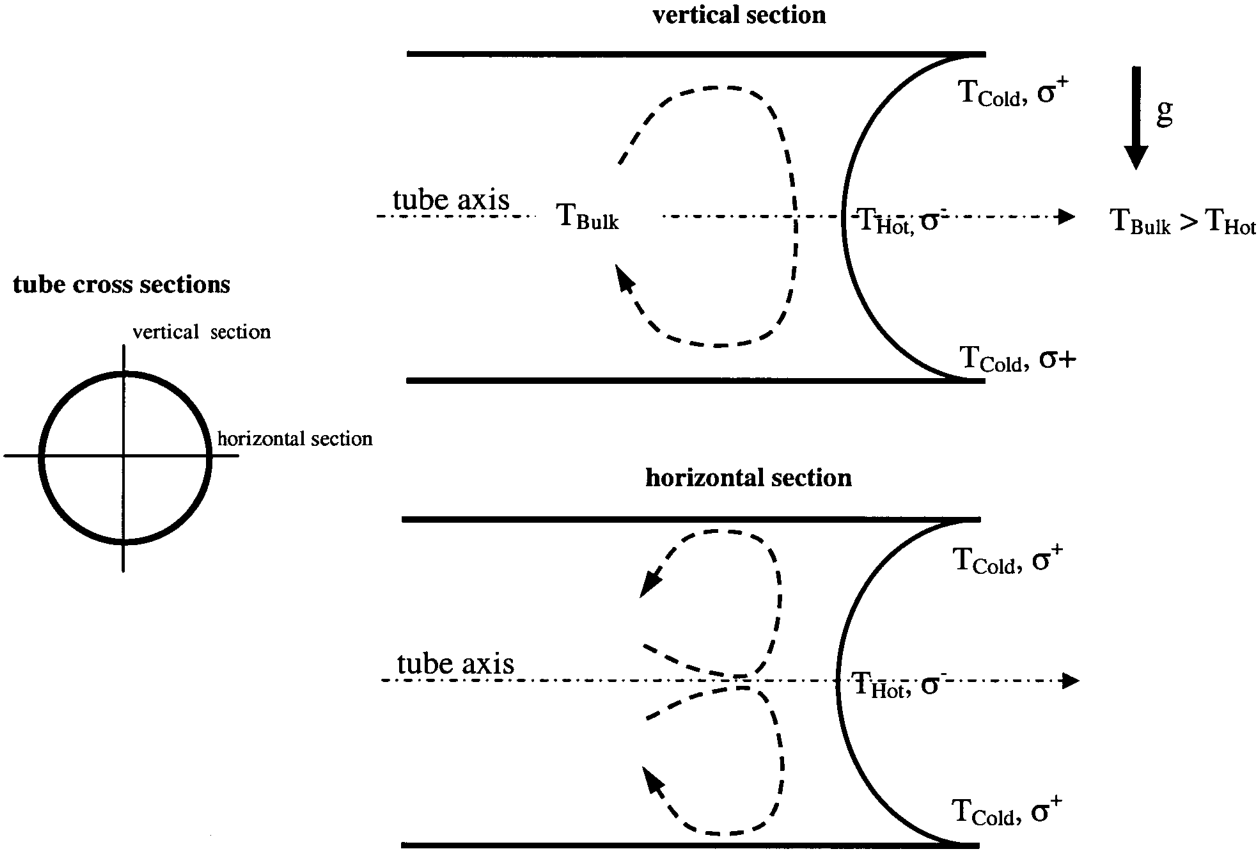

Figure 5.19 Schematic of the flow and thermal fields at horizontal and vertical sections of the tube (**g** is the gravitational acceleration).

It is worth noting that by simply looking at these figures (Figures 5.7-5.8) the aforementioned conclusion of a temperature gradient at the meniscus triple line higher for reduced tube size, becomes unclear especially at the smallest tube size. This is essentially due to the fact that by reducing the tube size a decreasing length of the meniscus interface lies in the camera focus. Therefore, to solve this problem the temperature gradients have been evaluated taking 3 consecutive unfiltered pixels along the meniscus in the tube wall region, starting from the one with the lowest temperature close to the tube wall and moving towards the meniscus center.

As pointed out in Chapter III, the Marangoni number evaluation is not easy in the present experimental investigation; essentially because of the non linear variation of temperature along the interface. Therefore, the analysis carried out in Chapter II was based on an average temperature difference between the wedge and the centre of the meniscus and it was concluded that the reason why the *Ma* of Table 3.1 is increasing with increasing tube size is because of the average temperature considered. In reality the *Ma* should be based on the temperature gradient at the meniscus triple line region and the present IR measurements allow this evaluation. Table 5.1 reports the temperature gradients at the triple line region and *Ma* for methanol and ethanol at various tube sizes. It can be seen now that, as expected because of a stronger convection at smaller tube sizes, the *Ma* (that is the convection driving force) is higher for smaller tube sizes.

Table 5.1 Temperature gradient at the meniscus triple line and Marangoni number for ethanol and methanol at different tube sizes.

Liquid	***Tube size ID (μm)***	$\nabla T = \frac{\partial T}{\partial r}$ ***(K m^{-1})***	$Ma = \frac{\left(-\frac{\partial \sigma}{\partial T}\right)\frac{\partial T}{\partial r}R^2}{\mu\kappa}$
Ethanol	600	4,965	31
	900	2,046	27
	1,630	164	7
Methanol	600	7,447	82
	900	2,983	73
	1,630	298	24

The comparison between liquids of Figures 5.9-5.10 shows that the more volatile the liquid is (lower boiling point) the higher is the evaporative cooling effect. The vertical temperature profiles of Figure 5.8 and Figure 5.10 show that the asymmetry is higher for larger tubes and less volatile liquids. This is probably due to the convection inside the tube that is more affected by gravity at larger tube sizes and with the use of less volatile liquids as also extensively discussed in Chapter III.

As mentioned earlier, borosilicate glass is an opaque material to the IR band of the camera; therefore, by looking from the side as in Figure 5.11 the external wall temperature is read. Because of the higher glass thermal conductivity compared to air, the minimum temperature of Figure 5.12 is close to the meniscus triple line temperature reported in Figure 5.7 (case of 900 μm tube size). However, the wall material and thickness as well as the roundness of the tube geometry, all contribute in broadening the dip shown in Figure 5.12 that is actually confined in 1-2% of the meniscus length as shown numerically by Sartre et al. [22]. The radial section **D-D** of Figure 5.13 shows a lower temperature on the middle of the capillary tube because this region of the tube is closer to the IR detector.

In Case (3) with the liquid-vapour interface laying in a gradient of temperature imposed by the heater positioned below the meniscus (Heater "OFF"), it is expected that the temperature profile along the liquid-vapour interface changes as schematically shown in Figure 5.20 with respect to the unheated case (Heater "ON"). As can be seen from the temperature profile of Figures 5.15-5.16, powering on the heater results in heating up the liquid and therefore reducing the evaporative cooling. The results of Figure 5.17 show that the temperature gradient at the meniscus triple line varies when powering on the heater, but its sign is not inverted. In particular, the temperature gradient increases with the applied power because the temperature at the meniscus centre (see Figure 5.20, bottom sketch) could be assumed the same as at the corresponding point *M* on the tube.

Note also that the convection patterns unveiled in Figures 3.8-3.9 are thought to be responsible for the difference in the temperature gradients at the meniscus triple line around the meniscus interface (positions A, B and C in Figure 5.17). As mentioned earlier, because surface tension gradient ($\nabla\sigma$) drives the observed convection in the liquid phase, powering on the heater results in changing the strength of convection; however, the flow pattern is kept similar (i.e., no inversion of the spinning movement like the one shown in Chapter III with the meniscus lying below the heater as described also in the following experiments where the tube was vertically plunged in a pool of liquid and the meniscus lay below the heating element).

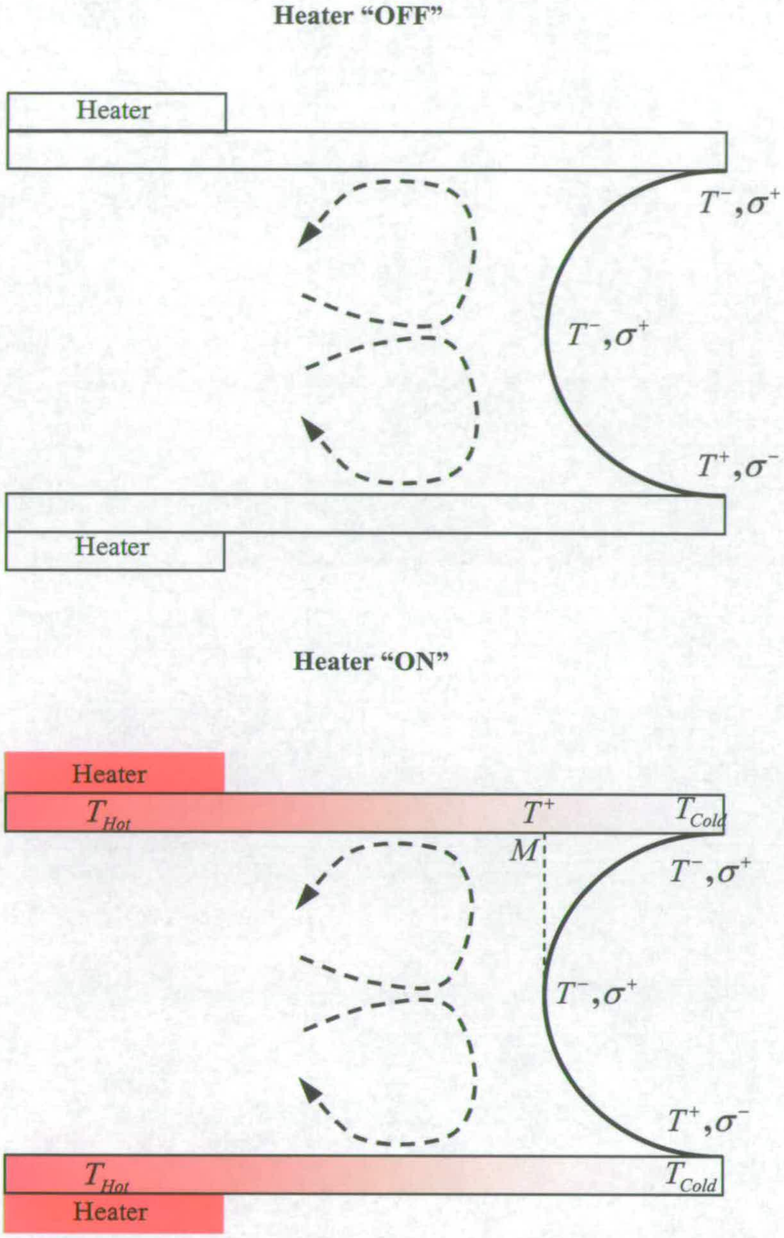

Figure 5.20 Temperature distribution along the meniscus for heater "ON" and "OFF".

5.4.2 Vertically oriented capillary tubes

We move now to the IR measurements made with the Agema 880 camera on a vertically positioned tube. The tube (600 μm ID) was vertically plunged in a pool of ethanol or methanol and the liquid was allowed to rise inside the tube above the liquid level of the pool because of the capillary action force.

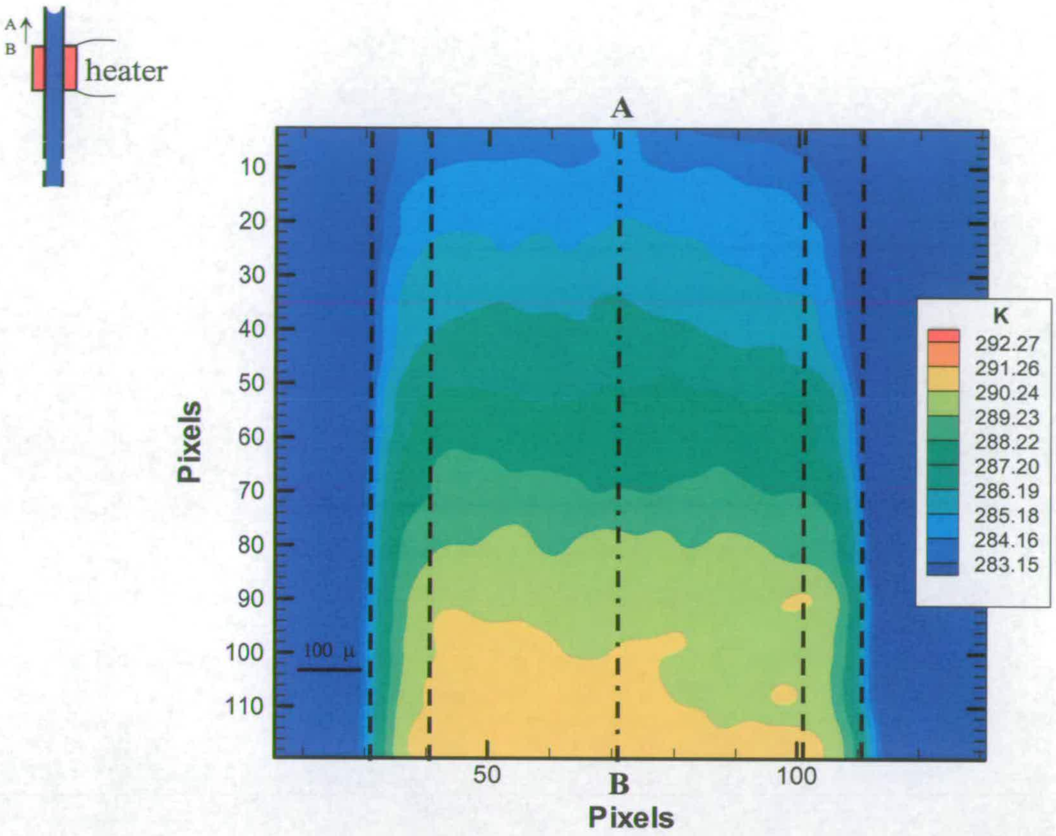

Figure 5.21 IR measurement for methanol as liquid and heater (1.08 W) in the meniscus liquid phase.

Two situations were investigated. In the first situation the meniscus is positioned at the capillary top and the heating element (deposited on the tube external surface as described earlier for μ-PIV experiments performed in Chapter III with the experimental layout shown in Figure 3.4) is down along the tube: this case is referred to as heating element in the liquid side of the meniscus. For the second situation, the heating element was built at the top of the tube and the meniscus was positioned just below it: this case is referred as heating element in the vapour side of the meniscus. Figure 5.21 is an IR image of the heated capillary (1.08 W heater power) with the heater in the meniscus liquid side. The tube walls positions are clearly marked with dotted lines. Note that the heater is located just below point B as schematically shown in the inset on the top left side of Figure 5.21. As already pointed out, air being transparent to IR, the information is therefore meaningless in the region outside the tube. The important information extracted from the IR images is the temperature gradient along the tube axis (section **A-B** of Figure 5.21) and most of all the temperature steps produced by the heater at different heating powers. This latter is an important input for the numerical simulations to be performed in Chapter VI.

The tube wall thermal resistance is evaluated with the use of the following formula valid in axi-symmetric geometry:

$$R_i = \frac{ln\left(\frac{r_{ext}}{r_{\text{int}}}\right)}{2\pi k} \tag{5.7}$$

with k the glass thermal conductivity (1.12 W K^{-1} m^{-1}), r_{ext} (= 400 μm) and r_{int} (= 300 μm) the tube external and internal radii. Assuming natural convection around the tube's external surface and with the above value of thermal resistance one gets a $\Delta T = T_{ext}\text{-}T_{int} \cong 0.2$ K. Therefore, we can assume that the temperature read by the IR camera on the external tube surface is very close to the one on the internal tube surface. This is also confirmed by the following Biot number evaluation. The Nusselt number for natural convection around a horizontally oriented capillary tube is given by (Incropera and DeWitt [23]) Equ. (4.6); the *Nu* so evaluated is of 0(1). Because at the tube-air side:

$$Nu = \frac{hr_{ext}}{k_{air}} \tag{5.8}$$

and

$$Bi = \frac{hr_{ext}}{k_{glass}} \tag{5.9}$$

one gets:

$$Bi = Nu\frac{k_{air}}{k_{glass}} \cong 2\,x10^{-2} \tag{5.10}$$

Therefore, it can be assumed here that the temperature variation inside the tube wall is negligible compared to the one in the thermal boundary layer at the tube-air side; and, the temperature read by the IR camera is actually very close to the tube internal one.

Figure 5.22 depicts the case of the heater in the vapour phase. The heater is now located just above point A as schematically shown in the inset on the top left corner. In the following Figure 5.23, the temperature gradient is plotted for the two liquids and the empty capillary tube, for the two heater location, at different heater powers. Clearly, the temperature gradient is higher when the tube is empty because when filled with liquid, the liquid evaporating cools the tube wall. At lower heater power there is no substantial difference between liquids, but at larger power the liquid of lower boiling point (methanol) evaporating more cools more efficiently the tube. Note also that when the heater lies in the liquid phase the temperature gradient is lower because heat is transferred to the bulk and contribute to its temperature rise.

When heat is applied, the thermocapillary stress generate must be taken into account; the thermocapillary stress acts in the same direction as gravity for the case of vertically oriented tube and heater in the meniscus vapour phase, therefore reducing the liquid wicking height. The meniscus is therefore pushed down until a new equilibrium is found. The effect of thermocapillary stress on the meniscus height is more pronounced when the meniscus is closer to the heater.

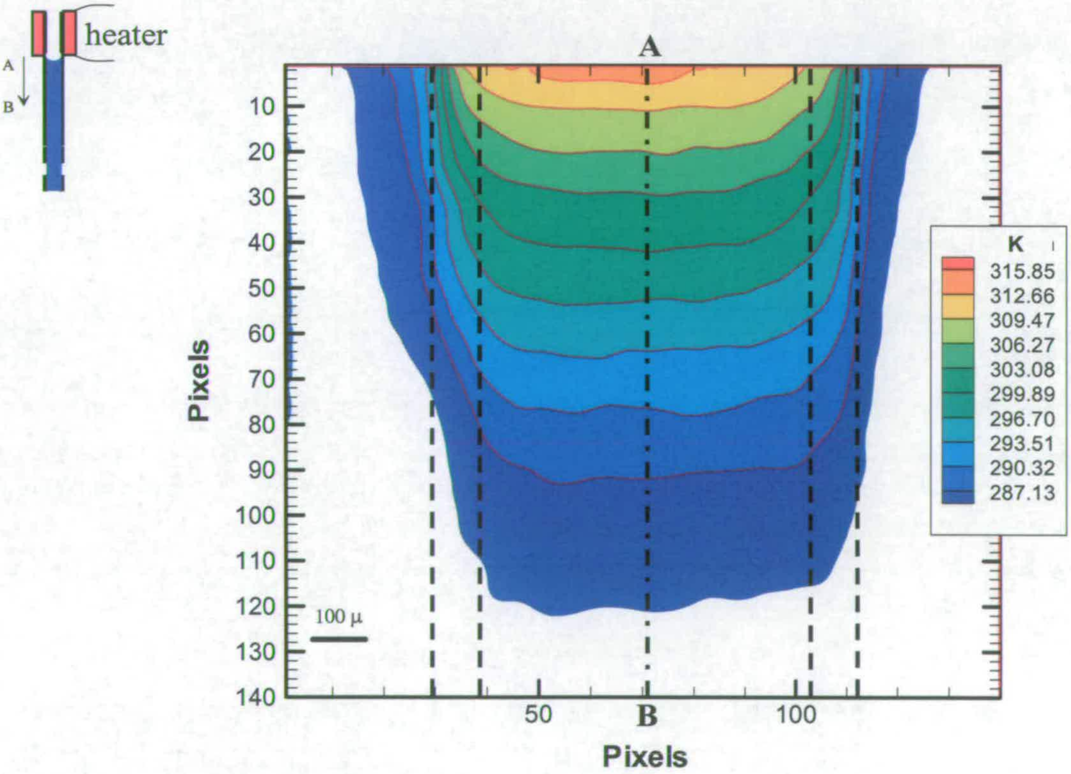

Figure 5.22 IR measurement for methanol as liquid and heater (1.5 W) in the meniscus vapour phase.

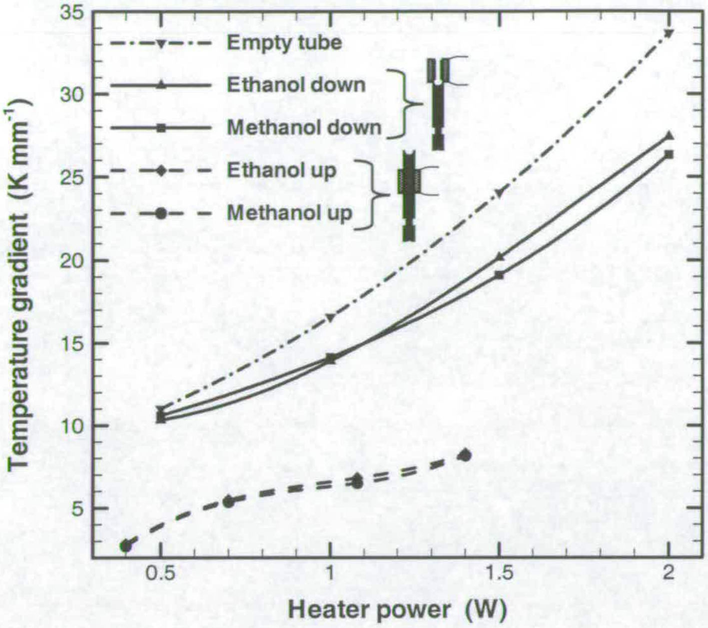

Figure 5.23 Temperature gradient along the tube wall vs. heater power; heater in the meniscus vapour –**down**- and liquid –**up**- phases (points are experimental data and curves best fit).

Figure 3.23 in Chapter III shows that the experimental plot of liquid wicking height versus the distance from the heater can be fitted approximately by an exponential curve essentially because the temperature gradient created along the capillary wall by the heater is expected to follow an exponential trend since it arises from conduction through a cylindrical fin. In the present investigation the temperature profile has been measured using an IR camera. This is a more refined technique than that employed in previous research (Pratt and Hallinan [24]) where the temperature gradient was measured by the use of thermocouples inserted inside holes drilled in the capillary wall. In the present case a spatial resolution of 10-15 μm is expected compared with 0.5 mm of Pratt and Hallinan [24]. On top of this, the tube used by Pratt and Hallinan [24] had a wall thickness of 1 mm in order to locate the thermocouples without compromising the material integrity. The advantage of using a non-invasive technique, such as IR, is that it allowed us to work with a wall thickness of 100 μm giving fewer problems in visualizing the convection. Unfortunately, the sink effect of the meniscus triple line cannot be captured by the present IR measurements for the case of the heater in the vapour side, essentially for three reasons. Firstly, the IR camera has a detector working in the long wavelength band (i.e. between 8-12 μm) making it difficult to resolve a temperature trough a few microns wide. Secondly, the trough spreading through a thick wall of 100 μm and the low glass thermal conductivity prevents a clear view of this region. Thirdly and most important of all, for this case the meniscus is far away from the capillary mouth and therefore the self induced temperature at the meniscus triple line is much lower than in the case of the meniscus stuck at the capillary edge as shown in Figure 5.12 for the case of horizontally oriented capillary tubes.

The temperature distribution along the capillary wall can be evaluated by solving the heat conduction through a cylindrical fin having its external surface in contact with air and its internal surface in contact with liquid or vapour, depending on the case analysed: heater in the meniscus liquid phase for the former and heater in the meniscus vapour phase for the latter. This is a reasonable order of magnitude analysis as the evaluation of the Biot number gives $Bi = \frac{h\,s}{k_{glass}} = \frac{k_{liquid}\,s}{k_{glass} d_{\text{int}}} Nu \cong 0.09$ (so, also the convection inside the tube, not only that outside it, is weaker than the conduction in the tube wall), where k_{liquid} and k_{glass} are the thermal conductivities of the liquid (~$1.69\text{x}10^{-1}$ W m^{-1} K^{-1}) and glass (~1.12 W m^{-1} K^{-1}), s and d_{int} are the wall thickness (100 μm) and internal (600 μm) tube diameter and $Nu = \frac{hd_{int}}{k_{liquid}}$ is the Nusselt number that is constant (~3-4) for an internal laminar, fully developed flow as shown in [23]. In the Bi we use the liquid thermal conductivity because the case with the heater in the meniscus liquid side is the worst of the two cases. It is assumed here that the liquid or vapour flow inside the tube is fully developed. The 1-D heat conduction equation for the tube assumed as a cylindrical fin along with boundary conditions are written as follows [23]:

$$kA_{\pi}\frac{d^2T}{dy^2} - hS(T - T_a) = 0 \qquad (5.11)$$

$$\left.\frac{dT}{dy}\right|_{y=0} = -\frac{W}{kA_{\pi}} \qquad (5.12)$$

$$T\big|_{x\to\infty} = T_a \qquad (5.13)$$

where k is the tube thermal conductivity, A_π is the tube cross section area, y is the spatial tube axial coordinate with the origin at the bottom of the heater, h is the heat transfer coefficient at the air side, S is the tube perimeter, W the fraction of the heater power that goes along the capillary wall and T_a is the ambient temperature.
The above equation has the following general solution (standard fin solution):

$$T = Be^{y} + Ce^{-y} \qquad (5.13)$$

with B and C determined by imposing the boundary conditions. This yields:

$$T = T_a + \frac{W}{k\,q\,A_\pi} e^{-qy} \qquad (5.14)$$

with $q = \sqrt{\frac{h\,S}{k\,A_\pi}}$.

The temperature profile along the tube allows evaluation of the temperature gradient at the meniscus position and the consequent thermocapillary stress as follows:

$$\sigma_{st} = \frac{\partial \sigma}{\partial y} r = \frac{\partial \sigma}{\partial T}\frac{\partial T}{\partial y} r \qquad (5.15)$$

Having assumed a linear relation between surface tension and temperature using Equs. (5.14) and (5.15), one gets:

$$\sigma_{st} = \frac{\left(\frac{\partial \sigma}{\partial T}\right) W\,r}{k\,A_\pi} e^{-qy} \qquad (5.16)$$

It is clear that as power is increased the meniscus is pushed down and the steady state value of the liquid wicking height versus power follows an exponential trend (see

Figure 3.23) as do both the temperature (Equ. (5.14)) and the thermocapillary stress (Equ. (5.16)) versus distance from the heater.

From the IR studies of two different configurations (tube horizontally and vertically oriented), it can be concluded that the temperature profile along the liquid-vapour interface is ultimately responsible for the vigorous liquid convection observed and described in details in Chapters II-III. It is also shown in the present IR investigation that the self-induced temperature differences along the meniscus can be altered and eventually inverted leading to the convection inversion described in Chapter III.

5.5 Conclusions

Generally speaking, making temperature measurement at the micro-scale is a quite difficult task. It is well established that the performance of important two-phase heat transfer systems such as heat pipes and those involving boiling in general, is dictated by what happens in the micro-region of the meniscus contact line. This study shows that IR technique could be successfully used to tackle this problem.

Two IR cameras have been employed to map the temperature along the interface and on the tube wall of an evaporating meniscus formed in a confined space. The use of a NDT technique like IR is the only tool available to measure the temperature of a liquid-vapour interface. The good spatial resolution (~30 μm), high sensitivity (20 mK at 30 °C) and great accuracy ±1% of the IR camera used for the interfacial temperature study has allowed to detect the strong evaporative cooling at the meniscus triple line. The liquid evaporates more at the meniscus wedge than in the middle of the capillary. This was found to be responsible for a strong thermocapillary Marangoni convection observed in the liquid phase as described in Chapters II-III. Broadly speaking, convection helps the heat and mass transfer by bringing hot liquid to the colder region; this affects also the driving force that sustains the convection itself. It is shown that this is the case also for the present investigation; the temperature difference is changed by the convection that brings hot liquid into cold regions of the flow. It is also shown that the evaporative cooling effect is stronger at smaller tube sizes and with the use of more volatile liquids. The present experimental evidence supports the hypothesis made in Chapters II-III of a differential evaporative cooling along the meniscus interface responsible for the observed convection.

A different IR camera (Agema 880 with a high spatial resolution of 12 μm, an accuracy of ±2% and a superb sensitivity of 70 mK at 30 °C) was used to map the capillary wall temperature in the case of a heated tube vertically immersed in a pool of ethanol or methanol for two positions of the heating element: above and below the meniscus. It is demonstrated that when the heating element lies below the meniscus in the liquid side, the temperature profile along the meniscus could be altered but not inverted in sign. Different is the case when the heating element is above the meniscus; in this case, the temperature profile along the interface could be inverted with respect to the unheated situation ultimately leading to the convection inversion outlined in Chapter III with the use of the μ-PIV flow investigation technique.

The substantial amount of experimental data gained through the μ-PIV investigation of Chapter III and the IR measurements of the tube and meniscus temperature presented in this chapter, allow us to set and perform the numerical study to be presented in the following chapter. Some experimental findings are reproduced numerically and the analysis is further extended to predict other interesting cases.

5.6 References

[1] Fang G. and Ward C.A., 1998, *Temperature measurement close to the interface of an evaporating liquid*, Physical Review E, Vol. 59, pp. 417-428.

[2] Hetsroni G., Mewes D., Enke C., Gurevich M., Mosyak A. and Rozenblit R., 2003, *Heat transfer to two-phase flow in inclined tubes*, International Journal of Multiphase Flow, Vol. 29, No. 2, pp. 173-194.

[3] Hetsroni G., Mosyak A., Segal Z. and Pogrebnyak E., 2003, *Two-phase flow patterns in parallel micro-channels*, International Journal of Multiphase Flow, Vol. 29, No. 3, pp. 341-360.

[4] Herchang A., JiinYuh J. and Jer-Nan Y., 2002, *Local heat transfer measurements of plate finned-tube heat exchangers by infrared thermography*, International Journal of Heat and Mass Transfer, Vol. 45, No. 20, pp. 4069-4078.

[5] Sgheiza J.E. and Myers J.E., 1985, *Behavior of nucleation sites in pool boiling*, AIChE J., Vol. 31, pp. 1605-1613.

[6] Theofanous T.G., Tu J.P., Dinh A.T. and Dinh T.N., 2002, *The boiling crisis phenomenon: Part I: nucleation and nucleate boiling heat transfer*, Experimental Thermal and Fluid Science, Vol. 26, No. 6-7, pp. 775-792.

[7] Rogalski A., 2002, *Infrared detectors: an overview*, Infrared Physics & Technology, Vol. 43, pp. 187-210.

[8] Rainieri S. and Pagliarini G., 2002, *Data processing technique applied to the calibration of a high performance FPA infrared camera*, Infrared Physics & Technology, Vol. 43, pp. 345-351.

[9] Horny N., 2003, *FPA camera standardization*, Infrared Physics & Technology, Vol. 44, pp. 109-119.

[10] Kaplan H., 1993, *Pactical Applications of Infrared Thermal Sensing and Image Equipment*, O'Shea, Series Editor, Georgia Institute of Technology, USA.

[11] Höhmann C. and Stephan P., 2002, *Microscale temperature measurement at an evaporating liquid meniscus*, Experimental Thermal and Fluid Science, Vol. 26, pp. 157-162.

[12] Farina D.J., Hacher J.M., Moffat R.J. and Eaton J.K., 1994, *Illuminant Invariant Calibration of Thermochromic Liquid Crystals*, Experimental Thermal and Fluid Science, Vol. 9, pp. 1-12.

[13] Hay J.L. and Hollingsworth D.K., 1996, *A Comparison of Trichromic Systems for Use in the Calibration of Polymer-Dispersed Thermochromic Liquid Crystals*, Experimental Thermal and Fluid Science, Vol. 12, pp. 17-12.

[14] Conn G.K.T. and Avery D.G, 1960, *Infrared Methods: Principles and Applications*, Academic Press, New York and London.

[15] Parker R., 1973, *Transient surface temperature response of liquid crystals films*, Mol. Crystals Liq. Crystals, Vol. 20, pp. 99-106.

[16] Ireland P.T. and Jones T.V., 1987, *The response time of a surface thermometer employing encapsulated thermochromic liquid crystals*, J. Phys. E: Sci. Instrum. 20 1195-1199.

[17] McDonald J., *Microthermal imaging in the infrared*, http://www.electronics-cooling.com/Resources/EC_Articles/JAN97/jan97_04.htm

[18] Payne B.O., 1954, *Microscope design and construction*, Cooke, Throughton & Simms, England.

[19] Schwabe D., 1981, *Marangoni effects in crystal growth melts*, Physico-Chemical Hydrodynamics, Vol. 2, pp. 263-280.

[20] Bikerman J.J., 1958, *Surface Chemistry*, 2nd Edition Academic Press, New York.

[21] Frischat V.G.H., Herr K. and Barklage-Hilgefort H., 1980, *Probleme bei der vorb creitung glastechnischer intersuchungen in weltraum*, Glastech. Ber., Vol. 53, pp. 1-9.

[22] Sartre V., Zaghdordi and M.C. Lallemand M., 2000, *Effect of interfacial phenomena on evaporative heat transfer in micro heat pipes*, International Journal Thermal Science, Vol. 39, pp. 498-504.

[23] Incropera F.P. and DeWitt D.P., 1996, *Fundamentals of heat and mass transfer*, 4th Edition, John Wiley & Sons, New York.

[24] Pratt D.M. and Hallinan K.P., 1997, *Thermocapillary Effects on the Wetting Characteristics of a Heated Curved Meniscus*, Journal of Thermophysics and Heat Transfer, Vol. 11, No. 4, pp. 519-525.

CHAPTER VI

Numerical investigation of self-induced thermocapillary convection due to phase transition in capillary tubes

6.1 Motivation

This Chapter describes a numerical analysis on the self-induced thermocapillary convection for an evaporating liquid from a meniscus formed in capillary tubes. In the previous Chapters different experimental techniques have been used to measure relevant parameters for this case. The aim of the numerical analysis presented here is to reproduce some of the results obtained experimentally and to investigate some others which were difficult to access experimentally. As will be shown later, the numerical analysis has proven to be a powerful tool to accurately predict the phenomena involved with the evaporation in capillary tubes. It was argued and also proven experimentally with the IR measurements, that is indeed the temperature distribution along the meniscus that ultimately dictates the liquid convection pattern. This will be confirmed in this chapter. One of the important findings of the present work (the inversion of convection) is reproduced numerically. Numerical simulations will provide also important information about the complete temperature field in the liquid phase, as this information was not obtained experimentally.

6.2 Background

It is recognised that in the last few years numerical analysis has become more and more an essential tool in industrial applications. Many world leading companies in the engineering sector are heavily investing in building up numerical teams to produce numerical tools because of the many advantages this approach offers in predicting and solving problems; firstly, time and money. Once a numerical code is built it can be adapted to simulate different configurations. Sometimes, as will be shown in the present case, few changes are needed to solve a completely different situation. Important parametrical analysis can be easily and cheaply performed using a code. If the same problem must be analysed experimentally, much more effort is usually necessary. Nowadays computers are becoming so powerful that complicated numerical analysis, just a few years ago possible to perform only on supercomputers, can be solved in much less expensive equipment. The other important advantage is that complete information can be gathered. All relevant variables are available at once, whereas for experimental analysis different tools must be used to measure temperature, velocity, pressure, etc. and most of these cannot be used simultaneously and are usually invasive if not destructive. The major drawback of the numerical analysis remains that it is essentially a model of the reality. The three principal steps involved in the numerical analysis are as follows: 1) a set of equations that describe the physics involved; 2) a numerical model to solve the mathematical model given by the set of equation provided in the previous step; 3) a computer solution of the problem. Passing from one step to the next, will produce a "degradation" of the information being investigated. In addition, even if a satisfactory solution is provided by one of the last two aforementioned steps, the results given can be worthless if the mathematical model developed is not suitable. The mathematical model of the reality is therefore of major concern in a numerical analysis. On the other hand, experiments are not free of errors and limits. As mentioned earlier, in many cases the technique being used to measure a parameter is invasive (at times could lead to serious misreading). In other cases, the scale of the problem is prohibitive and up- or downscaled models must be used. The major disadvantages are found with down scaled problems, as for instance model imperfections in a wing can substantially amplify their effect on the flow around it. Then, even using the same experimental apparatus, different researchers can most likely find different values, because the reading is subjective. These sort of problems do not exist in numerical analysis. However, by experimentation one goes to measure the reality, whatever it is and if suitable techniques and equipments are used that reality will be measured. For instance, the effect of surface roughness on the flow in a pipe can be experimentally detected whereas a complete model of roughness for a numerical analysis is much more complicated to build. What really makes things easier for numerical analysis is that the huge amount of experimentation available in many areas, makes phenomena more predictable and thus useful and fairly accurate models exist to predict certain behaviours.

As briefly mentioned earlier, the numerical model to be used is also crucial, as different problems require different techniques and approaches to be solved correctly. Over the years, since the appearance of computers, many numerical models have appeared to solve different engineering problems. In what follows we will concentrate on those relating to heat transfer and fluid flow only. The equations of the mathematical model involved in this area are: continuity, Navier-Stokes (momentum or Newton equation) and energy. Even in this "relatively small" area of engineering, large and variegated is the choice between the models available. A brief introduction will be made here. The major methods available can be classified in four different groups: Finite Difference Method (FDM), Finite Element Method (FEM), Finite Volume Method (FVM), and Spectral Method (SM). FDM consists in approximating the solution by polynomials and only the grid points are considered as solution of the problem. In FEM both the grid points and the interpolation functions between grid points are regarded as a solution. In the FVM something in between these two approaches is employed. The computational domain is divided in non overlapping control volumes surrounding the grid points and the differential equations are integrated over each control volume. The interpolation functions are assumed to evaluate the integrals and successively only the values of the relevant variables at the grid points are present in the discretization equations. The SM consists in approximating the solution by Fourier series of orthogonal polynomials. It is common knowledge that the SM offers the highest achievable accuracy, whereas the other cited methods have usually lower accuracy. The accuracy of these methods can however be increased involving more grid points in each derivative approximation and implicit schemes. On the other hand, SM can be used only in conjunction with periodic

Boundary Conditions (BC) and equidistant grid points. In the FEM, as in FDM and FVM with some minor extra complications, the grid can be refined where high local gradients are expected. Usually, when experiments are not available as benchmarks, SM can provide a reliable comparison.

In what follows a numerical method based on the FVM is used, but no special mention will be made regarding convergence, accuracy and stability of the method employed as it is beyond the scope of this work. In addition, satisfactory information on the mathematical aspects connected with convergence, accuracy and stability of the FVM employed here can be found in Patankar [1]. The code used in the present study was developed by Raspo and El-Ganaoui [2] for complex fluid mechanics problems and Bennacer et al. [3] for liquid bridge related issues. In the liquid bridge a solid is locally melted and successively solidified with the aim of producing high quality crystals. The phenomena are dominated by surface tension and a moving boundary (solid-liquid interface) is present. In the present case, evaporation is operating instead and most of it takes place in a confined region close to the triple line region leading to a Gaussian type heat flux profile, but the phenomena are essentially similar for both cases.

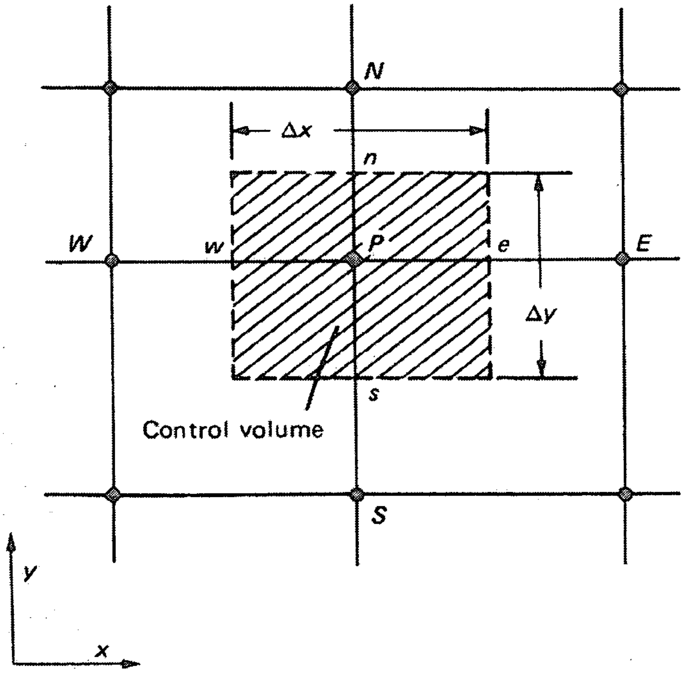

Figure 6.1 Computational molecule for FVM (taken from Patankar [1]).

The basic knowledge of the FVM formulation will be given in the following example for the case of heat conduction only as it simplifies the mathematical treatment. The extension to convection and diffusion because of the flow field will be mentioned highlighting the mean features. All what follows as mathematical procedure is summarised from Patankar [1] to whom the reader can refer for a more detailed and complete description.

The energy equation for the unsteady 2-D pure conduction problem is as follows:

$$\rho c\frac{\partial T}{\partial t}=\frac{\partial}{\partial x}\left(k\frac{\partial T}{\partial x}\right)+\frac{\partial}{\partial y}\left(k\frac{\partial T}{\partial y}\right)+S \qquad (6.1)$$

where ρ is density, c specific heat, k thermal conductivity, T temperature, t time, x and y coordinate system and S is the source term. An isotropic medium is assumed with ρ and c constant and uniform. The computational cell with the control volume is sketched in Figure 6.1. *PENS* are the grid points: P is the grid point; E stands for east of P; W stands for west of P; N for north of P; and, S for south of P. *wens* are the control volume faces and Δx, Δy the x and y control volume dimensions. For simplicity, it is assumed here that the control volume faces lie in the middle of the grid points ($\delta x=\frac{\Delta x}{2}$ and $\delta y=\frac{\Delta y}{2}$), but this is not necessary. By evaluating the derivatives in Equ. (6.1) from the piecewise linear profile one gets:

$$\frac{c\left(\rho_P T_P-\rho_P^0 T_P^0\right)\Delta x\Delta y}{\Delta t}=\frac{k_e\left(T_E-T_P\right)}{\delta x}\Delta x-\frac{k_w\left(T_P-T_W\right)}{\delta x}\Delta x+\frac{k_s\left(T_S-T_P\right)}{\delta y}\Delta y-\frac{k_n\left(T_P-T_N\right)}{\delta y}\Delta y+\bar{S}\,\Delta x\Delta y \qquad (6.2)$$

The discretization equation:

$$a_P T_P = a_E T_E + a_W T_W + a_N T_N + a_S T_S + b \qquad (6.3)$$

where:

$$a_E=\frac{k_e\Delta y}{\delta x}$$

$$a_E = \frac{k_e \Delta y}{\delta x}$$

$$a_W = \frac{k_w \Delta y}{\delta x}$$

$$a_N = \frac{k_n \Delta x}{\delta y}$$

$$a_S = \frac{k_s \Delta x}{\delta y}$$

$$a_P^0 = \frac{\rho_P^0 c \Delta x \Delta y}{\Delta t}$$

$$b = S_C \Delta x \, \Delta y + a_P^0 T_P^0$$

$$a_P = a_E + a_W + a_N + a_S + a_P^0 - S_P \Delta x \Delta y$$

and, S_C and S_P come from the linearization of the source term $S = S_C + S_P T_P$. It is worth mentioning that all the thermal conductivities are the harmonic means of the grid points. This is because of the possible abrupt change in thermal conductivity between materials (such as tube wall and liquid in the present case). In addition here we are talking of thermal conductivity, but in the general case this parameter could be viscosity or turbulent viscosity; therefore, even if a case of large thermal conductivity variations is not very frequent unless different material are involved, situations with large differences in viscosity or turbulent viscosity can easily be encountered in turbulent flows for instance. If one assumes that the thermal conductivity is a linear function of the values at P and E and the control volume face lies at midway between P and E, then:

$$k_e = 0.5 k_P + 0.5 k_E \qquad (6.4)$$

Another approach is to realize that what is important here is the heat flux at the boundary (that must be (?) the same for both materials) and thus by assuming that grid points P and E are part of two different materials and the faces of the control volume equally spaced between grid points, one gets:

$$q_e = \frac{T_P - T_E}{\frac{\delta x}{k_P} + \frac{\delta x}{k_E}} \tag{6.5}$$

but because $q_e = \frac{k_e(T_P - T_E)}{\delta x}$, one gets:

$$k_e = 0.5\left(\frac{1}{k_P} + \frac{1}{k_E}\right)^{-1} \tag{6.6}$$

Equ. (6.6) is a very powerful way to express thermal conductivity, because it can handle very sharp variation of thermal conductivity. In fact, if $k_E \rightarrow 0$ (the face is insulated) Equ. (6.6) gives $k_e \rightarrow 0$, meaning that the heat flux at this face is zero; Equ. (6.4) would have lead to $k_e = 0.5k_P$. More detailed information on this issue can be found in Patankar [1].

The solution of the discretization equations (Equ. (6.3)) in one dimension, because of its particular form gives rise to the Thomas algorithm also called the TDMA (Tri-Diagonal Matrix Algorithm). The same algorithm cannot be extended in multiple dimensions. Direct methods can be employed here, but for large numbers of grid points, the huge amount of computer memory and time make this operation quite expensive. A different approach is therefore adopted. The algebraic system can be solved iteratively with the Gauss-Seidel method, for instance evaluating the variables at each grid point. Only when all grid points have been visited, one iteration of the Gauss-Seidel method is done. The number of iterations stops when certain imposed residual has been achieved. A combination of the one dimensional TDMA and Gauss-Seidel methods can be made. This method is termed line-by-line method where the TDMA method is applied along each line and the entire computational domain is covered line-by-line. The advantage of this method is that the information from the ends of each line is brought into the domain at once. The idea behind the ADI (Alternating Direction Implicit) methods is to alternate the line direction along which TDMA is performed and bringing the information from all the boundaries into the domain. It is clear that sometimes, especially when the temperature at one specific boundary is known, this method results in a very powerful one.

So far, we have discussed the case of Cartesian coordinate system, but other systems can be employed (such as cylindrical) with very little differences. For more and detailed information on this issue the reader can refer to Patankar [1].

The next step is to introduce convection. We will assume first that the flow field is given for the time being. If so, the system of PDE to be solved includes N-S. There is no major difficulty in the discretization formulation as it remains of the same form as Equ. (6.3) and the only difference is in the expression of its coefficients that become:

$$a_E = D_e - \frac{F_e}{2}$$

$$a_W = D_w + \frac{F_w}{2}$$

$$a_N = D_n - \frac{F_n}{2}$$

$$a_S = D_s + \frac{F_s}{2}$$

$$a_P^0 = \frac{\rho_P^0 \Delta x \Delta y}{\Delta t}$$

$$b = S_C \Delta x \, \Delta y + a_P^0 \phi_P^0$$

$$a_P = a_E + a_W + a_N + a_S + a_P^0 - S_P \Delta x \Delta y$$

where ϕ is now a general variable (no longer temperature) and $D_e = \frac{\Gamma}{\delta x}$ and $F_e = \rho u$ are the diffusion conductance and convection strength respectively. Now an important problem arises: the competition between convection and diffusion forces. If F is many times larger than D, the solution given by Equ. (6.3) could become unrealistic. This because some of the coefficients of Equ. (6.3) can become negative and this goes against one of the rules for realistic solution given by Equ. (6.3) as discussed in Patankar [1]. This problem can be solved by introducing different solution schemes such as the up-wind scheme, the exponential scheme (also termed exact solution), the hybrid scheme, the central difference scheme, the power-law scheme. As extensively discussed in Patankar [1] each of this schemes is suitable in a particular range of

Peclet number. The Peclet number is the ratio of convection to diffusion ($Pe = \frac{F}{D}$). As shown by Figure 6.2 extracted from Patankar [1], the power-law scheme is the most accurate. The hybrid scheme is also good. The central difference scheme is fairly good for $Pe < 2$, whereas for larger Pe the up-wind is better. What is important, however, is the grid Peclet number. Therefore, by acting on the grid spacing one can in theory refine the grid to have local $Pe < 2$ and use a central difference scheme. Sometimes this is not possible because of the prohibitive number of grid points to be used in flows with very high velocity gradients. In these cases a different scheme must be used to obtain accurate predictions. In general the coefficients of Equ. (6.3) become:

$$a_E = D_e + \|-F_e, 0\|$$

$$a_W = D_w + \|F_w, 0\|$$

$$a_N = D_n + \|-F_n, 0\|$$

$$a_S = D_s + \|F_s, 0\|$$

where the symbol $\|A,B\|$ means the higher between A and B.

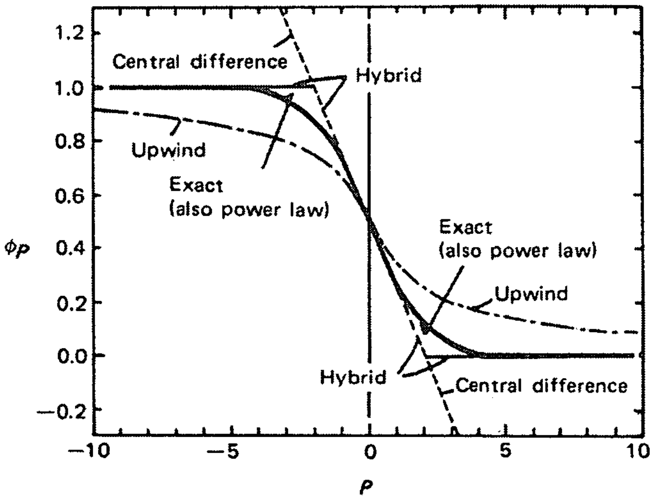

Figure 6.2 Influence of various schemes on the variable prediction (taken from Patankar [1]).

It is appropriate here to make a point on the false diffusion concept as it still leads to some misleading conclusions. It is said that the central scheme is more accurate than the up-wind one. This is misleading, because it is true only at small values of Δx, where the Taylor expansion really shows that central difference is more accurate than up-wind and this latter introduces an artificial diffusion coefficient. As properly shown in Patankar [1], what really matters is the *Pe* as it dictates which scheme is more accurate.

The next step is to seek a solution also for the flow field. For this we have to solve the continuity equation and introduce a representation for the pressure gradient in N-S. By integrating the continuity and the pressure gradient term on the control volume one gets a pressure drop on the control volume depending only on alternating grid points; no information on adjacent grid points is provided. This is a potential disaster as "zig-zag" pressure fields are accepted as solution. The same conclusion is valid for the continuity equation. The remedy to this issue is represented by what is called the staggered grid. In practice the velocity components are evaluated at the grid points on the faces of the control volume, whereas all other variables are evaluated in the usual grid points. A schematic of the staggered grid is presented in Figure 6.3.

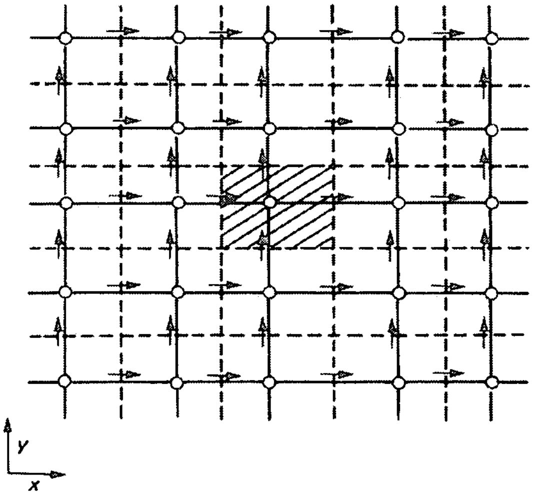

Figure 6.3 Staggered grid arrangement; → u, v ↑ and o all other variables (taken from Patankar [1]).

There is a further difficulty to be handled: the solution we seek is by means of iterative solvers. Therefore, we start, for instance, from a guessed field of pressure. Then the N-S discretization equation is solved for the velocity components that obey also the continuity equation. The pressure is thus evaluated and in general does not coincide with the one guessed. Therefore, a new value for pressure (solving the pressure correction equation) must be obtained and the iterative procedure goes ahead. This is the essence of the SIMPLE (Semi-Implicit Method for Pressure-Linked Equations) algorithm. Details on this procedure that has become a standard in iterative algorithms for CFD can be found in Patankar [1]. An extension of the SIMPLE algorithm is the SIMPLER or SIMPLE Revised one. In the derivation of the pressure correction equation for the SIMPLE algorithm a term with the velocity correction from neighbourhood points is removed, leaving therefore to pressure the task of correcting the velocities. This leads to quite large pressure correction that requires sometimes under-relaxation to speed up the convergence. An alternative way is to use the pressure correction equation to correct the velocities and use another equation of the same kind as Equ. (6.3) to obtain the pressure field. So, the pressure correction is used only to correct the velocity but is not added to the guessed pressure field. This procedure by splitting the task of correction between velocities and pressure, does provide an improved convergence rate.

We have now a fairly clear view of the FVM and all the tricks necessary to seek an iterative solution for the system of PDE for heat transfer and fluid flow. In what follows we will concentrate on the particular case to be simulated here by means of a numerical code based on FVM developed by Bennacer and El-Ganaoui in references [2-3]. The major contribution of the present work is the coordinate transformation employed. As discussed earlier, the faces of the control volume must be orthogonal in order to correctly evaluate the flux of the relevant variable across the boundaries of the control volume. The FVM elucidated earlier can be extended to all kind of orthogonal coordinate systems such as cylindrical, spherical and more generally curvilinear. Problems start arising when the geometry is irregular and no simple orthogonal coordinate systems can be employed. In such cases, two ways are possible. Either an orthogonal grid is constructed or the original problem is transformed. The construction of an orthogonal grid is itself sometimes a difficult task. So difficult, that many grid generator codes have appeared and are still being developed for commercial applications where the case of irregular domains is not unusual. The other strategy of transforming the original problem, relies on the fact that coordinate transformation techniques can be employed and the system of PDE is transformed; the computational grid however is very simple, at limit with proper choice can be reduced to square boxes. We will not attempt here to fully discuss all the related issues with these two techniques as specialised books are available on this interesting and commercially attractive subject. In order to understand how the grid generation is important it is worth saying that up to 80% of the time spent to perform a numerical analysis on real problems with an irregular domain is devoted to create a suitable grid. So, it makes sense to think of a good strategy when faced with the grid generation.

In what follows we will recall this problems and provide more insights into the subject also giving relevant references.

6.3 Numerical method

The physical domain representing half the tube diametrical section is sketched in Figure 6.4. Only the liquid phase is modelled here.

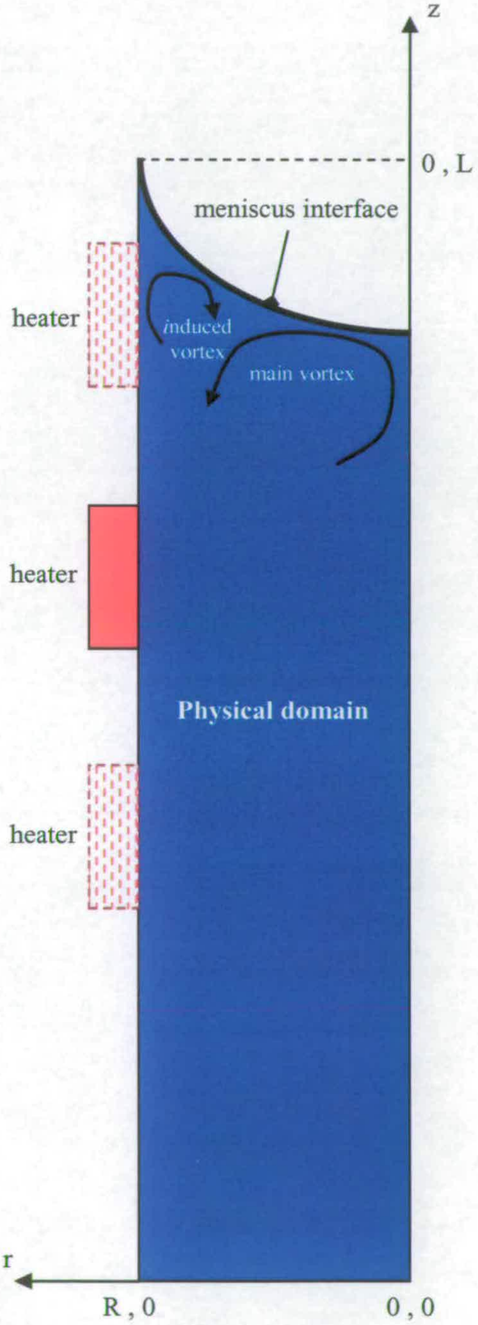

A = L/R = 5

Figure 6.4 Physical domain on the meniscus liquid phase showing heater positions and typical convection pattern.

It was demonstrated in Chapter II that the vapour phase influences the convection in the liquid phase essentially because of the vapour partial pressure. Therefore, in this model we do not account for the vapour phase. The natural convection outside the tube and the conduction through the wall material are also not accounted for in this study. Despite the fact that these aspects are important to completely describe the heat transfer mechanism between the liquid inside the pore and the surrounding environment, they are found not to be determining in the present case as the conclusions reached are independent of these parameters. In fact, the phenomena being described are essentially controlled by what happens at the meniscus interface where mass is transferred from the liquid to the vapour phase. The environment surrounding the capillary tube supplies or contributes in supplying (when the heater is turned on) the heat necessary to sustain the evaporation as demonstrated in Chapters IV-V with TLC and IR investigation. The 2-D axisymmetric computational domain reported in Figure 6.4 with an aspect ratio (A=L/R) of 5 suffices in describing the flow in the capillary tube.

6.3.1 Unheated capillary tubes

We consider first the case of the unheated tube. The meniscus studied is shown in Figure 6.5; the left part (**a**) is shows a portion of the capillary tube partially filled with liquid, and the right part (**b**) is the domain of study with boundary conditions in dimensionless form. The configuration contains liquid and vapor phases separated by an evaporation interface. In order to avoid the roughness of the tube and the contact angle effect a planar interface is considered for the time being to focus only on the interaction between the thermal conditions at the interface and the convection appearing in the liquid phase. The other issue of the curved interface will be addressed later when a coordinate transformation will be introduced. An axi-symmetric domain is considered for numerical simulation. It consists of a rectangular domain of length L and radius R ($A = L/R$). The solid wall is maintained at a temperature T_0. On the free surface a permanent heat flux is imposed, $Q(r) = Q_0\ q(r)$, where $q(r)$ is a dimensionless function of the axial coordinate r and Q_0 the constant flux case considered as the reference heat flux used for the dimensionless temperature. For the time being, because the objective of this first numerical investigation is to find out which kind of interfacial heat flux (essentially its profile) is working for the present case, we do not attempt here to impose a realistic value for Q_0. Later on, however, this issue will be addressed as the values of the evaporation mass flux are available from previous measurements (Chapter II).

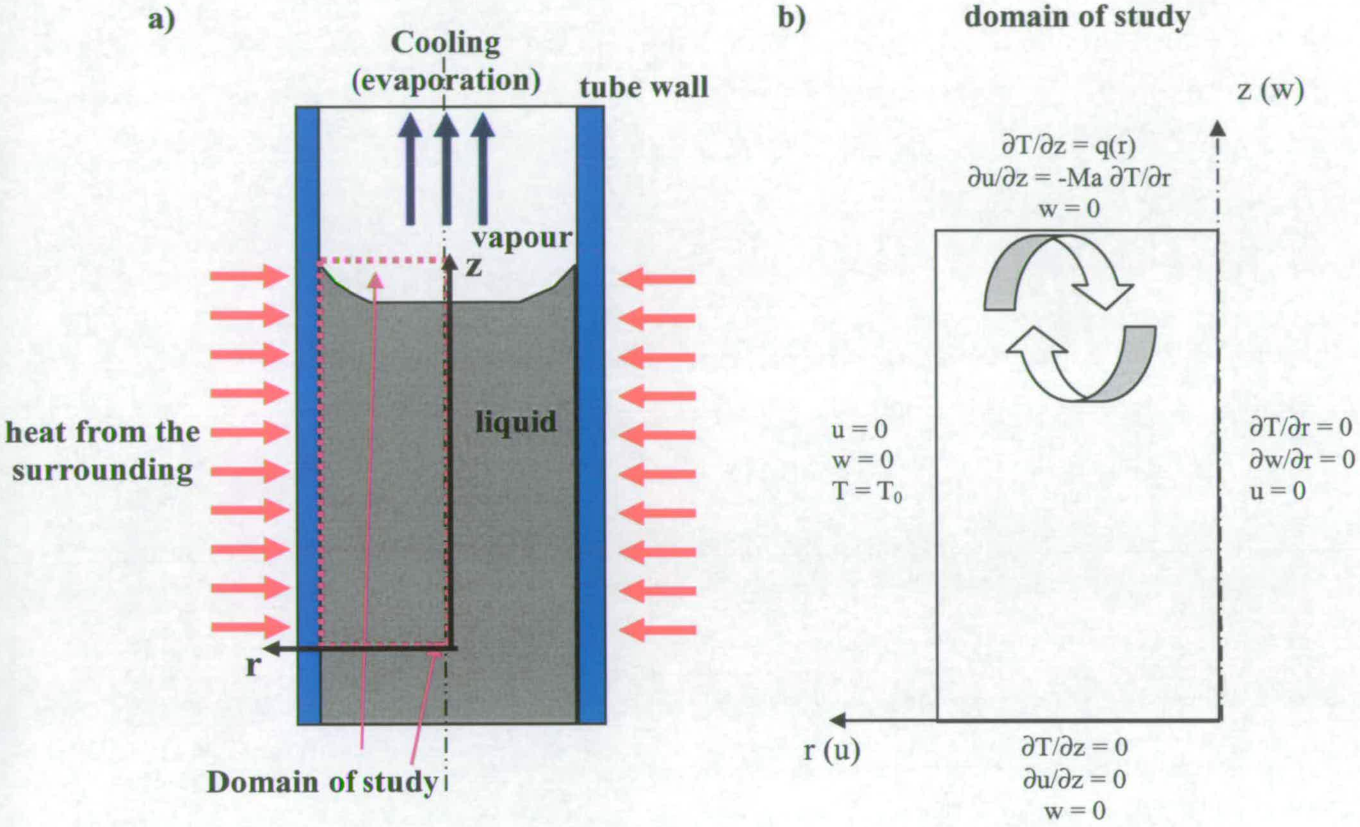

Figure 6.5 Schematic of the global problem (**a**) and domain of study with boundary conditions (**b**).

Constant, polynomial and Gaussian *q(r)* distributions (Figure 6.6) are used to model different evaporating (cooling) fluxes at the free surface.

It is worth noting that in a similar case relating to welding Ramanan and Korpela [4] used a Gaussian distribution of imposed heat flux since it is proven to be a realistic one for welding experiments.

The fluid is assumed Newtonian with constant physical properties (namely dynamic viscosity μ and thermal diffusivity α), the surface tension being linearly dependent on temperature as in Equ. (2.2).

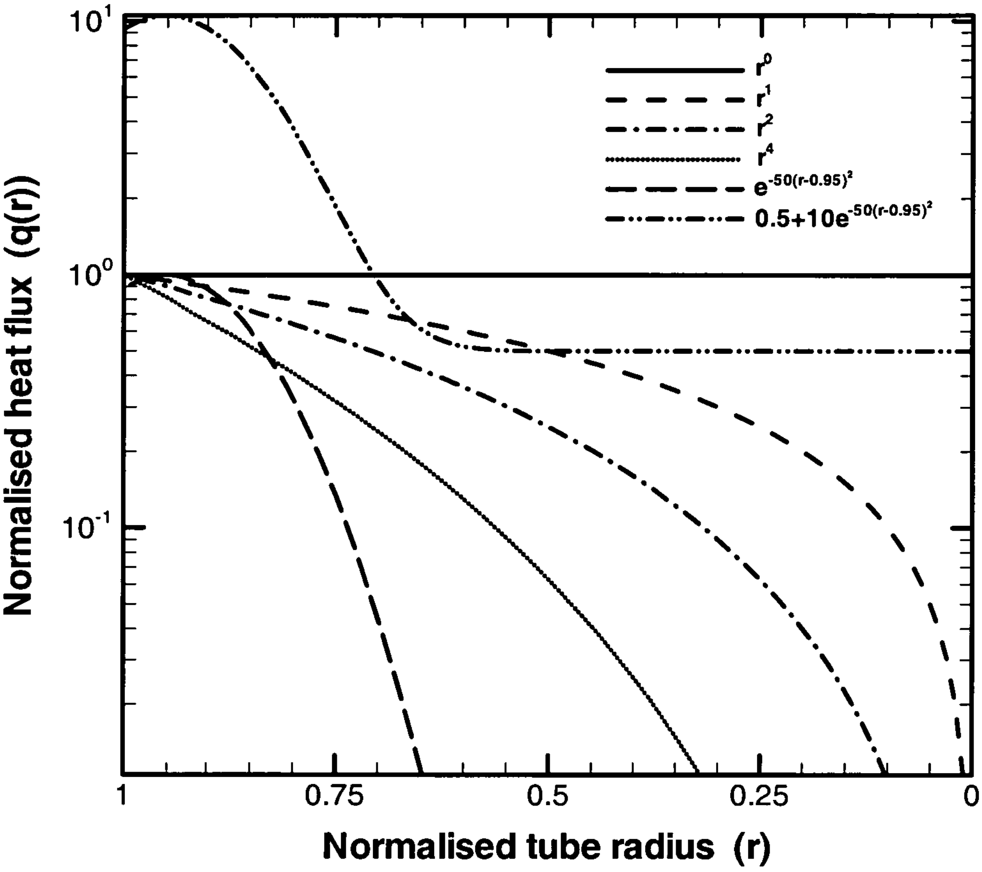

Figure 6.6 Various heat flux profiles imposed at the meniscus.

The liquid flow is assumed incompressible and laminar. Introducing R, κ/R^2, $\rho\kappa^2/R^2$ and Q_0R/k as length, time, pressure and temperature scale factor, the mass, momentum and energy conservation equations can be written in the following non-dimensional form:

$$\nabla \cdot \mathbf{u} = 0 \tag{6.7}$$

$$\frac{Du}{Dt} = -\nabla p + Pr\, \nabla^2 \mathbf{u} \tag{6.8}$$

$$\frac{DT}{Dt} = \nabla^2 T \qquad (6.9)$$

where $\mathbf{u} = u_r \vec{i} + u_z \vec{j}$, $\frac{D()}{Dt} = \frac{\partial()}{\partial t} + u\nabla()$ and $\nabla = \frac{\partial^2()}{\partial r^2} + \frac{1}{r}\frac{\partial()}{\partial r} + \frac{\partial^2()}{\partial z^2}$. The boundary dimensionless conditions (BCs) appearing on Figure 6.5 (**b**) are as follows.

At the upper boundary (r = 1) the temperature is assumed to be uniform (T_0) and the no slip condition is applied:

$$T(1,z) = 1 \text{ and } u(1,z) = 0 \qquad (6.10)$$

At the meniscus interface (z = A) the heat flux profile and the normal component of the velocity vector are imposed, whereas the tangent velocity component obeys to the surface tension driven equation:

$$\frac{\partial T(r,A)}{\partial z} = q(r),\ u_z(r,A) = 0 \text{ and } \frac{\partial u_r(r,A)}{\partial z} = -Ma\frac{\partial T(r,A)}{\partial r} \qquad (6.11)$$

At the symmetry axis (r = 0):

$$u_r(0,z) = \frac{\partial u_z(0,z)}{\partial r} = \frac{\partial T(0,z)}{\partial r} = 0 \qquad (6.12)$$

At the left side of the computational domain, far away from the meniscus interface (z = 0):

$$u_z(r,0) = \frac{\partial u_r(r,0)}{\partial r} = \frac{\partial T(r,0)}{\partial z} = 0 \qquad (6.13)$$

Appearing in the mathematical model, the Prandtl number defined as the ratio of kinematics to thermal diffusion is $Pr = \frac{\nu}{\alpha}$ and the Marangoni number defined as the ratio of surface tension to viscous forces is $Ma=-\frac{\partial\sigma}{\partial T}\frac{\Delta T R}{\mu\kappa}$. In this work, the liquid considered corresponds to *Pr=10* and high aspect ratio are tested to simulate a long tube, the ratio *A*=5 is found sufficient, for a range of *Ma* and slope and shape of the axial cooling.

A Peclet number ($Pe=\frac{V}{V_{ref}}=\frac{\frac{\dot{m}}{\rho A}}{\frac{\alpha}{R}}$) is introduced to account for the Poiseuille liquid re-supply flow established in the tube to bring liquid towards the meniscus where mass is lost because of evaporation.

The control volume approach of Patankar [1], showing good ability to describe heat and mass transfers for stiff fluid mechanics problems. The Raspo and El Ganaoui [2] approach is used for discretization of the governing equations Equ. (6.7-6.9) associated with boundary conditions Equ. (6.10-6.13). Because this algorithm is essentially a sequential one, the strong pressure-velocity coupling is poorly represented by an iterative solution. The convergence of such a method is low with fine grids and the information from the BCs are slowly propagated into the computational domain. Direct methods solve these problems but are too much demanding in terms of memory and computational time. The idea is to take the advantages of both indirect and direct methods avoiding their drawbacks. Therefore, the problem can be solved iteratively on a fine grid and directly on a coarse one. This is essentially the idea behind the multigrid approach [5-7]. Iterative methods are attractive for their low storage requirements, but suffer in dealing with the residual's low frequency components. An Alternating Direct Implicit (ADI) method (Patankar [1], Abbot [8]) coupled with block correction (Kelkar and Patankar [9], Kim and Ro [10]) is employed for the coarse grid. The block correction approach is of the multigrid methods family and consists in adding a uniform correction along the lines of constant index in the computational domain and then solving a TDMA system. It has been demonstrated that the ADI as well as the block correction method are able to cut off the low frequency component of the residual; they have been coupled here to reinforce their effect. The advection-diffusion terms in the PDE are approximated by a second order centred scheme which gives a good approximation in those cases with grid Peclet number below 2. The pressure-velocity interlinking is solved using the

SIMPLE algorithm. The advection-diffusion terms are approximated using a second order centered scheme. This is possible because the grid *Pe* is less than 2.

With the curved meniscus interface, a change is needed for solving the problem using the FVM method of Patankar [1]. The curved interface leads to a distorted grid and therefore the control volume approach cannot be used in this case. In fact, this method implies the control volume faces must be perpendicular to the velocity vectors in order to correctly evaluate the flux across the faces. Therefore, it is necessary that an orthogonal grid is employed in order to avoid complex discretization techniques (Patankar [1]). There are two general solutions to this problem: either the grid in the physical space is orthogonalized with the use of a conformal mapping technique and the same system of PDE and BC for cylindrical coordinates is used or the problem is transformed using coordinate transformation technique. In the former approach all the computational effort is devoted to create the orthogonal grid; as reported in Thompson et al. [11], this could be done for many configurations, solving essentially the Laplace system when the point distribution at all boundaries is given or a less complex parabolic or hyperbolic system when certain boundaries are left free. Solving the Laplace system is computationally more complex, but the result is a smoother grid even though a distribution point with strong skewness is given (Thompson et al. [11]). The orthogonal mapping technique is used by Cliffe and Tavener [12] to study stability problems on Marangoni convection in 2-D cavities with deformable free surface. However, the transformation technique seems to be strongly attractive for this particular case because it can easily handle moving boundary conditions as for the case of receding meniscus described in Chapter II. We will not attempt to solve the case of moving boundary conditions in the present work; however, the case is being considered for future development. The problem is solved on the computational space that is orthogonal (being rectangular or even square if a further dimensionalization is introduced). The set of PDE and BC to be solved is changed by some metric coefficients coming from the transformation law. The coordinate transformation used here is based on the Landau transformation (Tavener and Cliffe [13]):

$$\begin{aligned} X &= \frac{x}{C(y)} \\ Y &= y \end{aligned} \qquad (6.14)$$

The curve C(y) here is a circumference because we make the assumption of a spherical meniscus shape. The grid is thus transformed from the physical space (x,y) to the computational domain (X,Y) as schematically shown in Figure 6.7 (note that in this figure a general shape for the interface is assumed). A non uniform grid generation has been used for refinement close to the meniscus interface and at the tube's wall and axis.

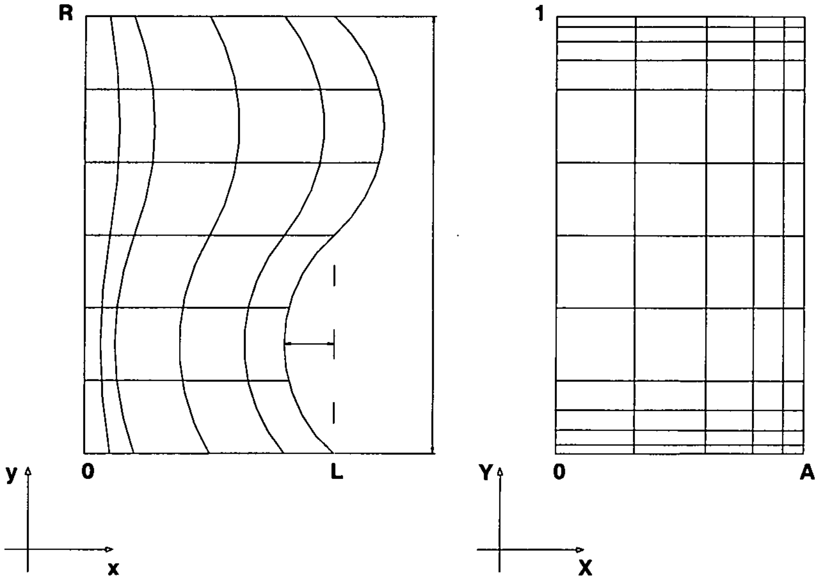

Figure 6.7 Physical (left) and computational (right) domains.

6.3.2 Heated capillary tubes

In the case of heated capillary tubes, the same set of PDE (6.7-6.9) and BC (6.11-6.13) is valid, apart from BC (6.10) that becomes:

$$T(1,z) = 1 + \Delta T_{Step}\,[1-25(z-z_0)^8]^2 \text{ and } u(1,z) = 0, \quad (6.15)$$

In order to take into account that at the upper boundary ($r = 1$) a step in temperature centred in z_0 is imposed (to simulate the heating element) must be applied.

6.3.3 Code validation and mesh sensitivity analysis

General validation of the code was undertaken by comparison to the spectral method results presented in Kasperski et al. [14] and Kasperski and Labrosse [15]; for details of this comparison see Bennacer et al. [3]. Table 6.1 reproduces a comparison of the dimensionless max temperature (T_{max}) and max velocity (U_{max}) for a range of Pr and Ma. Fairly good agreement is found between the results of the two codes although the differences increase at lower Pr.

Figure 6.1 Comparison between present FVM and SM of Kasperski et al. [14-15].

		Present FVM code		*Kasperski et al. [14-15]*	
Pr	**Ma**	**T_{max}**	**U_{max}**	**T_{max}**	**U_{max}**
100	5,000	0.39 (±0.5%)	31.7 (±0.7%)	0.39	31.50
	10,000	0.34 (±1.1%)	38.9 (±1.2%)	0.34	38.46
10	5,000	0.38 (±0.0%)	31.5 (±0.7%)	0.38	21.30
	10,000	0.33 (±0.9%)	38.6 (±0.3%)	0.33	38.69
0.01	500	0.73 (±8.6%)	9.2 (±6.6%)	0.67	9.80
	1,000	0.65 (±8.0%)	12.2 (±0.6%)	0.60	12.23
	5,000	0.49 (±5.3%)	21.6 (±5.2%)	0.47	20.43

In order to ensure that the results are grid size independent for the present problem, a mesh sensitivity analysis was undertaken which is summarized in Table 6.2. Very fine grids near the boundaries are adopted. This refinement is necessary to resolve narrow singularity flow. The difference between predictions using a 81x41 mesh and the reference grid (241x121) was less than 2.0% for the maximum T and U -velocity component on the free surface. The difference between the results obtained using a 121x61 and the reference was less than 0.4% and therefore 121x61 or 181x91 grids are used for the following computations

The equations were then solved to ensure conservation of mass, momentum and energy in the liquid phase, both globally and locally, to a prescribed tolerance (typically 10^{-6}).

Table 6.2 Effect of the mesh refinement on the maximum values of temperature (T_{max}) and velocity (U_{max}) on the free surface ($A = 2$, $Ma = 3\text{x}10^3$ and $Pr = 1$).

Nz x Nr	*81x41*	*121x41*	*161x61*	*161x81*	*241x121*
T_{max}	0.3037 (0.10%)[•]	0.3036 (0.06%)[•]	0.3035 (0.03%)[•]	0.3034 (0.0%)[•]	0.3034
U_{max}	104.31 (1.5%)[•]	103.79 (1%)[•]	103.20 (0.4%)[•]	102.92 (0.14%)[•]	102.77

[•] Deviation between the results (relative to the Nz x Nr = 241x121 case)

6.4 Results and discussion

As pointed out in previous chapters, the tube sizes considered in the present study allow us to neglect the gravity effect (buoyancy). Strong thermocapillary convection was experimentally observed to be resulting from evaporation. The orientation of the convective cells is found to be dependent on the heat flux distribution along the meniscus. In fact the real driving force for convection is the tangential capillary stress at the interface generated by the interfacial temperature gradient self created by evaporation. This gradient is itself influenced by the convection in the bulk liquid. Indeed the thermocapillary convection tends to bring hotter liquid from the bulk toward the interface increasing the temperature at the center and consequently the strength of the convection. On the other hand hot liquid is also brought from the meniscus centre to the wedge where most of the evaporation takes place. This produces a local increase of temperature at the wedge and a consequent reduction of the temperature gradient driving force.

The local evaporation rate is dictated by the local vapour pressure, which is strongly dependent on the local temperature and the vapour diffusion from the interface to the gas bulk phase. These values are ultimately dictated by the strong evaporation at the meniscus triple line region.

6.4.1 Unheated capillary tubes

Various heat flux distributions are applied along the meniscus to determine conditions under which thermocapillary convection develops and ultimately sets in (Figure 6.6) The applied fluxes consider polynomial, Gaussian and combined profiles. It is worth mentioning that the exponential profile is the closest to the realistic one as observed by Wayner and Potash [16] and Sartre et al. [17].

The direct numerical simulation allows the access to the interfacial temperature as reported in Figure 6.8.

It can be noticed that the saturated expression induces a temperature profile close to the one observed by Höhmann and Stephan [18] for a heated evaporating meniscus of water exhibiting a minimum value near the contact line and the IR results on the interfacial temperature profile presented in Chapter V.

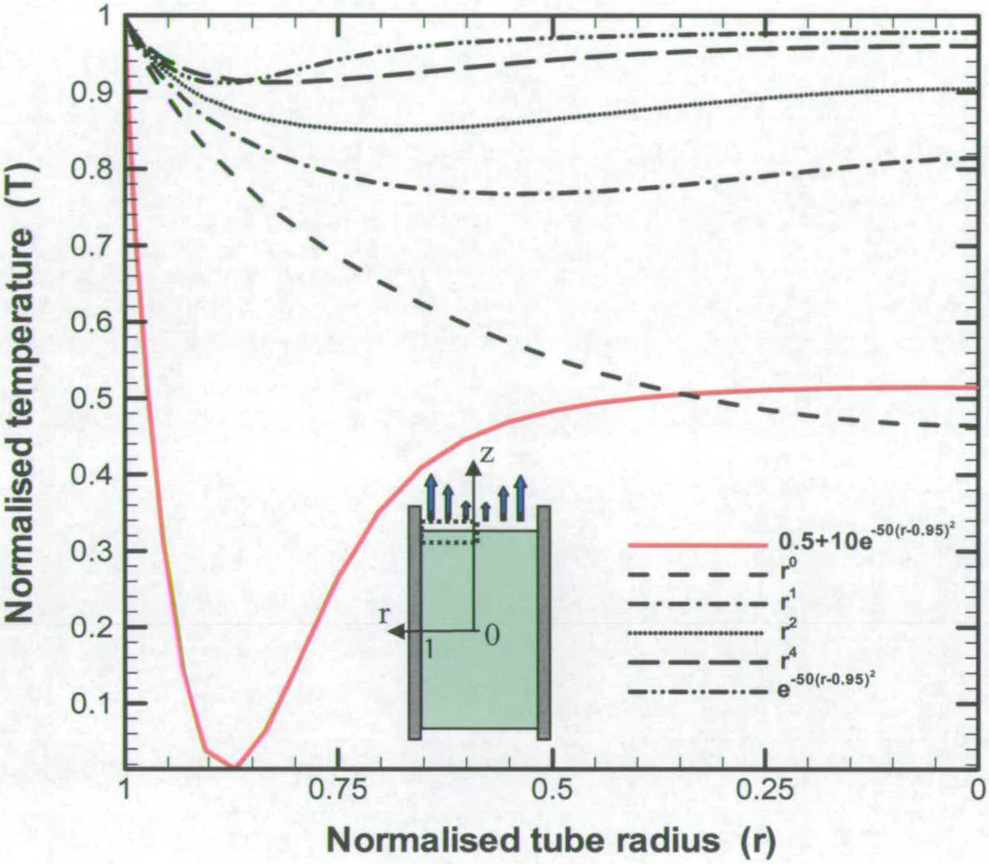

Figure 6.8 Interfacial temperature profile for the different heat flux profiles of Figure 6.6.

Figure 6.9 describes the resulting temperature gradients for the various investigated heat flux profiles. As a first observation, the inversion of the temperature gradient occurs for non-linear heat flux profiles. Polynomial profile induces weak radial temperature gradient leading to a rotating convective cell from the contact line to the centre in disagreement with experimental observations. Assuming an exponential heat flux profile, the radial gradient exhibits a minimum value near the contact line and the convective pattern is similar to the one observed experimentally (see Chapter III).

Two regions can be distinguished: the first one from the centre to the location of minimum temperature where the temperature gradient is supposed to generate a cell rotating from the centre to the contact line; the second region (near the corner) with a convective cell rotating in the opposite direction. In the experiment the second cell is not observed, only the main cell rotating from the centre to the contact line has been clearly identified. This can be explained by the fact that the second convective cell near the wall is hindered by wall friction forces and also because of an unsuitable particle size or a large optical distortion, as discussed in Chapter III. This implies that a minimum irregularity in evaporative heat flux will initiate Marangoni convection. Whilst it is experimentally difficult to access to the local evaporation rate, the numerical simulation can be an effective tool to describe the controlling parameters.

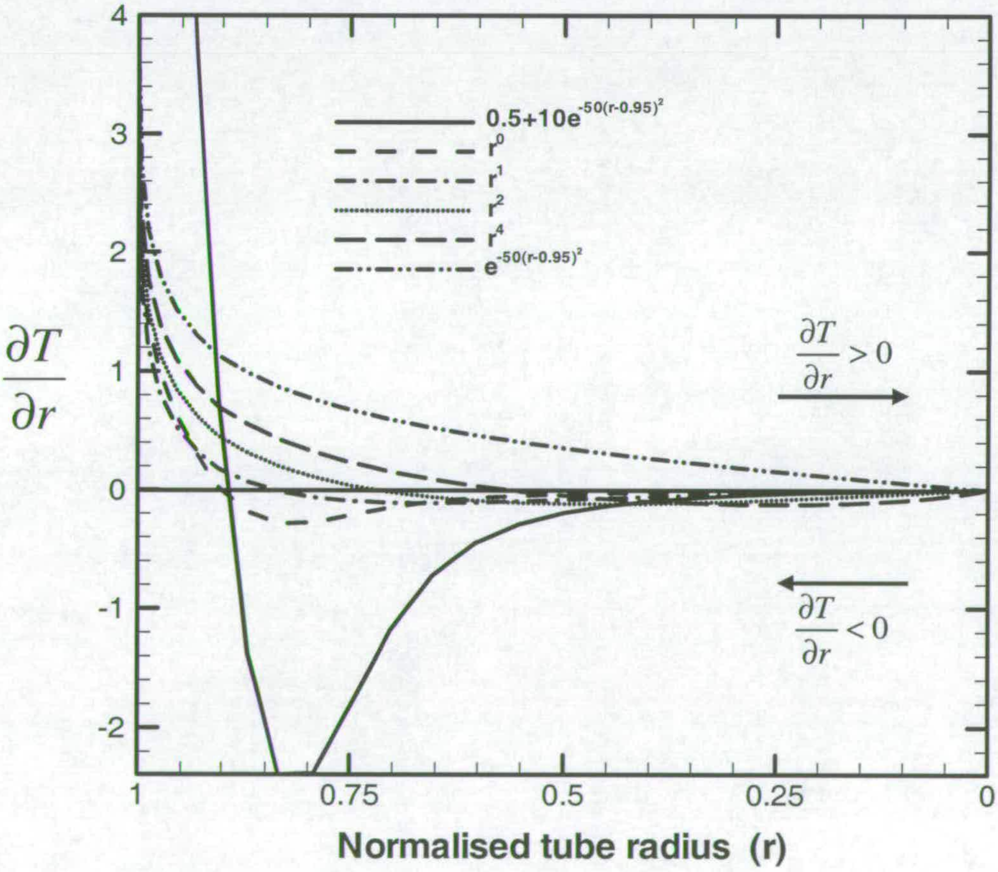

Figure 6.9 Temperature gradients for the various heat flux distributions of Figure 6.6.

The model has been applied for this first case of unheated tubes to find the interfacial temperature for a range of Marangoni numbers. An example of obtained temperature and flow field is shown in Figure 6.10 for the case of *Ma*=10 that reveals the existence of threshold for a thermocapillary convection. Note that the convection strength is represented by the stream function. Note also that the velocity vectors are superimposed to the stream function map. Figure 6.11 shows the temperature distribution for various Marangoni numbers. The temperature varies uniformly for the location *r*=3/4 of the radius and increases exponentially near the wall. This increase is similar for various considered *Ma*. It can be noticed that the minimum value of the interfacial temperature in Figure 6.11 for different *Ma* changes little whereas the interfacial temperature at the centre is strongly affected by the *Ma* variation essentially because of the stronger convection at higher *Ma* that bring more hot fluid from the liquid bulk.

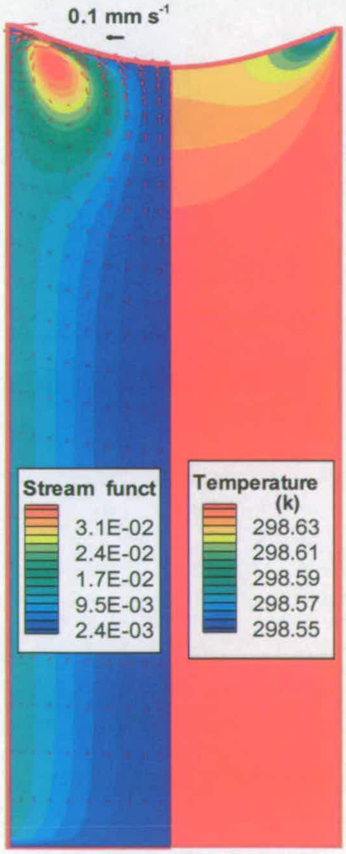

Figure 6.10 Flow field (left) and temperature field (right) for the unheated capillary tube.

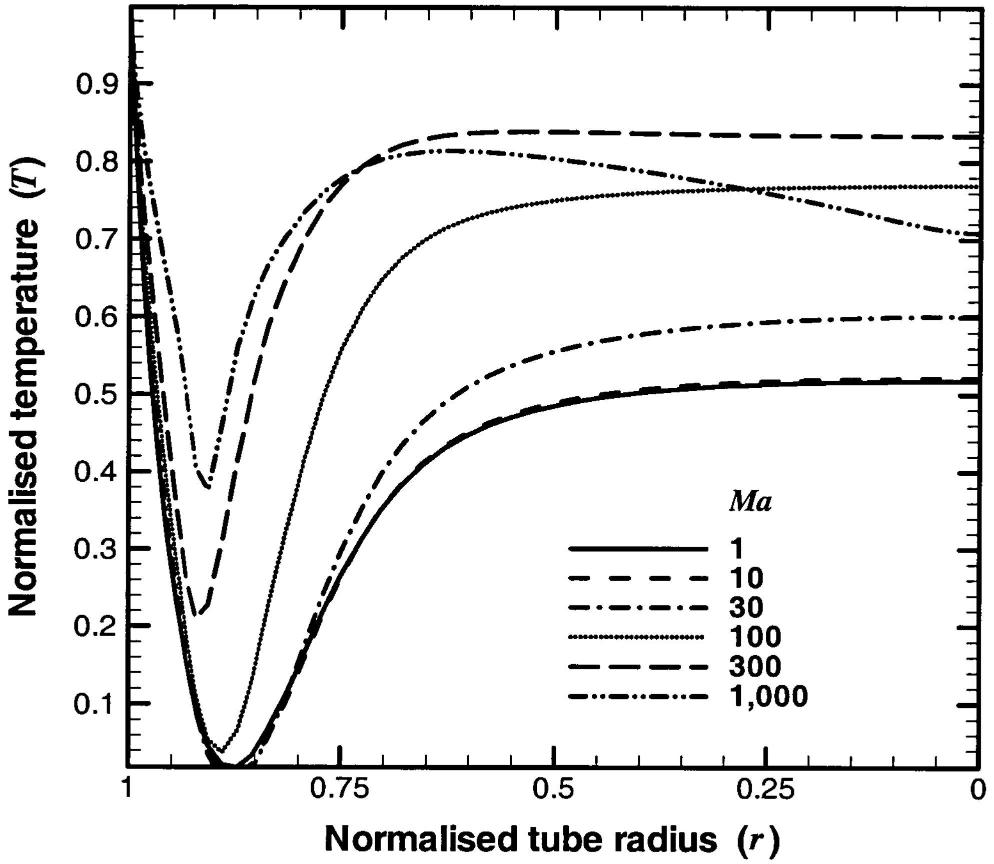

Figure 6.11 Temperature distribution along the meniscus interface for different *Ma*.

Figure 6.12 shows the profile of the interfacial radial velocity on the main cell versus *Ma*. This difference represents the magnitude of the driving surface tension forces. The interesting observation is the increase in the temperature difference with *Ma* resulting from the increase in flow strength (see Figure 6.13). The convective motion brings hot fluid to the centre of the interface allowing higher ΔT. When a particular *Ma* value is reached the ΔT decreases because of hotter fluid brought from the meniscus centre to the contact line region. It can thus be concluded that the system is regulated through the flow strength. We have also the appearance of a new cell in the tube axis region (as shown in the inset of Figure 6.12) that could be explained because of the symmetrical BC on the tube axis allowing physically a even number of cells; this loss of symmetry is possibly due to the 3-D flow structure as observed experimentally in Chapter III.

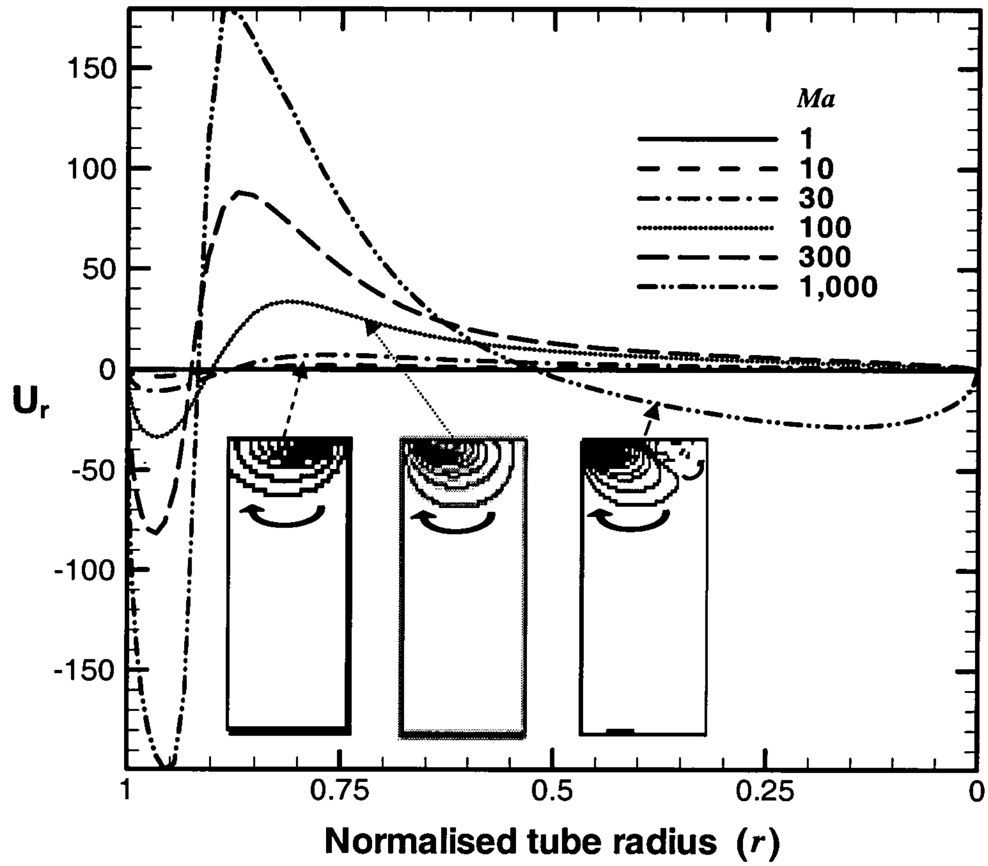

Figure 6.12 Profile of the interfacial radial velocity for different *Ma*.

The regression line drawn in Figure 6.13 has the following expression:

$$U_{max} = 0.11\, Ma^{1.24} \qquad (6.16)$$

In this preliminary study of unheated tubes it has been demonstrated that thermocapillary Marangoni convection can set in if a Gaussian heat flux distribution along the interface is present. The particular shape of the distribution is dictated by the evaporation mass flux that is larger in the contact line region of the meniscus compared to its centre. It is clearly shown that the heat flux distribution is indeed responsible for the orientation of the Marangoni cells.

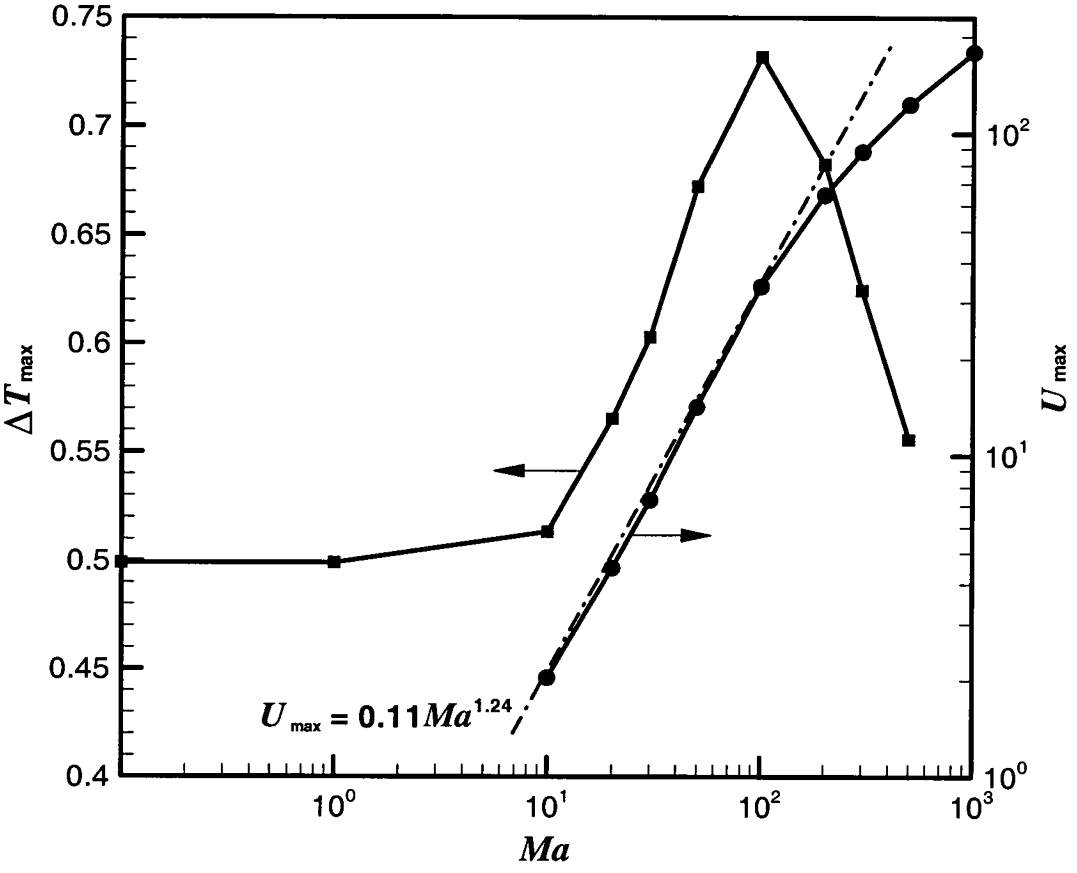

Figure 6.13 Max interfacial radial velocity and max temperature difference along the meniscus interface vs. *Ma*.

6.4.2 Heated capillary tubes

The results related to the case of heated capillary tubes are presented in this section through the investigation of the cases of the heater either in the vapour or the liquid side of the meniscus.

In the following numerical results we will concentrate on the stream function value as a measure of the convection strength. We will first make a quantitative comparison with the experiments in the case of the heater in the liquid side. For this case the model is closer to the reality because we know that the meniscus does not move from the tube mouth and the fraction of the heater power going into the system can be evaluated with confidence. The IR measurements of the tube temperature described in Chapter V define the temperature step applied in Equ. (6.15) and the measured mass flux defines the total evaporative heat flux imposed along the meniscus. The evaporative heat flux profile along the interface is kept similar regardless the heat power applied with the extra heating element. More difficult is the case with the heater in the vapour side. In fact, as the heater is switched on the temperature along the tube wall starts to rise. The meniscus lies in an increasing temperature gradient and is pushed down the tube (because not anchored) till a new equilibrium position is reached as described in Chapter V. In this case it becomes more difficult to estimate the fraction of power delivered by the extra heating element going into the liquid phase. In addition the higher the heater power the greater the fraction of heat transferred to the vapour inside the tube. Therefore, for the case of the heater in the vapour side the numerical analysis has to be considered in a qualitative way.

Table 6.3 Relevant parameters for quantitative comparison between experiments and numerical analysis.

Power ***(W)***	ΔT_{Menis} ***(K)***	ΔT_{Step} ***(K)***	$10^9 \dot{m}$ $(kg\ s^{-1})$	***Pe***	***Ma***
0	0.5	0	1.83	0.0267	10.0772
0.4	0.71	4.14	2.12	0.0310	14.3661
0.7	0.98	5.43	2.47	0.0361	19.7514
1.08	1.42	6.74	2.80	0.0409	28.6194
1.4	1.56	7.59	3.09	0.0451	31.4410

Table 6.3 reports all relevant parameters for the quantitative comparison in the case of the heater in the liquid side, such as evaporation mass flux and dimensionless numbers. ΔT_{Menis} and ΔT_{Step} are the temperature differences along the meniscus and on the tube this latter is generated by the heating element. Figure 6.14 shows the velocity map with superimposed stream lines (left) and temperature map (right) for the case of

heater off. Note that only a portion of the computational domain close to the meniscus interface is shown. There are typically two vortices, the main vortex occupies most of the computational domain and the induced one develops near the meniscus wedge. During experiments only the main vortex has been visualised. The induced vortex near the meniscus wedge was not seen probably because of large optical distortion in that region of the tube and non suitable tracer size.

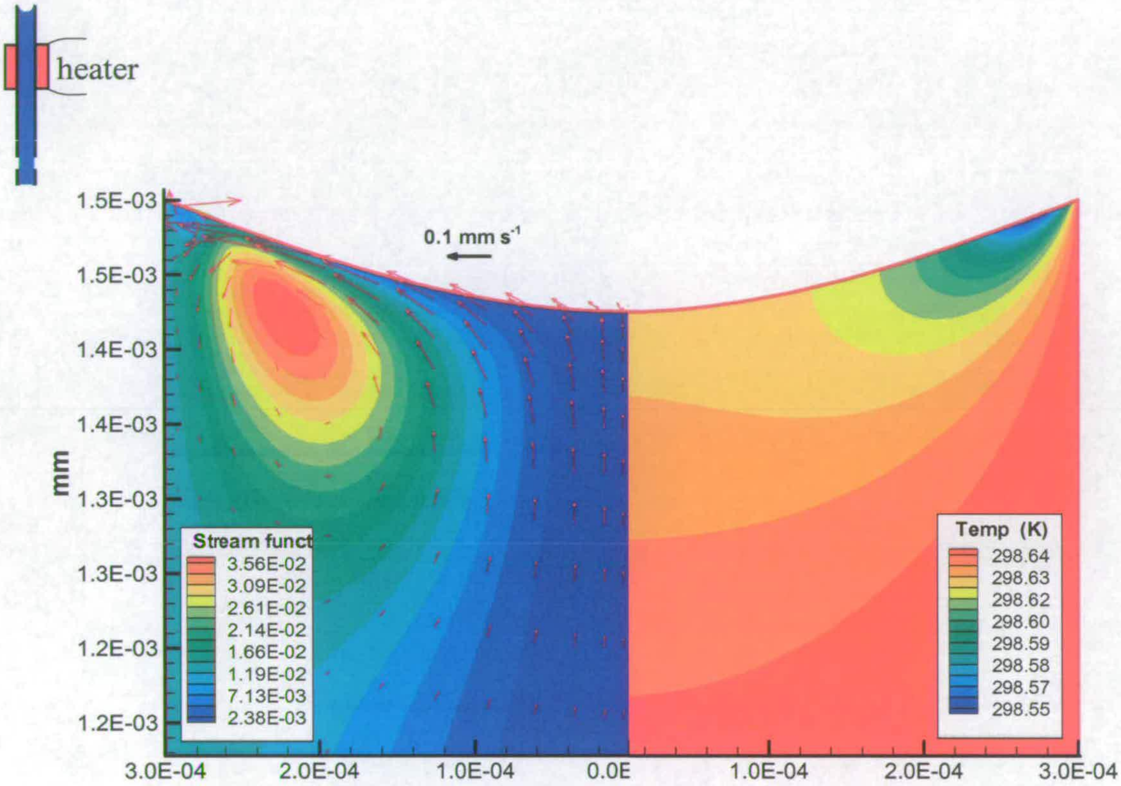

Figure 6.14 Temperature (right) and stream function superimposed to velocity vector fields (left) for heater in the liquid side (heater "OFF".

It can be seen that there is a fairly good qualitative agreement between the experimental (Figure 3.24, case of heater off) and the numerical results of Figure 6.14. This point is reinforced by the results of Table 6.4 for different heating powers, where a comparison between the experimental and numerical velocity value at one particular point on paths along and towards the meniscus has been made. As can be seen from

Table 6.4, there is a good agreement between experimental and numerical results, particularly for the velocity towards the meniscus. The less good agreement found along the meniscus could be due to the fact that in the simulations we have used *Ma* based on the temperature difference between the wedge and the centre of the meniscus, regardless to the real temperature profile. In reality, as shown in Chapter V, the temperature profile is highly non linear and therefore the assumption made here has probably led to less accurate results for the velocity along the meniscus. In addition, large differences in Table 6.4 as for powers 0 and 0.7 W are also due to poor cross-correlation for the μ-PIV measurements due to the lack of particles in that region (see Figure 3.24).

Table 6.4 Experimental-Numerical comparison of velocity value towards and along the meniscus.

Heater power (W)	V_{Exp} $(mm\ s^{-1})$		V_{Num} $(mm\ s^{-1})$		V_{Exp}-V_{Num} *(%)*	
	Towards	**Along**	**Towards**	**Along**	**Towards**	**Along**
0	0.039	0.008	0.035	0.011	10	27
0.3	0.053	0.024	0.056	0.021	5	13
0.7	0.065	0.037	0.064	0.025	2	32
1.08	0.068	0.027	0.071	0.03	3	10
1.4	0.079	0.038	0.081	0.04	2	5

As mentioned earlier, the case of the heater in the vapour side is more difficult to simulate, because of both the lack of experimental data (as the temperature profile along the interface was not measured because the meniscus lies far inside the tube and therefore no IR measurements were possible) and of a moving interface with the heater power as outlined earlier. Therefore, for this case the comparison between experiments and simulations must be considered as qualitative only. The extra heating element is localized at the end of the computational domain close to the interface as we do not consider here the vapour phase and the wall material. As shown in Figure 6.15 (where the heater power is increasing from left to right and top to bottom), with low power introduced by the heating element the convection pattern is affected but not inverted with respect to the unheated case. When sufficient power is delivered (Figure 6.15, bottom row), the convection pattern is inverted. This qualitatively agrees well with the experimental findings reported in Chapter III (Figures 3.26-3.27).

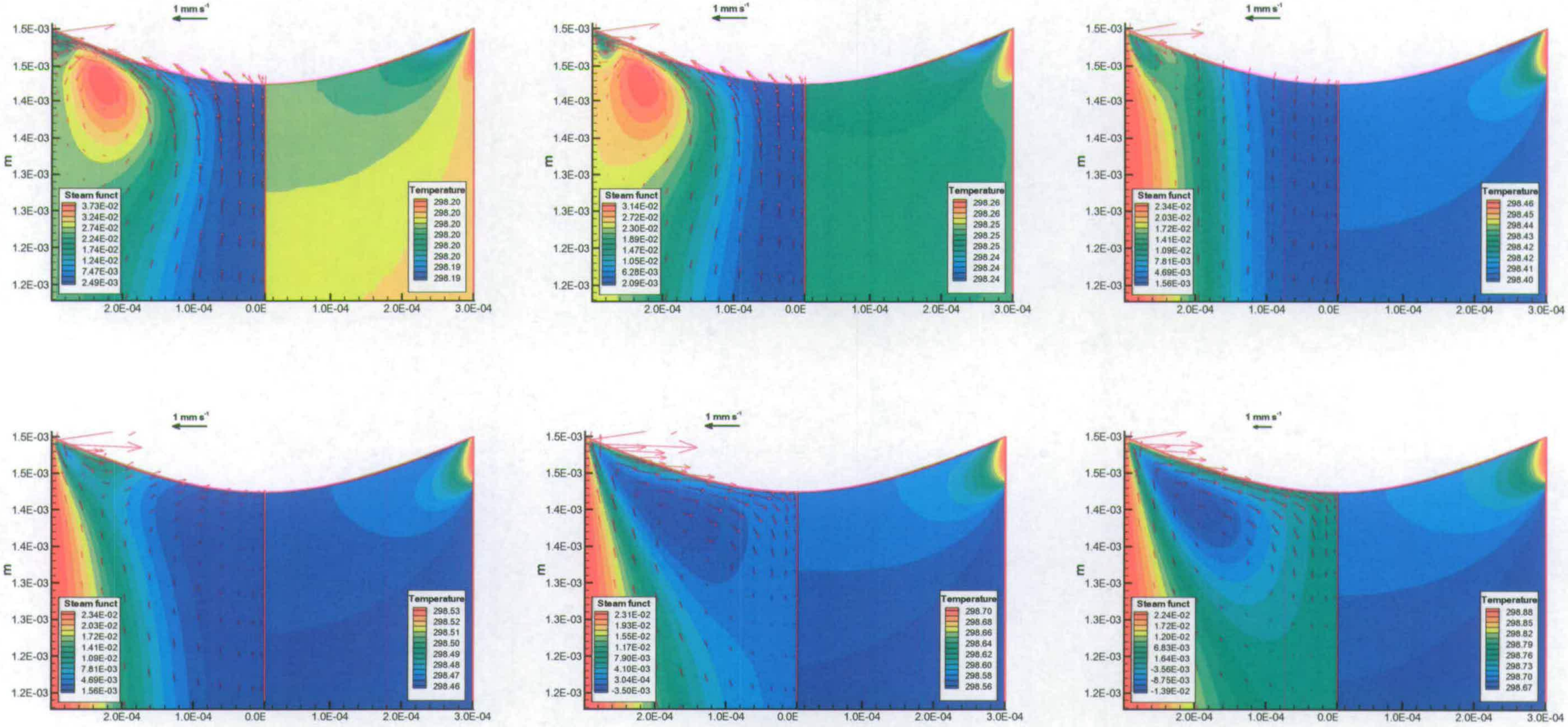

Figure 6.15 Temperature and stream function superimposed to velocity vector fields showing inversion of convection (heater power is increasing from left to right and top to bottom).

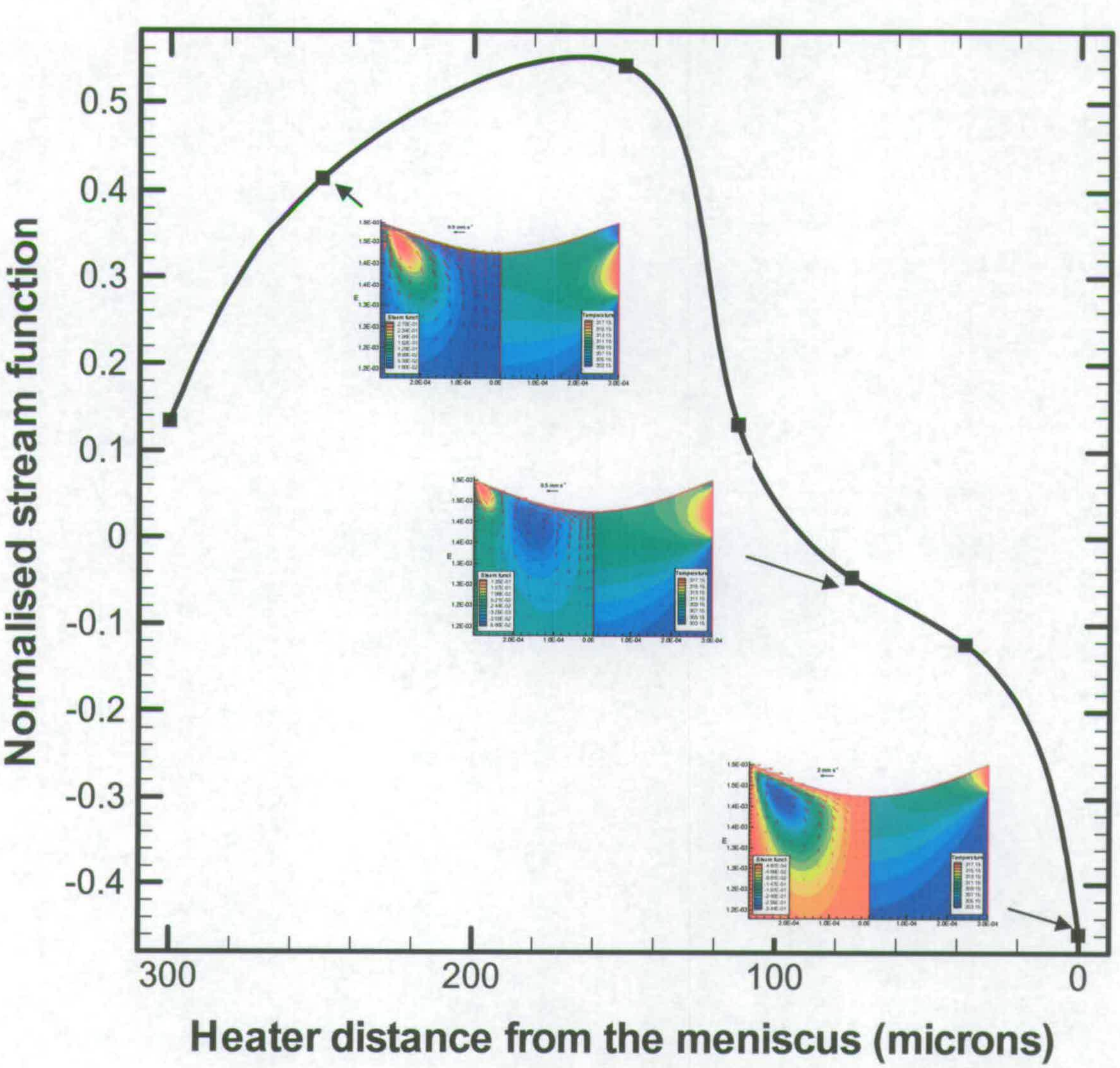

Figure 6.16 Normalised main vortex stream functions vs. heater position (points are numerical data and curve is best fit).

In the following we will describe the results obtained when moving the extra heating element in the fashion shown in Figure 6.4. The apparent meniscus contact angle is kept constant for the moment and we assume that the evaporation mass flux (and consequently *Pe*) and *Ma* are constant. The power of the heating element is also kept constant. These assumptions can be accepted here as we are looking for qualitative results only and in addition no experimental data are available. Figure 6.16 shows the effect that sliding the heater has on the convection stream function value. The convection pattern is not affected when the heater is far away from the interface. However, as the heater approaches the interface, the convection is strongly affected and eventually the pattern is inverted as also confirmed by the flow map in the insets of Figure 6.16.

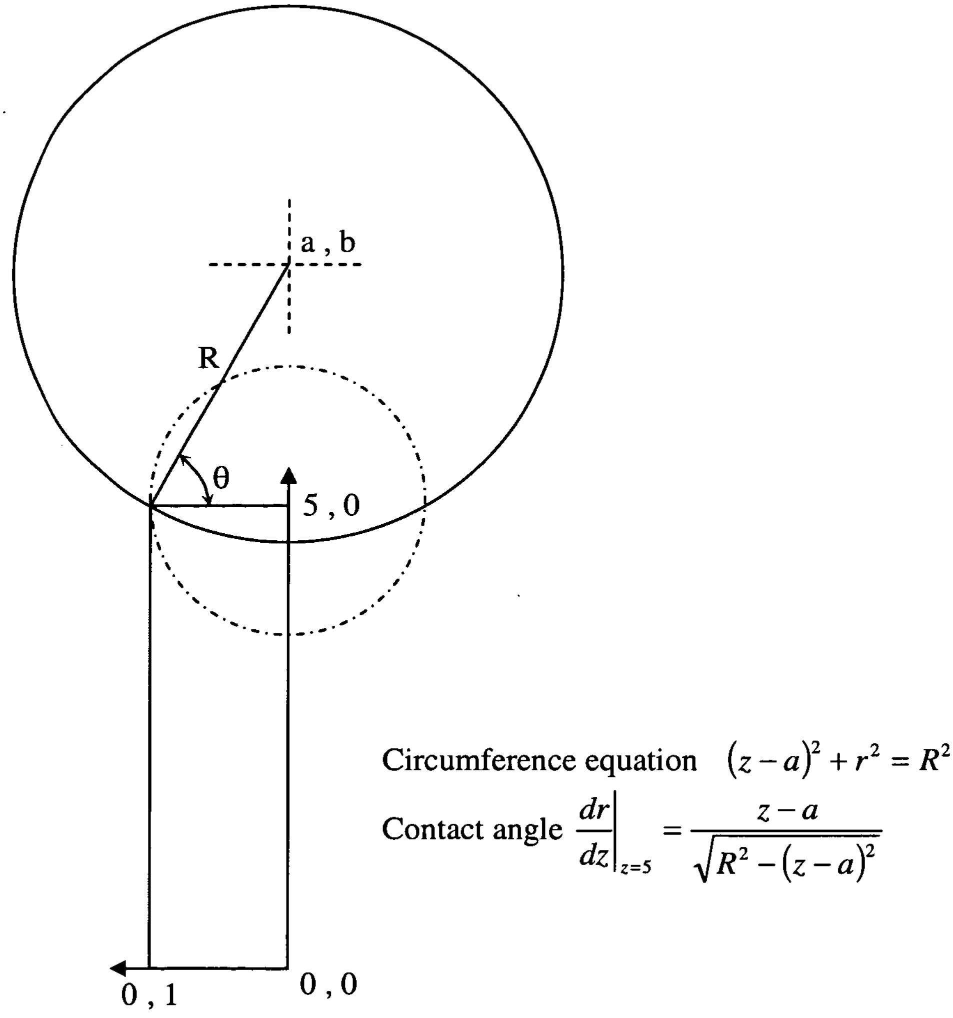

Circumference equation $(z-a)^2 + r^2 = R^2$

Contact angle $\left.\frac{dr}{dz}\right|_{z=5} = \frac{z-a}{\sqrt{R^2-(z-a)^2}}$

Figure 6.17 Meniscus shape and contact angle determination.

Another qualitative study can be made by changing the apparent contact angle. The apparent contact angle is an important parameter in the evaporation from a meniscus, as most of the heat and mass transfer is concentrated in the contact line region. In practice, the apparent contact angle can be altered by surface roughness or just altering the surface tension (by changing wall material and/or liquid, and using surface active agents). In this qualitative study about the apparent contact angle effect, we have kept constant the evaporation mass flux (and consequently *Pe*) and *Ma*; the heating element position and its power is also kept fixed. Because we assume here that the meniscus shape is a spherical cap the entire range of apparent contact angles (0-90 degree) can be studied by sliding the sphere centre while increasing its radius in the fashion shown schematically in Figure 6.17. Figure 6.18 illustrates the effect of apparent contact angle on the convection pattern. As the apparent contact angle is decreased, the main vortex is weakened; at a certain apparent contact angle the secondary vortex strengthens and the main one is further weakened.

In the following some useful discussion follows for the heated capillary tubes in order to explain the findings. Because of the liquids' low boiling point, there is a substantial evaporation even without extra heating provided. It has been understood (as also discussed in Chapter II) that the convection pattern revealed in this case is mainly due to a non uniform evaporation rate along the meniscus, being larger near the meniscus wedge than at the meniscus centre. This fact causes a non uniform interfacial thermal field that is basically responsible for the thermocapillary convection observed. When extra heating is supplied by the use of an electric heater, the convection pattern is altered and eventually reversed. In the two extreme situations experimentally tested in Chapter III, we have noticed that when the heater is positioned in the meniscus liquid side the convection is influenced but no flow inversion takes place at any heater power; eventually, at high powers the liquid starts to boil in the micro-channel. This could be explained with the use of the sketch in Figure 6.19. With the Heater "OFF", the expected temperature at the meniscus wedge (T^-) is lower than that in the centre (T^+). When the heater has been switched on, more energy is introduced into the system and a different gradient of temperature is created along the tube's walls, but the temperature differences along the meniscus interface keeps the same sign. This essentially because we can assume that the temperature at the meniscus centre for the Heater "ON" case of Figure 6.19 is the one at the tube wall (point *A*) which is higher than that at the tube mouth (T_c). A different scenario takes place with the heater lying in the vapour side (Figure 6.20). Again, with the Heater "OFF" the temperature difference is similar to the one in Figure 6.19 (Heater "OFF"). However, in this case switching on the heater creates a gradient of temperature along the tube's walls that will affect the temperature profile at the interface. Energy is conducted through the wall material and an opposite temperature gradient is established along the interface, basically because we can reasonably assume that the temperature at the meniscus centre is similar to the one at the correspondent point *A* on the wall. If the heater power is strong enough the temperature difference along the meniscus interface self-generated because of evaporation is counter balanced by the one imposed by the heater and a net nil gradient is present. So, despite the liquid continues to evaporate, no convection is observed. Increasing further the heater power, the resulting temperature gradient is eventually inverted with the lower temperature now at the meniscus centre. This leads to the convection inversion experimentally observed (Figure 3.27). The numerical results agree qualitatively well with the experiments when the heater is in the liquid side. Because we have not considered the vapour phase and the tube's external environment, no numerical investigation has been performed with the heater lying completely in the vapour side.

As pointed out earlier, more complicated to investigate experimentally is the case when the heater is aligned with the meniscus interface. The heater in not transparent for flow visualization and its length is higher than the meniscus cap height. We have thus used the numerical code to investigate these options. Depending on the heater position with respect to the meniscus interface and the contact angle, there could be some portions of the meniscus interface where the temperature gradient changes sign with respect to the case of the heater off. This is basically the reason why firstly a second vortex appears at the meniscus centre contra-rotating with respect to the main one and then the convection pattern is ultimately inverted as the heating element is moved towards the meniscus triple line. Although we have not numerically studied the case with the heating element in the vapour side, the results obtained when its position lies close to the meniscus interface but still in the liquid show clearly that it is indeed the interfacial temperature profile which dictates the convection pattern experimentally observed for the two extreme cases investigated.

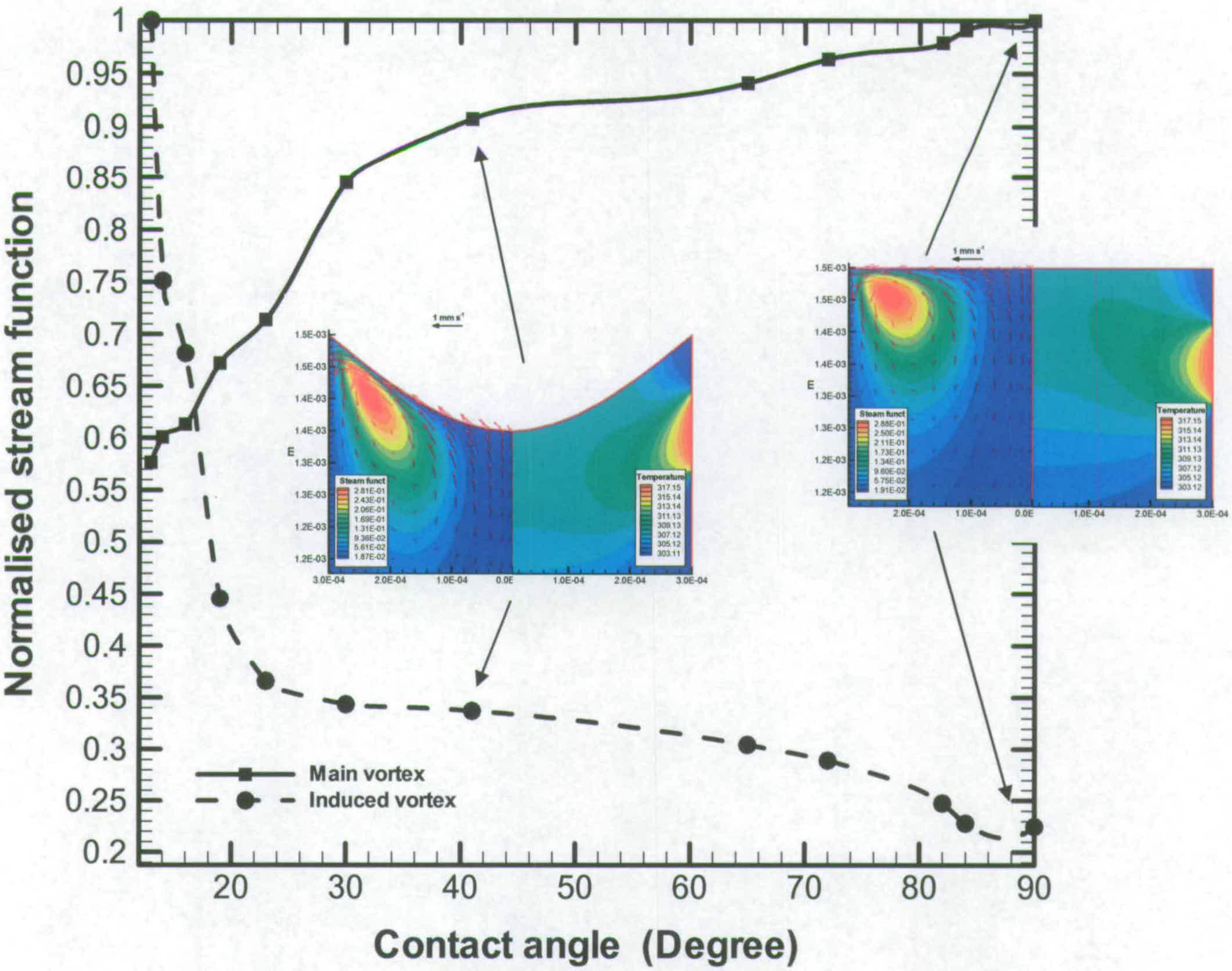

Figure 6.18 Normalised vortices stream function vs. meniscus contact angle.

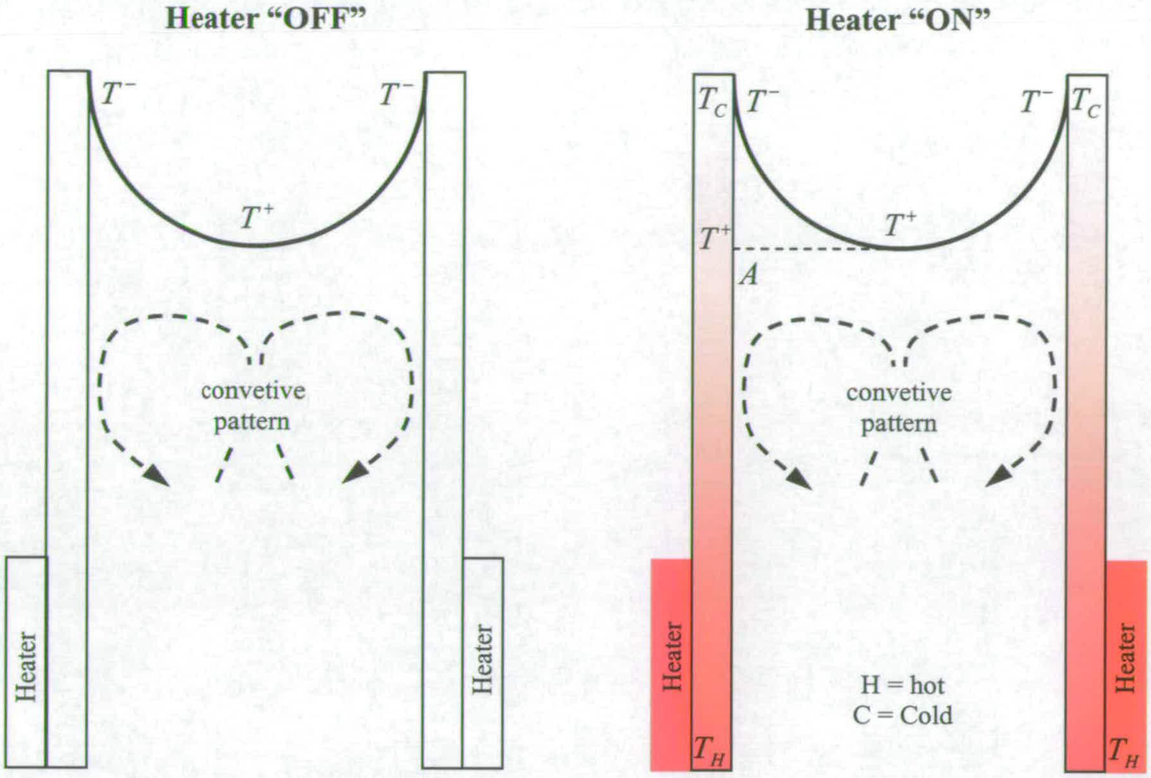

Figure 6.19 Temperature profile along the meniscus interface (heater in the meniscus liquid phase).

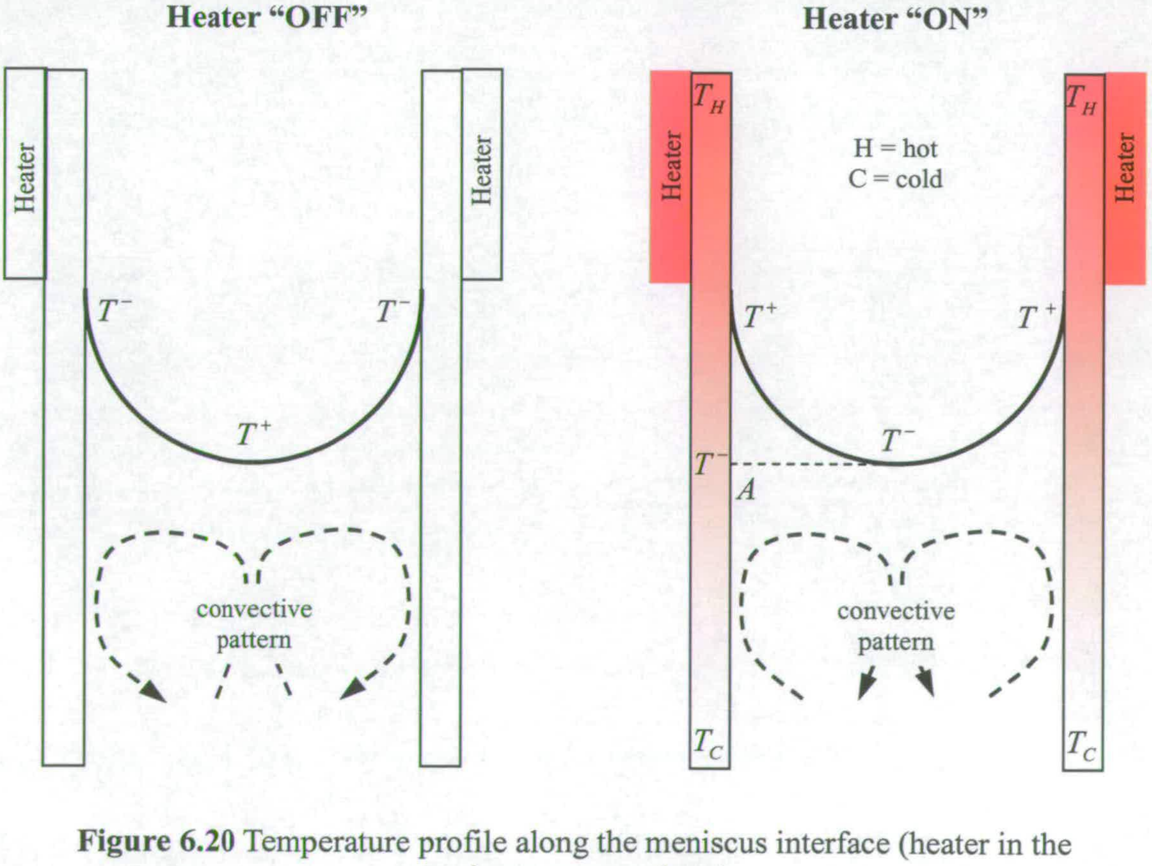

Figure 6.20 Temperature profile along the meniscus interface (heater in the meniscus vapour phase).

6.5 Conclusions and outlook

In previous chapters we have investigated experimentally the self-induced thermocapillary liquid convection for an evaporating liquid in capillary tubes. Experimental results on flow patterns and temperature distribution along the meniscus and on the capillary tube walls were gathered by means of different techniques such as μ-PIV, TLC and IR. Different cases were experimentally investigated: four liquids, four capillary tube sizes, horizontally and vertically oriented tubes as well as unheated and heated tubes. For the latter case, the meniscus was positioned above or below the heating element and it was observed that when the meniscus is below the heating element the convection pattern can be reversed with respect to the unheated case.

In the present chapter, we compare the experimental findings with the numerical results from a code based on FVM method. The contribution to the numerical code used here and developed by a French research group to study crystal growth related problems where a solid-liquid interface was present, has been to adapt the code to the present case where a liquid-vapour interface is present. In addition, a coordinate transformation technique is employed to take into account the curved meniscus shape. It is shown that the heat flux profile along the meniscus must have a Gaussian distribution to set in a convection pattern similar to the one experimentally observed for the unheated capillaries. A similar profile of heat flux is also used to investigate numerically the cases of heated capillaries. The code has been used first to reproduce the experimental results for the two extreme cases of heating element in the vapour and liquid side and was further used to investigate all those interesting situations not easily reproducible experimentally. The case of the heating element in the liquid side has shown a fairly good quantitative agreement with the experiments. Good qualitative agreement is also found in the case of the heating element in the vapour side. The change in the meniscus contact angle and the case with the heater aligned with the meniscus interface were easily reproduced numerically. The interesting results obtained allowed us to draw important conclusions on the driving mechanism for the convection observed experimentally in the liquid phase of the meniscus. The numerical method clearly confirms that the interfacial temperature profile is the key factor for the thermocapillary convection characteristic of the present investigation.

This numerical investigation confirmed what was guessed from the experimental findings described in previous chapters about the driving mechanism of the self-induced thermocapillary convection. In addition it has been proven how a numerical analysis can predict correctly the problem tackled and be effectively used for a parametric analysis.

6.6 References

[1] Patankar S.V., 1980, *Numerical heat transfer and fluid flow*, Hemisphere, New York.

[2] Raspo I. and El Ganaoui M., 2002, *Computations of instabilities in complex fluid mechanic problems using efficient finite volume methods. In Finite Volumes for Complex Applications-Problems and Perspectives*, Edited by R. Herbin and D. Kröner, Hermes Penton Science, pp. 631-638.

[3] Bennacer R., Mohamad A.A. and Leonardi E., 2002, *The Effect Of Heat Flux Distribution On Thermo-Capillary Convection In A Side-Heated Liquid Bridge*, Numerical Heat Transfer, Part A, Vol. 45, pp. 3725-3740.

[4] Ramanan N. and Korpela S.A., 1990, *Thermocapillary convection in an axi-symmetric pool*, Computers & Fluids, Vol. 18, No. 2, pp. 205-215.

[5] Brandt A., 1977, *Multilevel adaptive solution to boundary-value problems*, Math. Comp. 31, pp. 333-390.

[6] McCormick S.F., 1989, *Multilevel adaptive methods for partial differential equations*, Frontier on Applied Mathematics, SIAM, Philadelphia, PA.

[7] Hutchinson B.R. and Raithby G.D., 1986, *A multigrid method based on the adaptive correction strategy*, Numerical Heat Transfer, Vol. 9, pp. 511-537.

[8] Abbott M.B. and Basco D.R., 1989, *Computational fluid dynamics : an introduction for engineers*, 1st Edition, Addison Wesley, New York.

[9] Kelkar K.M. and Patankar S.V., 1989, *Development of a generalised block correction procedures for the solution of discretized Navier-Stokes equations*, Computer Physics Communication, Vol. 53, pp. 329-336.

[10] Kim C.-J. and Ro S.T., 1995, *A block correction aided strongly implicit solver for the five-point formulation of elliptic differential equations*, Int. Journal of Heat and Mass Transfer, Vol. 38, No. 6, pp. 999-1008.

[11] Thompson J.E., Warsi Z.U.A. and Mastin C.W., 1985, *Numerical grid generation: foundations and applications*, Elsevier Science Publishing Co., Inc.

[12] Cliffe K.A. and Tavener S.J., 1998, *Marangoni- Bénard Convection with a Deformable Free Surface*, Journal of computational Physics, Vol. 145, pp. 193-227.

[13] Tavener S.J. and Cliffe K.A., 2002, *Two-Fluid Marangoni-Bénard Convection with a Deformable Interface*, Journal of computational Physics, Vol. 182, pp. 277-300.

[14] Kasperski G., Batoul A. and Labrosse G., 2000, *Up to unsteadiness of axi-symmetric thermocapillary flows in a laterally heated liquid bridge*, Physics of Fluids, Vol. 12, No. 1, pp. 103-119.

[15] Kasperski G. and Labrosse G., 2000, *On the numerical treatment of viscous singularities in wall-confined thermo-capillary convection*, Physics of Fluids, Vol. 12, No. 11, pp. 2695-2697.

[16] Wayner J.P. and Potash J.M., 1970, *Fluid Flow in an Evaporating Meniscus.* in AIChE 63rd Annual General Meeting, Chicago.

[17] Sartre V., Zaghdordi M.C. and Lallemand M., 2000, *Effect of interfacial phenomena on evaporative heat transfer in micro heat pipes*, International Journal Thermal Science, Vol. 39, pp. 498-504.

[18] Höhmann C., Stephan P., 2002, *Microscale temperature measurement at an evaporating liquid meniscus,* Experimental Thermal and Fluid Science, Vol. 26, pp. 157-162.

CHAPTER VII

Conclusions

Surface tension driven phenomena are important in many industrial applications such as spreading of drops, surface acting agents, combustion, evaporation and condensation of thin liquid films. This work, despite its fundamental nature, was inspired by the important challenges faced by the micro-electronics industry. In the last few decades a trend has been established in integrated micro-chip technology leading to miniaturization and processor speed increase; these two factors have led to an important increase of the heat flux produced that air cooling technology is no longer able to remove. New technological solutions are therefore needed. The general solution proposed is to switch from a cooling solution involving single phase to a bi-phase one, essentially because of the very high heat fluxes experienced during phase change. Heat pipes are among the different technological solutions proposed involving phase change.

It has been pointed out that experimental difficulties in making small scale measurement of important parameters such as temperature, pressure and velocity still limit full understanding of the phenomena taking place at micro-scale. This work is an experimental and numerical study of the hydrodynamics of a meniscus formed by a liquid undergoing phase change in capillary tubes. The non uniform evaporation process occurring along the meniscus is responsible for a self-induced temperature field and consequent surface tension gradients that in turn drive a vigorous liquid convection. The study of this convection is the object of the present investigation. Different experimental techniques have been used to characterize the evaporation from a meniscus such as micro-Particle Image Velocimetry (μ-PIV) Infra Red (IR) and Thermochromic Liquid Crystal (TLC) techniques. These advanced techniques allowed us to unveil the liquid convection (μ-PIV), measure the interfacial temperature profile (IR) and external capillary tube temperature (IR and TLC). Numerical simulations have also been performed to reproduce the experimental findings. It is recognised that measuring velocity and temperature at such scales is not trivial. Therefore, comparisons between measurements gathered from different techniques have been carried out: TLC and IR measurements have been compared for temperature, and μ-PIV measurements and numerical analysis have been compared for velocity patterns.

Chapter I describes thermocapillary related issues investigated by other authors and positions the present work in the field, emphasizing that the thermocapillary effect being analysed here is of a different nature; in particular the driving force is self-induced by the evaporation process taking place at the curved meniscus.

In Chapter II the evaporation of various volatile liquids from capillary tubes has been investigated by measuring the evaporation rate and the spinning frequency of the liquid Marangoni convection; it is shown that the evaporation rate and the spinning movement are stronger at smaller tube sizes and for more volatile liquids. If the latter finding is quite easy to explain using the concept of partial vapour pressure, the formed results are a little less obvious as one expects that the evaporation is independent of the tube size. It is concluded that this behaviour might be due to the stronger evaporation at the meniscus triple line that ultimately dominates the scenario.

Chapter III unveils the liquid convection with the use of μ-PIV. Not only the cases investigated in Chapter II are deeply analysed but the tubes are differently oriented and are also heated with the use of a heating element positioned at different locations with respect to the meniscus. It is firstly shown that the convection is stronger at smaller tube sizes and for the more volatile liquids for the unheated tubes. For this case it is also shown that the convection has different patterns in diametrical horizontal and vertical sections of the tubes. Two sections of the toroidal shaped Marangoni roll are present in the tube's horizontal sections, whereas one appears in the tube's vertical sections. This is attributed to the action of gravity in the vertical diametrical sections leading to a distorted pattern mostly with only one vortex present. The distortion is lesser for the more volatile liquid and the smaller tube sizes. This is presumably because of the fact that for the more volatile liquids and at smaller sizes surface tension dominates buoyancy. The case of heated tubes gives some very interesting results. It is observed that when the heating element lies in the liquid side of the meniscus, the convection is indeed affected by the temperature gradients generated by the heater but is never inverted. Instead, when the heating element is positioned in the vapour side of the meniscus the convection is greatly affected and if sufficient power is applied the convection pattern is eventually reversed compared to the unheated situation. It is concluded that this is essentially due to the temperature profile established along the meniscus.

The TLC temperature measurements presented in Chapter IV show the important sink effect on the capillary tube wall close to the meniscus contact line region. By using the evaporation mass flux measured in Chapter II a heat and mass transfer balance analysis of the system was performed based on the measured wall temperature.Despite the fact that precise temperature measurements with the TLC sample used are possible only for a narrow range of temperature, fairly good agreement was found between the measured and calculated evaporation rate, giving great confidence in the temperature measurements using TLC and demonstrating that in the steady state the heating necessary to sustain the evaporation comes mainly from the environment surrounding the tube.

Temperature measurements with TLC offered also a benchmark for the following IR temperature measurements presented in Chapter V. Also for this IR investigation, as for the μ-PIV of Chapter III, different configurations were examined with both vertically and horizontally oriented capillaries, with and without external heating. The IR study also allowed measurement of the temperature of the liquid-vapour interface. These measurements revealed clearly the effect of the asymmetrical flow pattern shown in the tube diametrical vertical sections on temperature field as discussed in Chapter III for the unheated tubes. The IR measurements of the heated tubes allowed us to gather important information on the temperature gradients generated by the heating element to be used as input in the numerical analysis performed in Chapter VI.

A numerical code based on the FVM method is used in Chapter VI to reproduce the experimental findings and give more insight into the thermocapillary convection subject of this study. A coordinate transformation is introduced in order to take into account the curved meniscus. Very good quantitative (when possible) and qualitative agreement was found between experimental and numerical results.

All the results presented in the course of this work, both of flow patterns, meniscus and tube wall temperature and finally numerical analysis clearly lead to the conclusion that thermocapillary effects dominate and that the heat and mass transfer in such small systems is ultimately controlled by the strong evaporation taking place at the meniscus contact line region.

Two cases of practical interest were also examined as reported in the Appendices. The first is an experimental investigation of a heat pipe module for micro-electronics cooling where the effect of surface coating on the fin stack section was analysed. The second is an extension of existing heat pipe technology for high temperature application to cool a heavily thermally loaded nozzle of future spacecraft vehicles with high specific impulse.

It can be concluded that despite the very fundamental nature of this study some quite useful results could also be commercially exploited. For instance, the experimental observation of a higher evaporation mass flux at smaller tube sizes is clearly of commercial interest. The advanced coating technique on fins proposed in Appendix A is also of great importance as quite large heat transfer enhancements can be achieved. Using heat pipes to cool nozzles of future nuclear powered spacecrafts can solve one of the major problems faced by these advanced concepts for manned interplanetary missions.

APPENDIX A

Heat transfer enhancement in heat pipe applications using surface coating technique

A.1 Motivation

Despite the strongly fundamental nature of the work done in this thesis, it was inspired by the extreme challenges faced by the microelectronics industry in the thermal management sector. Existing cooling technology is seriously limiting the fast development of more powerful integrated micro-chips. We have also underlined that a possible solution to these problems could be the use of technological solutions adopting phase change, as this ensures very high heat fluxes compared to single phase cooling systems. One of the possible solutions proposed relies on the heat pipe concept with all its variant geometrical elaborations. It has been emphasised that the most thermally loaded heat pipe section is the evaporator, because its size is dictated by the size of the device to be cooled. Fewer problems are faced by the heat pipe condenser section. However, the condenser section has been also subject of a lot of work in recent years because of the recognition that it is ultimately the bottleneck of the entire cooling system. In fact, it is known that for a liquid-air cooling system up to 85% of the entire thermal resistance is concentrated at the air side. This figure is reduced to 50% when a liquid-liquid system is used, instead. Therefore, it is clear that any improvement made to the air side of a liquid-air cooling system is of preferential value. This is the principal reason behind the experimental study described in the following section, where a heat pipe unit using an advanced surface coating technique to cool a server processor has been tested. The work is the outcome of a three months project set in collaboration with Thermacore Europe Ltd., Praxair Surface Technology and the Universitá degli Studi della Calabria.

A.2 Background

We have seen that with increasing intensification and miniaturisation taking place in microelectronics, the current cooling strategies are rapidly reaching their thermal ceiling. The need for enhanced thermal management in electronics has impelled a continuous development of novel cooling techniques, such as liquid and two-phase cooling solutions as outlined by Groll et al. [1] and Lin et al. [2].

The heat pipe, as a two-phase thermal conductor, offers extremely high effective thermal conductivity (i.e. hundreds of times the thermal conductivity of copper) and is thus suitable for a wide range of applications in thermal management for microelectronics, telecommunications, power electronics, medical devices and space programmes as discussed in details by Dunn and Reay [3]. Heat pipes can have any cross section shape, but cylindrical or planar is preferred for construction simplification. With no mechanical moving parts, they are very reliable in practice. Heat pipes can also be embedded in a metal cooling plate, which is attached to the electronic component. Due to the high heat transport capacity, heat sinks with heat pipes have become much smaller than traditional extruded fins in handling high heat fluxes. With the working fluid flowing in a heat pipe, heat can be absorbed on the evaporator region and transported to the condenser region where the vapour condenses releasing the heat to the cooling media, as schematically shown in Figure A-1.

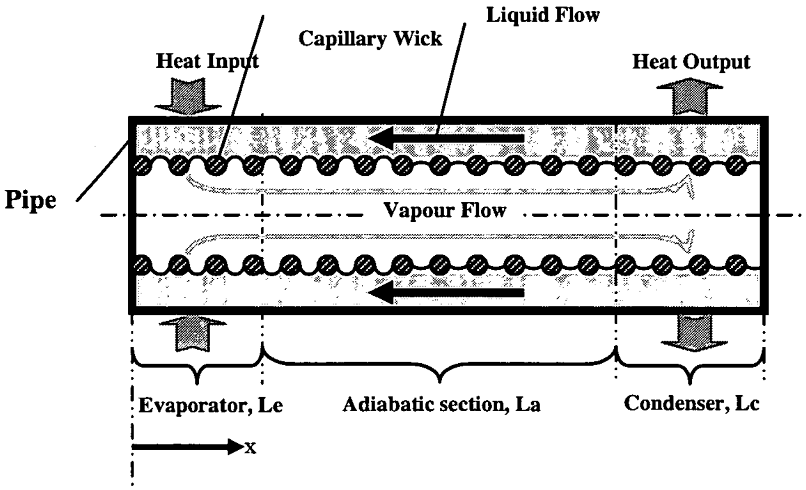

Figure A-1 Heat pipe operational principle.

In order to stretch the thermal ceiling of heat pipes for high power and compact applications, much research and development work has been carried out, including sintered wick structure, mixture working fluids, interface materials between heat pipes and fin stacks, and surface roughness of fin stacks. For a whole heat pipe assembly, the improvement of the heat transfer at the airside is still an important issue. The present work is a study of a surface coating technology to enhance the heat transport from the heat pipe fin stack to the ambient. The surface coating consists of a high thermal conductivity material with certain surface roughness.

It is important here to give a brief introduction to heat pipes presenting a relevant reference that is an important review in the field. In Manfred et al. [4] after a brief introduction pointing out the difference between conventional and micro heat pipes, the authors gave a very good description of the heat pipe technology for thermal control of electronic equipment, illustrating the heat pipe design by means of several figures. Heat pipes are used either as indirect or as direct cooling devices. For the indirect technique, the heat pipe is directly connected to the device to be cooled and has the same function of heat sink. In the direct technique, the device to be cooled is an integral part of the heat pipe and/or is in contact with the working fluid. The simplest heat pipe geometry is obviously cylindrical, but since a lot of electronic devices to be cooled are flat, it is not rare to have flat heat pipes. The thermal stresses between the heat pipe's condenser section and the electronic device must be controlled: to accomplish this, the heat pipe is equipped with a flexible metallic part (these heat pipes are called *bellows heat pipes*). In the direct technique important problems arise due to the generation of vapour bubbles (possible burn-out at high heat flux and subsequent device failure) and possible decrease of the electric breakdown voltage of the fluid. To overcome these problems two techniques have been adopted both of which try to avoid direct contact of the device with the vapour phase. In one technique the device is an integral part of the wick structure, therefore there is always some liquid in contact with it. In the other technique there is always a very thin evaporating liquid film in contact with the device. A satisfactory description of micro heat pipes is then also given. Micro heat pipes derive their capillary pumping from a non circular cross section. They are suitable where it is important to maintain uniform temperature with quite high heat fluxes. Micro heat pipes array have been developed to eliminate hot spots and smooth temperature gradients. The effects of working fluid, contact angle (solid/fluid interaction), micro heat pipe dimensions (length, diameter, heat pipe number) have been analytically and numerically investigated. The increase in length and the decrease in diameter of the micro heat pipe lead to an important reduction of the heat transfer rate. As the number of the heat pipes increases the maximum surface temperature of the heat pipe array decreases, but for arrays with more than 20 heat pipes this reduction becomes always less important. Another indirect heat pipe technology is using grooves as capillary structures. There are several kinds of grooved heat pipes: circular, flat, flat multiple parts, integral array. The temperature range for electronic application is 0-100 °C; therefore only water, acetone, ammonia, methanol, ethanol and freons are suitable working fluids. Freons are non advisable for their ozone depletion. Ammonia has a very high vapour pressure at low temperature (~ 30 bars at 60 °C). The most suitable fluid is water due to its very high surface tension and latent heat and to its very low liquid kinematics viscosity. These characteristics confer to water a very high heat transport capability. The most suitable wall materials are carbon and stainless steel, copper and aluminium with their alloys. Copper is the most used due to its high compatibility with water. Aluminium has low density and high compatibility with ammonia. The materials aforementioned are not suitable for applications where a low thermal expansion coefficient is needed. The work of Manfred et al. [4] ends with a very useful literature review. This paper is especially suitable for engineers because it gives detailed information about heat pipe design.

A satisfactory review on non convectional heat pipe technology can be found in the work of Garimella and Sobhan [5] in which the reader can find plenty of useful information on numerical and experimental investigations along with an extensive bibliography.

Generally speaking, almost 85% of the overall thermal resistance of any liquid-air cooling thermal unit is concentrated at the airside (Lyman et al. [6]). Therefore an improvement in this area is much more effective than in other already thermally stretched parts of a cooling thermal solution.

Khodabandeh and Palm [7] shows experimentally how surface techniques can be successfully applied for heat transfer enhancement in electronics cooling.

The size of electronic components has been dramatically reduced in the last two decades, leading to an important increase of heat flux to be dissipated. Using air cooling systems it is possible to remove a maximum of 0.05 W cm^{-2}. To dissipate up to 100 W cm^{-2} a heat sink 2000 times larger than the devices to be cooled is necessary and this area is not always available. The only way thus to meet this requirement is to use another system such as two-phase flow. An example of reliable two-phase device is the closed loop thermosyphon where the condensed liquid flows back to the evaporator sector because of gravity. Boiling is another powerful technique to cool electronic devices. To enhance the heat transfer coefficient in boiling, rough surfaces or screens attached to the evaporator section have been employed with the aim of increasing the nucleation sites. Transferring these enhanced techniques for boiling in the thermosyphon loop system, its heat transfer capabilities could be greatly improved. One smooth and another threaded surface have been tested in the work of Khodabandeh and Palm [7]. The temperature differences are smaller for the threaded surfaces than for the smooth one. The working fluids were isobutane (R600a) and HFC134a. The evaporator section was made with three small blocks of copper connected in parallel, in which five vertical channels (ID of 1.5 mm) were produced. The heat transfer coefficient was defined as the ratio of the total heat input over the total evaporator surface area to the temperature differences between the evaporator and the refrigerant's saturation temperature. The evaluated heat transfer coefficient was modified by a factor to take into account the threaded surface; the factor has a value of 0.33 for HFC134a refrigerant. The results show an almost linear increase of the temperature difference versus the heat load for both refrigerants. The ratio of the temperature differences between smooth and threaded surface is larger than the area ratio for the same surfaces; this could be explained by the increased heat transfer coefficient for the threaded surface due to more nucleate sites. The nucleate boiling mechanism overcomes the convective evaporation one as confirmed by both the value of the Boiling number (ratio of the heat flux to the product of mass flux with latent heat of vaporization) and the increased heat transfer coefficient with the heat flux. In conclusion the heat transfer coefficient of the threaded surface increases by 0-30% for R134a and by 0-56% for R600a referred to the smooth surface. This work clearly shows that surface properties can substantially contribute to heat transfer enhancement.

Previous investigations on surface enhancements on the airside in electronics cooling have mainly focused on the influence of the cooling fin shapes and surface roughness on flow pattern and turbulence promotion as outlined in many recent works such as Rowley and Patankar [8], Davalath and Bayazitoglu [9], Aliaga et al. [10], Henry et al. [11], Go et al. [12] and DeJong and Jacobi [13]. In particular Rowley and Patankar [8] and Henry et al. [11] demonstrated how the heat transfer can be reduced with increasing roughness in the laminar regime; an important heat transfer enhancement is achieved only if the roughness height is larger than the thickness of the thermal boundary layer. DeJong and Jacobi [13] investigated the effect of louvered-fin arrays on heat transfer and pressure drop in the near wall region. They found a decrease of 50% on the heat transfer at low Reynolds number due to the large separation zones in the near wall region; as unsteadiness was promoted by an increased Reynolds number, the heat transfer was enhanced by 15%, but the pressure drop penalty is several hundreds times larger. Louvered-fin arrays are becoming the standard technology used in compact heat exchangers. More recently, Leon et al. [14] studied numerically the advantages of using aerodynamic shaped fins if the Reynolds number, based on the spacing between the cooling fins, was greater than 800. It was suggested that the recommended fin shapes might yield about 15% improvement in heat transfer with considerable pressure drop.

Gentry and Jacobi [15] further investigated surface heat transfer enhancement by using delta wings placed at the leading edge of a flat plate to generate streamwise vortices within the channel flow. They found that the local heat transfer coefficients increased as much as 300% over the baseline flow, and vortex strength increased with Reynolds number, wing aspect ratio, and wing attack angle. Although considering the complete channel surface, the largest spatially averaged heat transfer enhancement was 55%, it was accompanied by a pressure drop penalty of 100% increase in the channel flow.

Biswas et al. [16] studied experimentally the flow structure behind a winglet type vortex generator placed in a fully developed laminar channel flow and the influence on heat transfer enhancement. They found that the vortex generators may lead to a great enhancement in heat transfer, however the optimal angle of attack of the vortex generator is important and the pressure drop increase must be considered.

Kiwan and Al-Nimr [17] estimated the thermal performance of porous fins in comparison with that of the conventional solid fins. They found that using porous fins might enhance the performance of equal size conventional solid fins. But there was a limit for the thermal conductivity ratio between solid and porous fins beyond which there is no further improvement in the Nusselt number.

The literature review has shown that typical investigations have focused on designing specific surface structures for heat transfer enhancement with a significant pressure drop penalty. However, in the present experimental investigation, a heat pipe unit built to cool server chips has been used to investigate the influence of surface coating technology on heat transfer enhancement from finned surface. In general, there are two ways to improve the thermal performance of the fin stack, i.e. increasing the number of fins or enhancing the heat transfer on the fin surface. The first approach may lead to a significant increase in pressure drop and thus a higher required fan power. However, by enhancing the heat transfer coefficient on each fin surface as was done in the present study, the total heat transfer rate in the fin stack would be augmented and the pressure drop through the fin stack would be maintained at the same level.

In the present study, two aspects of heat transfer coefficient enhancement on the fin surfaces were considered: surface roughness and surface coating of high thermal conductivity material. With surface roughness, the surface area can be increased and the turbulence in the boundary layer can be promoted. With high thermal conductivity coating material, the heat transfer from a fin surface can be enhanced. The influence of air flowrate and orientation of the heat pipe unit on the overall heat transfer performance were also investigated, as detailed in the following sections. This latter is significant in those applications such as aeronautics where the orientation can change during operation.

A.3 Experimental apparatus and procedure

A heat pipe unit has been tested using a laboratory wind tunnel in order to investigate the effect on the heat transfer of a highly conductive coating deposited on the fin surface of its fin stack. A real heat transfer unit with fin stack module has been tested instead of testing a single fin in order to simplify the experimental procedure. In fact, for one single fin the experimental set up would have been more complicated. The heat source would have been adapted to the fin dimensions and the fin positioning system would have been more sophisticated. In addition, the temperature monitoring system would have been completely different in order to avoid misreading due to factors such as fin orientation and thermocouple positions on the fin. Testing a whole heat pipe unit constitutes an invaluable advantage: firstly, because all the problems aforementioned can be simplified and secondly, because the heat transfer improvement is closer to the real one that can be found on any of the heat pipe units produced in series. Therefore, no special attention has been paid to building the unit tested in the present study.

As pointed out in Zhao and Avedisian [18], the maximum heat transferred by a heat source to a fin stack is realized when the heat source and the fin base have the same temperature. This can be done using a heat pipe that is thousands of times more conductive than copper. The drop in temperature along the condenser heat pipe's section is lower than that along a rod of copper, ensuring a higher heat transfer from each fin along the fin stack. The heat pipe fin stack was put inside the air stream in order to investigate the effect on the heat transfer of different parameters such as the heat pipe orientation and wind speed.

The fins' material is aluminum because of its high ratio of strength/density, ductility and thermal conductivity. However, the alumina (Al_2O_3) protective film formed on its surface is not desirable for heat transfer. In order to overcome this limit, the alumina barrier was removed and the fin surface was coated. The alumina layer is naturally formed on the aluminum surface and protects the material from a further oxidation. Therefore, the coating must be deposited in a controlled way prior to reformation of the alumina. To point out the enhancement on the heat transfer introduced by this technique, three different fin surfaces have been analyzed: one uncoated and two others with different coatings. One sample was covered with a very high thermally conductive coating and the other with a granular paint made of diamond particles. The coatings are produced by Praxair Surface Technology and are described in detail below. One surface is coated with a Diamond Like Carbon (DLC) coating after first removing the natural aluminium oxide layer. The DLC coating is deposited using a Plasma Enhanced Chemical Vapour Deposition (PECVD) technique. The removal of the aluminium oxide layer can be carried out by traditional methods such as bead blasting in a controlled inert atmosphere. The thickness of the DLC layer varies between 1 and 5 μm. The DLC layer is homogenously deposited and adheres well on metals and semiconductors forming carbides. The adhesion problems encountered on gold, copper and iron (because these materials cannot form carbides) can be solved by using an intermediate layer of aluminium, zinc, germanium or nickel which forms carbides. The roughness of the DLC coating is very similar to the base material coated, as will be demonstrated later with the roughness analysis. The peculiar properties of DLC coating are as follows: hardness, low friction, generally chemical inertness, hydrophobic and an amorphous structure that contributes to amplify the wear resistance of a hard material. The coefficient of sliding friction of a DLC layer against a steel ball is in the range of 0.005 – 0.02 under vacuum condition and of 0.2 in air. The deposition technique for DLC thin layer coating is a PECVD that involves either the dissociation of hydrocarbon gases or an extremely volatile hydrocarbon solvent. The system for PECVD is mainly composed of a vacuum chamber with its vacuum pumping system, a multiple gas manifold and an RF power generator. Introducing into the system a gas in a pressure range of 10^{-3} – 10^{-4} mbar and applying an RF voltage of one to several thousands, a self sustained glow discharge is ignited. With a DC supply, the smaller electrode is normally connected to the negative terminal. Between this electrode and the plasma that assumes a potential close to that of the anode, a dark space forms across which there is the main potential drop. The negative electrode is therefore bombarded with high energy ions. A DC supply generally cannot be used if an insulating layer forms on the cathode (as in the case of DLC). With RF the smaller electrode charges negatively because of the different mobility of ions and electrons. For a net zero current to flow during the cycle, the smaller electrode becomes negatively charged on average during a cycle and is again bombarded by energetic ions. With a carrier gas containing carbon, hydrogen or some ionized halogens, solid films are deposited on the electrode. The growing films are bombarded with ions, probably giving rise to the metastable, mostly amorphous structures of PECVD layers. The layers will be dense and hard because weakly bonded atoms will be resputtered. With this technique, hard amorphous hydrogenated carbon films are obtained from hydrocarbon gases. Several process parameters are to be considered: type of gas, gas pressure, gas mixture ratio, substrate temperature, electrode and substrate geometry and electric field frequency. The most important parameters to control are the self bias potential, gas pressure and gas mixture ratio. The preferred procedure for producing hard DLC layers consist of first introducing argon at a pressure of 10^{-2} – 10^{-3} mbar with an RF voltage of about 1 kV to clean components. Argon is then replaced by a hydrocarbon solvent (highly volatile at low pressure) at a pressure of 10^{-1} – 10^{-2} mbar and later mixed with another hydrocarbon gas as discussed above. The second surface was coated with industrial diamond particles which were attached to the fins by an electroplating technique with a thin layer of nickel. The natural aluminium oxide layer is removed first before the nickel can plate onto the aluminium substrate.

The unit tested is depicted in the front view inset of Figure A-2 and is the real unit used to cool the Intel® Xeon™ Processor. It is composed by an aluminium plate to be attached on the chip on the top of which two cylindrical slots are machined in order to hold the two heat pipes. The metal sintered wick heat pipes are made of copper and the working fluid is distilled water. The length of the heat pipe sections can be varied as needed. In the present case the evaporator section is 116 mm long, the condenser section is 48 mm long and the adiabatic section is 7 mm long. The heat pipe has an external diameter of 6 mm, a wall thickness of 1.5 mm and the passage available for the vapour flow is 3 mm. Between the heat pipes and the aluminium plate a thermally conductive paste is used in order to improve the adhesion and reduce the contact thermal resistance; thus the heat pipes are clamped. The fins stack module is composed by 25 fins, 23 internal and 2 external thicker to hold the inner ones. Each fin is 96 mm long, 34 mm large and the thickness is 0.4 mm for the internal and 1 mm for the external. The corners of each internal fin are folded to act like spacers for the 1.3 mm air passage.

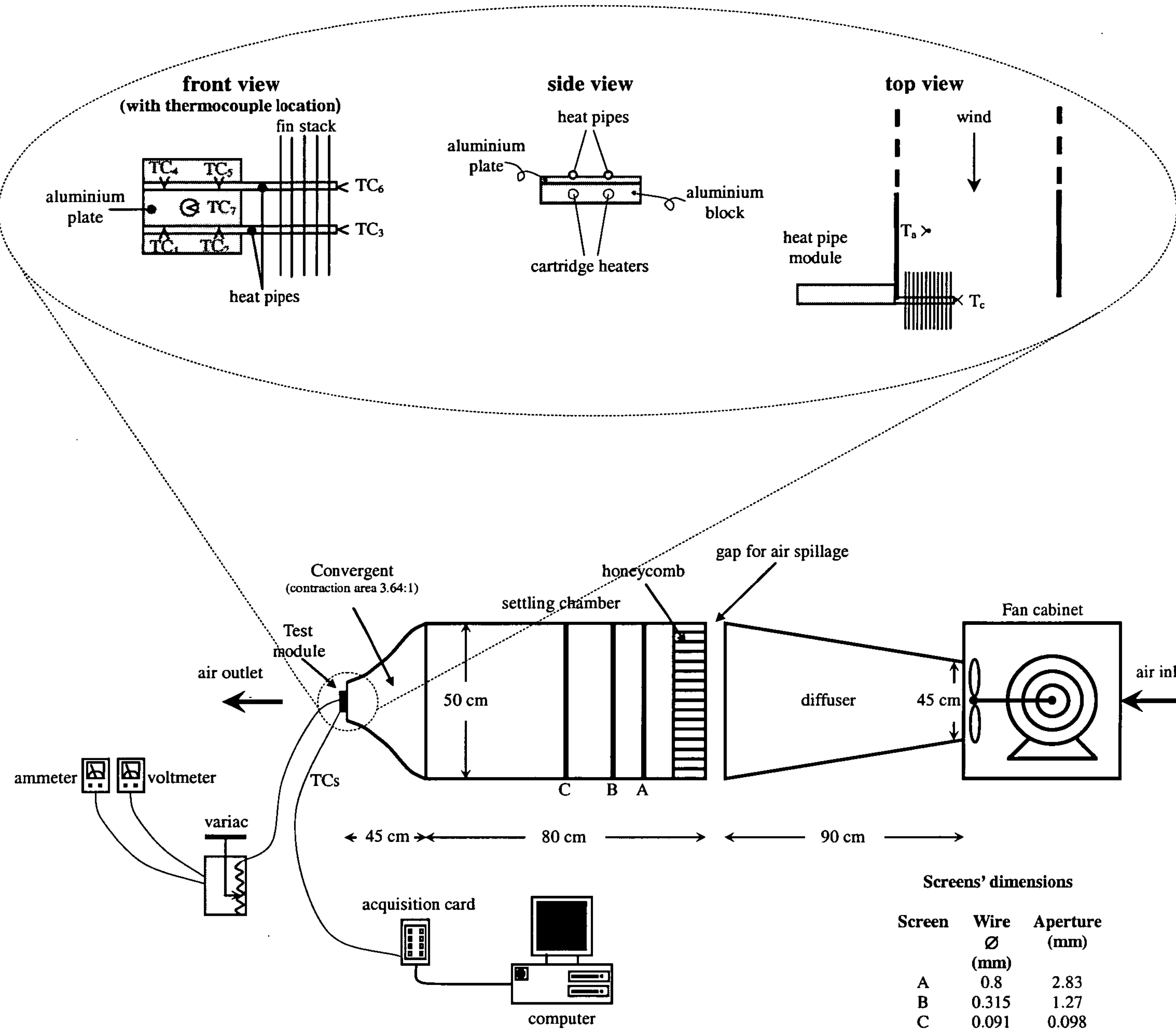

Screens' dimensions

Screen	Wire Ø (mm)	Aperture (mm)
A	0.8	2.83
B	0.315	1.27
C	0.091	0.098

Figure A-2 Schematic diagram of the experimental test facility with test unit insets. Front view: thermocouples location; side view: heater section; top view: test unit location at the tunnel exit.

The heated section (see side view inset of Figure A-2) consisting of an aluminium block (built in order to uniformly deliver the heat produced by the two heaters) and of the plate holding the two heat pipes, has been insulated with a 12.5 mm thick fermacell to limit the thermal losses. The cartridge heaters were bought from Omega Engineering Ltd., had a diameter of 6.35 mm and 101.6 mm long, and delivered 400 W each with a heat flux on their cylindrical surface of 18.6 W cm^{-2}. The power delivered by the cartridge heaters was controlled by a variac and its value was calculated by reading a voltmeter and an ammeter (see Figure A-2). The heat pipe unit was tested using a laboratory wind tunnel schematically sketched in Figure A-2. In operation the fins will be cooled by air blown from a fan, the flow of which has a greater turbulence level than that produced by the wind tunnel. In these conditions the results found through the present investigation in terms of heat transfer coefficient are underestimated; the chip temperature in real applications will be lower than that shown later in the present study. This further increases the safety margin from the unit operational limits. The wind tunnel is an open circuit (blockage and wake effect can be neglected) with dimensions reported in Figure A-2; the convergent contraction ratio is 3.64. The tunnel has been adapted from the existing one used for demonstration purposed at THE UNIVERSITY *of* EDINBURGH School of Engineering and Electronics. The fin stack of the heat pipe unit is accommodated at the tunnel square exit section as shown in the top view inset of Figure A-2. The tunnel fan is a synchronous motor of 750 W. The diffuser connects the circular fan section with the square settling chamber. The tunnel settling chamber has been slightly modified to have a low level of turbulence in the test section. The honeycomb is 100 mm long and has hexagonal holes with a side dimension of 4 mm and a thickness of 0.2 mm. Three stainless steel plain weave screens with decreasing mesh (see Figure A-2 for dimensions) have been placed before convergent section of the tunnel. According to Hinze [19] a turbulence level of 1.5-2% is expected. In order to work with different wind velocities, the limitation of the synchronous motor has been overcome by allowing air spillage from a section above the settling chamber (see Figure A-2). Three wind speeds have been chosen: 4.9, 8 and 16.5 m s^{-1} (the last with no air spillage). The wind speed profile in the test section has been mapped for all three wind speeds chosen using a pressure transducer previously calibrated with a pitot tube connected to an inclined U tube. The transducer was mounted on a transverse in order to map the whole tunnel cross section with a square grid of 12.7 mm side. The velocity profile was found flat for up to 80% of the tunnel cross section area.

Seven Chromega-Constantan calibrated thermocouples (Omega Engineering Ltd.) have been used to monitor the heat pipe unit temperature (see front view inset of Figure A-2); one in the middle of the aluminium heater block (to read the chip temperature) and three along each heat pipe – two on the evaporator section and one at the tip of the condenser after the fins stack. The very thin thermocouples (250 μm tip diameter) have a very short response time (0.05 seconds); despite the fact that they were already calibrated, their calibration was checked using a thermostatic bath to ensure that the stated manufacturer's specifications were met. The maximum discrepancy found in the range of temperature of interest (20-100 °C) was ±0.5 K. The thermocouples output was read using a Pico Card model TC-08 capable of acquiring eight channels simultaneously (the eighth for the inlet air temperature, T_a in the top view inset of Figure A-2). The Pico Card is connected to a PC where the thermocouples output can be read in real time on a chart and also stored for successive post-processing.

In order to understand the influence of the roughness on the heat transfer, the roughness of the three surfaces have been analysed using an interferometer profilometer (manufactured by Zygo Corporation) hosted at the School of Engineering and Electronics at THE UNIVERSITY *of* EDINBURGH. In the profilometer a beam is split in two: one goes on a reference smooth surface of known roughness and the other on the surface to be analysed. After reflection, the two beams interfere and from the interference pattern the roughness of the surface being analysed can be evaluated. The interferometer profilometer is a much simpler instrument to use compared to a contact instrument such as AFM (Atomic Force Microscope). No special sample preparation is required and it is not necessary to cut a small piece of the surface to be analysed, whereas these requirements are fundamental for AFM. The drawback is that while both instruments have the same z-direction resolution (~1 nm), the x/y-direction resolution is much greater for AFM. Several surface texture parameters are given by the profilometer, the most important of which are the *ra*, *rms* and *RSurfAreaRatio*. *ra* is the average surface roughness whereas *rms* is the root mean square of the measured height over a reference area. The *RSurfAreaRatio* (Roughness Surface Area Ratio) is also reported, being the ratio of the rough surface to the plane area scanned.

The *ra*, *rms* and *RsurfAreaRatio* of the three surfaces analyzed are given in Table A-1, from which it can be stated that the surface coated with diamond particles is between 6 and 8 times rougher than the other two surfaces. It is important for the conclusion reached in this study to note that both uncoated and DLC coated surfaces have the same order of roughness.

For each run the wind velocity was set before switching on the heaters. A steady state was reached and the thermocouples readings taken before changing the heat power with a step of 10 W starting from 10 W; the upper limit is dictated by the set limit chip temperature of 60 °C. The heat pipe unit was placed in three different positions around the test section as can be seen from Figure A-3, in order to investigate the role played by gravity on the heat pipe operation. A change of the unit performance is expected with the heat pipe orientation, essentially because in the heat pipes the liquid return to the evaporator section is influenced by the action of gravity.

Table A-1 Surface roughness analysis parameters.

Surface	*ra* (μm)	*rms* (μm)	sample size (mm)	*RSurfAreaRatio*
Uncoated	0.542	0.453	0.18x0.13	1.007
DLC	0.868	0.652	0.18x0.13	1.053
Diamond coating	4.112	4.843	0.18x0.13	1.095

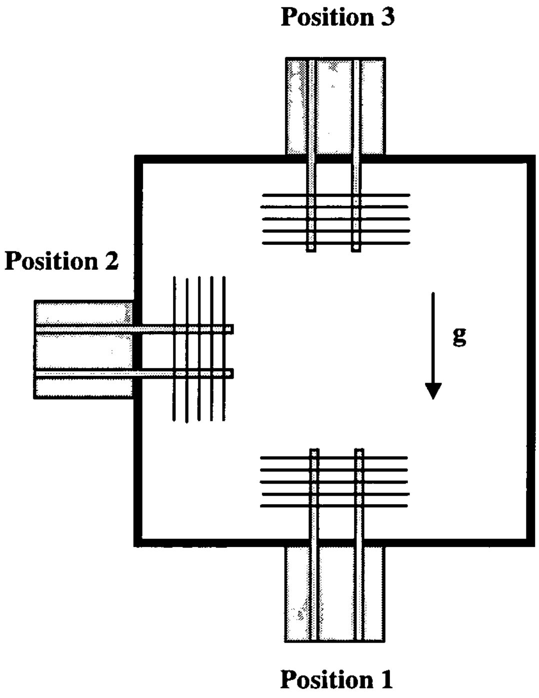

Figure A-3 Test unit position around the tunnel exit section with respect to gravity.

A.4 Results and analysis

The aim of the present work is to show that the heat transfer coefficient from a fin can be enhanced using a coating on the fin surface. Two different coatings have been tested and compared with the uncoated fins. The basic material of the fins is aluminum and it is well known that the natural oxides formed at the interface aluminum-air are a thermal barrier. The very thin layer of aluminum oxide (Al_2O_3) formed on the fin surface is responsible for the interfacial thermal resistance; the thermal conductivity is around 110-180 $WK^{-1}m^{-1}$ for aluminum alloys and 10-15 $W K^{-1} m^{-1}$ for Al_2O_3 as bulk; no information is available in the literature about the thermal conductivity of naturally thin layers of aluminum oxide. The oxide layer has been removed in this study and a layer of high thermally conductive material has been deposited on the fin surface. Using a granular coating in order to increase the roughness will also enhance the heat transfer due to two factors: the increase of surface area and the promotion of turbulence in the air-stream over the surface.

When a heat pipe unit is placed on a chip it is vital the chip temperature does not exceed a certain limit over which its functionality and/or integrity will be seriously affected. For the case investigated in this study, the limit was set to 60 °C by the manufacturer of the heat pipes (Thermacore Europe Ltd.); therefore, the chip temperature was also monitored. The condenser section of the unit was put inside the flow blown by a wind tunnel. As heat is removed from the fin stack by the air, the heat pipe condenser temperature decreases; this affects the heat pipe evaporator temperature and thus the chip temperature changes accordingly.

Figure A-4 reproduces the chip temperature against the chip heat power for the three different fin surfaces. The chip power was increased until its temperature reached the set limit of 60 °C. The performance of the unit with and without coating has been compared evaluating the overall heat transfer coefficient.

The overall heat transfer coefficient has been calculated measuring the temperature T_c (TC3-6 in the top view inset of Figure A-2) of the condenser section after the fin stack using the following well known definition:

$$U = \frac{Q}{A(T_c - T_a)} \qquad \text{(A.1)}$$

where U is the overall heat transfer coefficient, Q is the heat power delivered by the cartridge heaters, A is the total fin surface area and T_a is the air temperature. The surface area has been evaluated multiplying the measured surface area for an uncoated fin (96mm x 34mm) with the *RsurfAreaRatio* for each surface in order to take into account the effect of roughness.

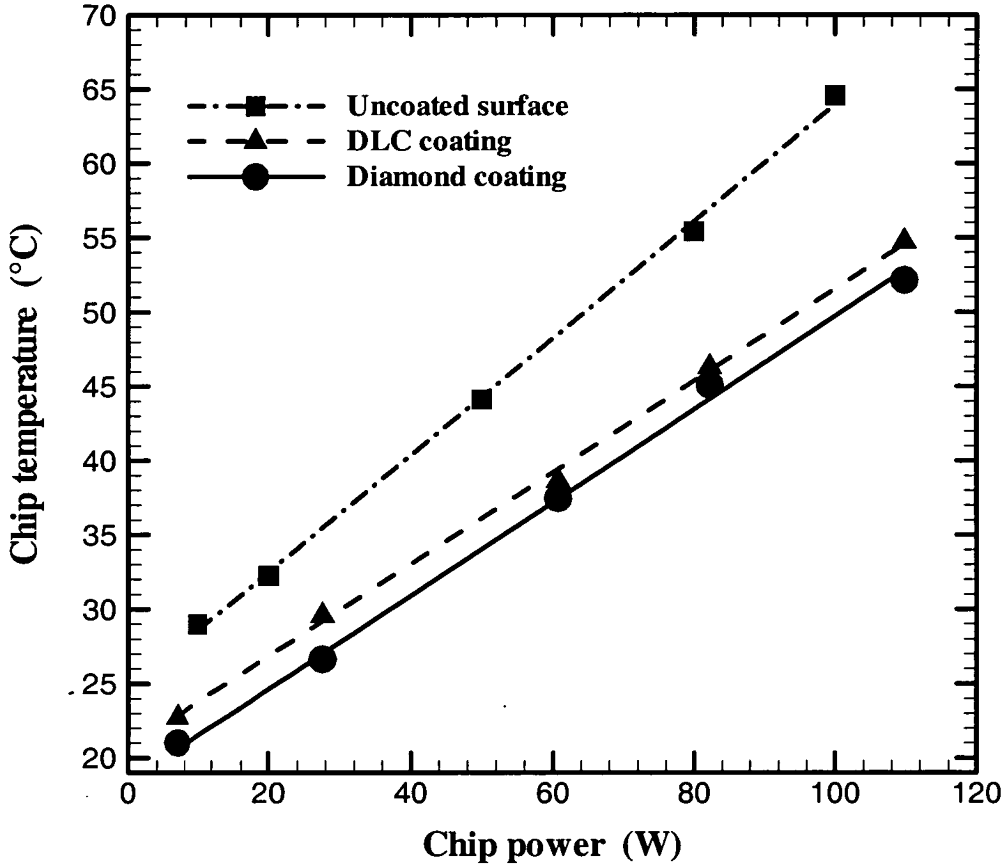

Figure A-4 Chip temperature vs. chip power for the three surfaces.

The error introduced with the evaluation of the overall heat transfer coefficient is estimated using standard methods as described by Kline and McClintock [20]. The overall heat transfer coefficient has been estimated using Equ. (A-1), for which the error can be expresses as follows:

$$\frac{\Delta U}{U}=\sqrt{(\frac{\Delta Q}{Q})^2+(\frac{\Delta A}{A})^2+(\frac{\Delta T}{T})^2} \qquad (A.2)$$

where $Q = VI$ and $A = bl$. V is voltage and I is current. In the definition of A b and l are the fin dimensions. The errors in reading the voltage and the current are of 1% for both the voltmeter and the ammeter. The fin dimensions were measured with a micrometer and according to their dimensions the relative error is of 0.05% for b and 0.1% for l. The air temperature (18 °C) was the minimum temperature read using a thermocouple with an accuracy of 0.5 K; the error is of 2.8%. Applying Equ. (A-2) the error on the heat transfer coefficient is found to be of the order of 3%.

The boundary layer develops on the fin width and is estimated to be in the range of 0.9 – 1.5 mm (values obtained from the Blasius solution), depending on the Reynolds number based on the fin width. Assuming the gap between the fins as the reference length, the Reynolds number ranges between 436 and 1,470 for wind speeds of 4.9 – 16.5 ms^{-1} respectively. Because the gap between the fins is of the order of 1.3 mm, the flow turns out to be 2-D fully developed mainly laminar, except for the highest velocity that lay at the lower edge of the transitional region.

The temperature readings collected during the tests are similar to those reproduced in Figure A-5. A stationary state is allowed to be reached before increasing further the chip power. The temperature along both heat pipes is monitored and Figure A-5 shows that the heat pipes perform slightly differently. This behavior could be due to a different filling amount of the heat pipe working fluid.

The overall heat transfer coefficient for the three surfaces as a function of the Reynolds number is reported in Figure A-6. For *Re* of 436 and 712, the increase in overall heat transfer coefficient U due to the coating is of 30% for both the DLC and diamond coatings. These figures slightly increase at *Re* 1,470; this is probably due to the transitional flow regime. As can be seen, the difference of the heat transfer coefficient for the DLC and the diamond coating is limited especially at low wind speed. For practical applications of the tested heat pipe cooling unit, the air is blown on the fins at no more than 5 ms^{-1}. From the results, it can be stated that the DLC coating gives a better performance than the diamond one. This is reinforced by the fact that the heat pipe unit made by DLC coated fins has 5 out of 17 fins uncoated for lack of coated fins available. Although the pressure drop on the fins stack has not been measured in the present investigation, from the roughness analysis and the Reynolds number it can be deduced that the three surfaces have similar pressure drop because hydrodynamically smooth.

A common practice to enhance the heat transfer between a solid and a fluid is to use an extended surface or finned surface. For the fin the direction of heat transfer within the solid material is perpendicular to the heat transfer direction between the fin and the fluid. In general the heat transfer within the fin is two-dimensional but because the temperature gradient along the x axis (Fig. 7) is greater than the one in the other direction, we can thus assume one dimensional conduction in the x direction. For an infinite fin of uniform cross sectional area the temperature distribution is given by (Incropera and DeWitt [1996]):

$$\theta(x) = T(x) - T_a = \theta_b \, e^{-mx} \qquad \text{(A.3)}$$

where $\theta_b = T_b - T_a$ with T_b the temperature of the fin base and T_a the fluid temperature, $m = \sqrt{\frac{hP}{kA}}$ with h is the convection heat transfer coefficient, P the fin perimeter, k the fin thermal conductivity and A the fin cross sectional area. However, because the fin introduces also a thermal resistance to heat transfer its efficiency in terms of heat transfer must be evaluated. It is common practice to introduce the fin effectiveness ε_f (Incropera and DeWitt [1996]). For the case of infinite fin of uniform cross section area one gets:

$$\varepsilon_f = \sqrt{\frac{kP}{hA}} \qquad (A.4)$$

The foregoing suggests that higher fin thermal conductivity is preferred along with high fin perimeter to cross section area and lower convection heat transfer coefficient. This will be recalled later as the use of high thermally conductive coating could change the equivalent thermal conductivity.

The barrier of aluminium oxide will degrade the heat transfer between the fin surface and air. A schematic of the equivalent thermal circuit for the fin in its transversal direction (y) is given in Fig. 7a. The total resistance is given by:

$$R_{Tot} = \underbrace{\frac{1}{h}}_{O(10^{-1})} + \underbrace{\left(\frac{s}{k}\right)_{Al}}_{O(10^{-6})} + \underbrace{\left(\frac{s}{k}\right)_{Al_2O_3}}_{O(10^{-6} \div 10^{-7})} \qquad (A.5)$$

It is clear that because of the small thickness involved in the present case all the thermal resistance is concentrated at the airside. Therefore, even using the DLC coating will not have any bearing on the total fin transversal resistance. So, the experimental findings cannot be explained with a change of the fin transversal thermal resistance. However, it must be considered that with the DLC coating the heat conduction inside the fin changes. In fact, as schematically shown in Fig. 7b, because of its very high thermal conductivity (6,000-8,000 W K^{-1} m^{-1}), the conduction through the coating along x becomes more important than the conduction through the aluminium core. The thermal resistance through the aluminum core is $R_{Al} = \frac{1}{k_{Al} A_{Al}} \cong 42\ Km^2W^{-1}$, whereas the thermal resistance through the DLC coating is $R_{DLC} = \dfrac{1}{k_{DLC} A_{DLC}} \cong 25\ Km^2W^{-1}$. Therefore, heat flows more along the coating than in the fin aluminium core. This produces smaller temperature gradients along the fin boundary in contact with the fluid and consequently the overall heat transfer at the airside is augmented. We can now evaluate the fin effectiveness with and without coating. The fin effectiveness with the coating is given by:

$$\varepsilon_{f\,DLC} = \sqrt{\frac{k_{DLC} A_{DLC} P}{h(A_{Al} + A_{DLC})^2}} \cong \sqrt{\frac{k_{DLC} A_{DLC} P}{h A_{Al}^{\ 2}}} \qquad \text{(A.6)}$$

whereas the fin effectiveness without coating is:

$$\varepsilon_f = \sqrt{\frac{k_{Al} P}{h A_{Al}}} \qquad \text{(A.7)}$$

and their percentage difference is:

$$\frac{\varepsilon_{f\,DLC} - \varepsilon_f}{\varepsilon_f} = \sqrt{\frac{k_{DLC} A_{DLC}}{k_{Al} A_{Al}}} - 1 \qquad \text{(A.8)}$$

Substituting in the above relation the thermal conductivity of the two layers one gets:

$$\frac{\varepsilon_{f\,DLC} - \varepsilon_f}{\varepsilon_f} = \sqrt{\frac{0.04}{0.024}} - 1 \cong 29\% \qquad \text{(A.9)}$$

The estimated enhancement in the fin effectiveness is very close to the overall heat transfer coefficient experimentally evaluated by Equ. (A.1).

It is worth mentioning that the above comparison is in fact a comparison between a fin of aluminium and another entirely made of DLC. The order of magnitude analysis gives an enhancement which is very close to the one observed experimentally, suggesting that the fin with a DLC coating would behave as if entirely made of DLC.

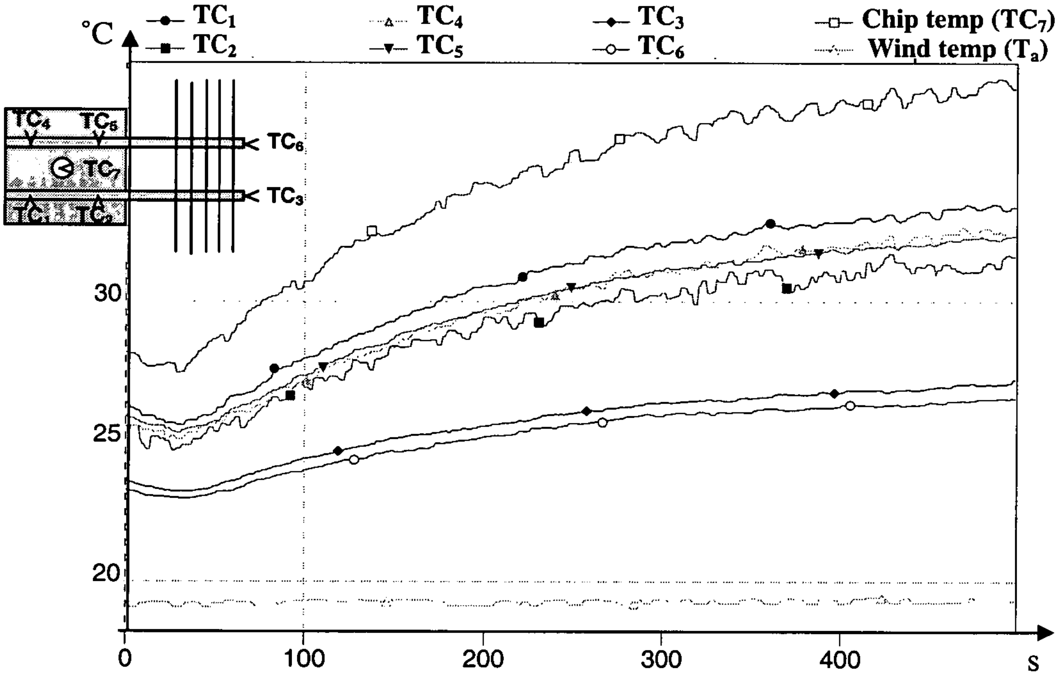

Figure A-5 Thermocouples readings for a transient on the Pico chart.

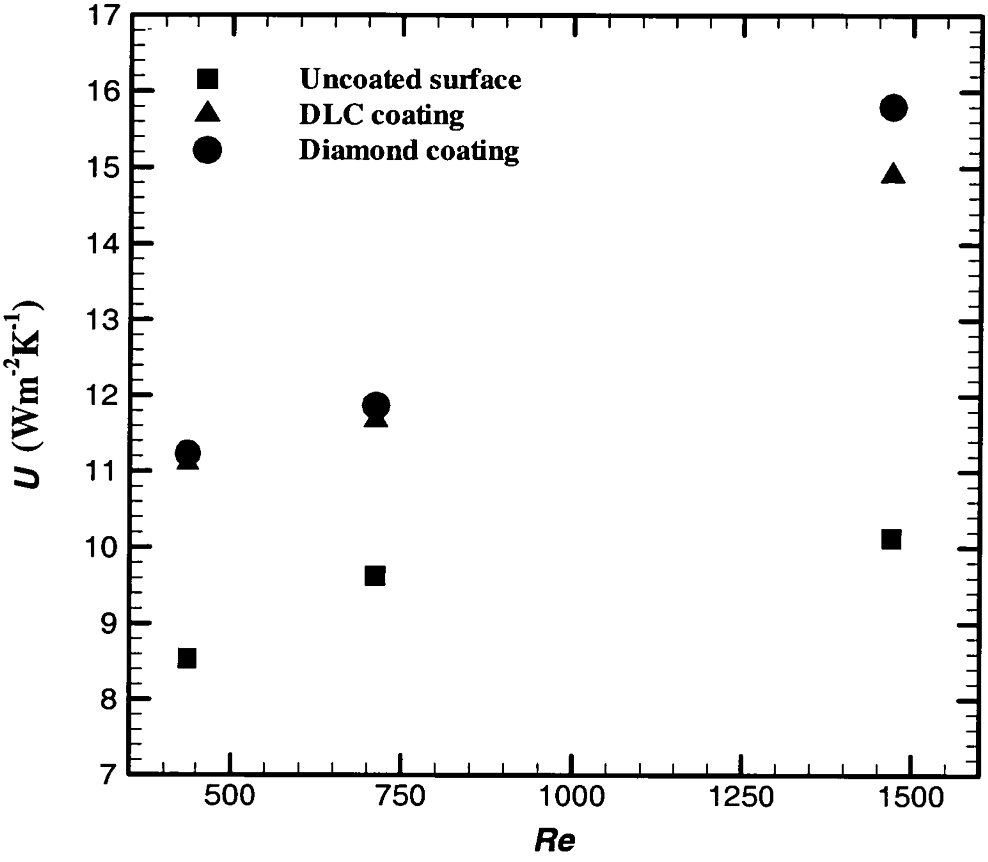

Figure A-6 Heat transfer coefficient vs. *Re* for the three surfaces.

The thickness of the coating does not influence appreciably the heat transfer coefficient for a reduced gap between the fins. The heat transfer coefficient is inversely correlated with the fins' gap for a laminar flow; in fact, the heat transfer coefficient can be written as follows using the Nusselt number:

$$h=\frac{Nu\,k}{d} \qquad \text{(A.3)}$$

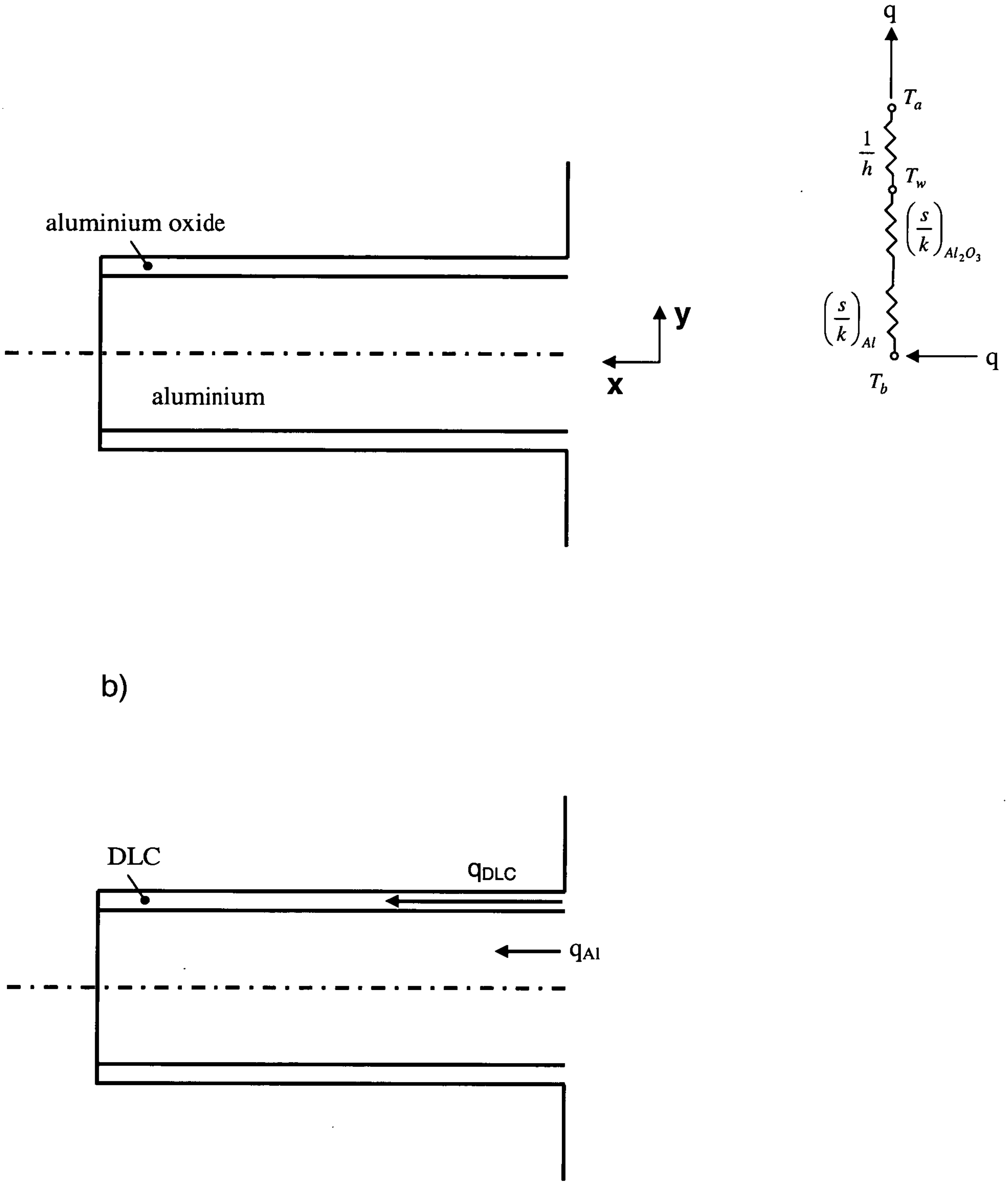

Figure A-7 Heat transfer paths and equivalent thermal circuits; a) is for the uncoated fin, b) is for the fin coated with DLC.

The estimated enhancement of the heat transfer coefficient due to the reduced fin gap because of the coating thickness is of few percent, negligible compared to the observed enhancement of 30%.

Considering practical development of the investigated technique, it would be much easier to deposit a conductive coating than to increase the surface roughness like has been done in previous works.

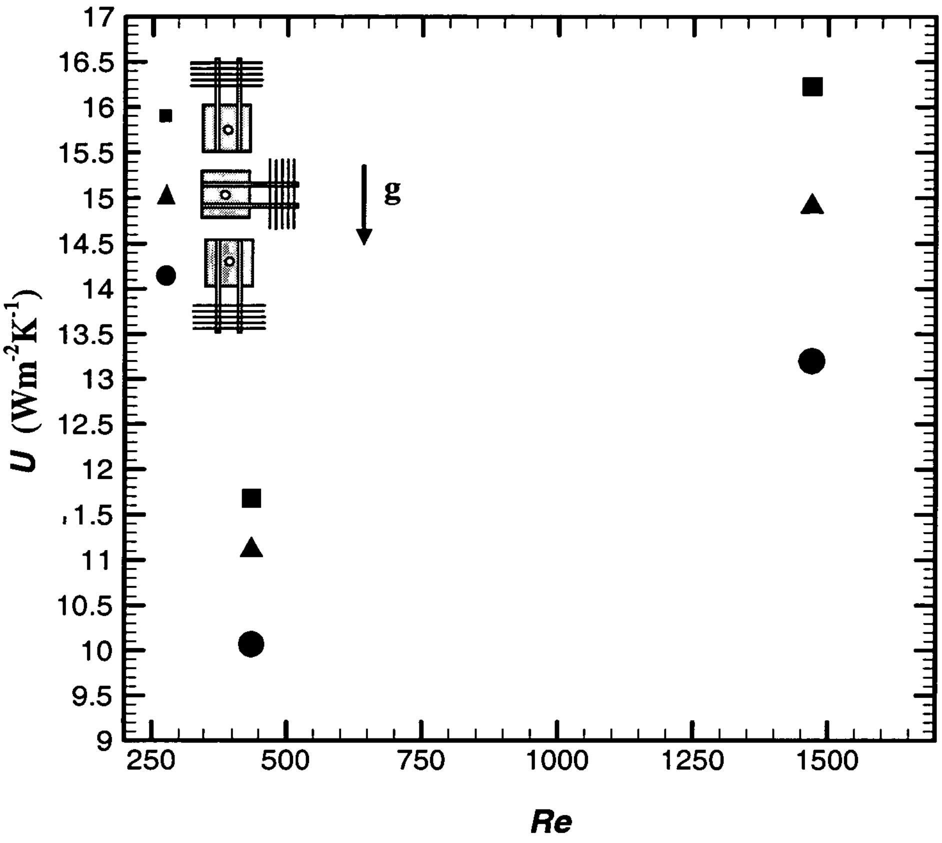

Figure A-8 Role of gravity on the heat transfer coefficient vs. *Re* for DLC coating.

Another aspect of the performance of the heat pipe has been investigated: the orientation with respect to gravity. Indeed microelectronics can be embarked onboard of vehicles where orientation can change, like aircraft. The unit has been tested in three different orientations: vertical, horizontal and upside down.

Results presented in Figure A-8 for the DLC coating show clearly the strong role played by gravity. This is only due to the hydrodynamics inside the heat pipes. Figure A-1 schematically depicts the hydrodynamics of the heat pipe internal operation. When heat is supplied to the heat pipe, evaporation occurs and the vapor with an increased pressure flows towards the condenser section where it condenses because heat is removed from the outside. The liquid is sucked in the wick structure and driven back to the evaporator because of the capillary forces action, closing the loop. Gravity influences the pumping effect in the liquid returning flow to the evaporator section. Gravity increases the pumping effect when the heat pipe is vertical, with the evaporator below the condenser, whereas it acts negatively if the heat pipe is upside down with the evaporator above the condenser. No effect of gravity is expected with the heat pipe in horizontal position.

A.5 Conclusions and outlook

It has been pointed out many times in this thesis that the most thermally loaded heat pipe section is the evaporator. However, the condenser section can also be important because it is ultimately the bottleneck of many cooling systems. In fact, more than 85% of the thermal resistance from a liquid-air cooling thermal solution is concentrated at its airside. A lot of work has been done in recent years on this section in order to improve the heat transfer resulting in a dramatic increase of the pressure drop penalty. In the present experimental study the overall heat transfer coefficient from the condenser section of a heat pipe made with aluminum fin surface has been enhanced by 30% with no penalty or even lower pressure drop.

A heat pipe unit used in cooling of microelectronics has been tested using a laboratory wind tunnel in order to investigate the effect on the heat transfer of a coating on the fin surface of the condenser heat pipe section. A DLC coating and another made of diamond particles have been compared with the uncoated surface. The results clearly demonstrated that using a highly conductive DLC coating has the same or even better effect in terms of heat transfer than that obtained using a granular coating made of industrial diamond particles. Although no measurement of the pressure drop has been performed in the present study, the same level of pressure drop is expected for the DLC coating, making of the present technique a quite attractive solution for heat transfer enhancement compared to other techniques.

Although the coating has been tested on the fin stack of a heat pipe unit, it can be applied successfully to enhance the heat transfer performance of any cooled extended surface heat exchanger that uses aluminum as substrate.

Finally, the effect of gravity on the heat transfer coefficient has also been investigated by positioning the heat pipe cooling unit around the tunnel exit section. The hydrodynamics of the heat pipe operation is thought to be responsible for the findings.

A.6 References

[1] Groll M., Schneider M., Sartre V., Zaghdoudi MC. and Lallemand M., 1998, *Thermal control of electronic equipment by heat pipes*, Rev. Gén. Therm., Vol. 37, pp. 323-352.

[2] Lin S., Sefiane K. and Christy J.R.E., 2002, *Prospects of confined flow boiling in thermal management of micro systems*, Applied Thermal Engineering, Vol. 22, No. 7, pp. 825-837.

[3] Dunn P.D. and Reay D.A., 1994, *Heat Pipes*, 4th ed., Pergamon Press Ltd., New York.

[4] Manfred G., Schneider M., Sartre V., Zaghdoudi M. C. and Lallemand M., 1998, *Thermal control of electronic equipment by heat pipes*, Rev. Gén. Therm. 37, pp.323-352.

[5] Garimella S.V. and Sobhan C.B., *Recent advances in the modeling and applications of nonconventional heat pipes*, Advances in Heat Transfer, Vol. 35, pp. 249-308.

[6] Lyman A.C., Stephan R.A., Thole K.A., Zhang L.W. and Memory S.B., 2002, *Scaling of heat transfer coefficients along louvered fins*, Experimental Thermal and Fluid Science, Vol. 26, pp. 547-563.

[7] Kobabandeh R. and Palm B., 2000, *An experimental investigation of heat transfer coefficients in vertical narrow channels*, Proc. Heat Transfer and Transport Phenomena in Microscale, Banff, Canada, Begell House Inc., ISBN 1-56700-150-5, pp. 217-221.

[8] Rowley F.J. and Patankar S.V., 1984, *Analysis of laminar flow and heat transfer in tubes with internal circumferential fins*, International Journal of Heat and Mass Transfer, Vol. 27, No. 4, pp. 553-560.

[9] Davalath J. and Bayazitoglu Y., 1987, *Forced convection cooling across rectangular blocks*, Journal of Heat Transfer, Vol. 109, pp. 321-328.

[10] Aliaga D.A., Lamb J.P. and Klein E.E., 1994, *Convection heat transfer distributions over plates with square ribs from infrared thermography measurement*, International Journal of Heat and Mass Transfer, Vol. 37, No. 3, pp. 363–374.

[11] Henry R.C., Hansman R.J. and Breuer K.S., 1995, *Hear transfer variation on protuberances and surface roughness elements*, Journal of Thermophysical Heat Transfer, Vol. 9, No. 1, pp. 175-180.

[12] Go J.S., Kim S.J., Lim G., Yun H., Lee J., Song I. and Pak Y.E., 2001, *Heat transfer enhancement using flow-induced vibration of a microfin array*, Sensors and Actuators, Vol. 90, pp. 232-239.

[13] DeJong N.C. and Jacobi A.M., 2003, *Flow, heat transfer, and pressure drop in the near-wall region of louvered-fin arrays*, Experimental Thermal and Fluid Science, Vol. 27, pp. 237-250.

[14] Leon O., De Mey G. and Dick E., 2002, *Study of the optimal layout of cooling fins in forced convection cooling*, Proceeding of 8th International Workshop on Thermal Investigations of ICs and systems, Madrid, Spain, pp. 260–265.

[15] Gentry M.C. and Jacobi A.M., 2002, *Heat transfer enhancement by delta-wing-generated tip vortices in flat-plate and developing channel flows*, Journal of Heat Transfer, Vol. 124, No. 6, pp. 1158– 1168.

[16] Biswas, G., Torii K., Fujii D. and Nishino K., 1996, *Numerical and experimental determination of flow structure and heat transfer effects of longitudinal vortices in a channel flow*, International Journal of Heat and Mass Transfer, Vol. 139, No. 16, pp. 3441–3451.

[17] Kiwan S. and Al-Nimr M.A., 2001, *Using porous fins for heat transfer enhancement*, Journal of Heat Transfer, Vol. 123, No. 4, pp. 790–795.

[18] Zhao Z. and Avedisian C.T., 1997, *Enhancing forced air convection heat transfer from an array of parallel plate fins using a heat pipe*, International Journal of Heat and Mass Transfer, Vol. 40, No. 13, pp. 3135-3147.

[19] Hinze J.O., 1975, *Turbulence*, 2nd ed., McGraw-Hill, New York.

[20] Kline S.J. and McClintock F.A., 1953, *Describing uncertainties in single sample experiments*, Mechanical Engineering, Vol. 75, pp. 3-8.

[21] Kundu M., Miyata N. and Ichikawa M., 2001, *Selective thermal desorption of ultrathin aluminum oxide layers induced by electron beams*, Applied Physics Letters, Vol. 79, No. 6, pp. 842-844.

[22] Cai A., Zhang H., Hua H. and Zhang Z., 2002, *Direct formation of self-assembled nanoporous aluminium oxide on SiO2 and Si substrates*, Nanotechnology, Vol. 13, pp. 627–630.

APPENDIX B

Tungsten-liquid metal heat pipes for cooling heavily thermally loaded rocket nozzle walls of spacecraft engine

B.1 Motivation

This work follows a previous investigation where a cooling solution based on traditional single phase technology using liquid metals was applied to cool the walls of a nozzle for a spacecraft rocket based on the Rubbia's idea for a Mars mission. It was concluded that a solution based on single phase cooling is possible only using a heavy and costly design that can only work for Earth tests. In fact, more than a third of the nuclear propulsion energy (1.5 MW) is necessary to run the cooling system using a substantial amount (6-7 Kg) of dangerous cooling fluid (sodium or at best lithium) which must also be warmed up and liquefied prior to engine start-up. This solution is an extreme one due to the very exceptional engine performance. The specific impulse (I_{sp}) of such a rocket must be of the order of 2,000–3,000 s, reachable only with a chamber temperature of around 8,000–9,000 K. These figures suggest that convectional cooling technology involving recirculation of the cryogenic propellant is insufficient and a different solution is sought. An effective solution to this problem could be based on the heat pipe concept. Heat pipes for high temperature and heat flux applications have appeared in the past even in the spacecraft sector, but this is the first time they are proposed to cool a rocket nozzle throat. The calculations performed in this study indicate that, by using a liquid metal as the heat pipe working fluid, a small number of heat pipes can effectively cool the throat region of one of the Rubbia Engine modules. The small temperature differences and especially the small amount of liquid metal needed, make of this solution a quite attractive and effective one not only for the Earth test module but also for the future spacecraft vehicle.

B.2 Background

Heat Pipes (HP) are widely used in thermal management of many high temperature devices. Born almost three decades ago specifically for space applications, they are now extensively and successfully applied to electronics and microelectronics cooling, bio-medical products and many others devices [1-3]. Lack of moving components and simple operation makes HP a very attractive, reliable and cost effective technology. HP are two-phase devices capable of transferring large heat fluxes (up to 200 MWm^{-2}) over a distance of the order of meters driven by small temperature drops (i.e., a few tens of degree), thus reducing drastically thermal stresses in the materials, and using a small quantity of working fluid.

Sodium and lithium HP can transfer heat fluxes up to 200 MWm^{-2} while remaining nearly isothermal along the evaporation-condenser direction [4-6]. The equivalent thermal conductivity of a HP is $\sim 10^4$ times that of copper and silver [6]. Although lithium HPs [7] can transfer along their evaporation-condenser (axial) direction heat fluxes up to 200 MWm^{-2}, the average transversal (radial) heat flux they can transfer is much less, being of the order of 20 MWm^{-2}. Alkali metal HPs are commonly used to cool fusion reactors in stationary and/or cyclic operation, with a lifetime ranging from a minimum of 3 years up to 10 years [6-7].

The HP solution suits space requirements very well due to their reliability and low weight, giving a positive impact on mission costs. In space applications HP have been extensively used for satellite thermal control and have been proposed to cool wing leading edges in future hypersonic vehicles. The high cooling demand ($\sim$0.5 MWm^{-2}) encountered on the leading edge of a hypersonic vehicle during re-entry or sustained flight led to the proposal [8] of using alkali metal HP as an alternative to the current passive concepts which typically use the radiative properties of carbon-carbon insulation. In fact, Camarda and Masek [8] pointed out how the HP concept overcomes the problem of non-symmetrical heat flux profile on the leading edge by adjusting the location and length of the evaporator and condenser section accordingly. Analysis of the HP startup presented by Camarda and Masek [8] shows that, upon reaching steady state operation, the temperature difference between the evaporator and the condenser might be as low as 5.6 °C, minimizing thermal stress encountered with a passive solution. Glass and Camarda [9] also proposed a refractory metal HP to cool carbon-carbon wing leading edges. Lithium was the working fluid and tungsten the HP wall material. The HP were embedded in the carbon-carbon structure and although the thermal expansion coefficient for tungsten is very similar to that of many carbon-carbon architectures, a layer of graphite was deposited between the two materials in order to reduce the thermal stress. Spanwise HP were used in order to redistribute the peaks of temperature around a failed chordwise HP. Many other authors [10-12] demonstrated numerically and experimentally the advantages of using alkali metal HP to cool the leading edges of hypersonic vehicles, focusing especially on HP startup; this, in fact, seems to be the most critical operation stage, implying temperature gradients of ~100 Kcm^{-1} along the walls while at the same time experiencing low heat transport due to the vapor sonic limit. Corrosion in alkali metal HP is a serious issue, because it can quickly lead to their failure since elements soluble in the alkali fluid can be transferred from the condenser to the evaporator where they can deposit. Life tests carried on with alkali metal HP [13-18] demonstrated how this problem could be responsible for HP failure. Alkali-resistant alloys have been developed: the lifetime of the lithium tungsten-rhenium alloy tested by Quataert et al. [13] varied from many years at 1,600 °C to one month at 1,800 °C. The corrosion pattern was found to be strongly dependent on the shell material rather than on the working fluid or the operational conditions [13]. Another important issue in the use of HP is the presence of non-condensable gases inside the pipe. These gases, coming either from shell-working fluid interaction, or more likely introduced during the manufacturing procedure, are swept to the end of the condenser and cause a considerable temperature drop in that region, resulting in non-isothermal HP operation [18].

B.3 Rocket nozzle cooling by heat pipes

Current Liquid Rocket Engine (LRE) nozzles are usually cooled by re-circulating cryogenic fuel. The pump maintaining the flow inside the nozzle jacket must also overcome the head loss inside the coolant passages (often of order many tens of bars), raising rocket launcher weight and mission costs accordingly. Ablative materials are instead typical used for the most thermally loaded sections of non reusable Solid Rocket Motors. For certain future applications, the I_{sp} of the rocket engine may be ~O(1,000) s: this is the case of nuclear thermal rockets and in particular of the so-called nuclear "Rubbia Engine" conceptually designed for a future manned Mars mission; the amount of propellant available is much less than that needed by convective cooling, while at the same time the large area contraction ratio (~400) along with the high temperature reached (7,500 °C) in the nozzle throat lead to heat flux peaks ~50 MWm^{-2}. Faced with this problem, Bruno and Buffone [19] demonstrated the feasibility of circulating an alkali metal (sodium or lithium) in the liquid phase inside the nozzle jacket. However, it was also pointed out that the associated power necessary to pump the coolant is relatively high (~0.5 MW, one third of the power of the engine considered) for the class of thrust of the Rubbia Engine (~1000 N), and that the mass of the coolant (6-7 Kg) may raise important safety concerns especially for Earth testing.

The purpose of the present study is to continue the analysis started in [19], focusing on cooling the Rubbia Engine using HP, in particular, on cooling the nozzle of an individual module of the Rubbia Engine already envisioned to be tested. In fact, proof-of-principle of this engine has been planned around a single engine module, which will be much smaller (about 1/40) of the full-size engine. While easing many testing problems, the reduced size of this module will in fact pose a much bigger cooling challenge, since the nozzle throat of such a module (radius ~0.5 cm) [19] will be roughly a factor of ten smaller than in the full size of the planned engine. These difficulties can be overcome using HP transferring the heat fluxes to a space radiator.

Figure B-1 is a sketch of the HP operation when none of the HP limitations (see [1] for details) is exceeded.

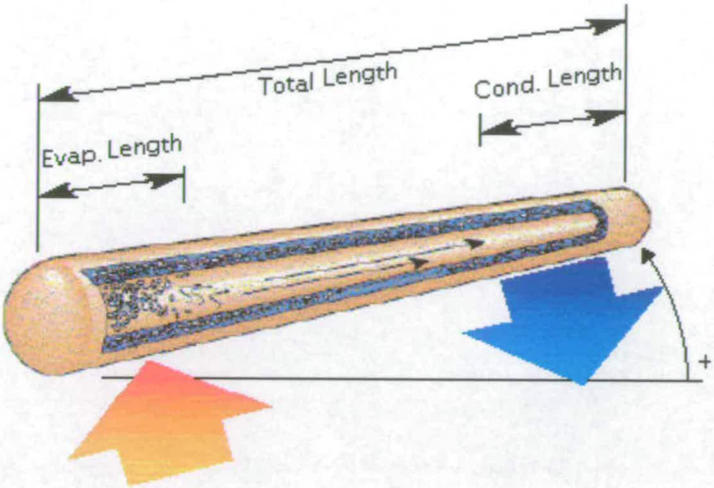

Figure B-1 Heat Pipe operational principle.

The working fluid circulates in the HP in a closed loop. At the evaporator section heat is transferred from the heat source to the working fluid inside the heat pipe; by evaporating, vapor pressure and temperature of the fluid increase. Because of the increasing pressure, the vapor flows along the adiabatic section reaching the condenser, where heat is released to the surroundings and condensation occurs. The condensed liquid is sucked in the capillary wick structure and driven back to the evaporator by capillary pressure, closing the loop. One of the advantages of using a HP is that the length of its various sections could vary greatly so that HP can redistribute thermal energy even when heating is non-symmetrical. This peculiar characteristic makes the HP a suitable solution for cooling nozzle walls, characterized by the strong non uniform heat flux profile along the nozzle axis. A typical heat flux profile of the Rubbia single module nozzle [19] is shown in Figure B-2, suggesting that HP absorbing heat from the convergent and throat region could transfer it down to the nozzle divergent section, where the temperature is much lower, and release it there to the surroundings.

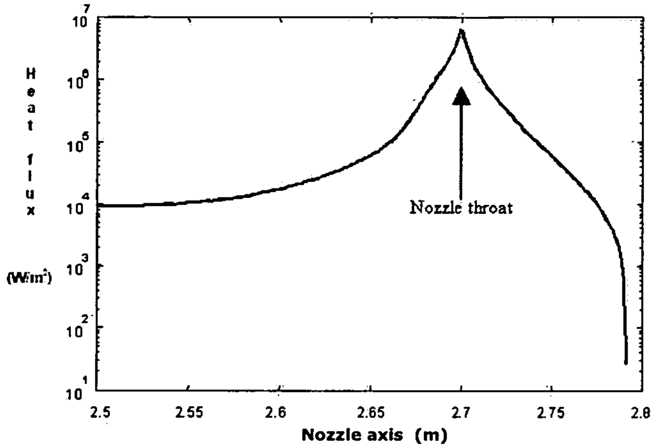

Figure B-2 Heat Flux profile along the nozzle axis.

Following this strategy, the HP evaporator should be wrapped around the nozzle convergent and throat, and the condenser somewhere around the divergent section of the nozzle (see Figure B-3).

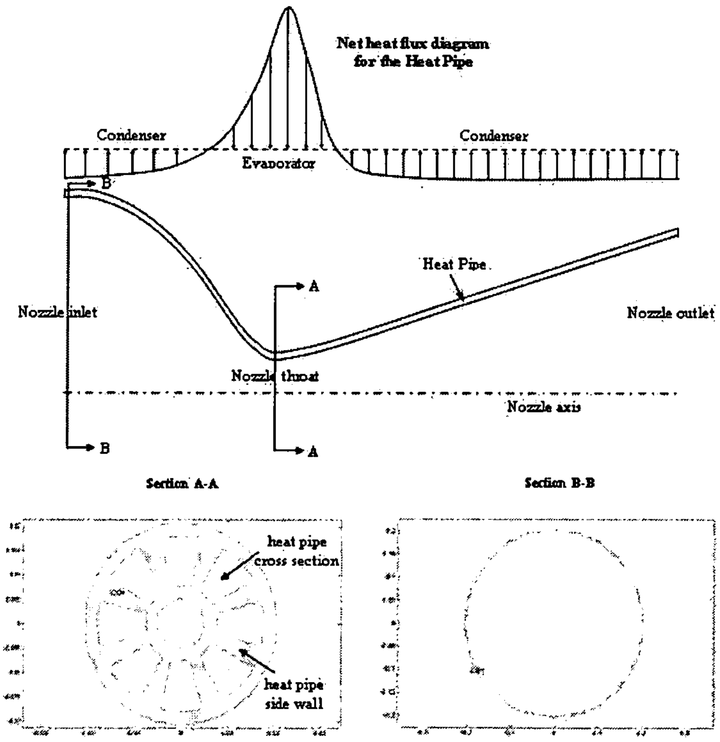

Figure B-3 Schematic of the heat distribution along the heat pipe longitudinal axis and heat pipe cross sections (cross sections to scale).

Heat abstracted by the evaporator and transferred to the HP condenser would be mainly radiated away, but could also be transferred to the colder engine propellant by forced convection. As already pointed out in [19], in a more conventional single phase cooling jacket system the alkali metal coolant, initially solid, must be liquefied prior to the engine startup. Using a HP this melting stage is no longer necessary, the only precaution being a uniform distribution of the working fluid in the wick structure of the HP prior to the engine startup. In fact, the HP can start to operate with frozen coolant, the only limitation being the operational sonic limit on the axial heat flux transferred. In fact, during the startup the heat abstracted is used to liquefy the working fluid and very little vapour is present. The low vapour density could then cause the vapor velocity to reach the sonic speed, thereby 'choking' the heat flux transferred [1]. The sonic limit does not necessarily result in HP failure, but can raise the operating temperature, weakening the shell structure and possibly leading to other and more dangerous HP limitations [9].

The simplest HP cross section is circular, but this solution does not necessarily suit all applications. In order to match different requirements, different shapes (rectangular, triangular, etc.) have been adopted in the past. In the present work a non-circular cross section is chosen (see Figure B-3). The disadvantage of using a non-optimal non-circular HP cross section is compensated here by a simpler construction and a more effective cooling capacity. The technology to build HP for high temperature applications with non-circular cross sections is already mature as shown in details in [10].

B.4 Materials and geometrical considerations

Bruno and Buffone demonstrated in a previous work [19] that, in order to handle a heat flux peak of 50 MWm^{-2}, the wall material must have both a high melting point and high thermal conductivity. In the cited work [19], tungsten was found to be the material suitable for this application. Therefore, also in the present numerical analysis tungsten was chosen as the reference wall material as it matches well with the alkali metals to be used as HP working fluids. Alkali metals (sodium or lithium) have been chosen as the HP working fluid along with silver, the main reason being their appealing thermal properties (i.e., high boiling point and high latent heat of vaporization). The role played by corrosion in high temperature alkali metal heat pipes is important, as underscored in past works [13-18]. The same considerations and suggestions made in the references cited can be applied to the present case.

The axi-symmetric nozzle geometry helps in the most loaded sections of the Rubbia Engine module. The heat flux peak (~50 MWm^{-2}) 'spreads' through the wall material decreasing linearly with the local radius; in fact, the product of heat flux times the section radius must be conserved in the radial direction of cylindrical geometry. The number of HP to insert circumferentially around the throat is a compromise between two different requirements. A large number of HP would help to keep the wall temperature below its melting point in case of HP failure. On the other hand, too many HP would result in their individual cross section being too small, raising pressure drop, weight and fabrication cost. As a result of these qualitative considerations, the number of HP assumed in the present analysis is just 8. Their cross sections are shown in the insets of Figure B-3. The HP shape in the throat nozzle section has been chosen such as to have a sufficient height of 2.5 mm at the exit nozzle section and 0.6 mm at the inlet nozzle section, keeping the HP cross section area constant. This is an essential requirement for efficient working operation. The side wall thickness of the HP is considerably high at the inlet and exit nozzle sections (see Figure B-3). This does not cause problems at the exit section, due to the fact that in this region the nozzle propellant temperature is much lower than the HP temperature and thus the HP can effectively release heat. Concerns exist at the inlet section, where the hot propellant is transferring heat to the walls. In fact, along the nozzle convergent the heat flux and temperature are high and the width of each HP is large. Should a HP fail, the integrity of the nozzle could be seriously threatened. A solution to this problem is adopting spanwise HP in the convergent section, as schematically shown in Figure B-4.

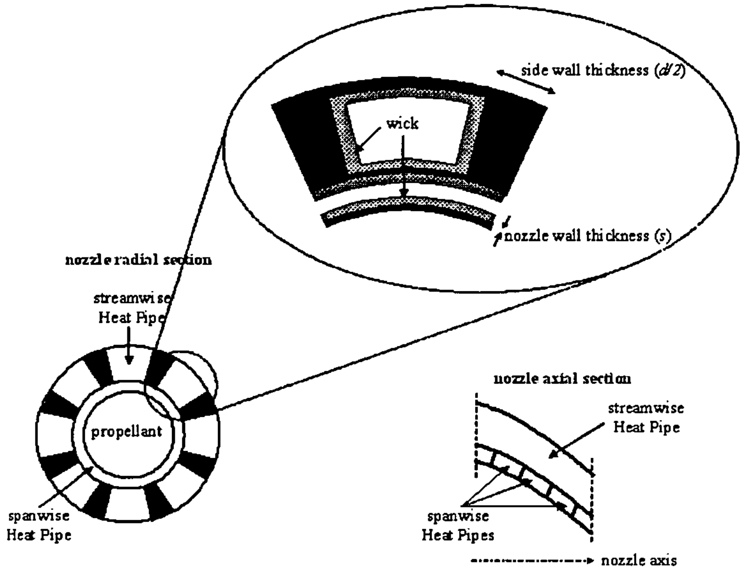

Figure B-4 Streamwise and spanwise HP.

Figure B-5a shows the spanwise HP operation with a failed streamwise HP. The spanwise HP redistributes the thermal load of the failed streamwise HP to the adjacent working HP of the row. Heat is adsorbed along the failed HP (arc A in Figure B-5a) and is released on the streamwise working HP (arcs B in Figure B-5a).

This solution is effective with a failed HP but not when all streamwise HP are working properly. A solution to this other problem is to have two consecutive streamwise HP operating at different temperatures (as sketched in Figure B-5b). This could be obtained in practice by filling consecutive streamwise HP with a different amount of working fluid. In fact, the filling charge strongly affects the HP performance and its temperature profile. For this scenario the evaporator and condenser sections of the spanwise HP are located in correspondence to the streamwise HP with high and low operational temperature, respectively.

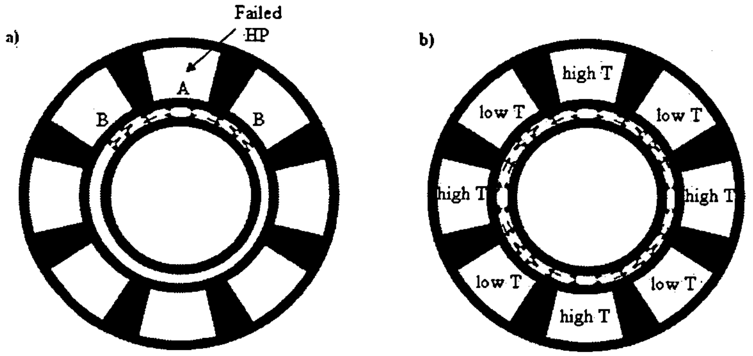

Figure B-5 Spanwise HP operation.

B.5 Physical and numerical model

The heat flux between the hot propellant (e.g., hydrogen) and the wall changes considerably along the nozzle axis (see Figure B-2). The heat flux peaks very close to the nozzle throat because of the high propellant temperature and the large gas velocity in this region. In order to predict the nozzle wall temperature, two critical nozzle sections have been examined: the throat, where the heat flux peaks, and the inlet, where the HP cross section is broader. The heat transfer problem though the nozzle wall shell has been modelled using the FEMLAB v.2.3 numerical code. FEMLAB is a Finite Element Method (FEM) commercial code developed by Comsol, Inc. working under the Matlab environment. The problem is axi-symmetrical, thus only a portion of the entire throat cross-section (inset of Figure B-3) is considered as a computational domain reproduced in Figure B-6 (that is, half the streamwise HP seen in the inset section of Figure B-3) in order to limit computational time. The boundary conditions associated to this computational domain are reported in Figure B-6. The heat flux peak of 50 MW/m^2 is imposed at the boundary A. As mentioned earlier, one of the principal features of a HP is its isothermal behavior along its whole cross sections. Therefore, the HP internal surface B in Figure B-6 is assumed to be isothermal and at the working fluid temperature; this is done in order to simulate an almost infinite thermal conductivity for the heat pipe (as stated earlier, the corresponding HP thermal conductivity is ~10^4 times that of copper).

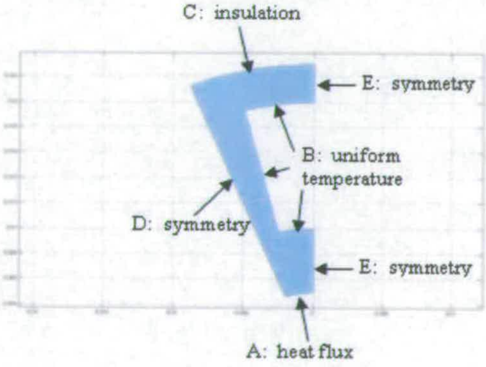

Figure B-6 Computational domain and boundary conditions.

The boundary C has been considered insulated (adiabatic); in reality, heat is radiated from this surface to the ambient surroundings (e.g., the ambient conditions in the test facility), but this heat flux is negligible, being of the order of few KWm^{-2} as shown clearly in [19] with respect to the incoming flux on the boundary A that is of the order of 50 MWm^{-2}. On the D and E boundaries a symmetry condition has been assumed.

Due to the nature of the problem, a linear time-independent solver has been used. The mesh for most of the simulations for the test case at the nozzle throat (shown in Figure B-7) consisted of 104 nodes and 157 elements.

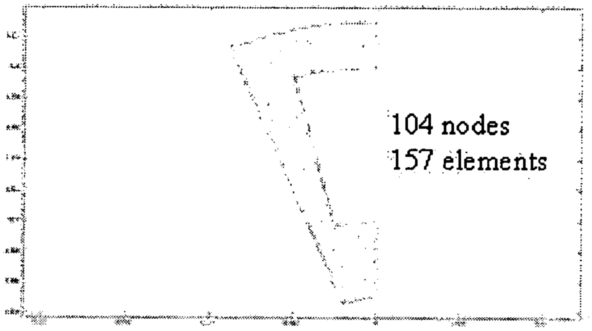

Figure B-7 FEM mesh for the case test.

The parametrical analysis on the test case yields the dependence of the nozzle wall temperature on three key parameters: the type of coolant, the nozzle thickness (*s*) and the HP side wall thickness (*d*) as indicated in the inset of Figure B-4.

The case of failed streamwise HP in the row has also been analyzed; the number of failed HP has been increased one by one from 1 to 7, this last leaving only one working HP. In this case the computational domain consists of all the HP in the row.

Suitable boundary conditions must be considered when spanwise HP are employed. In fact, here the whole length of the spanwise HP lies on the same nozzle cross section (as seen in Figures B-4-5), so that a constant temperature boundary condition is not appropriate: with no temperature gradients along the HP no heat is transferred. A more reasonable approach is to consider the spanwise HP like a thermally "super conductive" material. So, instead of applying boundary conditions, spanwise HP are mimicked by a material with a thermal conductivity of 10,000 $Wm^{-1} K^{-1}$. This is a reasonable assumption as the heat pipe is 10^4 time more conductive than copper.

B.6 Results and discussion

A parametric analysis was performed for the test case at the nozzle throat with the following quantities as parameters (see Figure B-4): nozzle wall thickness (*s*), HP side wall thickness (*d*) and type of coolant fluid. The three coolants considered were sodium, lithium and silver, at temperatures 1,000 °C, 1,600 °C and 2,000°C, respectively. These temperatures are chosen on the basis that the fluids can exist as liquid phases with sufficient margin of safety. The actual temperature then depends on the amount of fluid and the heat pipe dimensions. It is not attempted here to evaluate these aspects as a qualitative study is being carried out to support the idea. With a single failed HP the effect of the HP side wall thickness (*d*) has also been investigated (note that in this case two halves of two adjacent HP have been considered as the computational domain).

Figure B-8 shows a typical temperature map for the test case at the nozzle throat. As expected, the temperature peaks at the internal nozzle wall surface in correspondence of the middle of the HP side wall.

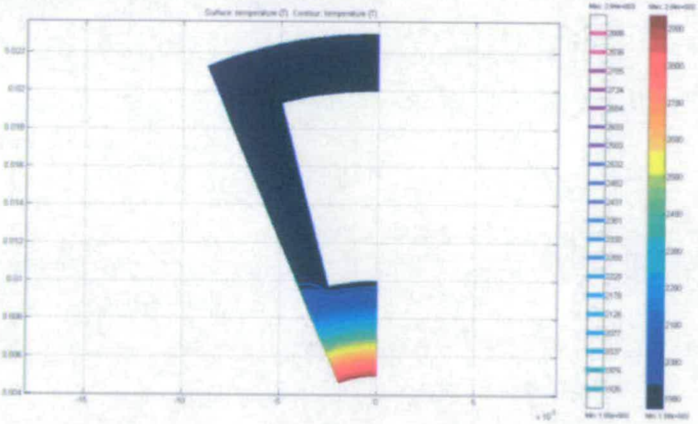

Figure B-8 Typical temperature map for the case test.

A HP could fail for many reasons. In such a case the HP acts like a cavity with no heat removal capability. The neighbouring HP will therefore cool the surrounding walls of the failed HP. Maintaining a wall temperature sufficiently lower than the melting temperature of the material depends essentially on the HP working temperature and on the geometry. In the present case, because of the particular geometry employed, one failed HP in a row does not affect the integrity of the nozzle, since the wall temperature remains sufficiently far from the tungsten melting point. The typical temperature map in the case of one failed HP is given in Figure B-9, showing that the peak occurs now in the middle of the failed HP.

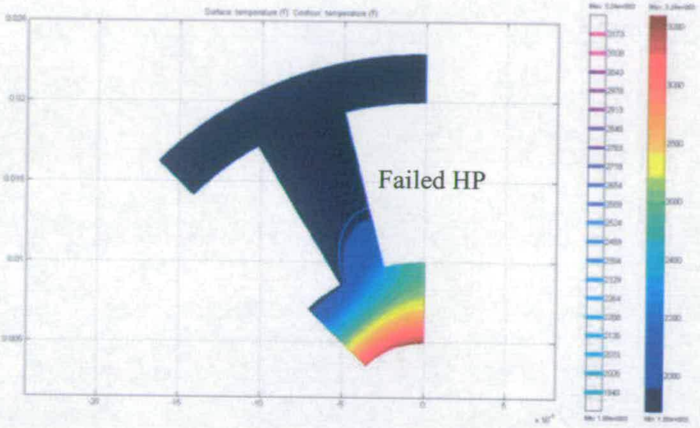

Figure B-9 Typical temperature map for a failed heat pipe.

Results of the parametric analysis performed are reproduced in Figure B-10-12. Figure B-10 shows the maximum nozzle wall temperature versus the nozzle wall thickness (*t*) for the three coolants considered; the dotted line is the tungsten melting point (3,400°C). The minimum wall thickness considered is dictated by structural limitations, not by heat transfer; although the maximum engine module pressure (in this particular group of simulations) is 6 atm, the high operational temperature may weaken the shell material strength. Although no structural analysis is performed here, a nozzle wall thickness (*s*) of 5 mm is assumed in the following simulations for the analysis of the other parameter.

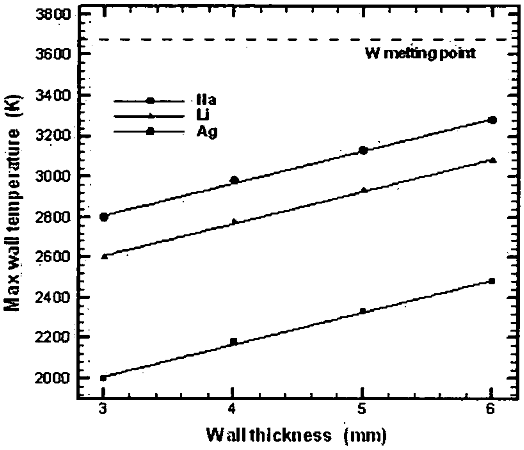

Figure B-10 Max nozzle wall temperature vs. wall thickness.

Figure B-11 shows the maximum nozzle wall temperature versus the HP side wall thickness (*d*), indicating this parameter plays a marginal role with respect to the nozzle wall thickness (*s*). This is essentially due to the shape and dimensions of the HP with respect to the nozzle throat dimensions.

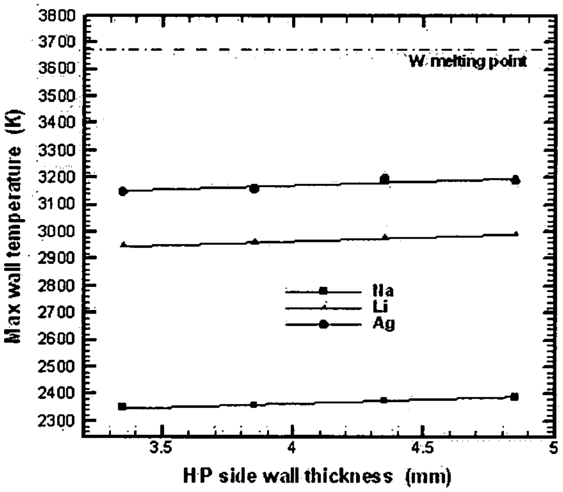

Figure B-11 Max nozzle wall temperature vs. heat pipe side wall thickness.

The results shown in Figure B-12 for the case of a failed HP, where the HP side wall thickness (*d*) has been varied, can be explained in the same way as those of Figure B-11 and will not be repeated again. When the number of failed HP increases, the ability of the working HP in the row to cool the entire cross section is dramatically reduced.

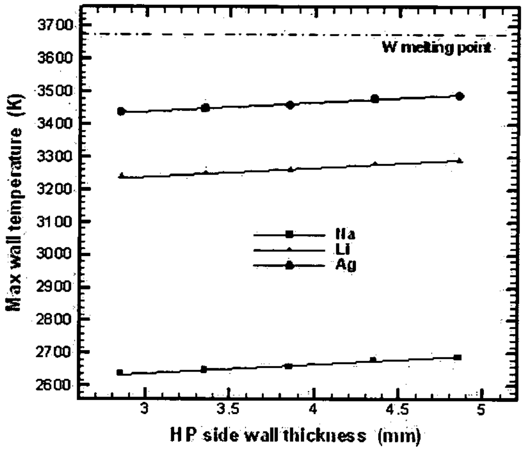

Figure B-12 Max nozzle wall temperature vs. heat pipe side wall thickness for a failed heat pipe.

As can be seen from Figure B-13, with three consecutive failed HP the wall maximum temperature jumps to 4,320 K, that is, above the tungsten melting point. Adopting spanwise HP also in the nozzle throat section, would redistribute more evenly the thermal load among the working streamwise HP of the row allowing a large number of possible failed streamwise HP.

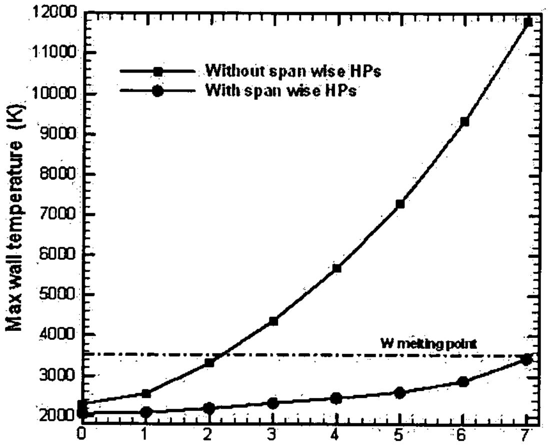

Figure B-13 Max nozzle wall temperature vs. No. of failed streamwise HP at the nozzle throat.

Figure B-14 shows the temperature map with (**a**) and without (**b**) spanwise HP. Note the difference in the maximum wall temperature with all streamwise HP working with and without spanwise HP: this is due to the large thermal conductivity of the spanwise HP.

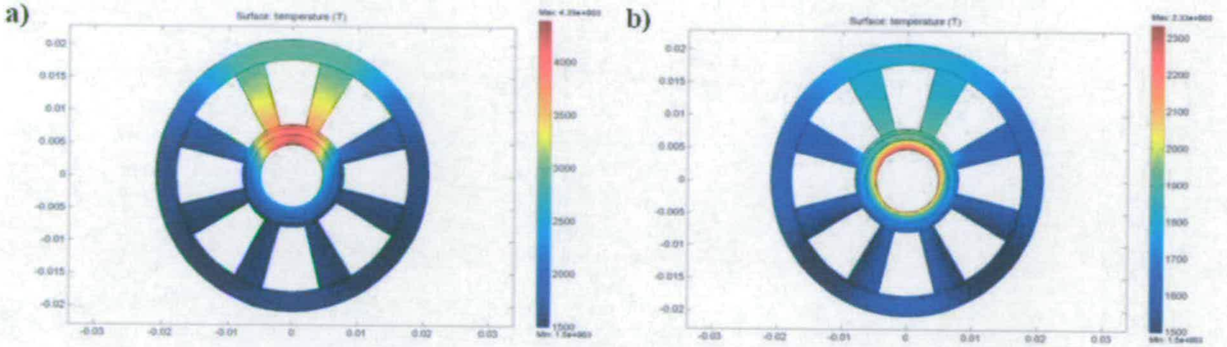

Figure B-14 Temperature map without (**a**) and with (**b**) spanwise HP.

It might be pointed out that although these results show that even with only one streamwise HP working the integrity of the nozzle is preserved using spanwise HP, this picture is a bit unrealistic. The simulations do not consider the limit imposed by the maximum heat flux handled by the alkali metal HP. In fact, the heat flux transferred by the hot propellant gas to the nozzle wall must be handled by the working streamwise HP in the row. Assuming the HP can soak a maximum heat flux limit of 25 MWm^{-2} and a nozzle wall thickness (s) of 5 mm, the maximum number of failed HP in the row is therefore 3. Figure B-15 shows the maximum wall temperature versus the number of failed streamwise HP in the row at the nozzle inlet section. The reduced heat flux in this region of the nozzle leads to lower wall temperatures with respect to those at the throat section.

In conclusion, for all cases analyzed in this study, the maximum predicted nozzle wall temperature could be kept sufficiently lower than the tungsten melting point. This shows the HP concept can be successfully applied to the cooling of extremely high temperature nozzles.

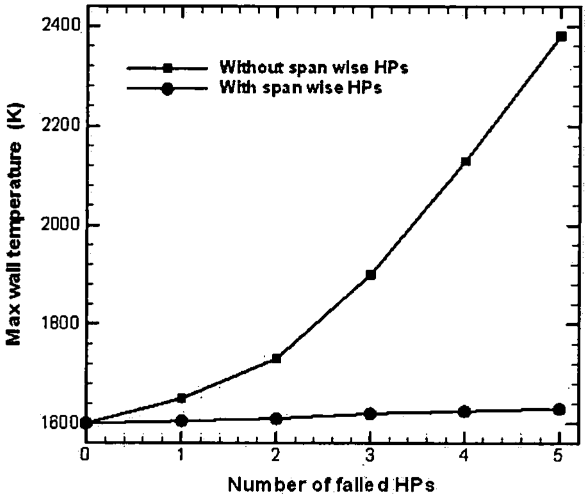

Figure B-15 Max nozzle wall temperature vs. No. of failed streamwise HP at the nozzle inlet.

B.7 Conclusions

This analysis follows up a previous study where the cooling problem of the so called "Rubbia Engine" module of a spacecraft vehicle for manned Mars mission was investigated. In the present study HP are proposed as an alternative to single phase cooling solution suggested in the former study.

The results of this analysis, conceptual as they are, indicate that HP (using alkali metals or silver as working fluids and tungsten as shell material) may be a very effective technology for difficult or extreme cooling problems as in the case of future high specific impulse rocket engines, and especially for those cases where the flow rates of cryogenic liquid is insufficient. The Rubbia Engine chosen as an application for HP technology is such an extreme case, given its 2,000–3,000 s impulse and its 8,000–9,000 K chamber temperature. This temperature notwithstanding, the calculations reported indicate HP can cool the throat region of one of the engine modules.

A parametric analysis of the nozzle wall thickness (*s*), HP side wall thickness (*d*) and working fluid show that even in the case of a failed streamwise HP, neighboring streamwise HP in that row can effectively keep the nozzle wall temperature below the shell material melting point. The nozzle wall thickness (*s*) was found to be the most influential parameter. This fact is explained with the particular geometry and dimensions of the streamwise HP with respect to the nozzle throat dimension. For all cases analyzed, the nozzle wall temperature is predicted to be sufficiently lower than the melting point of the shell material.

In conclusion, the analysis demonstrates that alkali metal or silver HP are applicable to highly thermally loaded nozzles when a conventional solution is not possible.

B.8 References

[1] Dunn P.D. and Reay D.A., 1994, *Heat Pipes*, 4th ed., Chapter 7, Pergamon Press Ltd., New York.

[2] Faghri A., 1995, *Heat Pipe Science and Technology*, Taylor & Francis, London.

[3] Peterson G.P., 1994, *An Introduction to Heat Pipes*, Wiley, New York.

[4] Bystrov P.I., Kagan D.N. and Shpilrain E.E., 1990, *Liquid-Metal Coolants for Heat Pipes and Power Plants*, Hemisphere, New York, p. 272.

[5] Ivanovsky M.N., Sorokin V.P. and Iagodkin I.V., 1978, *Physical Principles of Heat Pipes*, Atomizdat, Moscow.

[6] Kovalenko V., Khripunov V., Antipenkov A. and Ulianov A., 1995, *Heat-pipes-based first wall*, Fusion Engineering and Design, Vol. 27, pp. 544-549.

[7] Makhankov A., Anisimov A., Arakelov A., Geov A., Jablokov N., Yuditskiy V., Kirillov I., Komarov V., Mazul I., Ogorodnikov A. and Popov A., 1998, *Liquid metal heat pipes for fusion applications*, Fusion Engineering and Design, Vol. 42, pp. 373-379.

[8] Camarda C.J. and Masek R.V., 1981, *Design, Analysis and Tests of a Shuttle-Type Heat-Pipe-cooled Leading Edge*, Journal of Spacecraft and Rockets, Vol. 18, No. 1, pp. 71-78.

[9] Glass D.E. and Camarda C.J., 1990, *Preliminary Thermal/Structural Analysis of a Carbon-Carbon/Refractory-Metal Heat-Pipe-Cooled Wing Leading Edge*, Proceeding of the 1st Thermal Structural Conference, Nov. 13-15, Charlottesville, USA, pp. 301-322.

[10] Boman B. and Elias T., 1990, *Tests on a Sodium/Hastelloy X Wing Leading Edge Heat Pipe for Hypersonic Vehicles*, 5th Joint Thermophysics and Heat Transfer Conference, June 18-20, Seattle, WA, USA.

[11] Clark L.T. and Glenn G.S., 1988, *Design Analysis and Testing of Liquid Metal Heat Pipes for Application to Hypersonic Vehicles*, AIAA Thermophysics, Plasmadynamics and Laser Conference, June 27-29, San Antonio, Texas, USA.

[12] Colwell G.T., Jang J.H. and Camarda C.J., 1987, *Modelling of startup from the frozen state*, Proceeding of the 6th International Heat Pipe Conference, May, Grenoble, France.

[13] Quataert D., Busse C.A. and Geiger F., 1973, *Long time behaviour of high temperature tungsten-rhenium heat pipes with lithium or silver as working fluid*, Proceeding of the International Heat Pipe Conference, October 15-17, Stuttgart.

[14] Busse C.A., Geiger F., Quataert D. and Pötzschke M., 1966, *Heat pipe life-tests at 1600 °C and 1000 °C*, Record of the Thermionic Conversion Specialist Conference, Institute of Electrical and Electronic Engineers, New York, USA, pp. 149-158.

[15] Grover G.M, Kemme J.E. and Keddy E.S., 1968, *Advances in heat pipe technology*, 2nd International Conference on Thermionic Electrical Power Generation, Euratom Report EUR 4210 f.e., pp. 477-490.

[16] Quarterly status report on the space electric R and D program for the period ending January 31, 1969, part I, Los Alamos Scientific Laboratory, Report LA-4109-MS.

[17] Sena J.T. and Merrigan M.A., 1990, *Niobium 1% zirconium/potassium and titanium/potassium life-test heat pipe design and testing*, Proceeding of the 7th Symposium Space Nuclear Power System, January 7-11, Albuquerque, NM, pp. 848-852.

[18] Tu S.T., Zhang H. and Zhou W.W., 1999, *Corrosion failures of high temperature heat pipes*, Engineering Failure Analysis, Vol. 6, pp. 363-370.

[19] Bruno C. and Buffone C., 2002, *Nozzle Cooling in the Future: Rubbia's Engine Test Facility*, Proceeding of the 23rd International Symposium on Space Technology and Science, May 26-June 2, Matsue, Japan.

VITA

Cosimo is a simple guy from a small village in the Southern Italy. Growing up in a quite contradictory land (Northern Calabria) where the amazing and breathtaking landscapes formed by green hills covered by olive trees, the florid Sibari plain immersed in the aroma of juicy oranges and lemons, surrounded by mountains at north (Pollino) and in the middle (Sila) and gently touched by two marvellous and calm seas (Jonico and Tirreno) in the heart of the Mediterranean sea, make a rough contrast with up to 40% of unemployment among the younger population, emigration and criminality. After completing his secondary school, he moved in Rome for undergraduate studies where he graduated in Aerospace Engineering in October 2000 from the Universitá di Roma "La Sapeinza". Just after a brief experience at the Italian Space Agency (ASI) he joined THE UNIVERSITY *of* EDINBURGH for his PhD in October 2001.